A RANDOM MATRIX APPROACH TO LONG RANGE ACOUSTIC PROPAGATION IN THE OCEAN

By

KATHERINE CHRISTINA HEGEWISCH

A dissertation submitted in partial fulfillment of
the requirements for the degree of

DOCTOR OF PHILOSOPHY

WASHINGTON STATE UNIVERSITY
Department of Physics and Astronomy

DECEMBER 2010

ProQuest LLC
789 East Eisenhower Parkway
P.O. Box 1346
Ann Arbor, MI 48106-1346

To the Faculty of Washington State University:

The members of the Committee appointed to examine the dissertation of KATHERINE CHRISTINA HEGEWISCH find it satisfactory and recommend that it be accepted.

Steven Tomsovic, Ph.D., Chair

Philip L. Marston, Ph.D.

Mark G. Kuzyk, Ph.D.

ACKNOWLEDGMENT

The author would like to thank the thesis advisor, Dr. Steve Tomsovic, for his patience, kindness, guidance and support throughout this project. The author would like to thank past group members, Dr. Nicholas Cerruti and Dr. Konstantin Kouptsov, for their guidance, teachings and encouragement. The author would like to thank friends, Dirk Robinson and Xavier Perez-Moreno, for their encouragement, support and advice.

The author would like to thank the organizations who funded this research. The work contained in this dissertation was supported by the National Science Foundation, a NASA space grant fellowship and a College of Sciences research assistantship. The computational resources for this research was supported in part by the National Science Foundation through TeraGrid resources provided by NCSA. TeraGrid systems are hosted by Indiana University, LONI, NCAR, NCSA, NICS, ORNL, PSC, Purdue University, SDSC, TACC and UC/ANL [1]. The author was supported by the Open Science Grid to attend a grid computing summer school, which was instrumental in utilizing the resources of the Teragrid to completion of this research.

A RANDOM MATRIX APPROACH TO LONG
RANGE ACOUSTIC PROPAGATION
IN THE OCEAN

Abstract

by Katherine Christina Hegewisch, Ph.D.
Washington State University
December 2010

Chair: Steven Tomsovic

Low frequency sound propagates in the ocean within a wave guide, formed by the confining effects of temperature, salinity and pressure on the sound speed. This wave guide enables long range acoustic propagation upwards of 3000 km. Within the wave guide, sound scatters due to range dependent sound speed oscillations from internal waves. These weak perturbations in the sound speed serve to randomize the acoustic signal so that the structure formed by the time series of arrivals at the receivers (i.e. the timefront) contains only minimal average information about the propagation through the action of a generalized central limit theorem. The goal of this study is to characterize this remaining information by the parameters of a statistical ensemble model for the propagation. The propagation is described by the evolution of a unitary propagation matrix, whose elements are the complex probability amplitudes for modal transitions during the propagation. The ensemble model is constructed from a product of unitary random matrices utilizing complex Gaussian random variables with minimal information about the propagation to 50 km stored in a matrix of variances and a vector of mean phases. A comparison of the properties of the average intensity timefront resulting from this ensemble model is made with those from the simulated propagations for several ranges. The results of this study suggest that a random matrix model is an appropriate model for characterizing the information contained in the acoustic timefronts at long ranges.

TABLE OF CONTENTS

List of Tables

List of Figures

LIST OF SYMBOLS

Acoustic Propagation Model Notation

$Re[\Phi]$	Acoustic Pressure	35
$\Phi(z,t;r)$	Acoustic Timefront	35

Sound Speed Model Notation

c	Speed of Sound in Ocean	35
$c_0 = \frac{1.49km}{s}$	Minimum Sound Speed	38
δc	Fluctuations about c_0	38
c_{wg}	Sound Speed Due to Wave Guide	40
c_{iw}	Sound Speed Due to Internal Wave Fluctuations	40
n	Branch Number	20
$V_j(z)$	Depth dependence of internal wave mode j in sound speed model	48
$g(z;z_{st}$	Filter Function for smoothing of internal wave sound speed model	47
$h(z)$	Smooth filtering function	47
τ_{st}	Filter width for surface filter	47
z_{st}	Depth Location for Beginning of Filtering of internal wave sound speed model	47

Ensemble Model Notation

C	Unitary Propagation Matrix of complex probability amplitudes	65
$C_{m,n}$	Either a general matrix element or the off-diagonal elements of the matrix C (depending on context)	65
$C_{n,n}$	The diagonal elements of the matrix C	65
U	Building Block Model for the Unitary Propagation Matrix at 50 km	139
A	Hermitian Matrix Used in Construction of Unitary Matrix	140
$A_{n,n}$	The diagonal elements of the matrix A	**??**
Λ	Unitary Diagonal Matrix of Average Phases of $C_{n,n}$	140

Timefront Analysis Notation

ϕ	Acoustic Timefront 56
n	Branch Number 20
t_{max}	Location in time along a trace where there is a peak value in intensity . 232
Δ'	Separation of Classical Branches determined to give pulses which are well-separated enough 231
Δ	Half the region in time describing a pulse arrival 235
$\sigma_t^{\epsilon=0}$	Pulse width for an unperturbed ($\epsilon = 0$) arrival in a timefront trace 239
μ_{σ_t}	Travel time spread: average width σ_t of arrivals over ensemble of timefronts 239
μ_t	Mean location of a pulse arrival 243
σ_{μ_t}	Travel time wander: standard devation of mean travel time arrivals over ensemble of timefronts 243

Math Notation

I	Identity Matrix 139
$J_a(x), Y_a(x)$	The Bessel and Neuman functions 350
$\hbar$	Planck's fundamental constant 58

Internal Wave Sound Speed Model Notation and Constants

ϵ	Small parameter scaling internal wave sound speed model ($\epsilon = \frac{\mu}{g}\frac{2B}{\pi}\left(\frac{E}{M}\right)^{1/2} N_0^2 \approx 2.02 \times 10^{-3}$) 75
$\zeta(z)$	Vertical fluctuations of ocean water 346
$\zeta_j(z)$	Vertical fluctuations of ocean water due to the j-th internal wave mode 349
j	Internal wave mode number 349
$j^* = 3$	Internal wave mode scale number 354
ρ_0	Density of fluid 346
$g = \frac{9.81m}{s^2}$	Gravitational Acceleration 346

$N(z)$	Brunt-Vaisala buoyancy frequency	346
$N_0 = \frac{1cycle}{10min}$	Brunt-Vaisala buoyancy frequency at the ocean surface	346
B	Vertical Scale of buoyancy frequency	346
H	Approximate Depth of the Ocean	348
$\mu = 24.5$	Dimensionless constant representing $\frac{\rho_0}{c}\frac{\partial c}{\partial \rho_0}$	346
k_r	Horizontal wavenumber of an internal wave	347
k_j	Wavenumber associated with an internal wave mode j	350
ω_f	Angular Frequency of Internal Wave Oscillations($\omega_i < \omega_f < N(z)$)	347
ω_i	Inertial Frequency Associated with Rotation of Earth	347
$w(z)$	The vertical velocity of fluid motion in the Ocean	347
$W(z)$	The amplitude of the vertical velocity of fluid motion in the Ocean	347
$\xi(z)$	Functional form determining the frequency of oscillation of the internal wave sound speed	351
$g(k_r, j)$	Complex Gaussian Random Variable Weighting internal wave mode displacements	352
$G(k_r, j)$	Variance of Complex Gaussian Random Variable $g(k_r, j)$	352
ϕ_{j,k_r}	Random Phase of internal wave mode displacements	353
$E_{GM} = 6.3$ x 10^{-5}	Dimensionless Garrett-Munk Energy scale factor	354
$< U >$	Total vertically integrated potential energy density	354
M	Normalization constant for j dependence of internal wave sound speed model	45

Dedication

This dissertation is dedicated to my husband and my son.

Chapter 1

INTRODUCTION

In the 1940's, Ewing and Brekhovskikh independently discovered that the deep ocean environment creates a waveguide which 'channels' low frequency sound (less than a few hundred Hz) and enables acoustic propagation to long distances (several thousands of kilometers) in the mid-latitude oceans [2]. This deep sound channel waveguide, sometimes referred to as the SOFAR channel (short for Sound Fixing and Ranging), is created from the competing effects of decreasing temperature and salinity and increasing pressure with depth to form a minimum in the sound speed. The location in depth of the minimum, called the 'sound channel axis', varies with latitude and season, from nearly 1 km in Bermuda up to the surface for latitudes above 60^0 [3]. Sound propagates in this channel by refraction of sound back toward the depth of slowest speed, resulting in an oscillation of sound about the sound channel axis to create the waveguide confinement. For low enough frequencies, there is very little dissipation in the sound intensity, so that sound trapped in this ocean waveguide is able to propagate thousands of kilometers [4].

In addition to the wave guide effect, the ocean also behaves as a weakly turbulent medium [5, 6]. In the early 1900's, Peterson, Helland-Hansen and Nelson observed that there were fluctuations in the vertical structure of temperature and salinity in the ocean [7]. These vertical fluctuations have sources such as internal gravity waves [3] and ocean spice [8]. Fluctuations in the horizontal structure are due to ocean circulation, which is dominated by mesoscale eddies [3] associated with planetary waves such as Rossby waves. All of these fluctuations create a structured random medium on the waveguide for the speed of sound, which is responsible for multiple, forward scattering of the acoustic wave [3].

For low frequency experiments to long ranges, internal wave fluctuations are the principle fluctuations studied to gain insight into the scattering physics. This is due to their horizontal length scales (on the order of 1 km) and time scales (on the order of 10 minutes to 1 day) being on the same order as the experiments. The scattering due to internal waves takes place mainly in the vertical plane, with negligible scattering in the horizontal plane perpendicular to the propagation. The size of the scattering is very weak compared to that of the waveguide, with dominant amplitudes in the upper ocean (i.e. at and above the sound channel axis). Though each scattering event is weak, many scattering events added coherently amplify the effect, while many scattering events added incoherently can result in a loss of information as the acoustic signal is randomized to noise.

Since the discovery of the sound channel, its understanding has become extremely important for a wide range of applications, ie. imaging locations of submarines [9] or biological populations [10], understanding undersea communications [9], and monitoring the state of the ocean [11]. A good understanding of the role of internal waves in acoustic scattering is

also extremely important for those applications in which sound encounters many scattering events during its propagation. It is understanding the state of the ocean which motivates the work presented in this thesis.

The application of sound to monitor the state of the ocean provides a method of studying global climate change via the mean ocean temperature [4]. In experiments for these studies, sound propagates over long ranges (i.e. thousands of kilometers) through deep water. Changes in the ocean temperature affect the speed of sound [4, 12]. Acoustic waves are refracted and reflected by variations in their propagation speed. By measuring the time for an acoustic wave to travel from the source to a receiver through a large slice of ocean, the data can be inverted to obtain an average wave speed [13]. Changes in the average wave speed can then be related to average temperature changes and climate change.

General problems in which wave scatterers have random spatial locations and random amplitudes (which may vary with time) belong to a general class of problems termed 'wave propagation in random media' (WPRM) [14, 15]. Due to internal wave effects, long range acoustic propagation in the ocean [13, 16] belongs to this class of problems. Some other examples of problems in WPRM include gravitational lensing [17], Anderson localization [18] and the twinkling of starlight. Techniques used with problems in WPRM include Green's function expansions[19], statistical approaches (transfer matrices, S matrices, unitary matrices) [20] and semiclassical theory (ray methods) [19]. A large, successful body of work in WPRM relies on stochastic analysis and ensemble methods in order to obtain statistical measures of the properties of the wave fields [21].

In ocean acoustics, ray methods are usually relied upon at various stages and with varying

levels of complexity in the resulting experimental analyses [12, 22, 4]. Classical rays depict the movement of the wave front as a trajectory of points in depth and range. The intensity and phase contributions of each ray can be computed using semiclassical theory, information about the stability of the rays and the number of turning points in each ray. Classical rays for the waveguide are oscillatory, periodic functions about the sound channel axis. For the case of a waveguide with a random media superimposed, the rays remain oscillatory, but are not entirely periodic and many of the rays are fully chaotic [23, 24, 25]. Therefore, the use of ray methods in long range acoustic propagation is severely limited.

Wave problems whose corresponding classical rays are chaotic are termed problems in wave chaos [26]. Due to the sensitivity in making predictions in the presence of chaos, problems in wave chaos usually utilize techniques such as semiclassical theory [19], random matrix theory [27, 28] and symmetries [29] of the problem to come to statistical predictions. Statistical models utilizing random matrix theory [27] often capture the minimum information (maximum entropy) contained in systems.

Statistical models were first applied to acoustic propagation in the ocean by Kohler and Papanicolaou [30] and Dozier and Tappert [31, 32]. These statistical models evolved from those used in radiophysics for propagation through the atmosphere [33, 34, 14]. The statistical models consisted of Fokker-Planck equations and Langevin equations with a Markov approximation. With these equations, Dozier and Tappert [31, 32] studied the statistics of mode intensities in the presence of internal waves. Morozov and Colosi [35, 36] used the Markov approximation to investigate the mode cross correlation. Virovylansky [37] used the stochastic Langevin equations in the creation of a statistical description of chaotic classical

rays and derived analytical estimates for properties of the timefronts [38].

The acoustic timefront is the principal data obtained and analyzed from long range acoustic experiments. Long range acoustic experiments use broad band sources and a set of receivers located down range from the source to create a 'timefront' of data. The timefront is the structure formed by considering all of the arrivals of the acoustic wave at different receiver locations in depth and at different times. The complicated nature of the timefront structure arises from the various pathways along which the sound travels. The 'steeper' energy (which turns near the surface and bottom) arrives earlier, whereas the 'flatter' energy (which propagates near horizontal in the neighborhood of the sound channel axis) arrives last. Simulated timefronts constructed from waveguide sound speed models exhibit a branched structure where the time pulses are connected in an 'accordion' shape. Real timefront data shows that the structure of the early arrivals retains these clear branches. But there is considerable broadening, shifting and overlapping of the arrival times for the pulses in the late arrivals due to the scattering events so that very little branch structure is resolvable in the late arrivals.

The properties of the acoustic timefront are very dependent on the experimental (i.e. source and range) and ocean (i.e. sound speed and internal wave) parameters. The basic accordion shape formed by the branches of the timefront is due to the waveguide, whereas the smearing of the timefront is due to the scattering from internal waves. The timefront data potentially holds information on all of the parameters of the experiment, though the information that remains in the timefronts after propagation through an internal wave field of scattering events is not obvious. The level of interference in the late arrivals is similar to noise, but does have some structure suggesting that information about the propagation has

been degraded. Due to this degradation, there appears to be only minimal information about the propagation stored in the timefront data for long range propagation.

1.1 Aims of the Research

The ultimate objective of this research is to understand what information about the experiments are stored in the timefront data and to design a method for extracting this information. Towards this goal, the aim of this thesis is to construct a statistical ensemble model for long range ocean acoustics, which agrees with the average properties and the fluctuation properties of the acoustic propagation and contains the minimal information about the propagation which survives to long ranges. The construction and testing of such an ensemble model is the thesis objective accomplished through several intermediate goals.

The first goal in achieving the thesis objective is to create a sound speed model and a method of propagating sound to create a timefront. The sound speed model should have realistic 'features' and experimental parameters chosen near those of real experiments. This model is for purposes of numerical comparison not for analyzing or making conclusions about real experiments. The theoretical simplifications along the way allow the general theory to move forward, but do not compromise the essential physics of the problem. The achievement of this goal is described in Ch. (3).

The second goal in achieving the thesis objective is to study the propagation of the eigenmodes of the background potential and to determine the statistical properties of the mode propagation. Acoustic modes are propagated through several internal wave sound speed real-

izations to generate a unitary propagation matrix of transition probability amplitudes for each mode for the short range of 50 km. Statistics of these matrices are obtained and analyzed. The achievement of this goal is described in Ch. (4).

The third goal in achieving the thesis objective is to create a statistical ensemble model for the unitary propagation matrices at short range (i.e. 50 km) which reproduces some of the statistical properties of the propagation for that short range. This model is a building block for the matrices at longer ranges. Sample matrices and timefronts from the building block ensemble model are compared with those from the simulated propagation for 50 km to determine the properties the ensemble model is capturing correctly. The achievement of this goal is the ensemble model described in Ch. (5), where timefronts are analysed in Ch. (6).

The fourth goal in achieving the thesis objective is to use the statistical model for the unitary propagation matrices at short range to generate a set of independent unitary propagation matrices for each 50 km segment of propagation. Since the range of 50 km is chosen so that successive propagation matrices from the propagation are uncorrelated, a multiplication of several of the matrices from the ensemble creates an ensemble of transition matrices for longer ranges (ranges which are multiples of 50 km). The achievement of this goal is the long range ensemble model described in Ch. (5).

The fifth goal in achieving the thesis objective is to analyze the timefront structure and develop a set of observables to characterize the average properties of the timefront remaining at long ranges. The average properties of the late arrivals are characterized with the vertical and temporal extent of the decay from the peak value. The average properties of the early branch arrivals are characterized by the fluctuations in the width and mean location of the

branches of the timefront. The achievement of this goal is described in Ch. (6).

The sixth goal in achieving the thesis objective is to compare the ensemble model to the simulated propagations for long range. This is done by comparing the properties of the average intensity timefront generated from the average intensity of independent timefront realizations from each model. The properties of the average intensity timefront reflect the minimal information remaining in the timefronts for long ranges. The achievement of this goal is described in Ch. (6).

1.2 Importance of the Research

Though stochastic models have been developed for acoustic mode propagation in the ocean, the stochastic properties of internal wave scattering from ocean sound speed models are still poorly understood. Currently, the experimental analysis of timefront data involves Monte Carlo simulations of the acoustic propagation to infer information about the experimental propagation [39, 40, 41]. Such simulations provide no insight into how information from the experiments effect the properties seen in the data. Additionally, the simulations are computationally expensive so that only a few realizations of the propagation are simulated to analyze the data. This results in great statistical error in the analysis.

The ensemble model constructed and verified in this thesis makes progress towards the lack of understanding about the stochastic properties of internal wave scattering by providing a physical picture for the scattering of the modes as a statistical process with average properties. The statistical properties of the ensemble model contain average information about

the propagation to 50 km and statistical mixing with range provided by the multiplication of random matrices. The benefit of such an ensemble model is that the important information about the propagation is captured in the simplicity of the structure and in the few parameters of the model. This type of model enables the formation of a physical picture for the propagation which gives insight to any analysis. With such a simple model, theorists can work on the establishment of a clear connection between the statistics of the timefront and the parameters of the experiment that can be extracted. With this connection, the process of tomography for extracting information from the acoustic data can be improved.

The ensemble model constructed in this thesis requires only the calculation of a product of random matrices. The minimal amount of information from the propagation in captured by the few statistical parameters for the random matrices. The computation of a product of random matrices can be extremely fast, allowing the generation of a large ensemble of timefronts for accurate statistics in the analysis. This is important because currently the computational time for acoustic propagation to long ranges through a single ocean sound speed realization with a step size necessary to ensure the required accuracy is prohibitive (even on a grid of processors), making only a few propagations possible. Since internal waves are statistical fields, a few timefronts from propagation through an internal wave field are not very useful in getting at the statistical properties of the true population of timefronts. With inaccurate statistics, comparison of numerical models with statistics of real timefront data is not reliable. The importance of this research lies in the ability of the ensemble model to capture the information about the propagation and to generate a large number of timefronts in a reasonable amout of time.

The understanding necessary to study the state of the ocean requires an improved scientific understanding of how sound propagates in the ocean. This fundamental understanding is useful for other ocean applications, such as imaging locations of biological populations [10] and buried physical objects (i.e. ships, mines) [42] and even for communications between ships and submarines [9]. The understanding improved by the simplicity of the ensemble model developed in this thesis may well be useful for other acoustic applications in the ocean.

1.3 Composition of the Thesis

The composition of this thesis follows in the next paragraphs.

Chapter 2 presents the details of the acoustic ocean experiments and the open questions regarding the experimental data analysis. This chapter sets the climate for how the current work fits among the previous work. This chapter explains the resolution at which the physical experiments can take measurements, which drives the level of accuracy that is acceptable for the simulations and the level of agreement between the statistics of the ensemble and the simulated timefronts.

Chapter 3 explains the modeling of the physical experiments which are performed. The ocean's effect on sound propagation is captured in an ocean sound speed model. The two main components of the sound speed model are presented and motivated. In modeling the experiments, a source model is motivated, a method for propagating sound is derived, a method for including the boundary effects (ocean surface and floor) is explained and finally a method for constructing the timefronts from the simulations is derived.

Chapter 4 begins the research explored in this thesis. The important statistical properties of the unitary propagation matrix elements are investigated. The statistical properties of the unitary propagation matrices from simulated propagation to 50 km are analysed.

Chapter 5 explains the construction of the ensemble method for long ranges and for the building block of 50 km. The unitary propagation matrix for long ranges is constructed from a product of random building block matrices. The construction of the building block matrices utilize statistical information about the propagation to 50 km. The ensemble model is verified by calculating statistics of the resulting matrices and comparing sample matrices to those from the simulated propagation.

Chapter 6 explains an investigation into the properties of the acoustic timefront. Semiclassical, perturbation and mode theories are utilized to gain insight into the timefronts. Sample timefronts and average intensity timefronts resulting from the ensemble model are compared to those resulting from the simulated propagation. Properties of the average intensity timefront are calculated and compared to deduce the quality of the ensemble model in capturing the important features of the propagation.

Chapter 7 presents the conclusions of this work and recommendations for future research.

After the conclusions lie a list of references and three appendices. Appendix A describes the details of several numerical methods utilized for simulating the acoustic propagation and the classical ray propagation. Appendix B describes a derivation of the internal wave sound speed model using details from many different sources. Appendix C describes Semiclassical theory applied to the timefront construction, the calculation of classical rays and some statistical averaging used in Chapters 4 and 5.

Chapter 2

LONG-RANGE OCEAN ACOUSTIC EXPERIMENTS

Acoustic waves are able to propagate for long ranges in the ocean with a low signal-to-noise ratio for two main reasons. First, acoustic waves have a slow rate of absorption by ocean sea water, i.e. only a few decibles per 1000 km, especially when compared to electromagnetic waves which are absorbed more quickly. Since the absorption of sound increases with frequency, only low frequency sound is used for long range experiments. Second, though high angled acoustic energy from the source is eventually absorbed by the ocean floor, the presence of a minimum in the sound speed creates a sound channel waveguide [2] which traps the remaining acoustic energy and allows it to propagate thousands of kilometers. In the Heard Island experiments [43], low frequency sound at 57 Hz was observed 18,000 km from

the source.

Using the long range potential of acoustic waves, sound can be used to probe or image large segments of the ocean. For example, sound can be used to monitor bulk ocean properties over time or to obtain information about the internal state of the ocean, such as currents, eddies, internal waves or seafloor properties [3, 13]. Mean ocean temperatures can give important information for studying global warming[4]. Other bulk properties have value in improving the basic scientific understanding of how sound propagates in the ocean.

Ocean acoustic tomography is the process by which information about the state of the ocean during the experiments is extracted from the measured acoustic data. Generally, in the process of tomography[13], a model of the sound speed medium is evolved until a numerically generated timefront (the forward problem) converges to the experimental timefront measurements. The parameters of the sound speed model that minimize the difference between the data and the simulations is then taken to be the best estimate for the bulk properties of the experiment.

The analysis of the average state of the ocean is complicated by the ocean's dynamical state, caused by surface winds and interior temperature/salinity gradients. Variations in the sound speed can come from many different sources with different spatial and time scales. These variations pose a fundamental limit to the resolution of the average sound speed (and average temperature) that can be done with tomography in acoustic experiments [44].

Ocean experiments intended to measure bulk properties of the ocean often probe large segments of the ocean at a time. These experiments are done with acoustic sources and receivers suspended in open water to minimize reflections from objects or seamounts. As

the sea branch of the United States Armed Forces, the United States Navy has the ships and expertise necessary for conducting such experiments on the open sea. Additionally, since a better understanding of sound propagation in the ocean has applications to national security, i.e. submarine communication[9] and visibility, the Office of Naval Research (ONR) funds these basic science experiments.

Under support from ONR, many long-range acoustic experiments have been done (i.e. SLICE89 [45, 46], the Acoustic Engineering Test [47], the Acoustic Thermometry of Ocean Climate(ATOC) Acoustic Engineering Test(AET) [4, 44], the 1998-1999 North Pacific Acoustic Laboratory experiment [48] and the North Pacific Acoustic Laboratory 2004 Long-Range Ocean Acoustic Propagation Experiment (LOAPEX) [49, 40, 41]). The analysis of these experiments have focused on internal waves [44], internal tides and ocean spice [8] as sources of environmental variability. The goal of these experiments is to use tomography and travel time data to understand the bulk ocean properties throughout the North Pacific Ocean basin. These experiments are done with source frequencies on the order of 100 Hz and with receiver locations usually $1000 - 3500$ km from the source. It is the analysis of these types of experiments which this thesis aims to improve.

2.1 Experimental Design

Different experimental design techniques are used to limit the effect of noisy sound speed variations. Experiments are done over large segments of deep ocean to improve the bulk averages. Low frequency sound is used to limit the size of the fluctuations that contribute to

the timefronts. Timefronts are averaged to reduce the effects of variations with time scales much shorter than the experiment. Unfortunately, these techniques do not remove the effects of internal wave fluctuations so that they must be understood and dealt with in order to obtain an average ocean temperature.

Further design techniques can be used to minimize the 'noisy' effects of internal waves. Experiments are done in the North Pacific Ocean, where internal wave fluctuations are minimal compared to other oceans. Receivers are placed at multiple ranges from the source to get range dependent information on the internal wave scattering. Statistical properties of the timefronts are calculated to aid in learning about the frequency and range dependence of the internal wave scattering.

This section discusses the basic experimental design utilized in most long range acoustic experiments in the ocean. This includes the experimental setup, the measurements taken and a method for analyzing the data.

2.1.1 Experimental Setup

The basic experimental setup of long-range ocean acoustic experiments is that depicted in Fig. (2.1). An acoustic path for the experiments is chosen through uniformly deep water, typically $4-5$ km deep without any obvious obstructions like seamounts. An acoustic source is suspended at a certain depth, usually chosen to be near the sound channel axis to minimize reflections from the surface and ocean bottom in the data. Source frequencies are typically in the range $28-250$ Hz for these low frequency experiments, in order to minimize dissipation

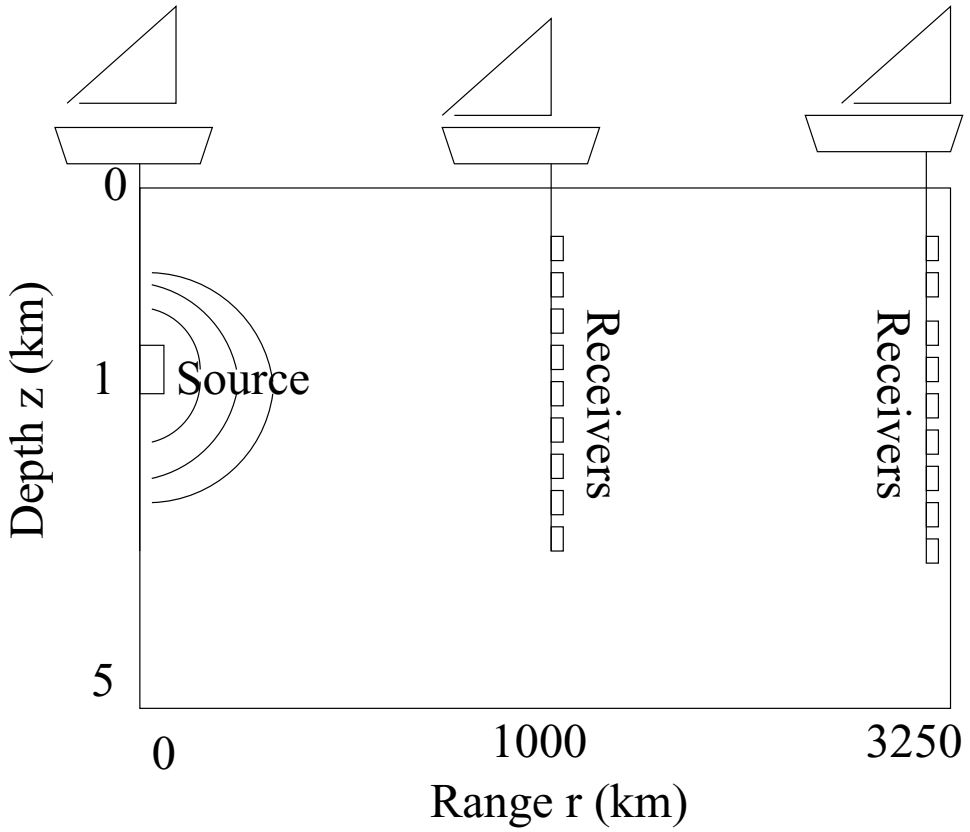

Figure 2.1: Experimental setup. Different boats tow a source and a receiver array. Receivers at a fixed range, r, and depth, z, measure the the acoustic arrivals in time after they have propagated through a segment of ocean.

of the acoustic signal and the effect of high frequency sound speed structures. A receiver array of hydrophones is suspended at a range from the source. The hydrophones include global positioning devices to track their locations with time [44] and typically have vertical spacings of 35 m [44, 40]. In the AET experiments [44], the array was situated at depths $200 - 1600$ m from the surface [44], which is roughly centered about the sound channel axis. Planar billboard arrays and bottom mounted arrays [48, 50] have been tried in different experiments, but without real success.

The acoustic signal is a transmission of many acoustic pulses, where each acoustic pulse is transmitted as an M-sequence, a phase-modulated carrier with two cycles of the carrier frequency [22, 49]. The M-sequence is used in order to detect a signal in the noisy ocean environment by improving the resolution on the time axis after a correlation of signals [51].

2.1.2 Experimental Data

During the experiments, precise locations of the source and receiver are recorded using Global Positioning System (GPS) navigation. Additionally, temperature and salinity measurements are made at different ranges along the acoustic path during the experiment, so that an approximate sound speed model can be constructed for the upper ocean along the transmission path (a model for the lower ocean is made using World Atlas data [44] and the two models are smoothly joined). In the AET experiments [44], environmental measurements were taken for the upper 760 m of the ocean every 30 km in range, so that structures with horizontal wavelength larger than 60 km are present in the model. This includes mesoscale ocean structure,

with horizontal scales on the order of hundreds of kilometers and time scales on the order of a month. The Long-Range Ocean Acoustic Propagation Experiments (LOAPEX) utilized autonomous vehicles to collect the environmental data over 3000 km with approximately 600 dives to depths of 1000 km [50]. The measurements capture the adiabatic change in the sound speed with range. These precise measurements and the approximate sound speed model are both used to generate accurate simulations in the post-experimental tomography analysis.

The primary data obtained from the experiments is that of the acoustic time series of arrivals of acoustic pressure at the receivers. By merging the arrivals at each receiver, an arrival pattern in the time-depth plane, called the timefront, is created. Even after processing the data (by accounting for the doppler shifts due to the moving source and the moving receivers), and removing noise from extraneous sources (such as ships, weather, organisms and vibrations) [44], a single timefront still has quite a bit of noise upon the arrival pattern. By averaging timefronts which are deemed to be coherent transmissions, the signal-to-noise ratio is enhanced as the smaller incoherent effects of internal tides, eddies and small scale turbulences are diminished in the averaging. The resulting timefront looks like that in Fig. 7. of Ref. [44].

The accuracy of the experimental data is vital to the technique of tomography. Uncertainty in the locations of the source and receiver due to ocean movement is typically $1 - 1.5$ m vertically and 2 m horizontally[44]. Uncertainty in the average sound speed model is typically 0.05 m/s rms [44]. Despite the many possible sources of uncertainty in the acoustic travel times, the uncertainty in the timefront is estimated at only a few milliseconds [44].

The signal-to-noise ratio severely limits the ability of the experimenters to distinguish pressure arrivals along the timefront from the noise. Due to the coherent averaging of the

timefronts in the Acoustic Engineering Test (AET), there remained 13 - 18 dB of signal to noise in the intensity along each branch with more signal-to-noise in the early arrivals and less signal-to-noise in the late arrivals [22]. Since 3 dB represents the half power point, 18 dB is the $(1/2)^6 \approx 10^{-2}$ power point and due to the noise, the power in the signal can only be measured accurately to 2 significant figures. Power varies directly with intensity and intensity is pressure amplitude squared. Measurements of power to only 2 significant figures indicates that pressure amplitudes also can only be measured accurately to 2 significant figures.

2.2 Experimental Analysis

After the timefronts have been averaged, structure emerges in the time-depth plane, as shown in the lower figure of Fig. (3.7). The time-series of arrivals at the depth of each receiver is called a 'trace' and is illustrated in Fig. (2.5). Early portions of the timefront exhibit separated pulses along each trace, which are connected along a line, called a 'branch', as shown in Fig. (3.7). Since classical ray arrivals for propagation through a range-independent sound speed model exhibit distinct uniform branches as shown in Fig. (2.4), these early arrivals are termed 'ray-like arrivals'. Later portions of the timefront exhibit arrivals that are smeared together in depth and time, with no clear branch structure visible. For portions of the timefront in between early and late arrivals, the arrivals exhibit some branch structure among the great amounts of smearing.

Using the average sound speed model created from the environmental measurements and a model for internal wave sound speed fluctuations (i.e. the Brown-Colosi model [52]), numer-

ical simulations of the acoustic wave propagation and the generation of an acoustic timefront are made. Fig. (3.7) illustrates simulated timefronts made for propagation in both the full range-dependent sound speed model and in solely the range-independent model. These calculations take on the order of weeks to perform due to the necessity for a fine grid in depth and range for propagation to long ranges. Additionally, classical rays are propagated in the sound speed model and classical timefronts are generated, such as in Fig. (2.3).

Branches of the classical timefront can be labeled with an identifier $\pm n$ as in Fig. (2.3), where $+$ $(-)$ indicates a ray that initially travels upward (downward) at the source and has a total of n upper and lower turning points between the source and receiver [13]. Since the branch number takes on only one of a discrete set of values and arises from geometrical considerations, to physicists the branch number serves as a kind of topological quantum number [53] for the arrivals along a branch.

The acoustic timefronts exhibit stable, measurable features called measurement observables. Some examples include the width of arrivals about the timefront branches (the 'spread'), the variance in branch locations between propagations (the 'wander'), the statistics of the intensity fluctuations in the arrivals and the vertical spread of the arrivals. The accuracy to which any observable can be measured is dependent upon the accuracy in which pressures can be measured along the timefront and the accuracy in which the raw data can be processed. This severely limits the accuracy of any measurement observables on the data.

Two experiments in the North Pacific Acoustic Laboratory 2004 experiments aimed to determine the range and frequency dependence of some measurement observables. The Long-range Ocean Acoustic Propagation EXperiments (LOAPEX) [49, 50] used 68.2 and 75-Hz

sources and several transmitter stations at different ranges from the receiver array to obtain range dependent data [54]. The Spice Experiment (SPICEX) used 250-Hz sources and fixed receiver ranges of 500 and 1000 km. The bulk of the experiments analysis which has been published at this time has focused on the analysis of the vertical extent of the arrivals in the timefront [40, 41].

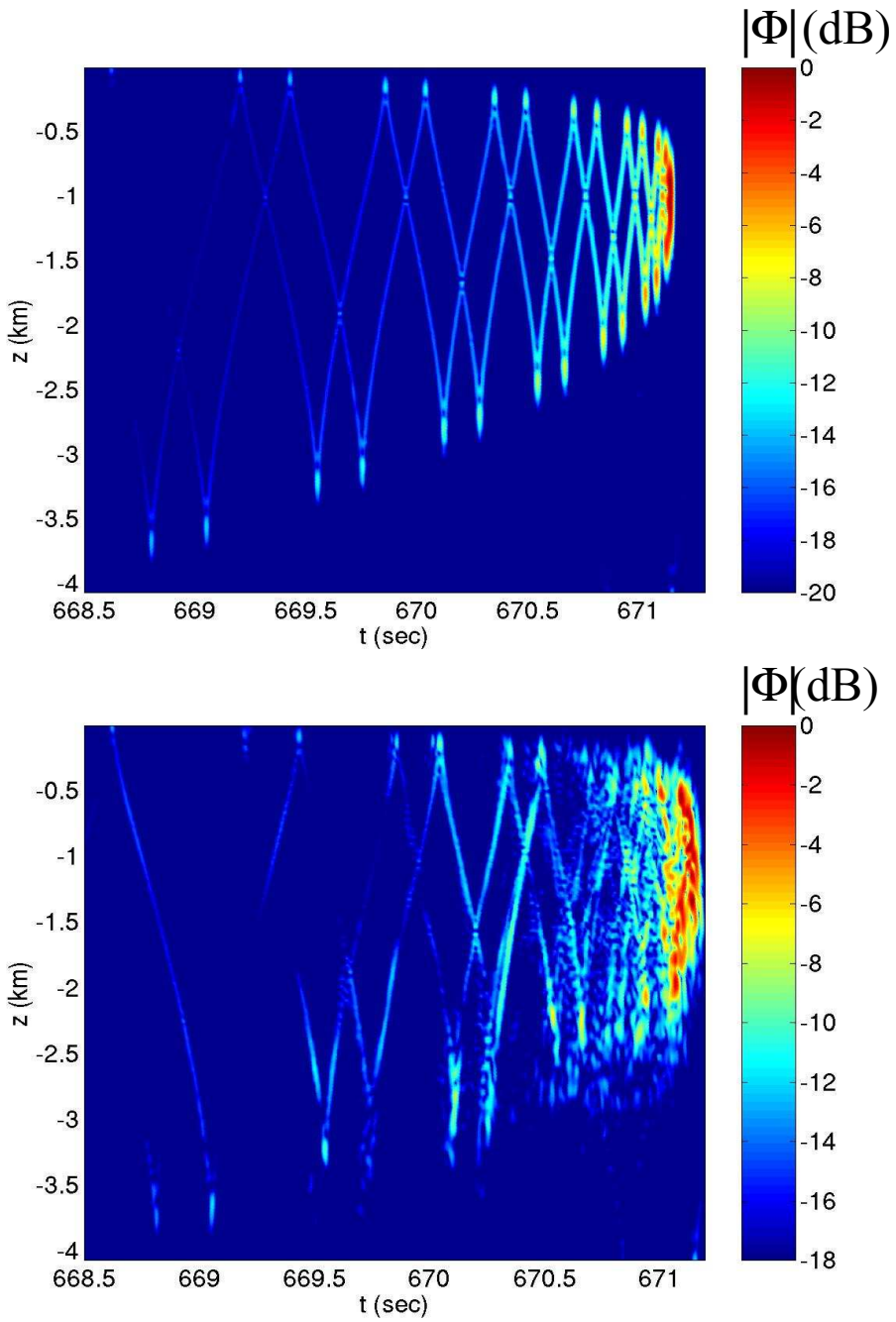

Figure 2.2: Simulated timefront of acoustic arrivals at a fixed range of $r = 1000$, plotted in time, t, and final depth, z with intensity amplitude $|\Phi|$ on a decible scale. (Upper) Simulated acoustic propagation for the range independent in Eq. (3.11). (Lower) Simulated acoustic propagation for the full range dependent model including internal wave fluctuations. Note that the intensities are highest at the turning points of the arrivals.

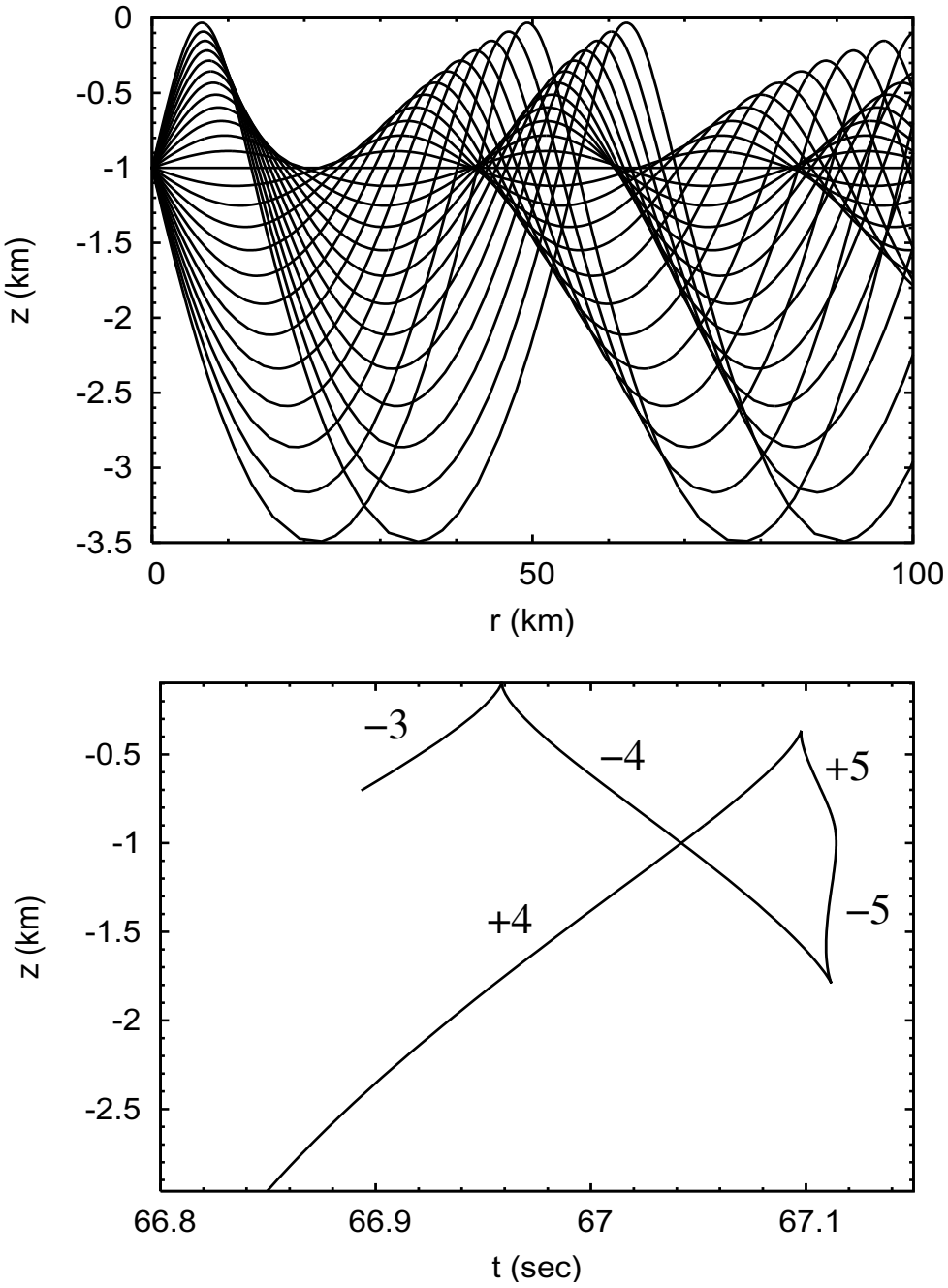

Figure 2.3: Classical rays with initial ray angle of $-12^o < \theta_0 < 12^o$ in increments of 1^o are propagated through the potential consisting of just the Munk potential in Eq. (3.11) to a range of $r = 100$ km. (Upper) Location of the classical ray as a function of depth, z, and range, r. (Lower) Timefront $|\phi|^2$ for classical ray arrivals at a depth, z, and time, t. Each branch of the timefront structure is labeled with a branch number which has a sign corresponding to the initial direction of the ray and an integer amplitude corresponding to the number of turning points encountered in the propagation of the ray.

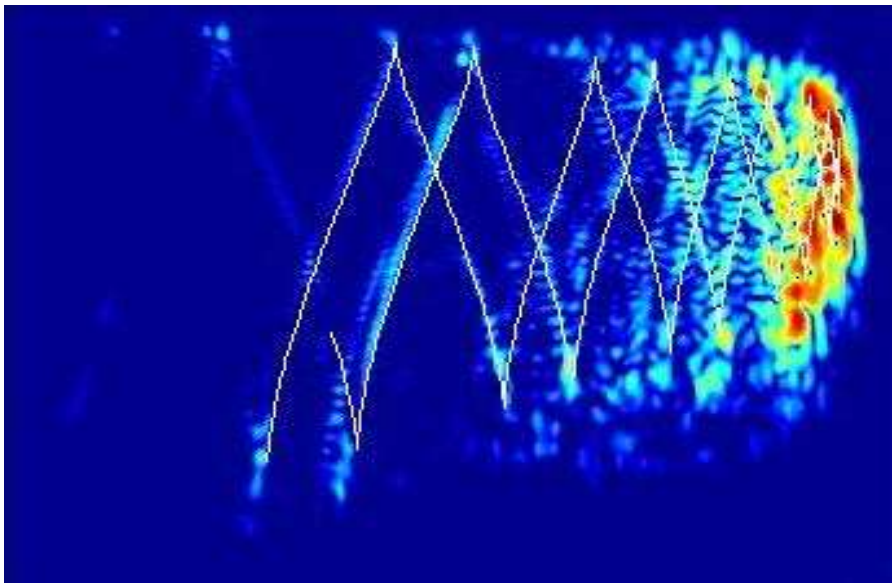

Figure 2.4: Branches of the classical timefront are overlaid on the simulated acoustic timefront for a fixed range of $r = 1000$, plotted in time, t, and final depth, z. Note that there is a time shift of the early arrival acoustic branches from the classical branches. This is called the time bias.

2.2.1 Travel Time Bias

The travel time 'bias' is a 'measurement' of the timefront that is usually calculated in the experimental analysis [39]. However, there is no direct measurement of the 'bias' possible from the experimental data.

The 'bias' of the timefront is generally defined to be any shift in the time location of the timefront for the arrivals between the unperturbed and the perturbed wavefield. An example of this shift is shown in Fig. (2.4). The theoretical interpretation of the time bias by some authors [55] is the time difference between the location of a branch for propagation in a range independent sound speed model and the branch for propagation in this model perturbed by range dependent fluctuations. With this interpretation of the time bias, the slight time shift to

the left of the acoustic branches from the classical branches in Fig. (2.4) indicates a negative time bias toward earlier times.

Since the travel time bias is a measure of the shift in timefront arrivals of a range-dependent sound speed model compared to a range-independent sound speed model, there is no way to experimentally measure the travel time bias. The state of the ocean always consists of range-dependent sound speed fluctuations and there is no way to turn these fluctuations 'off'.

Travel time biases are measured in the experimental analysis by comparing the travel times from experiments to the travel times generated from simulations using the range-independent average sound speed model. Calculated travel time biases for the AET experiments were found to be between -45 and -22.5 ms at the 3000 km range [39]. It was estimated that the bias at a range is roughly 1 ms per surface interaction for rays with upper turning depths in the upper 50 m [39].

The procedure for measuring the bias is strongly affected by the accuracy of processing the raw data and by the accumulation of measurement and simulation errors. The concept of the travel time bias is not a reliable measurement on the data, but is merely a calculation that can be done with the data, which may have meaning.

2.2.2 Travel Time Pulse Spread and Wander

The arrivals in time at a single receiver, i.e. the traces, resemble a string of pulses as in Fig. (2.5) and Fig. (2.6). Since the ocean is a non-dispersive medium for sound propagation

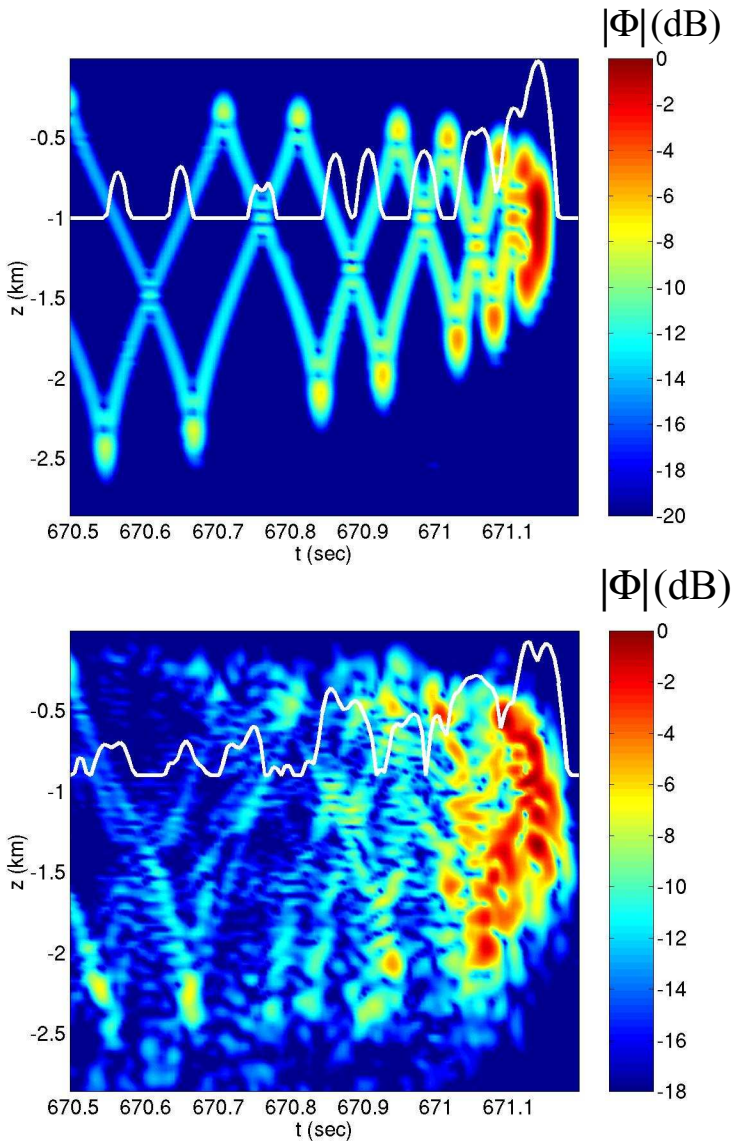

Figure 2.5: Timefront traces of the magnitude of the timefront, $|\phi|$, as a function of time, t. This trace is done at a fixed depth of $z = -1$ km. (Upper) The unperturbed potential is just the Munk potential. (Upper) The perturbed potential is the Munk potential with internal wave fluctuations. Range is 1000 km.

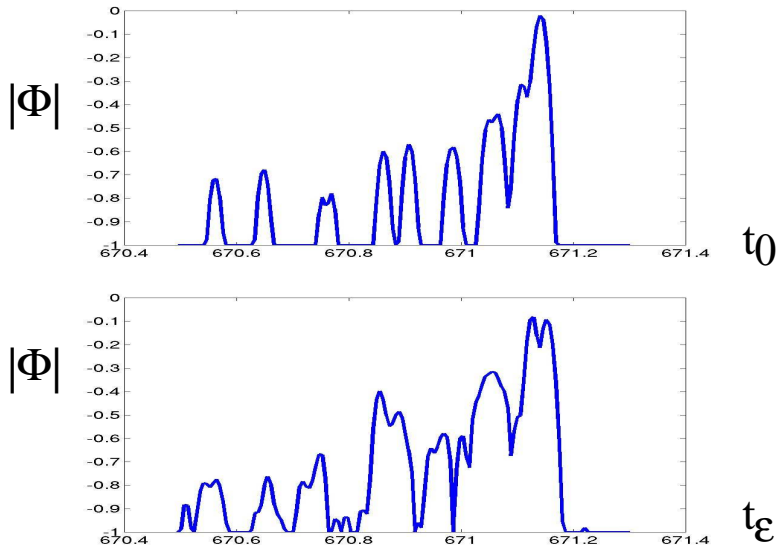

Figure 2.6: Comparison of traces for depth $z = 1$ km and range 1000 km.

at low frequencies [56], the speed of sound is not dependent on frequency and the pulse arrivals are images of the original source.

For locations in the timefront where only a single ray arrival contributes to the timefront, the pulse width is related to the bandwidth of the source by a fourier transform relation. Larger source bandwidths in frequency result in smaller pulse widths in time. For locations in the timefront where many ray arrivals contribute to the pressure amplitude of the timefront, the width of the arrival is broadened by the constructive and destructive interference of multiple ray arrivals. For example, the source in the AET experiments has a bandwidth of 37.5 Hz [44] and the approximate width of a single pulse arrival in time is 2 ms.

A measure of the width of a branch about its mean location in the timefront is termed the 'spread'. Single ray arrivals at each location of the branch would result in a spread that is the width of a single pulse arrival. The pulse spreads in the early arrivals of the timefronts in the

AET [39] experiments were qualitatively observed to be between $0 - 5$ ms, indicating that multiple arrivals contributed to the branch formation with both constructive and destructive interference. Colosi et. al. [39] calculated the spread by first finding the variance of the travel times about each hydrophone. They calculate the variance by taking the width of the pulse envelope at $e^{-.5}$ of the peak value as the standard deviation of a Gaussian pulse [39]. Then they consider the variance minus the expected value of the width of an unperturbed pulse to get a value for the spread with the perturbation [39]. They average over hydrophones to give a single variance estimate [39]. Quantitative measures found larger pulse spreads for branches with deeper upper turning points than for those branches with shallower upper turning points [39]. The spread gives information about the scattering due to the range-dependent fluctuations in the ocean sound speed.

A measure of the time drift in the mean location of a branch between ocean realizations is termed the 'wander'. In timefronts resulting from significantly different oceans, the wander is the deviation of the travel times about the mean travel time for a branch. In the AET experiments [39], the wander is referred to as the 'travel time variance' and was calculated by finding the variance in the mean location of the travel times about each hydrophone. The wanders were found to be approximately the same for arrivals along different branches. In the AET experiments, average pulse spreads were found to be 3 times smaller than the average pulse wanders [39].

The spread and wander of an arrival in the timefront can only be reliably measured at locations where the pulses are distinguishable, i.e. well separated, from each other. The separation of the branches in the late arrivals in the AET experiments [39] was less than the

typical pulse spread, so that the arrivals were not separated well enough to distinguish the branches for determining the pulse spread. Generally, the early arrivals are distinguishable except near the turning point caustics and at the 'accidental' crossings of other branches, where there are multiple ray arrivals. Generally, late arrivals are not distinguishable because the branches are very close together in this region of the timefront and the pulse broadening is such to create a lot of constructive and destructive interference between ray arrivals from different branches.

2.2.3 Vertical Extension of Arrivals

In the unperturbed timefront, the maximum depth of the arrivals at a fixed time corresponds to the cusps (or caustics). The depth of the cusps in the timefront is near the depth of the classical turning point. Below the classical turning point, the structure of the arrival in depth can be described by an Airy function [57]. The peak of the Airy function is close to the classical turning point.

In the perturbed timefront, the maximum depth of the arrivals at a fixed time corresponds to the cusps in the timefront [41]. However, there is a mixing of acoustic energy from the internal wave effects which causes the vertical extension of the arrivals to increase downward. This results in both a deepening of the cusps from that of the unperturbed timefronts and a more gradual decay below the cusp, than that of the Airy function [41].

Relating to the analysis of the SPICEX experiment, Uffelen et. al [41] created a quantitative measure of the energy $E = \int_\tau I dt$ in a cusp arrival at a particular depth, where I is the

intensity about a peak arrival and τ is a time window about the peak arrival. Only qualitative analysis of this measure for different cusp arrivals was used to compare the deepening of the cusp arrivals over the months of the experiment. Dushaw et. al. found the vertical extension of the cusps in timefronts from the ATOC project to be qualitatively $500 - 1000$ km [58].

The vertical extension of the cusp arrivals was found to be more significant below than above the sound channel axis [41]. Therefore, in Ch.(6), only the vertical extent below the sound channel axis will be considered as an observable.

2.2.4 Intensity statistics

The intensity I of the acoustic timefront is $I = |\phi(z, t; r)|^2$, where $\phi(z, t; r)$ is the complex amplitude of the timefront. The intensity in locations of the timefront vary between the ensemble of perturbed timefronts, resulting from different random seeds for the internal wave effects. The statistics of these intensities is of interest in understanding the effects of the perturbations to the sound speed.

Along a branch, the average intensity is greatest at the depths of the turning point caustics with usually just a single peak in the intensity of the arrivals in time. In the finale region of the timefront, the intensity is greatest along the sound channel (i.e. $z = 1$ km) near the time $t = \frac{r}{c_0}$, where r is the range of the timefront and c_0 is the minimum sound speed. Due to the interference of branch arrivals in this region, there are usually several peaks in the intensity with time.

Using the intensity at the peak arrivals at each hydrophone depth, Colosi et. al [39] found

the probability density function (pdf) of peak intensities for both early and late arrivals to be distributed near lognormal. This result was later corrected by Colosi et. al [59] by using an integrated energy $E = \int_\tau I dt$ over the intensity I over a region of time within ± 50 ms about the peak intensity. This resulted in a conclusion that the intensities of the late arrivals were distributed 'much closer' to an exponential instead. Granted, the Kolmogorov-Smirnov test did not support the conclusion of either result [39, 59].

The exponential distribution of peak intensities in the late arrivals is consistent with full saturation [3], in which the acoustic field in the finale behaves like Gaussian random noise. The lognormal distribution of peak intensities in the early arrivals is consistent with unsaturation [3], in which the acoustic field in the branches are the result of only a few classical rays since the scattering is weak.

The theory group of the North Pacific Acoustic Laboratory calculated the intensity peaks of the ray arrivals. This was done by taking rays equally spaced in launch angle in both the finale and wavefront regions and finding the distributions of intensities among the rays in these two regions [22].

2.3 Open Questions

The analysis of the experimental timefronts resulting from the North Pacific Acoustic Laboratory experiments (i.e. SLICE89, LOAPEX, SPICEX) has left many open questions. Colosi et. al. have expressed that there is a need for a fully broadband fluctuation theory, since the use of classical rays for a single frequency have dramatic limitations [39]. The design

Table 2.1: Predicted range scaling for measurement observables, where R is the range of the data at which the measurement observable is calculated.(J.A. Colosi, personal communication)

Observable	Approximate Range Scaling
Vertical Extension of Arrivals	$R^{1/2}$
Pulse Timespread	$R^{3/2}$
Pulse Time Bias	R^{2}
Pulse Time Wander	$R^{1/2}$

of the LOAPEX experiments [49] had a goal of finding the range and frequency dependence of some measurement observables on the timefronts, such as those termed the 'LOAPEX Observables' in Table. (2.1). The range and frequency dependence of the LOAPEX observables would lead to a better understanding of the relationship between the forward problem of tomography and the measurement observables on the experimental timefronts. The exponents of the range dependence on the LOAPEX observables would give analysts a better understanding of the stochastic processes (i.e. weak or ballistic diffusion) dominating the experimental measurements in the ocean [22]. The estimates shown in Table. (2.1) are based on some assumptions for the dynamics of the propagation. In Ch. (6), all the observables except pulse time bias will be used to analyse simulated timefronts.

Chapter 3

ACOUSTIC MODEL

"Everything should be made as simple as possible, but not simpler". -Albert Einstein

This chapter introduces the acoustic model for the propagation of sound from a source, through a segment of ocean to a set of receivers and the generation of the acoustic timefront at the final range.

The acoustic propagation simulated in this thesis uses the parabolic equation method, first used in underwater acoustics in 1973 by Hardin and Tappert [60]. In this method, each frequency in the source is propagated as a continuous wave by using the parabolic equation, which utilizes a sound speed model. A weighted superposition of the resulting wave field for each frequency is used to create the timefront of the arrivals at the receivers.

The acoustic source model is that of a broadband, chirped source as in Hegewisch et. al. [61]. This model is a Gaussian pulse in both depth and frequency and is intended for use with the parabolic equation. This model does not account for the effect of the ocean surface and floor in removing acoustic energy from long range propagation, but does remove

high-angled energy by restricting the initial momenta in the source.

The propagation region is chosen to be artificially extended from the vertical boundaries of the ocean. Since the ocean floor absorbs sound and the ocean surface reflects sound [3], this extension reduces the complexity associated with modelling the boundary conditions.

The ocean sound speed model captures the waveguide effect of the ocean in refracting sound with a range-independent model by Walter Munk. Munk's canonical sound speed model [62] gives an average model of the depth dependence of the sound speed due to the effects of pressure, temperature and salinity. These effects are predominantly responsible for the refraction of sound toward the depth of the sound speed minimum, i.e. sound channel axis, and the resulting acoustic oscillation about the sound channel axis [3].

The ocean sound speed model captures the effect of internal gravity waves in scattering sound with a range-dependent model of fluctuations by using the prescription of Brown and Colosi [52], with the modifications proposed by Hegewisch et. al. [61]. The Brown and Colosi internal wave model captures the physics of internal waves and the statistics of the Garrett-Munk spectrum [63, 64] of internal wave energies and allows for the generation of a random ensemble of sound speed fields. The modifications by Hegewisch et. al. remove the high frequency components from the Brown-Colosi model which are not physical for the wave propagation using a 'smoothing filter' and slowly diminish the internal wave model in the upper 200 meters of the ocean using the 'surface filter'.

3.1 Acoustic Propagation

The wave equation accurately describes the acoustic waves which propagate through the ocean since density fluctuations in the ocean are small and for low frequency acoustic waves, the dissipative losses can be neglected [3]. The wave equation is

$$\frac{\partial^2}{\partial t^2}\Phi(\vec{r},t) = c^2(\vec{r},t)\nabla^2\Phi(\vec{r},t)\ , \tag{3.1}$$

where $\mathrm{Re}\{\Phi(\vec{r},t)\}$ is the acoustic pressure and $c(\vec{r},t)$ is the sound speed at a location $\vec{r}$ and time t . At most mid-latitudes locations in the ocean, the sound speed lies between 1480 m/s and 1520 m/s [3].

The sound speed, $c(\vec{r},t)$, varies with distance from the source, r. In this thesis, the range dependence of the sound speed is attributed only to internal wave sound speed fluctuations. Since internal waves travel several orders of magnitude more slowly than the acoustic waves, sound passes through the ocean far faster than any variation in $c(\vec{r},t)$ due to the internal waves so that it is a reasonable approximation to 'freeze' the state of the ocean and let $c(\vec{r},t) = c(\vec{r})$ [3].

For long range propagation of sound, the acoustic scattering in the azimuthal direction is minimal and is neglected [3]. Since the important components of the acoustic wave field propagation take place in two spatial dimensions with $\vec{r} = (z,r)$, where z is depth in the ocean and r is range from the source, the wave equation can be written in the reduced coordinates

of (z, r)

$$\frac{\partial^2}{\partial t^2}\Phi(z,r,t) = c^2(z,r)\frac{\partial^2}{\partial^2 z}\Phi(z,r,t)\ . \tag{3.2}$$

The acoustic wave field, $\Phi(z, r, t)$, can be written as a superposition of fixed frequency, continuous wave sources, $\Phi_\omega(z, r, t)$,

$$\Phi(z,r,t) \;\; = \;\; \int a(\omega)e^{-i\omega t}\Phi_\omega(z,r,t)d\omega\ , \tag{3.3}$$

where $a(\omega)$ is the weight of each frequency contribution and $\omega = 2\pi f$ is the angular frequency of the pure sinusoidal source with frequency f , whose amplitude is constant in time. A functional form for the weightings $a(\omega)$ is given in Eq. (3.16) consistent with the acoustic source model motivated in Sec. 3.3.

3.1.1 Parabolic Equation for Wave Propagation

The wave field for a continuous wave source has a frequency response, $\Phi_\omega(z, r)$, where $\Phi_\omega(z, r, t) = \Phi_\omega(z, r)\, e^{-i\omega t}$ so that the wave equation in Eq. 3.2 reduces to the Helmholtz equation in the cylindrical coordinates (z, r)

$$\nabla^2\Phi_\omega(z,r) + \kappa^2(z,r)\Phi_\omega(z,r) = 0\ , \tag{3.4}$$

where the wave number $\kappa(z, r) = \omega/c(z, r)$. Since the index of refraction is $n = \frac{c_0}{c(z,r)}$ and the wavenumber is $k = \omega/c_0$, then $\kappa^2(z, r) = k^2n^2$. In the cylindrical coordinates (z, r), the

Helmholtz equation with no azimuthal variation is

$$\frac{1}{r}\frac{\partial}{\partial r}\left(r\frac{\partial \Phi_\omega(z,r)}{\partial r}\right)+\frac{\partial^2 \Phi_\omega(z,r)}{\partial z^2}+k^2n^2\Phi_\omega(z,r)=0\,. \tag{3.5}$$

For long range propagation, waves that propagate too steeply with respect to the horizontal strike the ocean bottom and are strongly attenuated (those initially angled upwards first reflect from the ocean surface) [3]. For long range propagation, the surviving waves propagate at small angles with respect to the horizontal so that a Fresnel approximation [65] is possible which expresses the acoustic frequency response as the product of an outgoing cylindrical wave, $e^{ikr}/\sqrt{r}$, and a slowly varying envelope function, $\Psi_\omega(z,r)$, where the horizontal wavenumber $k \approx \omega/c_0$ and a flat Earth model is assumed. Thus,

$$\Phi_\omega(z,r) \;=\; \Psi_\omega(z,r)\frac{e^{ikr}}{\sqrt{r}}\,. \tag{3.6}$$

Substituting Eq. (3.6) into Eq. (3.5) gives

$$\frac{1}{8k^2r^2}\Psi_\omega(z,r)+\frac{1}{2k^2}\frac{\partial^2}{\partial r^2}\Psi_\omega(z,r)=-\frac{i}{k}\frac{\partial}{\partial r}\Psi_\omega(z,r)-\frac{1}{2k^2}\frac{\partial^2}{\partial z^2}\Psi_\omega(z,r)+V(z,r)\Psi_\omega(z,r)\,, \tag{3.7}$$

where $V(z,r)=\frac{1}{2}(1-n^2(z,r))$.

For long range propagation in the ocean, $kr >> 1$, so that the first term on the left side of

Eq. (3.7) falls off rapidly with range [3] and

$$\frac{1}{8k^2r^2}\Psi_\omega(z,r) \quad << \quad V(z,r)\Psi_\omega(z,r) \; .$$

Note that though this is not valid for V near zero, this expression is true in an average sense for even very short ranges.

Since the envelope function, Ψ, is slowly varying with range, the curvature is weak so that the parabolic approximation [65] applies. Then the second derivative on the left side of Eq. (3.7) can be neglected since

$$\left|\frac{1}{k^2}\frac{\partial^2}{\partial r^2}\Psi_\omega(z,r)\right| << \left|\frac{1}{k}\frac{\partial}{\partial r}\Psi_\omega(z,r)\right| \; .$$

Neglecting the two terms on the left side of Eq. (3.7) gives the parabolic equation

$$\frac{i}{k}\frac{\partial}{\partial r}\Psi_\omega(z,r) = -\frac{1}{2k^2}\frac{\partial^2}{\partial z^2}\Psi_\omega(z,r) + V(z,r)\Psi_\omega(z,r) \; . \tag{3.8}$$

Note that the derivation of the parabolic equation assumes negligible azimuthal scattering with no backscattering and negligible time dependence of the internal waves. See the discussion in Flatte's book [3] for more details on all of the terms that have been dropped and an order of magnitude estimate for the size of the various contributions.

The index of refraction, n, is related to the sound speed through $n(z,r) = \frac{c_0}{c(z,r)}$ [3] . Decomposing the sound speed $c(z,r)$ into the reference sound speed, c_0, and fluctuations, δc, about the reference, the sound speed can be written $c(z,r) = c_0 + \delta c(z,r)$ with $\delta c(z,r) <<$

c_0. Then, the potential,V, is approximated as follows:

$$V(z,r) = \frac{1}{2}\left(1 - n(z,r)^2\right) = \frac{1}{2}\left(1 - \left(\frac{c_0}{c(z,r)}\right)^2\right) \approx \frac{\delta c(z,r)}{c_0} \,. \tag{3.9}$$

Since sound speed fluctuations δc are less than 0.01 percent of the sound speed c [3], the potential V can be approximated to first order with the form $\delta c/c_0$ in Eq. (3.9) with up to 0.03 percent error in the potential. Due to its simple form, the approximation to the potential is used in all calculations in this thesis. It is not expected that this change will alter the physics of the propagation substantially, but this approximation may change differences in travel times more substantially. In that case, the more exact form may have to be used in order to detect significant travel time differences.

3.2 Ocean Sound Speed Model

The model for the speed of sound at different ocean locations at depths , z, and ranges, r from the acoustic source consists of two main components. The first component of the model is an adiabatic, large scale behavior which is responsible for creating the ocean's 'sound channel' [2]- an effective wave guide for acoustic propagation in the deep ocean. This general behavior has a minimum sound speed at the sound channel axis (with a typical depth of 1 km), and varies slowly with latitude and season, with the sound channel axis moving toward the surface for higher latitudes and colder seasons [3]. The second component is local fluctuations in the sound speed due to the ocean's internal waves. These fluctuations are much smaller in

magnitude [3] than the wave guide confining behavior, but describe the range dependence. The model potential $V(z,r)$ takes the form

$$V(z,r) = \frac{\delta c(z,r)}{c_0} = \frac{\delta c_{wg}(z)}{c_0} + \frac{\delta c_{iw}(z,r)}{c_0}\,, \tag{3.10}$$

where δc_{wg} represents the change of the sound speed due to the wave guide and δc_{iw} represents the fluctuations due to internal waves. An example of each of the pieces of the model in Eq. (3.10) is shown in Fig. (3.1) to give an idea of the scale of the fluctuations.

Note that even though the sound speed waveguide due to temperature and pressure actually changes with range over the changing latitudes of the acoustic path in the experimental model, this range dependence is adiabatic [3]. Considering a slowly varying range dependent waveguide model would only complicate the analysis, but would not change any of the essential physics. Therefore, the waveguide model is taken to be range independent.

3.2.1 Acoustic Wave Guide

The average speed of sound in the ocean is a confining potential. The sound speed varies directly with temperature, salinity and pressure. Pressure increases linearly with depth, temperature decreases exponentially with depth and salinity is a more negligible effect [66]. The result is the creation of a minimum in the sound speed at the axis of the sound channel, with sound speed decreasing exponentially near the surface and increasing linearly in the deep ocean [3].

Since sound bends toward regions of lower velocity, the shape of the sound speed profile re-

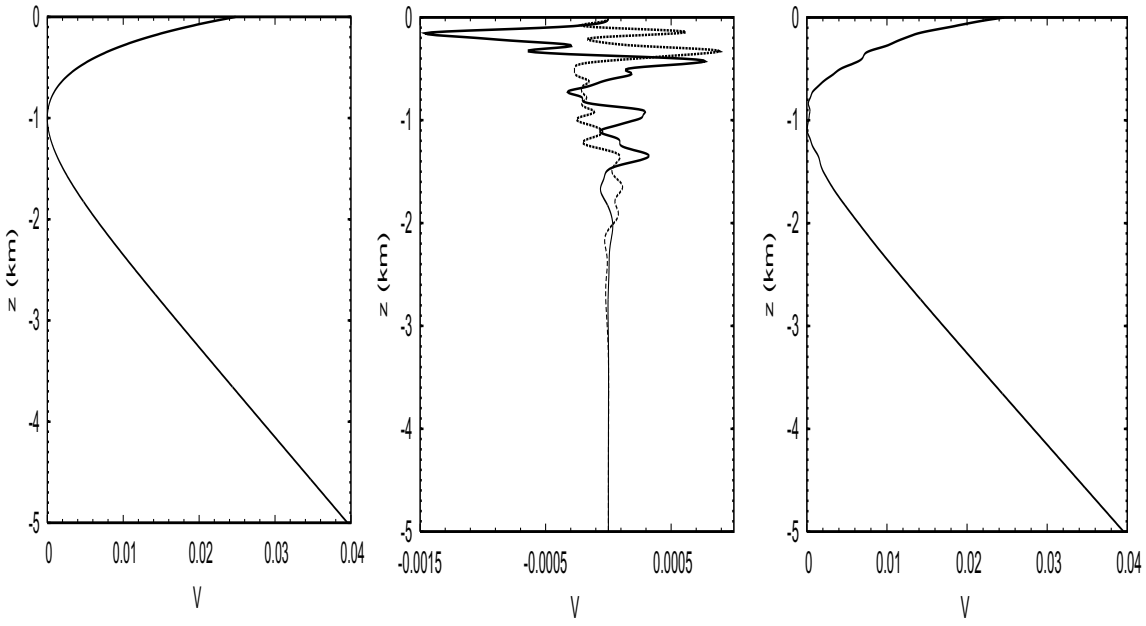

Figure 3.1: Profiles of the waveguide and internal wave potentials $V = \frac{\delta c}{c_0}$ are shown with depth z. (Left) Munk's canonical model, $V = \frac{\delta c_{wg}}{c_0}$, from Eq. (3.11) is shown with depth z. (Middle) A vertical slice through two different realizations of the range dependent internal wave fluctuations, $V = \frac{\delta c_{iw}}{c_0}$ from Eq. (3.12) at a range of $r = 0$ are shown with depth z. (Right) The full potential $V = \frac{\delta c}{c_0}$ (when the Munk's canonical model and the internal wave fluctuations are added) is shown with depth z.

fracts propagating waves toward the sound channel axis and this minimum creates an acoustic wave guide. This effect is captured in a smooth, average model proposed by Walter Munk known as Munk's canonical model [62]

$$\frac{\delta c_{wg}}{c_0} = \frac{B\gamma}{2}\left[e^{-\eta(z)} - 1 + \eta(z)\right] \ , \tag{3.11}$$

where $\eta(z) = 2[z - z_a]/B$, z_a is the sound channel axis, B is the thermocline depth scale giving the approximate width of the sound channel, and γ is a constant representing the overall strength of the confinement. This model has its minimum speed at $z = z_a$ and captures the right exponential and linear trends near the surface and bottom.

Environmental measurements have been done by several different experiments [45, 46, 44] to give estimates of good parameter choices for this model. The parameters for this model are chosen to be $B = 1.0$ km, $z_a = 1.0$ km, $c_0 = 1.49$ km/s and $\gamma = 0.0113\ \mathrm{km}^{-1}$, which are most consistent with the Slice-89 experiments [45, 46]. Though the location of the sound channel, z_a, is not consistent with the mid-latitudes in the AET experiments [44], this choice allows better resolution of the physical phenomenon in the upper ocean. The sound speed model shown in Fig. (3.1) uses these parameters.

3.2.2 Sound Speed Fluctuations Due to Internal Waves

Sound speed fluctuations due to internal waves [63] are caused by local temperature and salinity fluctuations which exist within the ocean. These variations cause small variations in the local density of the water, which cause vertical oscillations of columns of water as gravity

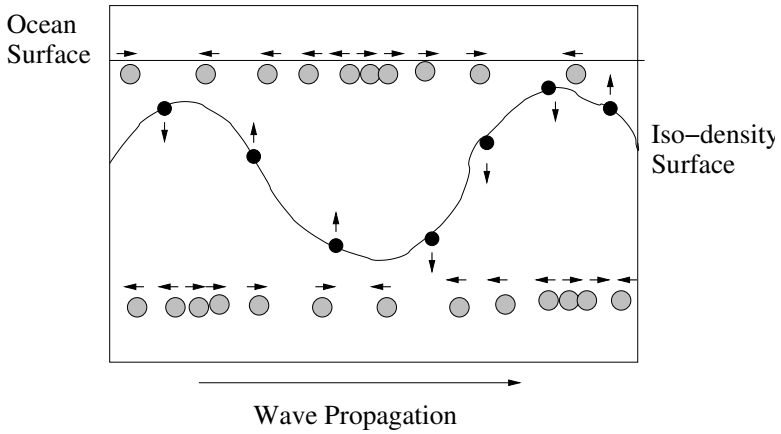

Figure 3.2: An internal wave propagates on an iso-density interface between two layers of different densities. Points on the surface move only vertically, while points directly above and below the wave move only horizontally so that the ocean surface is not disturbed by the oscillations in the body.

attempts to restore the equilibrium density stratification [13]. These gravity waves are internal to the ocean (with little effect on the surface) and propagate along iso-density surfaces. For example, the fluid motion due to an internal wave propagating on a surface between just two densities is shown in Fig. (3.2).

The resultant displacements of the isodensity surface are both depth and range dependent. As sound passes through an internal wave, it scatters and refracts differently than in the surrounding water so that internal waves are responsible for multiple, weak, forward scattering of acoustic waves [3]. Typically in the ocean, relative sound speed fluctuations, $\frac{\delta c}{c}$, from internal waves are 10^{-4} for a depth of 1 km, and $\frac{\delta c}{c} \approx 3 \times 10^{-6}$ at abyssal depths (i.e. 5 km) [3].

An analytic model for sound speed fluctuations due to internal waves was constructed by Brown and Colosi [52] using several physical and phenomenological approximations. The

Brown and Colosi model is

$$\frac{\delta c_{iw}(z,r)}{c} = \frac{\mu}{g}\frac{2B}{\pi}\left(\frac{E}{M}\right)^{1/2} N_0^2 e^{-\frac{3z}{2B}} (\Delta k_r)^{1/2} \sum_{j=1}^{J_{max}} \frac{\sin(j\pi\xi(z))}{(j^2+j_*^2)^{1/2}} \sum_{k_r} I_{j,k_r}^{1/2} \cos\left[\phi(j,k_r)+k_r r\right] , \tag{3.12}$$

where the sum over j is a finite sum restricted to the maximum internal wave mode, J_{max}. The details of the construction of this model are derived in Appendix B. Specific choices for the parameters in this model are given in Sec. (3.2.2) and (3.2.3).

Choice of Experimental Parameters

There are particularly good choices for parameters for the components of the sound speed model in Eq. (3.11) and (3.12) base on the properties of the experiments in Ch. (2). Along the experimental paths in the Pacific Ocean, the depth of the ocean is $4-5$ km so the ocean depth parameter is taken to be $H = 5$ km. A good model for the buoyancy frequency is $N(z) = N_0 e^{-z/B}$ [64], with $B \approx 1$ km and $N_0 = \frac{1}{10min} = \frac{2\pi}{600}\frac{rad}{s}$ the buoyancy frequency at the surface [3]. The latitude is approximately 30° so the the frequency of the inertial wave due to Coriolis force (from rotation of the earth) is taken to be $\omega_i = \frac{2\pi}{12hr}\sin 30^\circ = \frac{2\pi}{24hr}$ [3]. The gravitational acceleration is to good approximation $g = 9.81 \times 10^{-3}$ km/s^2.

Internal waves have been observed to have horizontal wavelengths in the range $1-100$ km. In the superposition of internal wave displacements, 512 linear internal waves are taken equally spaced in horizontal wavenumber by Δk_r with $k_r \in 2\pi[\frac{1}{100}, 1.0]\ \frac{cycle}{km}$. The energy parameter is taken to be $E = E_{GM}$, the full Garrett-Munk 'energy' parameter in all calcula-

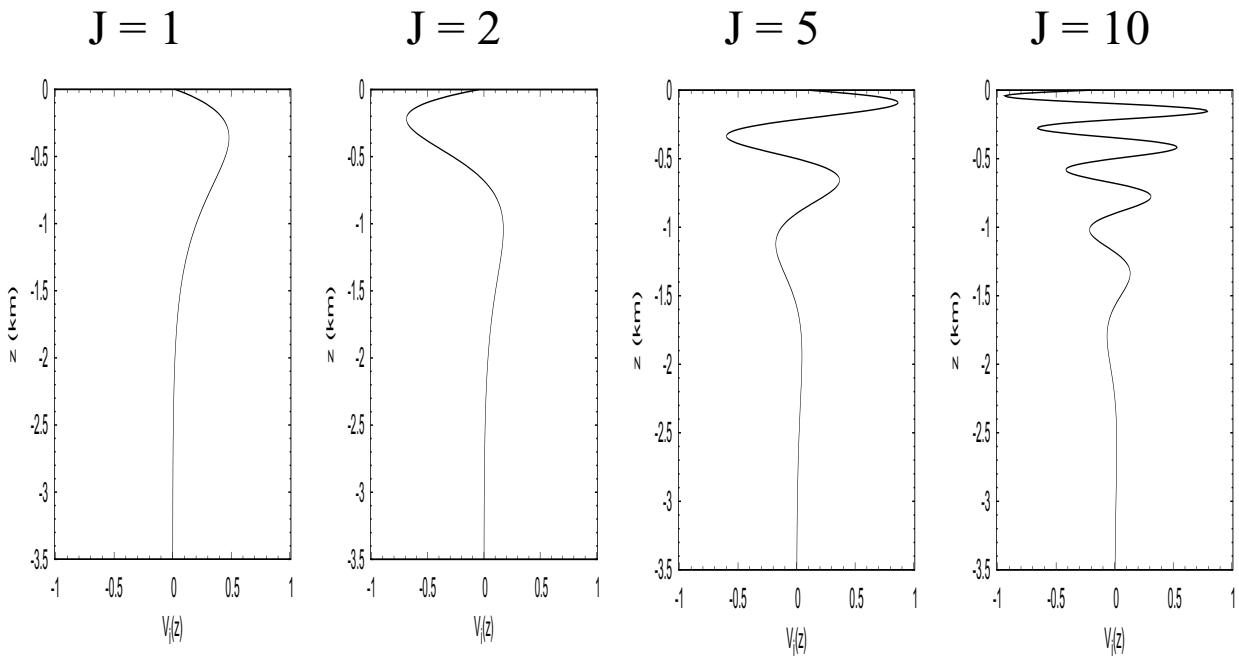

Figure 3.3: The depth dependence of the vertical modes of the sound speed fluctuations due to internal waves is $V_j(z) = \exp(-3z/2B)\sin\left(j\pi\left(e^{-z/B} - e^{-H/B}\right)\right)$. $V_j(z)$ for $j = 1, 2, 5, 10$ are plotted as a function of depth, z. The internal wave sound speed fluctuations model in Eq. (B.2) is a weighted sum of these vertical modes, $V_j(z)$. Each mode oscillates more rapidly as the surface at $z = 0$ is approached. All modes die off with depth in the ocean and are negligible below 3 km depth. The modes corresponding to lower j - number have lower frequencies and are weighted with a root mean square amplitude that goes as $j^{-1.1}$.

tions. The j normalization has been approximated using $M = \sum_{j=1}^{\infty} \frac{1}{j^2+j_*^2} \approx \pi(j_* - 1)/2j_*^2$, where $j_* = 3$ is taken as the "mode scale number" [67].

The range dependent internal wave sound speed fluctuations for two realizations from Eq. (3.12) are plotted in Fig. 3.1. A surface plot of a realization of an internal wave sound speed field is shown in Fig. 3.6. The depth dependence for the vertical modes of the sound speed fluctuations is plotted in Fig. 3.3. One can see that the lower modes have lower frequency oscillations.

f (Hz)	J_{max}
25	20
75	50
150	90
225	145

Table 3.1: The sound speed fluctuations model in Eq. (3.12) includes internal wave modes up to $j = J_{max}$. From the study by Hegewisch et. al.[61], the maximum mode to include is dependent up on source frequency f and is shown in the table.

3.2.3 High Frequency Filtering of Sound Speed Fluctuations

The Colosi and Brown numerical scheme in Eq. (3.12) for generating internal wave sound speed fluctuations has no constraints on the maximum number of vertical modes j_{max} to include the model. Since the higher modes have higher frequency oscillations, more modes are needed to capture the proper physics at higher frequencies[61]. For a fixed frequency, there should be a critical number of modes that are necessary to capture all of the physics for the wave propagation. The maximum number of vertical internal wave displacement modes is taken to be frequency dependent consistent with the results of the study by Hegewisch et. al.[61] and is summarized in Table 3.1.

Though adding more modes than necessary would not change the physics of the wave propagation, there is a problem if ray methods are being used to model the wave propagation. Unlike a wave, a classical ray is refracted by all structures in a sound speed model. The features in the model which are ineffective in refracting the wave, but fundamentally alter the rays are physically irrelevant. Since these features have no influence on the wave propagation, they should be eliminated before applying a ray method analysis [61].

In preparation for the use of ray methods to analyze the wave propagation, the high frequency components of the sound speed fluctuations in Eq.(3.12) are removed by applying the analytic 'smoothing' filter introduced by Hegewisch et. al. [61] to the fluctuations. This filter was motivated by the chirped structure of the fluctuations in the vertical modes of Eq.(3.12), where the oscillations increase with frequency as they approached the surface. Hegewisch et. al. remove structures in the model above a certain frequency by simply cutting out the parts of each vertical mode that had larger frequency oscillations as illustrated in Fig. (3.4). This method was tested and did very well as an analytic high frequency filter for the specific form of the internal wave fluctuations in the Colosi and Brown model. This smoothing was accomplished by multiplying the depth dependence of the sound speed fluctuations in Eq. (3.12) by the continuous filter function of depth

$$g(z; z_{st}, \tau_{st}) = \begin{cases} 0 & \text{for } z' \leq -1/2 \\ h(z') & \text{for } |z'| \leq 1/2 \\ 1 & \text{for } z' \geq 1/2 \end{cases} , \tag{3.13}$$

where $z' = (z - z_{st})/\tau_{st}$, the filter width is $\tau_{st} = 2\lambda_s$ m, the location of the filtering is $z_{st} = Bln\,(j\lambda_s/2B) = 100$ m, and the smooth function in between is

$$h(z) = \frac{1}{2} + \frac{9}{16}\sin(\pi z) + \frac{1}{16}\sin(3\pi z)\,. \tag{3.14}$$

This filter is a continuous function of depth with the properties that it is unity below the depth of the filtering, z_{st}, and smoothly transitions to zero within τ_{st} of that depth. This filter has

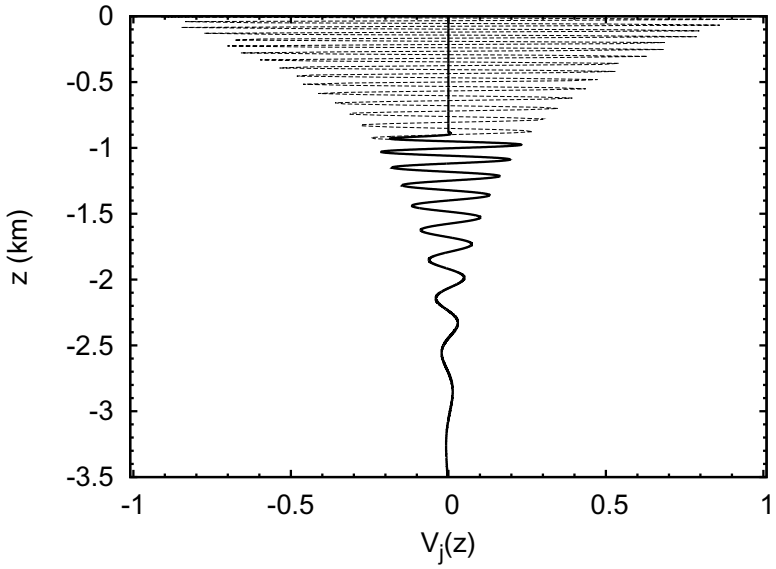

Figure 3.4: 'Smoothing' of the depth dependence of the modes of the internal wave sound speed fluctuations in Eq. (3.12). The depth dependence $V_j(z) = \exp(-3z/2B)\sin\left(j\pi\left(e^{-z/B} - e^{-H/B}\right)\right)$ for $j = 50$ is plotted as a function of depth, z. The dashed line shows the depth dependence of a vertical mode of the internal wave sound speed fluctuations, while the solid line shows the application of the smoothing filter from Eq. (3.13) with $\lambda_s = 0.1$ on the mode. Notice how the high frequency oscillations are simply cut off.

continuous first and second derivatives.

The effect of this smoothing on the internal wave sound speed fluctuations model given by Eq. (3.12) is illustrated in Fig. (3.5) to smooth out some of the fluctuations.

3.2.4 Surface Cutoff of Sound Speed Fluctuations

In the implementation of the acoustic model described in Appendix A.3.2, the acoustic wave is allowed to propagate into artificial region above and below the surface and floor. Though this does not adequately model the boundary conditions of reflection and absorption by the ocean surface and floor, which would remove the tails of the acoustic wave from the propagation, this is done for simplicity.

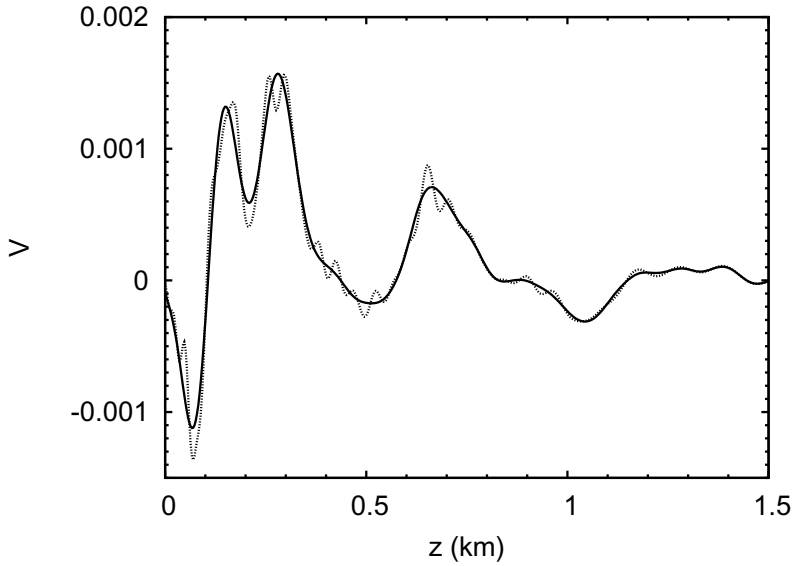

Figure 3.5: Smoothing of the internal wave sound speed fluctuations, $V = \frac{\delta c}{c_0}$, in Eq. (3.12). The dotted line shows a single realization of the internal wave sound speed fluctuations V versus depth z. The solid line shows the application of the smoothing filter to the sound speed fluctuations with the parameter choice $\lambda_s = 1.0$. This parameter choice filters out structures in the potential with wavelengths less than approximately 0.1 km. The figure illustrates that the structures in the potential V with wavelengths less than 0.1 km have been visibly filtered by the smoothing filter. The maximum number of modes taken is $J_{max} = 90$.

A consequence of this choice is that the internal wave sound speed fluctuations in Eq. (3.12) increase exponentially in the artificial region above the ocean surface which substantially scatters the acoustic wave in a very nonrealistic way. To counter this nonrealistic consequence, the sound speed model is modified near the surface by slowly damping the internal wave sound speed model in the upper 200 m of the surface. The damping is achieved by multiplying Eq. (3.12) by the surface filter introduce by Hegewisch et. al. [61] in Eq. (3.13) where $z' = (z - z_{st})/\tau_{st}$, the width is $\tau_{st} = 200$ m, the center is $z_{st} = \tau_{st}/2 = 100$ m, and the smooth function in between is

$$h(z) = \frac{1}{2} + \frac{9}{16}\sin(\pi z) + \frac{1}{16}\sin(3\pi z)\ . \tag{3.15}$$

This filter is a continuous function of depth with the properties that it vanishes above the ocean's surface, is unity below 200 m, and has continuous first and second derivatives. In this way, $\delta c_{iw}/c_0$ and its derivative vanish at the surface and are fully, smoothly restored below 200 m. This filtering is done slowly in depth, so that the filter does not introduce any high frequency components to the sound speed model. This surface filter should not impact the essential physics of the results, since there is no simple, general sound speed model near the surface anyway. The effect of the surface filter on the sound speed fluctuation field is cutting out fluctuations in the upper ocean is illustrated in the contour plot in Fig. (3.6).

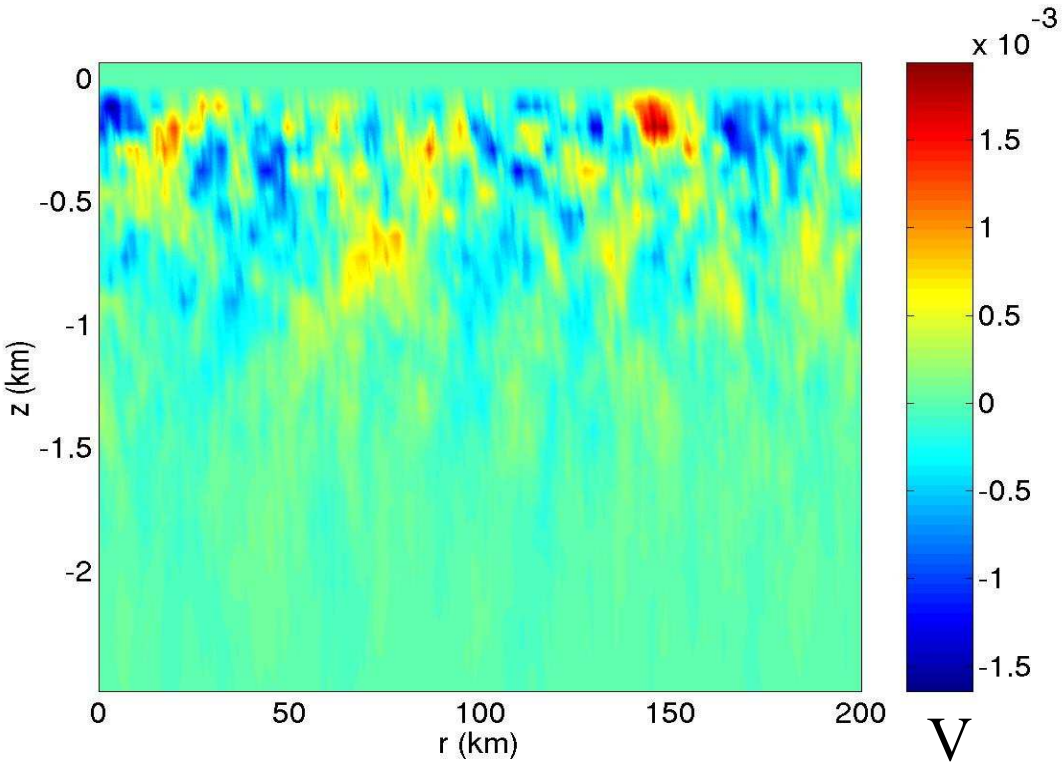

Figure 3.6: A single realization of internal wave fluctuations, $V = \frac{\delta c_{iw}}{c_0}$ from Eq. (3.12) is shown as a contour plot with depth, z, from the ocean surface and range, r, from the acoustic source. This realization has been filtered with the surface and smoothing filters described in Sections 3.2.4 and 3.2.3. Note that these fluctuations die off with depth in the ocean and oscillate in both depth and in range. The surface filter causes the fluctuations to die off as they approach the surface as well.

3.3 Acoustic Source Model

Typical experimental acoustic sources consist of several frequencies, are directional and have a spatial extent in depth. The frequency spectrum of the source is created by a superposition of continuous wave fields at a fixed range [65]. The depth dependence and directionality of the source is modified in the intial wave field at $r = 0$.

A Gaussian wave field was first proposed as a starter for the parabolic equation in Eq. (3.8) in 1973 [60]. The simulations for this thesis will use the specific Gaussian source proposed by Hegewisch et. al. [61], which limited the size of the Gaussian taking into account the effects of the boundary conditions in stripping out part of the wave field to long ranges.

3.3.1 Frequency Dependence of Initial Wave Field

Typical experimental acoustic sources are broadband, consisting of a range of angular frequencies, ω. A model for a broadband source is a normalized Gaussian centered about the central frequency, ω_0, with a standard deviation, σ_ω, which is roughly half the 'band-width' of the source. This gives the weightings $a(\omega)$ for Eq. (3.3),

$$a(\omega) \quad = \quad \frac{1}{\sqrt{2\pi\sigma_\omega^2}} \exp\left(-\frac{(\omega-\omega_0)^2}{2\sigma_\omega^2}\right) . \tag{3.16}$$

The AET experiments used a 75 Hz source with a 3-dB bandwidth of 37.5 Hz, so a realistic model has $\omega_0 = 2\pi 75$ and $\sigma_\omega = \pi 37.5$.

In Sec. 3.1, the wave field for a constant frequency source was $\Phi(z, r, t) = \Phi_\omega(z, r)e^{-i\omega t}$,

where $\Phi_\omega(z,r) = \Psi_\omega(z,r)\frac{e^{ik_0 r}}{\sqrt{r}}$. For a broadband source composed of several frequencies, the a superposition of the continuous wave fields $\Phi(z,r,t)$ at a range r, depth z and time t is necessary. Then the initial acoustic source in time takes on the form

$$\phi(z,r;t) = \frac{1}{\sqrt{2\pi\sigma_k^2}\sqrt{r}} \int_{-\infty}^{\infty} dk \exp\left(-\frac{(k-k_0)^2}{2\sigma_k^2} + i(kr-\omega t)\right) \psi(z,r;k) \,, \quad (3.17)$$

where $\sigma_k = \frac{\sigma_\omega}{c_0}$ and $k_0 = \frac{\omega_0}{c_0}$.

3.3.2 Depth Dependence of Initial Wave Field

The parabolic equation requires an initial wave field $\Psi_\omega(z, r=0)$ as input, which can then be propagated to the desired range of interest. It is important to understand the connection between the initial wave field and the localized, continuous wave source.

Typical sources can be thought of as point sources whose acoustic energy disperses broadly. However, due to the previously mentioned fact that all the steeply propagating waves are strongly attenuated, instead only that wave energy moving sufficiently close to the horizontal (within a spread of angles from the sound channel axis) that would have avoided the ocean's surface and bottom is propagated [13]. Restricting the propagation angles limits the size of the vertical wave vector and necessarily creates "uncertainty" in the location of the point source. It is appropriate to choose $\Psi_\omega(z,0)$ to be a minimum uncertainty wave packet. This implies using a normalized Gaussian wave packet of the form

$$\Psi_\omega(z,0) = \left(\frac{1}{2\pi\sigma_z^2}\right)^{\frac{1}{4}} \exp\left(-\frac{(z-z_0)^2}{4\sigma_z^2} + ik_{0z}(z-z_0)\right) \,, \quad (3.18)$$

where z_0 centers the field, σ_z is the standard deviation of the Gaussian intensity and k_{0z} gives the propagating field an initial wavenumber in the z-direction. In all the calculations, $k_{0z} = 0$ in order to maximize the horizontally propagating energy, and $z_0 = z_a$, to center the energy on the sound channel axis.

A Fourier transform of Eq. (3.18) yields a complex Gaussian distribution of initial vertical wave numbers, k_z, centered at k_{0z} with standard deviation in intensity, σ_k. Since σ_z^2 and σ_k^2 are the variances of the intensity and not the amplitude of the wave, their relation is $\sigma_z^2 = 1/4\sigma_k^2$. By a simple geometrical argument, a vertical wavenumber can be related to the horizontal wavenumber by $k_z = k_0 \tan\theta$, where θ is the angle with respect to the sound channel axis. Utilizing classical ray theory which is described in Appendix (C.1.1) , it is seen that $p = \tan\theta$ is a generalized momentum for a classical ray corresponding to the wave. Classical rays with the maximum angle θ_{max} just barely graze the surface or bottom, and thus, rays are limited in their vertical wave numbers. Yet, for Gaussian wave packets, all wave numbers are in principle present, though most are weighted negligibly by the tails. It is the width, σ_k, which determines if the wave contains wave numbers large enough for a substantial amount of the wave to hit the surface or the ocean floor. One can determine a proper Gaussian width, in order for only the Gaussian tails to pass the surface or bottom (in analogy with the limiting classical rays) by letting the maximum classical wavenumber $k_0 \tan\theta_{max}$ correspond to three standard deviations out in the initial Gaussian wavenumber distribution, i.e. set $4\sigma_k = k_0 \tan\theta_{max}$. Then

$$\sigma_z^2 = \frac{16}{4k_0^2 \tan^2\theta_{max}} \,. \tag{3.19}$$

The explicit dependence of σ_z on the angular frequency, ω, of the continuous wave source is realized using the approximate relation $k_0 \approx \omega/c_0$.

The specific choice of θ_{max} depends on the vertical confinement. For the background confinement in Eq. (3.11), those rays departing the sound channel axis with an angle of $\theta = \pi/18\ (10^\circ)$ come within 150 m of the surface, and those with $\theta = \pi/15\ (12^\circ)$ come within 30 m. The addition of internal waves to the sound speed model randomly alters the ray energy so that initially higher energy rays end up with lower energy and avoid the surface to remain the propagation to long range. For Eq. (3.19), $\theta_{max} = 10^\circ$ is chosen.

Typical acoustic sources are broadband and thus consist of several wavenumbers, k. A typical model for a broadband source is a gaussian centered about the central wavenumber, k_0, with a variance, σ_k, roughly $1/2$ the 'band-width' of the source. Thus, for the 75 Hz source with a bandwidth of 37.5 Hz, the frequency is chosen $f = 75$ with standard deviation, $\sigma_f = \frac{1}{2}37.5$ so that the central wavenumber is $k_0 = 2\pi 75/c_0$ with standard deviation $\sigma_k = \pi 37.5/c_0$.

3.4 Acoustic Timefront

The acoustic timefront $\Phi(z, r, t)$ is given by Eq. (3.3), where $\Phi_\omega(z, r)$ is given by Eq. (3.6) and $a(\omega)$ is given by Eq. (3.16). Then the complex acoustic timefront takes the form

$$\Phi(z, r, t) \;=\; \frac{1}{\sqrt{r}\sqrt{2\pi\sigma_\omega^2}} \int_{-\infty}^{+\infty} \Psi_\omega(z, r) \exp\left[-\frac{(\omega-\omega_0)^2}{2\sigma_\omega^2} - i\omega\left(t - \frac{r}{c_0}\right)\right] d\omega \;, \tag{3.20}$$

where r is the propagation range, t is the travel time and z is the final arrival depth. The acoustic timefront is numerically simulated using the methods and details described in Appendix A. Sample timefronts for a range of $r = 1000$ km are shown in Fig. (3.7) for propagation through both the unperturbed potential (the Munk potential) and the full potential (the Munk potential with internal wave fluctuations). The properties of the timefronts will be further discussed in Ch. (6).

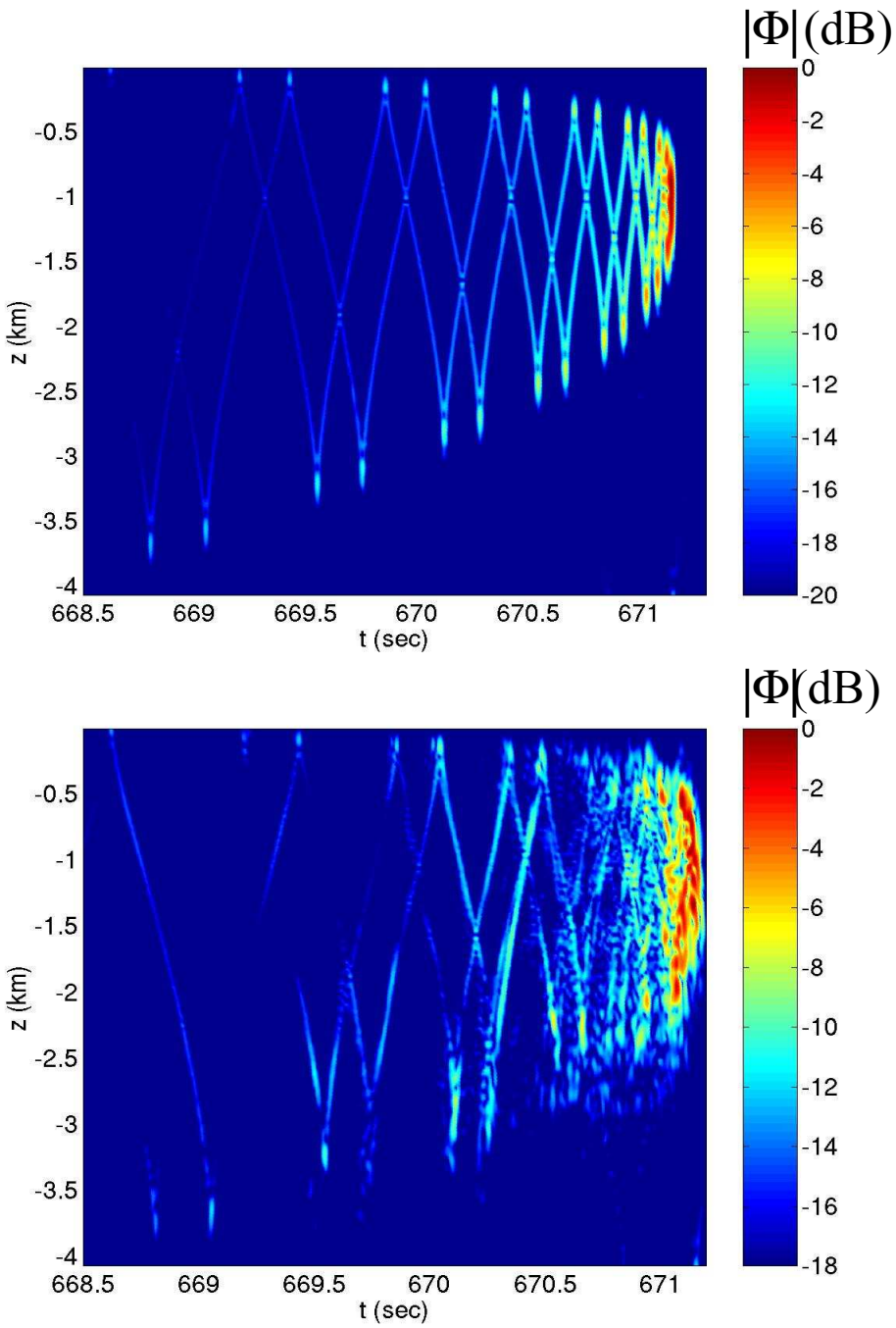

Figure 3.7: Magnitude of the complex acoustic timefront $|\phi|$ of acoustic arrivals at a fixed range of $r = 1000$ is plotted in decibels as a contour plot in time, t, and final depth, z. The decible value is $3log_2\left(\frac{|\phi|}{max[|\phi|]}\right)$, where $max[|\phi|]$ is the maximum amplitude in the timefront construction. (Upper) Propagation is through only the Munk potential. (Lower) Propagation is through the Munk potential with internal wave fluctuations.

Chapter 4

UNITARY PROPAGATION FOR LONG RANGE OCEAN ACOUSTICS

The acoustic simulations described in Ch. (3) utilize the parabolic equation to propagate each frequency component of the acoustic wave field. The parabolic equation in Eq. (3.8) has the same form as the one dimensional time-dependent Schrödinger equation in Eq. (4.1),

$$i\hbar\frac{\partial}{\partial t}\Psi(z,t) = -\frac{\hbar^2}{2}\frac{\partial^2}{\partial z^2}\Psi(z,t) + V(z,t)\Psi(z,t)\,, \tag{4.1}$$

if the identifications: $t \rightarrow r$, $m \rightarrow 1$, and $\hbar \rightarrow 1/k_0$ are made. The one dimensional time-dependent Schrödinger equation describes the time dependence of the wave field of a quantum mechanical wave propagating through a one dimensional time dependent potential [53], V, where Ψ is the wave field, t is the propagation time, z is the one dimensional spatial coordinate and $\hbar$ is Planck's constant. Due to the analogy of the parabolic equation to the Schrödinger

equation, methods derived from quantum mechanics can be used to gain insight into the important physics of ocean acoustic propagation. Since the acoustic sound speed potential can be split into range-independent and much smaller range-dependent parts, the quantum mechanical analogy to this acoustic problem would be a time-dependent perturbation theory problem (since $t \rightarrow r$ in the identification).

In quantum time dependent perturbation theory [53, 68], the state of the system is written as a superposition of the time-independent eigenstates (associated with the time-independent part of the potential). The coefficients in the superposition are complex probability amplitudes, whose magnitude represents the probability of transition between the modes and whose phase gives information about the interference of the states. The coefficients evolve with time and capture the physics of the problem. If the system starts in an eigenstate, the time-independent potential only results in the multiplication of the state by a constant rotating phase. However, propagation of an eigenstate in the time-dependent potential results in transitions to other eigenstates. The resulting matrix of complex probability amplitudes gives insight into how perturbations in the potential mix the eigenstates of the quantum system. The same insight this matrix provides for quantum systems can be utilized for a better understanding of propagation in long range ocean acoustics.

The sound speed waveguide potential in the ocean slowly changes with range, so that the eigenmode basis slowly changes at each range of the propagation. Though there is a possibility of a slight alteration in the phase of the diagonal elements with the propagation [69], there is no mixing of modes to give rise to interesting scattering physics and the matrix remains purely diagonal [70] during the propagation (in the slowly changing basis). Since there

are no real benefits to considering an adiabatic waveguide but there is additional complexity required to account for the changing basis with range, the basis states are chosen to be the range-independent basis of the waveguide potential in Eq. (3.11), a convenient part of the dynamics which is understood [12, 22].

The evolution of the complex probability amplitudes for the eigenstates (termed the 'unitary propagation matrix' in this thesis) is an alternative description [53] to the propagation of the acoustic wave field. However, a simple numerical evaluation of the matrix does not reveal the underlying physics involved.

Recently, Perez et al. [21] studied a quasi-1D disordered system by using the concept of a statistical ensemble of 'building blocks' to simulate the statistical properties of the transfer matrix for their system. From this model, they were able to extract expected values of physical quantities for the transfer matrix which were in good agreement with the statistics of the numerical solution of the Schrödinger equation [21]. The building block was constructed from an ensemble of random matrices, which had statistical properties of the transfer matrix for propagation to a small length δL in the system. The random matrices were independent, identically distributed and contained only minimal information about the physics of the problem. The model for the transfer matrix to length L was built by multiplying the building blocks drawn from the statistical ensemble. The expected value of physical quantities was calculated from the statistics of the product of random matrices.

The powerful use of the concept of a 'building block' with ensemble methods [21] could also be utilized for unitary propagation in long range ocean acoustics. Building blocks for acoustic propagation to a short range R could be constructed and multiplied to reveal informa-

tion about the physics involved in the propagation to a longer range in the ocean. The range for the building block model would be chosen as short as possible, but long enough such that certain dynamical correlations have died off and can be neglected when constructing the statistical models. The ensemble of building blocks would consist of independent, identically distributed random matrices, whose important statistical properties are derived from the propagation. The statistical properties included in the model would be the minimum necessary in order for the statistics of the ensemble model to agree with the statistics of the propagation. An ensemble model utilizing building blocks for unitary propagation in ocean acoustics will be developed in Ch. (5).

In this chapter, the properties of the unitary propagation matrix for ocean acoustic propagation are investigated for use in constructing the building block ensemble model. This includes determining a good range for the building blocks and determining the statistical properties (distribution, means, variances and correlations) of the unitary propagation matrix for that range.

4.1 The Unitary Propagation Matrix

The unitary propagation matrices are the matrices of complex probability amplitudes, which represent the coefficients of the propagated wave in terms of eigenstates of the unperturbed system.

4.1.1 Eigenmodes and Eigenenergies of the Unperturbed System

The parabolic equation in Eq. (3.8) with potential $V(z,r)$ can be written in the form

$$\frac{\partial \Psi(z,r)}{\partial z} = \left(\frac{i}{2k} \frac{\partial^2}{\partial z^2} - ikV(z,r) \right) \Psi(z,r) \; .$$

For a range independent potential $V = V_0(z)$, a general solution to the parabolic equation can be written in terms of separable solutions

$$\Psi_\omega(z,r) = \sum_m e^{-ikrE_m} \psi_m(z) \; , \tag{4.2}$$

where $\psi_m(z)$ satisfies the Sturm-Liouville eigenvalue problem,

$$-\frac{1}{2}\frac{d^2\psi_m}{dz^2} + k^2 V_0(z)\psi_m = k^2 E_m \psi_m \tag{4.3}$$

$$\frac{i}{k}\frac{\partial}{\partial r}\psi_m = E_m \psi_m \; , \tag{4.4}$$

where $\psi_m(z)$ and E_m the eigenfunctions (modes) and eigenvalues, respectively. The eigenmodes $\psi_m(z)$ are orthonormal.

The range-independent potential used in this thesis is $V_0(z) = \frac{\delta c_{wg}}{c_0}$ with the functional form in Eq. (3.11). This is a confining potential. Therefore, the mth eigenmode has m zeros and the eigenmodes are oscillatory between the classical turning points (the depths z where $V_0(z) = E_m$) and exponentially decaying beyond the turning points. The numerical method used for calculating the modes $\psi_m(z)$ of the potential V_0 is described in Appendix A.4. Fig-

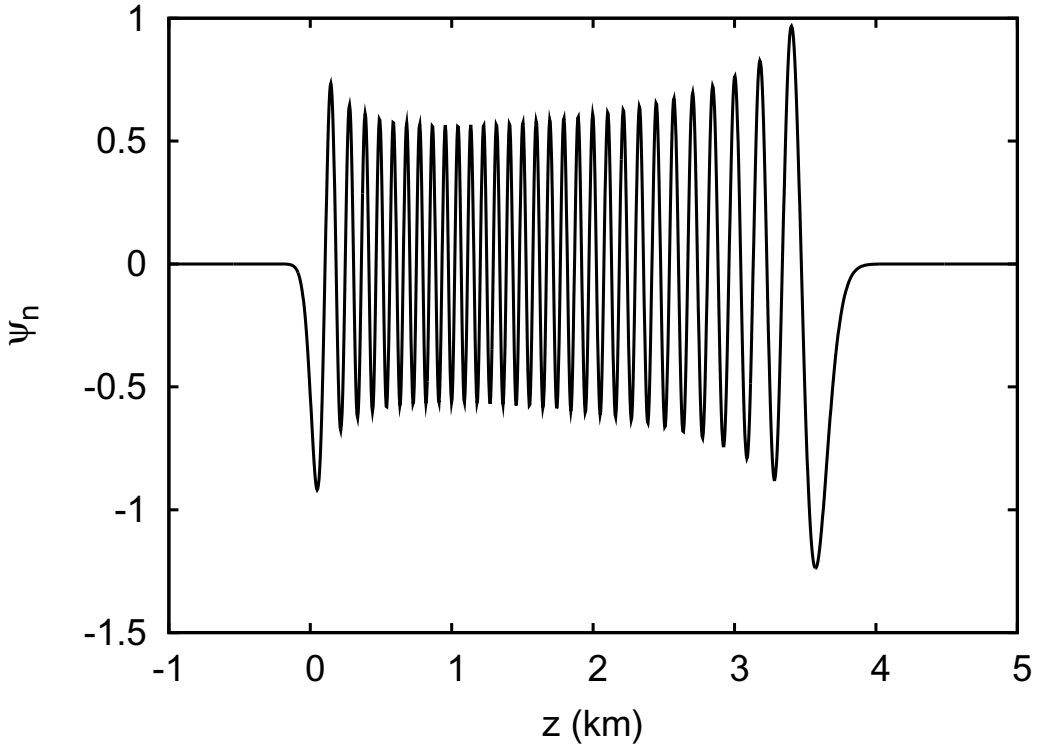

Figure 4.1: The $n = 60$ eigenmode, $\psi_n(z)$, of the Munk potential, V_0, is plotted versus depth in the ocean, z, for a source frequency of 75 Hz. This eigenmode has 60 zeros. Beyond simple classical turning points, wave functions take on an approximate Airy function form. The tail fo the approximate Airy function is thinner near the surface and broader near the ocean floor, since the slope of the potential is steeper near the surface than at the conjugate point near the floor. The amplitude near the classical turning point is higher near the ocean floor than near the surface. This can be explained by interpreting the envelope of $|\psi_n|^2$ as the classical probabilities of confinement in the Munk potential. The probability is larger for a classical particle to be found near the ocean floor than the surface because less time is spent near the surface than the floor due to the steepness of the potential.

ures 4.1 and 4.2 show numerical approximations to several eigenmodes of the system with the potential V_0 from Eq. (3.11).

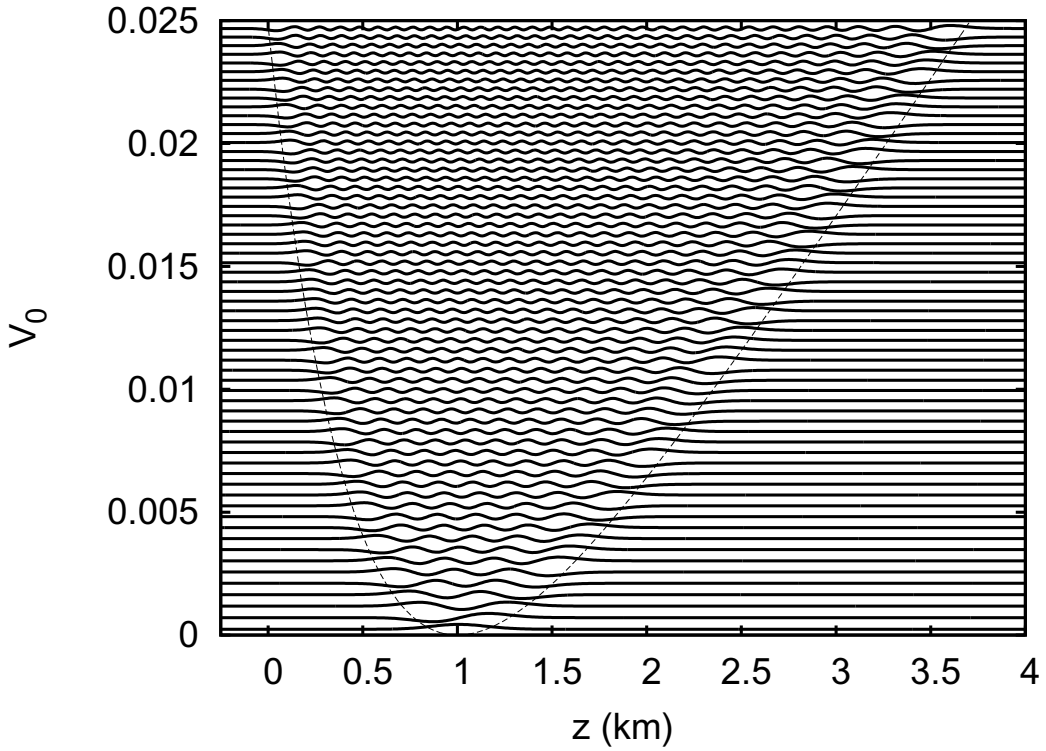

Figure 4.2: Eigenmodes, $\psi_n(z)$, of the Munk potential, V_0, plotted versus depth in the ocean, z, at the energy level of their eigenenergies,E_n, for a source frequency of 75 Hz. Eigenmodes are plotted for $n = 1, 2, ..., 61$. The Munk potential is overlaid on this plot to illustrate how each mode has oscillations between their classical turning points (where the energy level intersects the potential) and is exponentially damped (with an approximate Airy function form) beyond the classical turning points. The spacing of the energy levels decreases with higher energy levels.

4.1.2 The Coefficients in the Superposition of Eigenmodes

In the case of a range dependent potential, $V = V(z, r)$, a general wave field solution, $\Psi_\omega(z, r)$, to the parabolic equation is not known. Yet, since the eigenmodes $\psi_m(z)$ from the range-independent potential are orthogonal, they can serve as a basis for the range-dependent solution by decomposing Ψ_ω into the eigenmodes $\psi_m(z)$ as

$$\begin{aligned} \Psi_\omega(z, r) &= \sum_m a_m(r)\psi_m(z) \\ a_m(r) &= \int \Psi_\omega(z, r)\psi_m(z)dz \ , \end{aligned}$$

where the coefficients a_m evolve with range as the range dependent scattering mixes energy between the modes ψ_m.

If the initial wave function is taken to be a pure mode $\Psi_\omega(z, 0) = \psi_m(z)$, then the propagated wave field can be written

$$\begin{aligned} \Psi_\omega(z, r) &= \sum_n C_{m,n}\psi_n \\ C_{m,n} &= \int \Psi_\omega(z, r)\psi_n(z)dz \ , \end{aligned} \tag{4.5}$$

where $C_{m,n}$ is the transition probability amplitude of energy transitioning from a mode m to a mode n in a propagation range, r. Note that the modes ψ_n are normalized.

For a more general initial wave function $\Psi(z,0)$ written

$$\Psi_\omega(z,0) \;=\; \sum_m a_m(0)\psi_m(z)\;,$$

the propagated wave field can be written

$$\begin{aligned}\Psi_\omega(z,r) &= \sum_{m.n} a_m(0)C_{m,n}(r)\psi_n(z) \\ &= \sum_n a_n(r)\psi_n(z)\end{aligned} \tag{4.6}$$

so that the range dependent coefficient is

$$a_n(r) \;=\; \sum_m a_m(0)C_{m,n}(r)\;. \tag{4.7}$$

4.1.3 Sample Unitary Propagation Matrices

The unitary propagation matrix element $C_{m,n}$ is calculated by propagating the mode $\psi_n(z)$ through the ocean potential of Eq. (3.10) to obtain the final wave field $\Psi_\omega(z,r)$ at the frequency ω. Then the final wave field $\Psi_\omega(z,r)$ is overlapped with the mode $\psi_n(z)$ as in Eq. (4.8),

$$C_{m,n} \;=\; \int \Psi_\omega(z,r)\psi_n(z)dz\;. \tag{4.8}$$

This gives the complex probability amplitude, $C_{m,n}$, of transitioning from the n-th mode to the m-th mode during the propagation. Note that $C_{m,n}$ is both dependent on source angular frequency ω and range r.

Figures (4.3)-(4.7) illustrate the magnitude and phase of a single realization of the matrix elements $C_{m,n}$ for several propagation ranges. In Fig. (4.3), the phase of the unitary propagation matrix elements $C_{m,n}$ take on the appearance of a random field by a range of 50 km. In Fig. (4.4), the evolution of the magnitude of the matrix elements $C_{m,n}$ are shown with range. Initially (at $r = 0$), the magnitudes are unity along the diagonal and zero elsewhere. With range, the width of the band about the diagonal increases for all mode number n. The band width is larger for the lower modes than for the higher modes. This indicates a spread of energy both perpendicular to the diagonal and along the diagonal as the range of consideration increases.

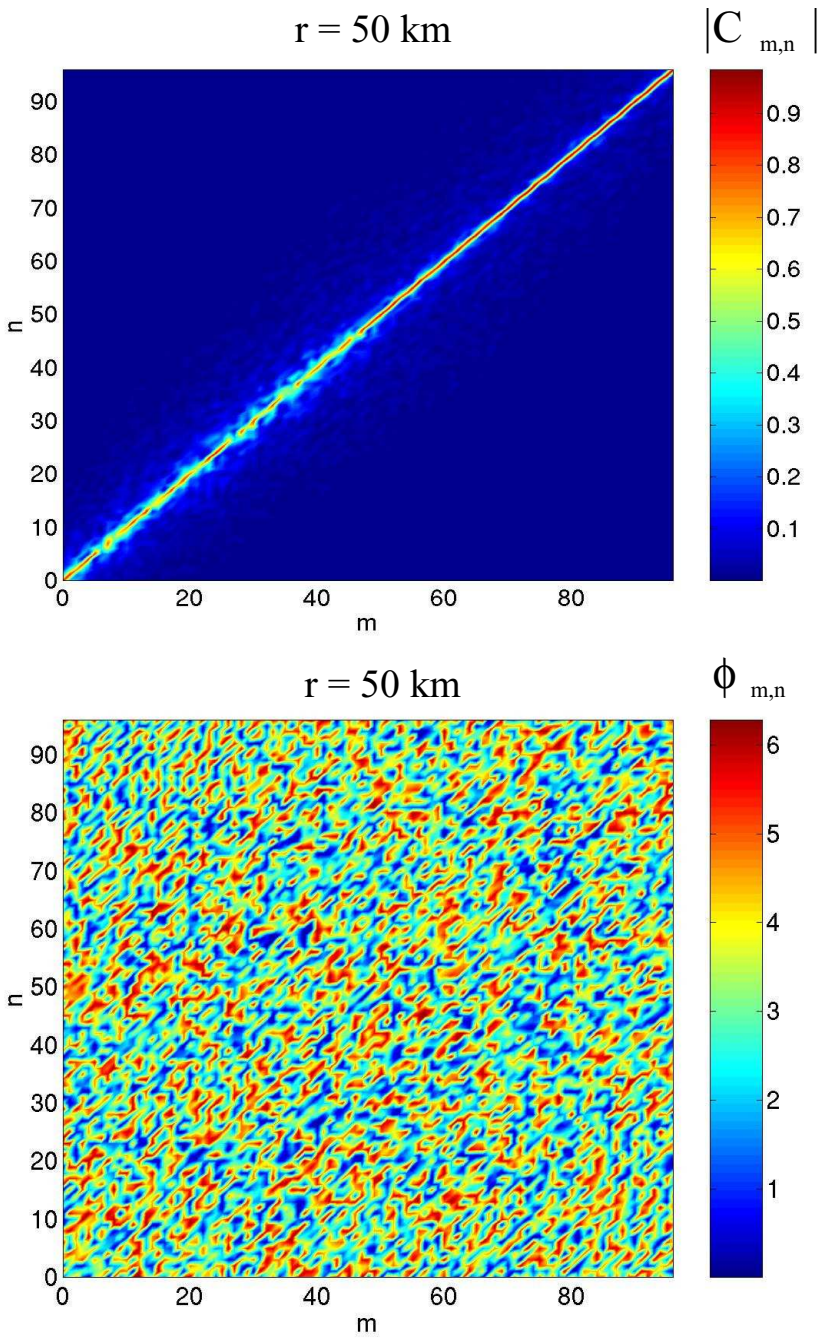

Figure 4.3: A sample unitary propagation matrix C for propagation through a single internal wave field is illustrated through a contour plot of (Upper) the magnitudes of the matrix elements $|C_{m,n}|$ and (Lower) the phases $\Phi_{m,n} = Arg(C_{m,n})$ of the matrix elements $C_{m,n}$ are both plotted with initial wave number n and final wave number m for the propagation range $r = 50$ km. The source frequency is 75 Hz.

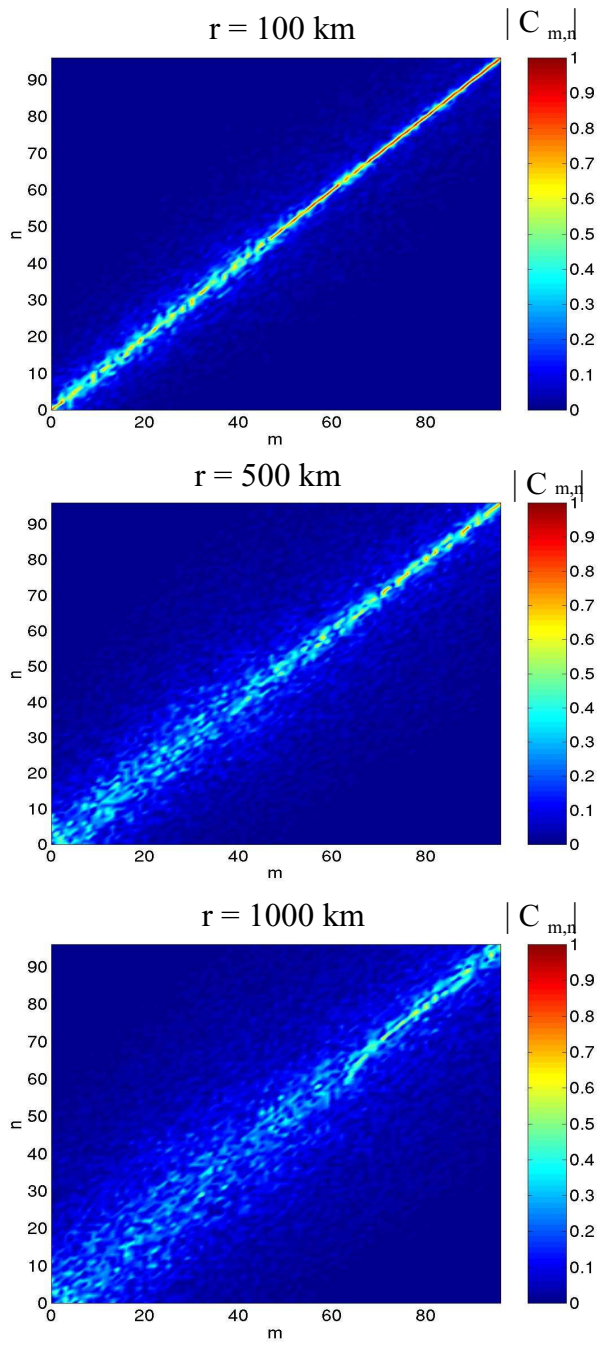

Figure 4.4: A sample unitary propagation matrix C for propagation through a single internal wave field is illustrated as a contour plot of the magnitudes of the matrix elements $|C_{m,n}|$ plotted with initial wave number n on the vertical axis and final wave number m on the horizontal axis. The propagation ranges are $r = 100, 500, 1000$ km. The source frequency is 75 Hz.

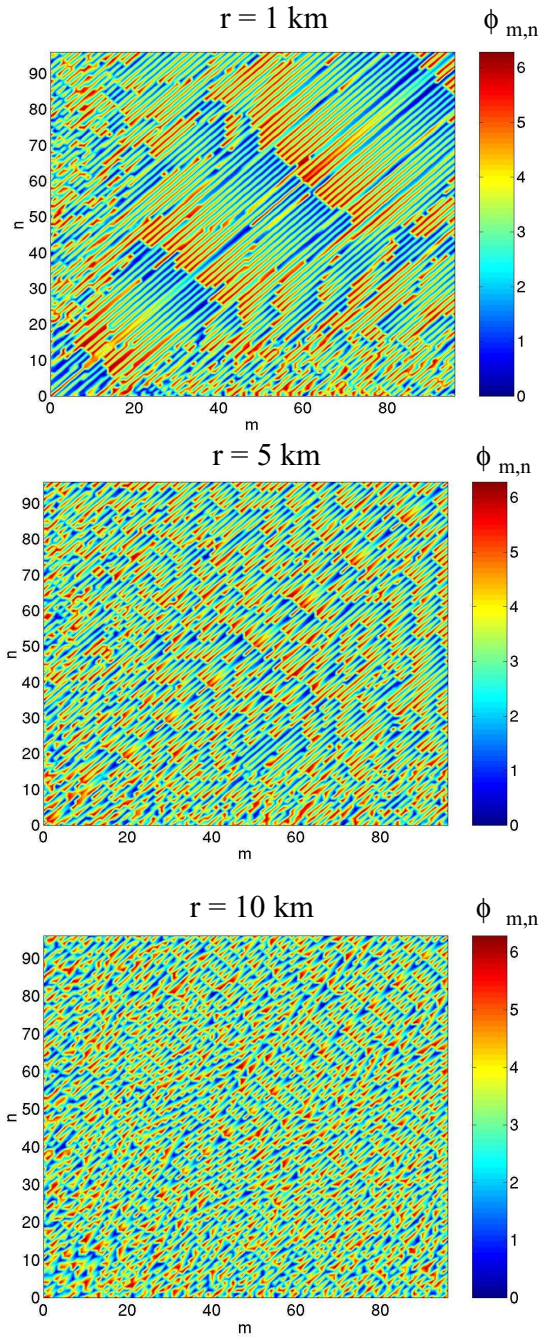

Figure 4.5: The phase of sample unitary propagation matrices C for propagation through a single internal wave field are illustrated as a contour plot of the phases of the matrix elements $C_{m,n}$ plotted with initial wave number n on the vertical axis and final wave number m on the horizontal axis. The propagation ranges are $r = 1, 5, 10$ km. The source frequency is 75 Hz.

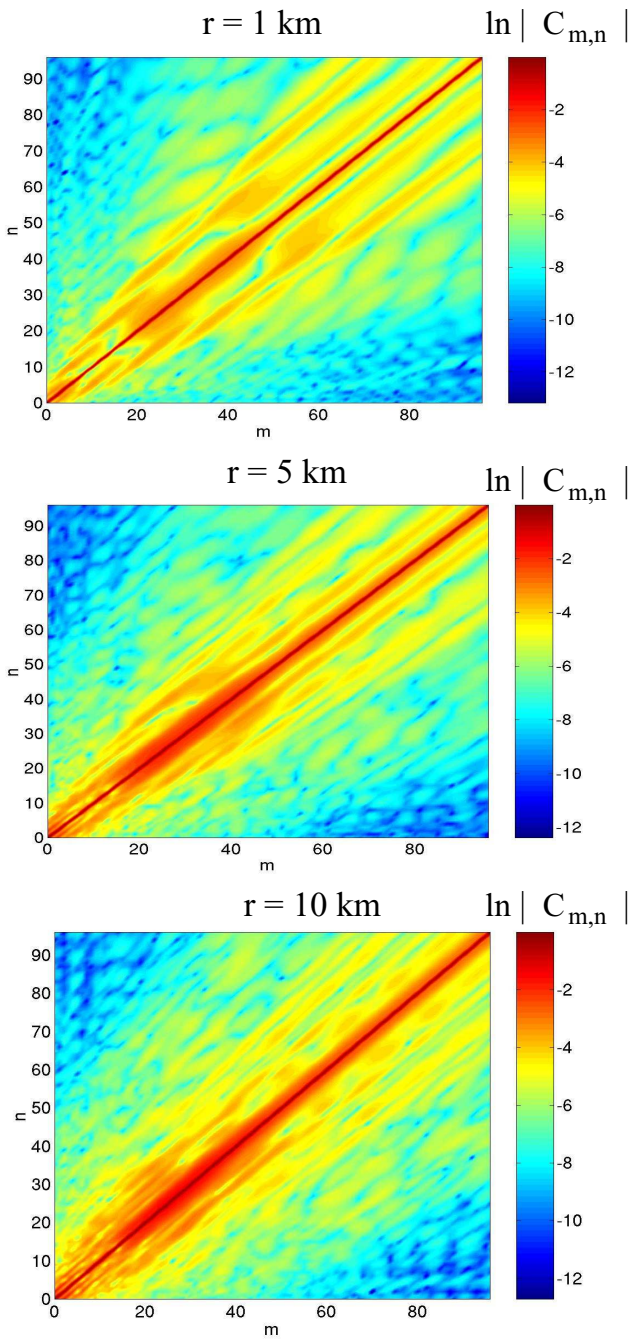

Figure 4.6: A sample unitary propagation matrix C for propagation through a single internal wave field is illustrated as a contour plot of the logarithm of the magnitudes of the matrix elements $ln|C_{m,n}|$ plotted with initial wave number n on the vertical axis and final wave number m on the horizontal axis. The propagation ranges are $r = 1, 5, 10$ km. The source frequency is 75 Hz.

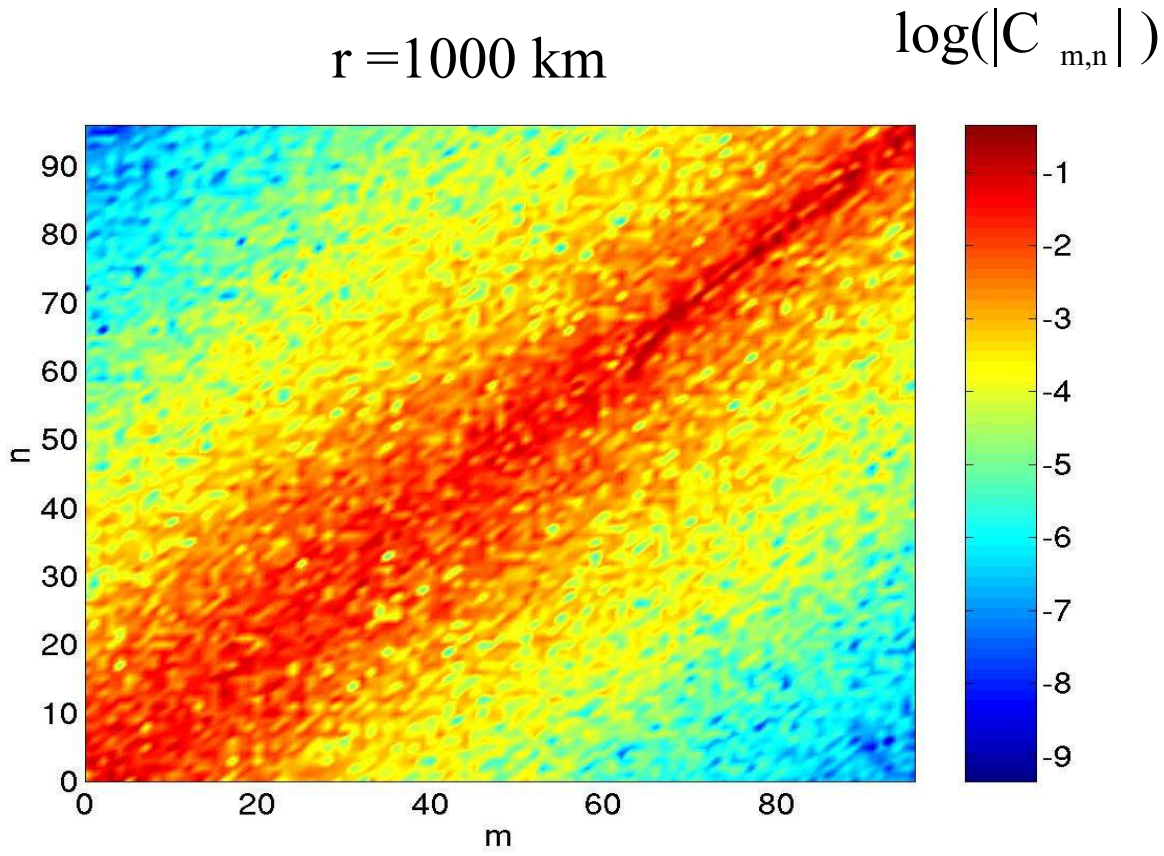

Figure 4.7: A sample unitary propagation matrix C for propagation through a single internal wave field is illustrated as a contour plot of the logarithm of the magnitudes of the matrix elements $ln|C_{m,n}|$ plotted with initial wave number n on the vertical axis and final wave number m on the horizontal axis. The propagation range is $r = 1000$ km. The source frequency is 75 Hz.

4.1.4 Dynamical Multiplication Property of Unitary Propagation Matrices

The formal solutions of the parabolic equation in Eq. (3.8) satisfy the property that the solution $\Psi(z, 2R)$ (for propagation of the initial wave field Ψ_0 from $r = 0$ to the range $r = 2R$) is equal to the propagation of the solution $\Psi(z, R)$ (for propagation of the initial wave field Ψ_0 from $r = 0$ to the range $r = R$) from $r = R$ to the range $r = 2R$.

The interpretation of this property for the unitary propagation matrices C results in a dynamical multiplication property. Let $C(0, R)$ denote the unitary propagation matrix for the propagation from the initial range $r = 0$ to the long range R and let C_{R_i,R_j} denote the unitary propagation matrix for the propagation from ranges R_i to R_j, where $R_i \leq R_j$. Then the multiplicative property for unitary propagation matrices is that the full matrix $C(0, R)$ can be written as a product of N short range matrixes $C(R_i, R_j)$,

$$C(0, R) \quad = \quad \prod_{j=0}^{N-1} C(R_j, R_{j+1}) \ ,$$

where $R_0 = 0 < R_1 < R_2 < ... < R_{N-1} < R_N = R$.

Note that the matrix product is only exactly $C(0, R)$ for infinite dimensional matrices which have all possible states represented in the matrix. In this thesis, the unitary propagation matrices C are finite dimensional, so that only states for $0 \leq n \leq 97$ are represented. A consequence of this is that the above product is not exact for the numerical matrices calculated. The error in the matrix multiplication is to first order the value of $C_{n,n}$ for $n > 97$ at the

intermediate ranges of the matrix multiplication. The error in the matrix multiplication due to not representing the propagation in some modes is not a large concern as long as the errors are less than the error already made in the wave propagation by not representing the propagation of the modes properly. The choice of vertical extent of the grid, as described in Appendix A, limits the resolution of the tails of the modes and the choice of vertical resolution determines the resolution of the frequencies of oscillation of the modes.

4.2 Perturbation Theory Model

4.2.1 First Order Range Dependent Wave Perturbation Theory

In the analogy of the parabolic equation with the one dimensional Schrödinger equation of quantum mechanics, first order time dependent quantum perturbation theory [53] can be used to estimate the transition matrix elements $C_{m,n}$ from propagation in the potential $V(z,r)$ from Eq. (3.12). The first order approximation is

$$\begin{aligned} C_{m,n} &= \delta_{m,n} e^{-ikrE_n} - ike^{-ikrE_m} \int_0^r dr' e^{i\omega_{m,n} r'} V_{m,n}(z,r') \\ &= \delta_{m,n} e^{-ikrE_n} \\ &\quad -ike^{-ikrE_m} \epsilon \sum_j \frac{V_j^{m,n}}{\sqrt{j^2 + j*^2}} \sum_{k_r} (\Delta k_r)^{1/2} \sqrt{I_{j,k_r}} \int_0^r dr' e^{i\omega_{m,n} r'} \cos(k_r r' + \Phi_{j,k_r}) \ , \end{aligned}$$

where $\omega_{m,n} = k(E_m - E_n)$ is like the Bohr angular frequency [53] , the small parameter is $\epsilon = \frac{\mu}{g}\frac{2B}{\pi}\left(\frac{E}{M}\right)^{1/2} N_0^2 = 2.02 \times 10^{-3}$ and the potential is

$$V^j(z) = e^{-3z/2B}\sin(j\pi(e^{-z/B} - e^{-H/B}))g(z, z_{st}, \tau)g(z, z_{sm}, \tau)$$

with $g(z, z_{st}, \tau)g(z, z_{sm}, \tau_{sm})$ the surface and smoothing filters described in Secs. (3.2.3) and (3.2.4). Integrating the perturbation theory expression for $C_{m,n}$ over range r gives

$$\begin{aligned} C_{m,n} &= \delta_{m,n}e^{-ikrE_n} - \frac{k\epsilon}{2}e^{-ikrE_m}\sum_j \frac{V_j^{m,n}(z)}{\sqrt{j^2 + j*^2}}\sum_{k_r}(\Delta k_r)^{1/2}\sqrt{I_{j,k_r}} \\ &\times \left[\frac{\left(e^{i(\omega_{m,n}+k_r)r} - 1\right)e^{i\Phi_{j,k_r}}}{\omega_{m,n} + k_r} + \frac{\left(e^{i(\omega_{m,n}-k_r)r} - 1\right)e^{-i\Phi_{j,k_r}}}{\omega_{m,n} - k_r}\right], \end{aligned} \tag{4.9}$$

where the simplification $e^{2iA} - 1 = 2ie^{iA}\sin(A)$ and the identification $\int dk_r = \sum_{k_r}(\Delta k_r)^{1/2}$ (from the derivation of the internal wave potential in Appendix (B)) have been used. Since these equations have a uniform random variable Φ_{j,k_r}, they describe a statistical ensemble. However, these equations do not predict a unitary model for C, which is required by the propagation [53]. In Ch. (5), a construction will be made to improve on the perturbation theory model to incorporate the unitarity for the ensemble model.

4.2.2 Perturbation Theory Predictions

Some of the statistical predictions implied by first order perturbation theory in Eq. (4.9) are consistent with the propagation results, while others are not. Averaging over the uniform random phases in Eq. (4.9) using $\langle e^{i\phi_{j,k_r}}\rangle = 0$ and $\langle e^{-i\phi_{j,k_r}}\rangle = 0$ gives that first order per-

turbation theory predicts that the average value of the off-diagonal elements $C_{m,n}$ for $n \neq m$ is $\langle C_{m,n} \rangle = 0$ and the mean phase for the diagonal elements $U_{n,n}$ is $-krE_n$. The zero average for the off-diagonal elements is supported by the analysis of the propagation results in Sec. (4.3.1). However, the propagation results in Sec. (4.3.2) do not support the conclusion about the mean phase, since the difference of the mean phase from $-krE_n$ in Figs. (4.20) and (4.22) is non-zero beyond statistical deviations.

Differences in the phase from the first order prediction appear to be of third order. Yet, second and third order differences are not enough to account for the differences in Figs. (4.20) and (4.22). Since perturbation theory cannot account for the mean phases seen in the propagation, an approximate model derived from the propagation results will be utilized.

4.2.3 Prediction for Effect of Potential on Unitary Propagation Matrix

For a constant confining potential, V (i.e. $V = 0$), the unitary propagation matrix elements are diagonal $C_{m,n} = e^{-ikrE_n}\delta_{m,n}$. A potential $V(z, r)$ with structure in depth or range allows a mode to mix to other modes as it propagates. To gain some knowledge of how the potential effects the unitary propagation matrix elements, consider propagation to a short range, r. After even a short range of propagation, the mixing of energy between the states has begun.

Utilizing the analogy with the Schrödinger equation, where range takes the place of time, first order time dependent quantum perturbation theory [53] gives an expression for the uni-

tary propagation matrix elements $C_{m,n}$ after propagation in the potential $V(z,r)$.

$$\begin{aligned} C_{m,n} &\approx \delta_{m,n} e^{-ikrE_n} - ike^{-ikrE_m} \int_0^r dr' e^{i\omega_{m,n}r'} \int \psi_n(z) V(z,r') \psi_m(z) dz \\ &= \delta_{m,n} e^{-ikrE_n} - ike^{-ikrE_m} \int_0^r e^{i\omega_{m,n}r'} V_{m,n}(r') dr' \,, \end{aligned} \tag{4.10}$$

where

$$V_{m,n}(r) = \int \psi_n(z) V(z,r) \psi_m(z) dz \tag{4.11}$$

and $\omega_{m,n} = k(E_m - E_n)$.

Though quantum time-dependent perturbation theory is valid only for extremely short times (here for only short ranges), Eq. (4.10) illustrates that the amount of mixing is controlled by the function $V_{m,n}(z)$. If the potential V is constant (i.e. zero), the unitary propagation matrices are purely diagonal and there is no mixing. If the potential $V(z,r)$ is range-independent or has adiabatically changing range dependence, then the basis can be changed to one in which the unitary propagation matrices are purely diagonal. If the potential $V(z,r)$ has significant range dependence, there will be mixing between the modes during the propagation.

Prediction for Effect of Range Dependence of Potential on Transition Matrix

The range dependence of the potential is a factor that enables the mixing between states n and m. This can be understood by noting that in the range dependent potential, energy is not

conserved during the propagation so that mixing between the modes alters the energies.

From the dependence of $C_{m,n}$ on $\int_0^R V_{m,n} dr$, a propagating mode which gains or loses energy from the internal waves can transition into another mode if the energy difference is enough to reach the eigenvalue of another mode or even by tunneling to the next level [53]. This transition is easiest at the upper turning points of the rays, where the density of modes is highest due to the steepness of the potential. The upper turning point is also the location where the perturbation due to the internal waves is strongest.

If the range dependent perturbations are indeed adiabatically changing with range, then the basis adiabatically changes with range, but the propagation of a mode n stays in mode n [56] so that the unitary propagation matrix remains diagonal in the modified basis.

For the internal wave perturbations, the amount of mixing attributable to the range dependence is much less than the amount of mixing due to the vertical oscillations in the perturbing potential.

Prediction for Effect of Vertical Oscillations of Potential on Transition Matrix

The vertical dependence of the potential is the dominant factor that enables the mixing between states n and m. The amplitude of the overlap quantity $V_{m,n} = \int \psi_n(z) V(z,r) \psi_m(z) dz$ dictates how the depth dependence of the potential enables mixing. If the potential is constant, then the matrix is purely diagonal. In order for the states m and n to be connected from a single scattering from the potential, the potential needs to have oscillations with the difference between the frequencies in the states m and n. If this is the case, then the integral will have value for $m \neq n$ and there will be mixing.

Using the internal wave potential V in Eq. (3.12) with ϵ a small constant, the overlap quantity can be written

$$V_{m,n} = \epsilon \sum_j \sum_{k_r} \frac{\sqrt{I_{j,k_r}} V_j^{m,n}}{\sqrt{j^2 + j*^2}} \cos\left(k_r r + \phi_{j,k_r}\right) , \tag{4.12}$$

where

$$V^j(z) = e^{-3z/2B} \sin(j\pi(e^{-z/B} - e^{-H/B})) g(z, z_{st}, \tau) g(z, z_{sm}, \tau) \tag{4.13}$$

and $g(z, z_{st}, \tau)g(z, z_{sm}, \tau_{sm})$ are the surface and smoothing filters described in Sec. (3.2.3) and Sec. (3.2.4) and

$$V_j^{m,n} = \int \psi_n(z) V_j(z, r) \psi_m(z) dz . \tag{4.14}$$

In this form, the factor $V_j^{m,n}$ holds the effect of vertical oscillations of the potential on the mode mixing. Figures (4.9 -4.10) illustrate the dependence of the overlap $V_j^{m,n}$ for some values of internal wave mode j and mode number n, m.

In Fig. (4.10), non-negligible values of $V_j^{m,n}$ are for final states 'near' the initial state m. The values in this non-negligible region show the degree to which the internal wave mode j connects the initial mode m to the final mode n. The width of this region indicates the extent to which the mode j mixes modes during the propagation. Smaller mode numbers j are able to connect the initial state to a smaller window of final states than large mode numbers j. For most values of j and n, m, the function $V_j^{m,n}$ is very symmetric about the initial state n.

As seen in Eq. (4.12), the frequency of the oscillations in the potential come from the sum over the internal wave mode contributions j, where the maximum mode contribution is j_{max}. Since the potential has been smoothed [61] to restrict vertical structures to have minimum wavelength $\lambda_s = \frac{c_0}{f \tan \theta_{max}}$, where $\theta_{max} = 10\,^\circ$, the maximum wavenumber k_s and maximum frequency ω_s in the potential has been restricted to approximately $k_s = k_0 \tan 10\,^\circ$ and $\omega_s = k_0 c_0 \tan 10\,^\circ$. As seen in Fig. 4.8, each eigenmode $\psi_n(z)$ has a wide range of frequencies of oscillation which are peaked near the wavenumber corresponding to the largest classical momentum $p = \sqrt{2E_n}$ for mode n. The mode n has an approximate largest wavenumber of $k = k_0 p = k_0 \sqrt{2E_n}$ and an approximate largest frequency of $\omega = k c_0 = k_0 c_0 \sqrt{2E_n}$.

Assuming that the propagation range is less than the scattering length so that only single-scattering occurs, a smaller mode m can be connected to a larger mode $n > m$ (with largest frequencies ω_m and ω_n respectively) if the potential possesses frequencies $\omega_n - \omega_m = k_0 c_0 \left(\sqrt{2E_n} - \sqrt{2E_m}\right)$. This frequency difference must be smaller than the largest frequency in the potential, $\omega_n - \omega_m = k_0 c_0 \left(\sqrt{2E_n} - \sqrt{2E_m}\right) < \omega_s = k_0 c_0 \tan 10\,^\circ$ or $\left(\sqrt{2E_n} - \sqrt{2E_m}\right) < \tan 10\,^\circ$. Thus, after a single scattering event, a classical ray with energy E_m can be mixed into the energy E_n corresponding to a classical ray which initially differed by $10\,^\circ$ in starting angles. From the above criteria, the largest mode n to connect to initial mode m has energy $E_n = \frac{1}{2}\left(\tan 10\,^\circ + \sqrt{2E_m}\right)^2$. For the initial mode $m = 0$, $E_0 \approx 0.0002373$ so that $E_n \approx 0.01962$, which is closest to the energy for mode $n = 47$. For the initial mode $m = 50$, $E_0 \approx 0.02077$ so that $E_n \approx 0.07225$, which is closest to the energy for mode $n = 227$. For a final mode of $n = 150$, $E_n \approx 0.052$ and $E_m \approx 0.0107$ corresponding to an initial mode of $m = 23$. From these calculations, the potential has frequencies that can easily mix modes

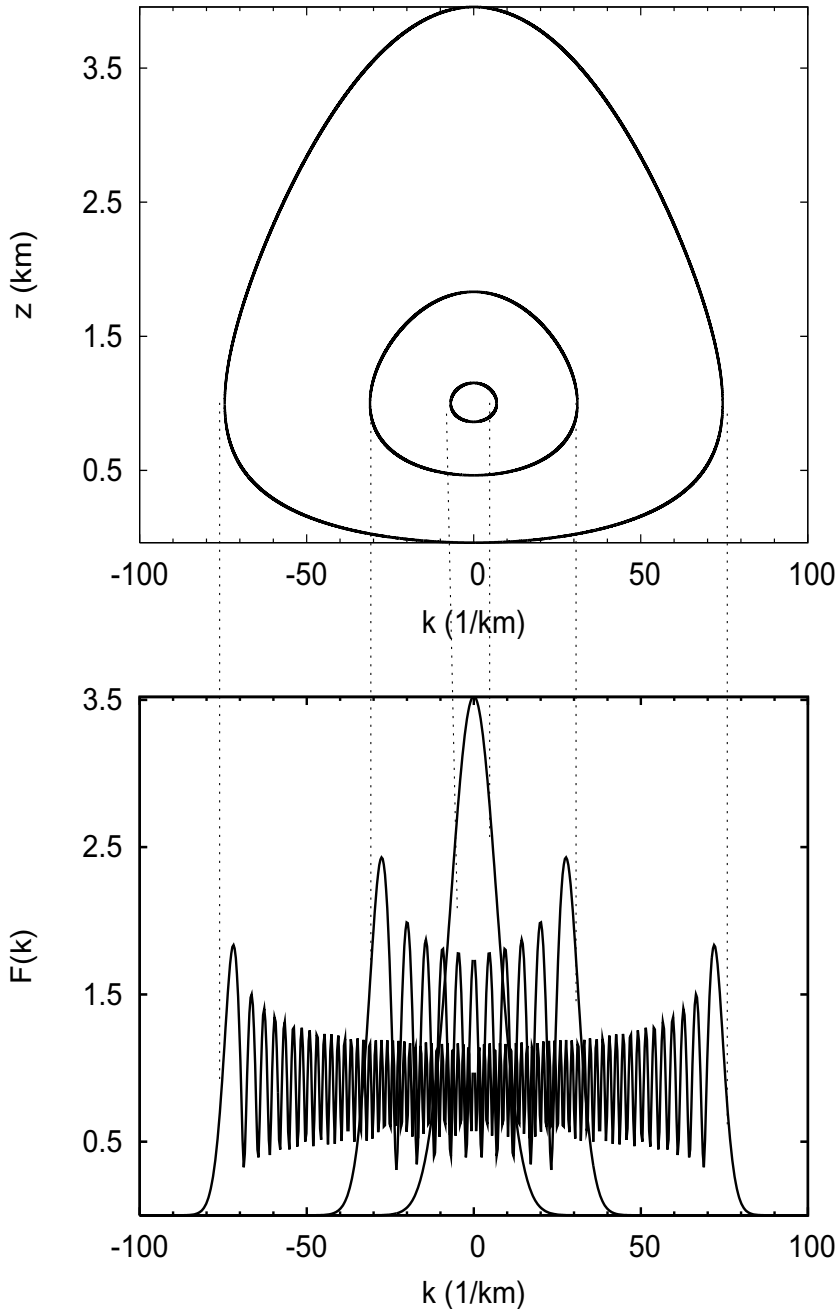

Figure 4.8: (Upper) Phase space portrait of the propagation in depth z and vertical wavenumber k, for a complete cycle in the Munk potential in Eq. (3.11) at the energies E_n of the Munk potential for $n = 0, 10, 70$. (Lower) Eigenmodes $\psi_n(k)$ of the Munk potential for $n = 0, 10, 70$ plotted versus vertical wavenumber k, where $k = k_0 p$, with $k_0 = \frac{2\pi f}{c_0}$ and $p = \tan\theta$.

separated by more than 100 in mode number.

Though the potential has frequencies which can mix modes separated by 100 modenumbers, the modes with the dominant contributions to the construction of the timefront are the lower modes. Only roughly the first 80 modes have significant contributions to the construction of the timefront due to the weightings of the modes in the initial Gaussian source in Eq. (3.18).

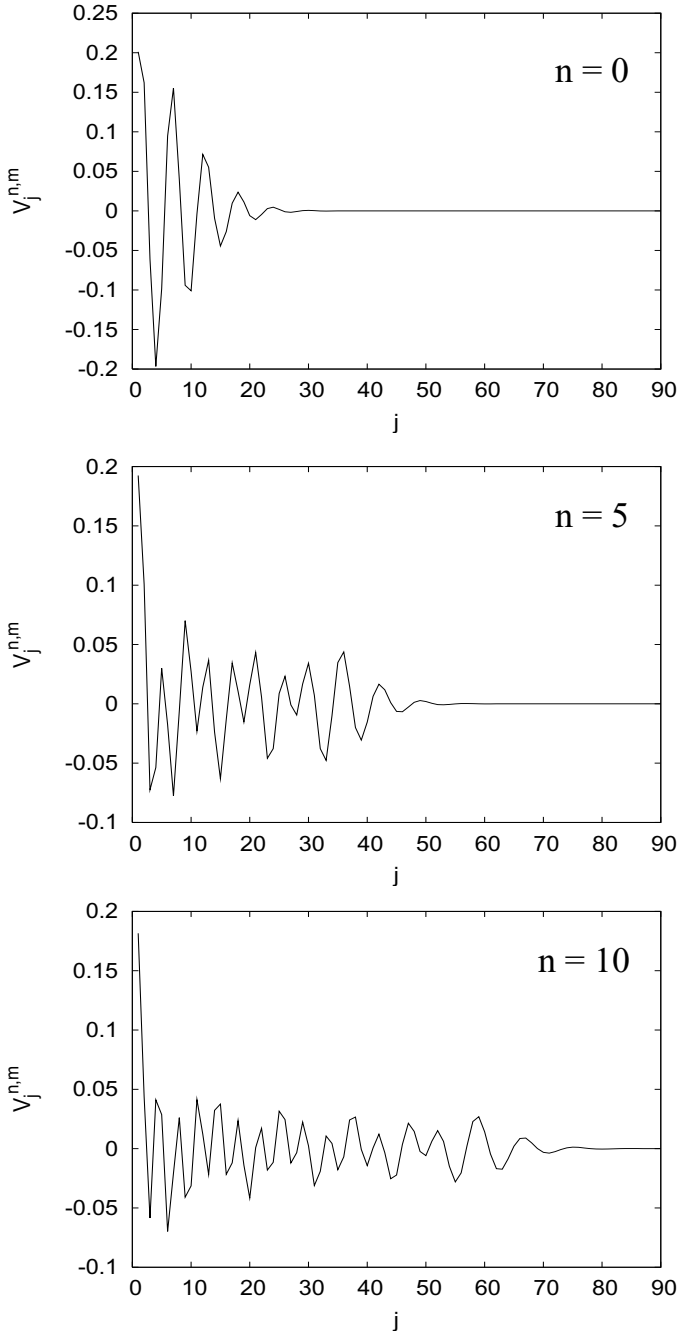

Figure 4.9: The overlap $V_j^{m,n} =< m|V_j(z)|n >$ in Eq. (4.14) for $n = m$ is plotted versus internal wave mode number j for $n = 0, 5, 10$. As n increases, the oscillations increase in their extent in n.

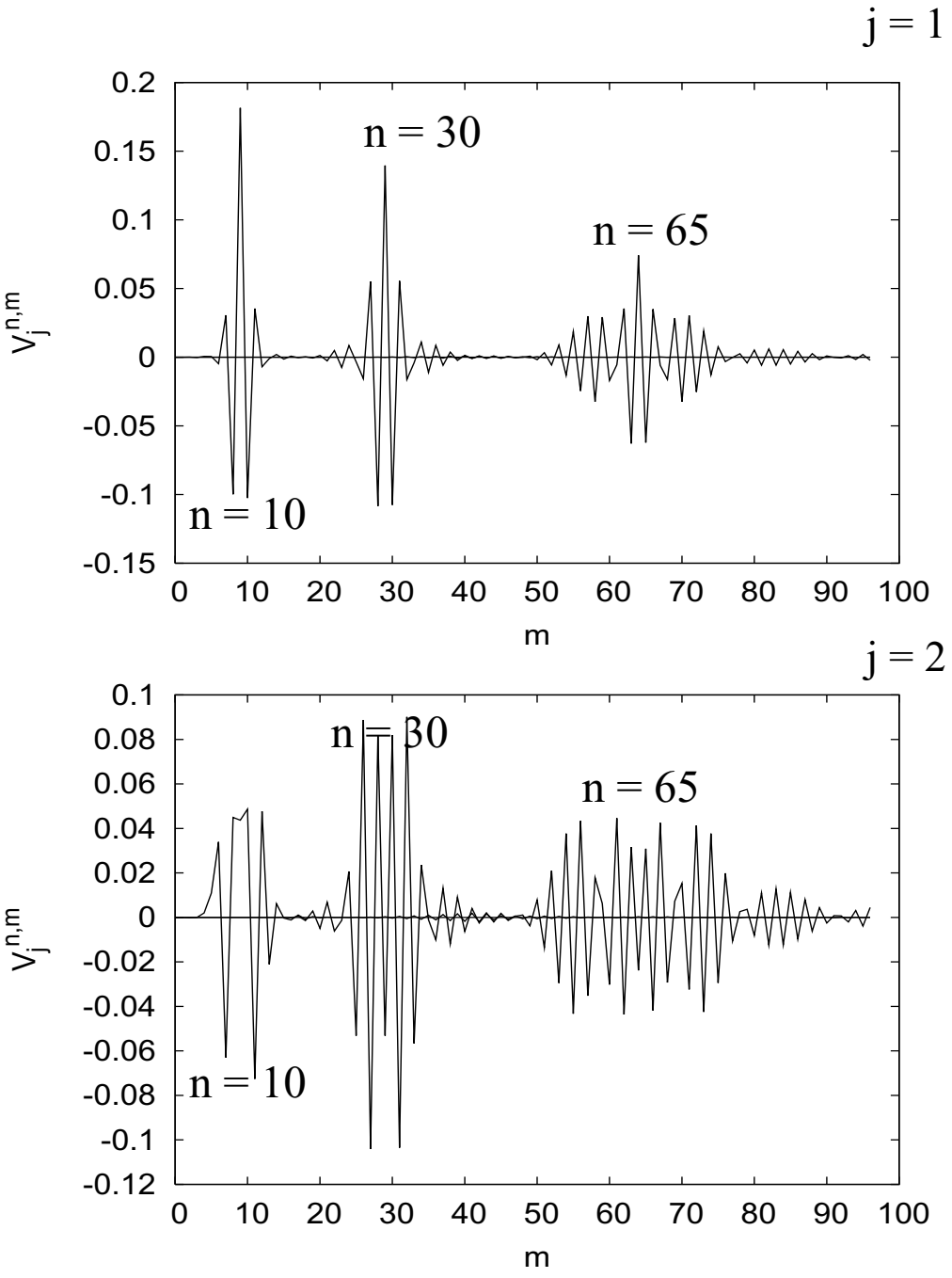

Figure 4.10: The overlap $V_j^{m,n} =< m|V_j(z)|n >$ in Eq. (4.14) for $n = m$ is plotted versus mode number m for $n = 10, 30, 65$ and $j = 1, 2$.

4.2.4 Prediction for Correlation Range of Unitary Propagation Matrix

The members of the ensemble of building blocks used for the long range ensemble model in Ch. (5) will be multiplied to generate independent unitary propagation matrices for the long range. It is ideal for the building blocks to be identically distributed and independent, in the sense that the correlations between successive building blocks should be zero.

In building the ensemble model, the range R to take for the building block model is an important parameter in the model construction. In this section, a calculation of the correlation between successive unitary propagation matrices is made as a function of range in order to determine an ideal range for the building block matrix.

Let $C_{m,n}(r_i, r_f)$ be the unitary propagation matrix when propagation is from initial range r_i to the final range r_f. It is desired to find the range, R, such that the unitary propagation matrices $\{C_{m,n}(0, R)$, $C_{m,n}(R, 2R)$,$C_{m,n}(2R, 3R)$,$C_{m,n}(3R, 4R), ...\}$ are approximately independent.

Consider the correlation function $\rho_{C_{m,n}}(r)$ of the unitary propagation matrices $C_{m,n}(0, r)$ and $C_{m,n}(r, 2r)$,

$$\rho_{C_{m,n}}(r) \quad = \quad \frac{\langle C_{m,n}(0,r)C^*_{m,n}(r,2r)\rangle - \langle C_{m,n}(0,r)\rangle\langle C^*_{m,n}(r,2r)\rangle}{\sigma_{C_{m,n}}(0,r)\sigma_{C_{m,n}}(r,2r)}\,, \tag{4.15}$$

where $\langle\cdot\rangle$ denotes the average over the internal wave fields and the variance is $\sigma^2_{C_{m,n}}(r) = \langle C_{m,n}(r_i, r_f)C^*_{m,n}(r_i, r_f)\rangle - \langle C_{m,n}(r_i, r_f)\rangle\langle C_{m,n}(r_i, r_f)\rangle^*$ for initial and final ranges r_i and r_f, respectively. For a range independent potential V, the unitary propagation matrices over the range intervals $[0, r]$ and $[r, 2r]$ would be identical giving a correlation $\rho_{C_{m,n}}(r) = 1$ for

all ranges, r. For a range dependent potential V, the correlation $\rho_{C_{m,n}}(r)$ between the unitary propagation matrices over the intervals decays from unity related to the decorrelation with range of the potential.

The correlation of the potential V with displacements in range $r' - r''$ is described by the correlation function, $\rho_V(r' - r'')$.

$$\rho_V(r' - r'') \;=\; \frac{\langle V_{m,n}(r')V_{m,n}(r'')\rangle - \langle V_{m,n}(r')\rangle\langle V_{m,n}(r'')\rangle}{\sigma_{V_{m,n}}(r')\sigma_{V_{m,n}}(r'')} \,,$$

where $\langle V_{m,n}(r)\rangle = 0$ has been used and the variance is $\sigma^2_{V_{m,n}}(r) = \langle V^2_{m,n}(r)\rangle - \langle V_{m,n}(r)\rangle^2$. An analytic expression for the quantity $\langle V_{m,n}(r')V_{m,n}(r'')\rangle$ can be derived using the definition of $V_{m,n}$ in Eq. 4.11 and the internal wave expressions in Eq. 3.12, giving

$$\begin{aligned} V_{m,n}(r')V_{m,n}(r'') \;=\; & \epsilon^2 \int\int dz dz' \psi_m(z)\psi_m(z')\psi_n(z)\psi_m(z') \sum_{j,j'} \Delta k_r \int dz \psi_m(z)\psi_n(z) \\ & \int dk_r \int dk'_r \sqrt{\frac{I_{j,k_r} I_{j',k'_r}}{(j^2 + j*^2)(j'^2 + j*^2)}} \\ & \cos\left(\Phi_{j,k_r} + k_r r'\right) \cos\left(\Phi_{j',k'_r} + k'_r r''\right) \,, \end{aligned}$$

where $\epsilon = \frac{\mu}{g}\frac{2B}{\pi}\left(\frac{E}{M}\right)^{1/2} N_0^2 = 2.02 \times 10^{-3}$ is a small constant in the internal wave expression and $V_j(z) = e^{-1.5z/B} \sin\left(j\pi\left(e^{-z/B - e^{-H/B}}\right)\right)$. In performing the ensemble average $\langle V_{m,n}(r')V_{m,n}(r'')\rangle$ over different internal wave realizations, recall that ϕ_{j,k_r} is uniformly distributed on $[0, 2\pi]$ and delta-correlated. The needed averages (which are derived in Appendix (C.4)) are $\langle\cos(\phi_{j,k_r} + k_r r)\rangle = 0$ and $\langle\cos(\phi_{j,k_r} + k_r r')\cos(\phi_{j',k'_r} + k'_r r'')\rangle =$

$\frac{\delta_{j,j'}\delta_{k_r k_r'}}{2}\cos\left(k_r(r'-r'')\right)$. Then the ensemble average over $V_{m,n}$ simplifies to

$$\langle V_{m,n}(r)V_{m,n}(r'')\rangle = \frac{\epsilon^2}{2}\Delta k_r \sum_j \frac{\left(V_{m,n}^j\right)^2}{j^2+j*^2}\int dk_r\ \cos(k_r(r'-r''))\ I_{j,k_r}\ . \tag{4.16}$$

Using the first order perturbation theory result in Eq. (4.10), the expression for $\langle V_{m,n}(r)V_{m,n}(r+r')\rangle$ in Eq. (4.16) and performing the averaging using $\langle V_{m,n}(r)\rangle = 0$ gives

$$\begin{aligned}
& \langle C_{m,n}(0,r)C_{m,n}^*(r,2r)\rangle - \langle C_{m,n}(0,r)\rangle\langle C_{m,n}^*(r,2r)\rangle \\
\approx\ & k^2\int_0^r\int_r^{2r} e^{i\omega_{m,n}(r'-r'')}\langle V_{m,n}(r')V_{m,n}(r'')\rangle dr'dr'' \\
=\ & \frac{\epsilon^2k^2}{2}\sum_j \frac{\left(V_{m,n}^j\right)^2}{j^2+j*^2}\Delta k_r\int dk_r\ I_{j,k_r}\int_0^r\int_r^{2r} e^{i\omega_{m,n}(r'-r'')}\cos(k_r(r'-r''))dr'dr'' \\
=\ & (k\epsilon)^2(\Delta k_r)\sum_j \frac{\left(V_j^{m,n}(k)\right)^2}{j^2+j*^2} \\
& \int dk_r I_{j,k_r}\left[\frac{e^{-i\omega_1 r}\sin^2(\omega_1 r/2)}{\omega_1^2} + \frac{e^{-i\omega_2 r}\sin^2(\omega_2 r/2)}{\omega_2^2}\right],
\end{aligned} \tag{4.17}$$

where $\omega_1 = \omega_{m,n} + k_r$ and $\omega_2 = \omega_{m,n} - k_r$.

Figure (4.11) illustrates the magnitude of the correlation $|\rho_{C_{m,n}}(r)|$ from the approximation in Eq. (4.17) for some sample diagonal and off-diagonal elements. Notice there is beating in the correlations due to the interference of the contributions with frequency $\omega_{m,n} + k_r$ and $\omega_{m,n} - k_r$. This is due to the presence of two resonance frequencies when $\omega_{m,n} = \pm k_r$. The envelope of the decay in the correlation function is the desired quantity. The decay of the diagonal elements are approximately the same, while there is some variation in the decay of the off-diagonal elements. The envelope function on the magnitude of the correlation

decays to roughly the e^{-1} decay scale at a range approximately equal to 50 km. Since 50 km is the average period of a classical ray propagating in the potential (see Fig. (C.1)), it is concluded that a 'good' range for the decorrelation of the unitary propagation matrices is approximately 50 km. This range is chosen for the range of the 'building block' model of the unitary propagation matrix.

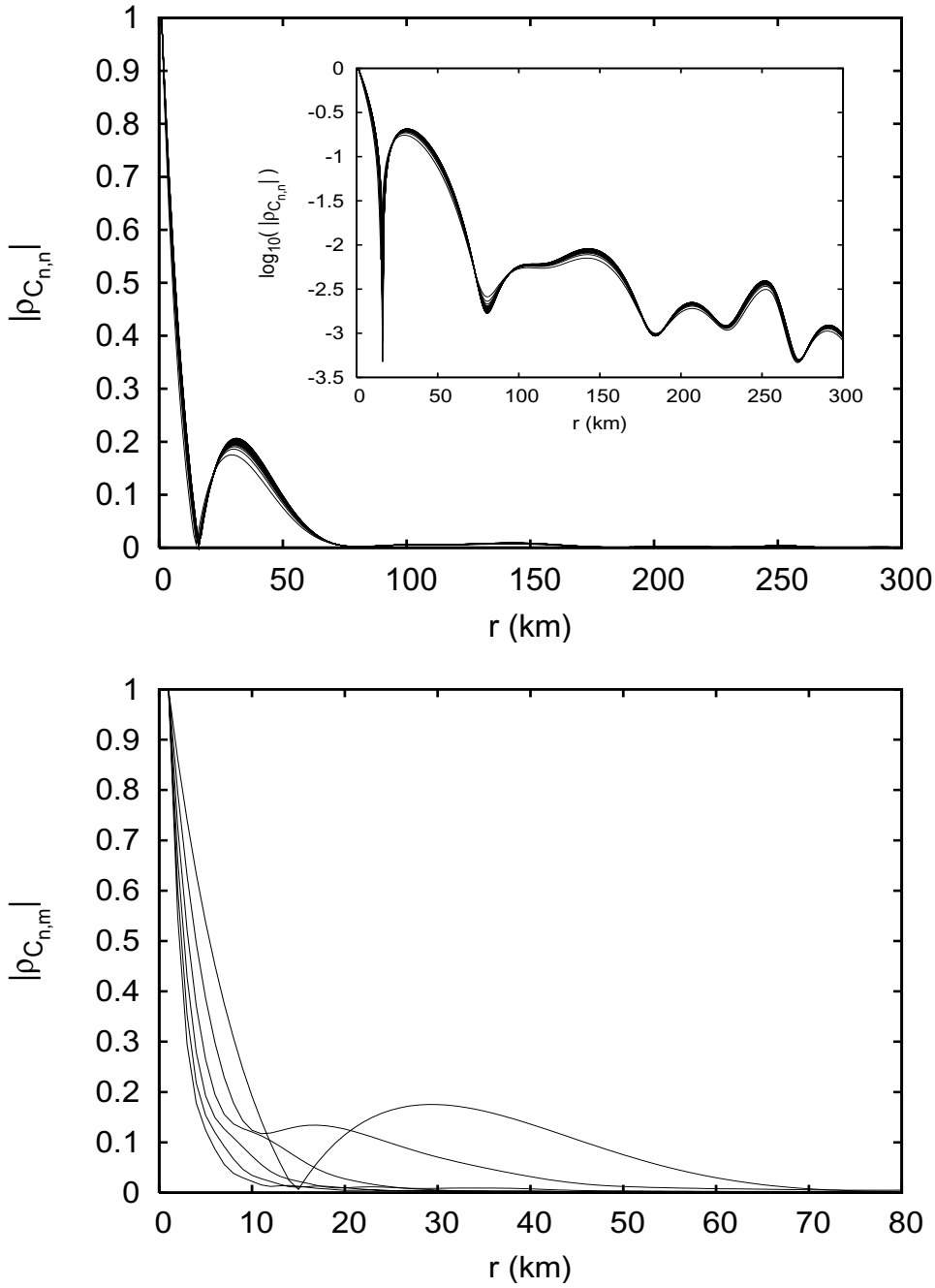

Figure 4.11: The magnitude of the correlations $|\rho_{C_{m,n}}(r)|$ are plotted with range r. The correlations $\rho_{C_{n,n}}(r)$ are calculated using Eq. (4.17). (Upper) Amplitude of the correlations for the diagonal elements, $|\rho_{C_{n,n}}(r)|$ for $n = 0, 5, ..., 60$ are plotted with range r. The inset in the plot is the logarithm $log\left(|\rho_{C_{n,n}}(r)|\right)$ plotted with range r. The second dip in the correlation occurs at $r = 80$ km. (Lower) Amplitude of the correlation of some of the offdiagonal elements, $|\rho_{C_{m,n}}(r)|$ for $n = 0$ and $m = 0, 1, ..., 5$ are plotted with range. The magnitudes of the offdiagonal correlations decay much faster with range than do the diagonal correlations. The magnitudes of the diagonal correlations in n all decay roughly equally.

4.3 Propagation Results for the Unitary Propagation Matrix Statistics at 50 km

In Ch. (5), the 'building blocks' will be constructed as a statistical model for the unitary propagation matrices for the range of $R = 50$ km (chosen to be an approximate range where unitary propagation matrix elements calculated between consecutive ranges of length R can be considered independent). In this section, the statistical properties of the unitary propagation matrix for 50 km are investigated in order to aid the construction and verification of the building block ensemble model. The general unitary propagation matrices so far were given the variable C, but the unitary propagation matrix for 50 km will be given the varialbe U to distinguish this matrix from the general matrices at other ranges.

For propagation in the unperturbed potential in Eq. (3.11), the energy is conserved, so that the unitary propagation matrix for 50 km, U, is diagonal. In this case, $U_{m,n} = \delta_{m,n} e^{-ikE_m R}$, where E_m are the eigenenergies corresponding to the unperturbed potential [53]. The diagonal elements $U_{n,n}$ only accumulate a phase $e^{-ikE_n R}$ from their initial value of one as they propagate to a range R.

For propagation in the perturbed potential in Eq. (3.10), the energy is not conserved due to the range dependence of the potential. Therefore, energy mixes between the modes as the wave propagates. This results in flow of energy off of the diagonal so that the unitary propagation matrix becomes banded for small ranges as illustrated in Fig. (4.4).

The unitary propagation matrices U are calculated using Eq. (4.5). The modes are propagated through several independent realizations of sound speed fluctuations using the nu-

merical methods described in Appendix A.3. The modes corresponding to the unperturbed potential are calculated by using the numerical methods described in Appendix A.4.

4.3.1 Statistics of Off-Diagonal Elements $U_{m,n}$

The off-diagonal elements $U_{m,n}$ (where $n \neq m$) of the unitary propagation matrix for 50 km hold information on the amount of mixing between modes. The off-diagonal elements are in general complex numbers, with a significant real and imaginary part. They are functions of range r, source wave number k and the mode numbers n, m.

Numerical simulations of the unitary propagation matrix elements U for propagation to 50 km were calculated using $10,000$ internal wave seeds for the sound speed fluctuations and 114 different wavenumbers k. The computational resources of the Teragrid [1] were utilized for these simulations.

Distribution of Off-Diagonal Elements

The phase of the off-diagonal element $U_{m,n}$ is found to be approximately that of a uniform distributed random variable, for all n, m combinations. A uniform distribution for the phases of the off-diagonal elements implies identical, zero-centered, uncorrelated probability densities for the real and imaginary parts separately.

The distribution function for the real and imaginary parts of $U_{m,n}$ is found to be zero-centered. Histograms and sample cumulative density functions for the distribution of the real part of $U_{m,n}$ are shown for some values of n, m in Fig. (4.12) and (4.13). Visually, these plots suggest that the real part of $U_{m,n}$ is distributed approximately as a Gaussian random

number. Plots of the distribution of the imaginary part similarly suggest that the imaginary part is distributed approximately as a Gaussian random number.

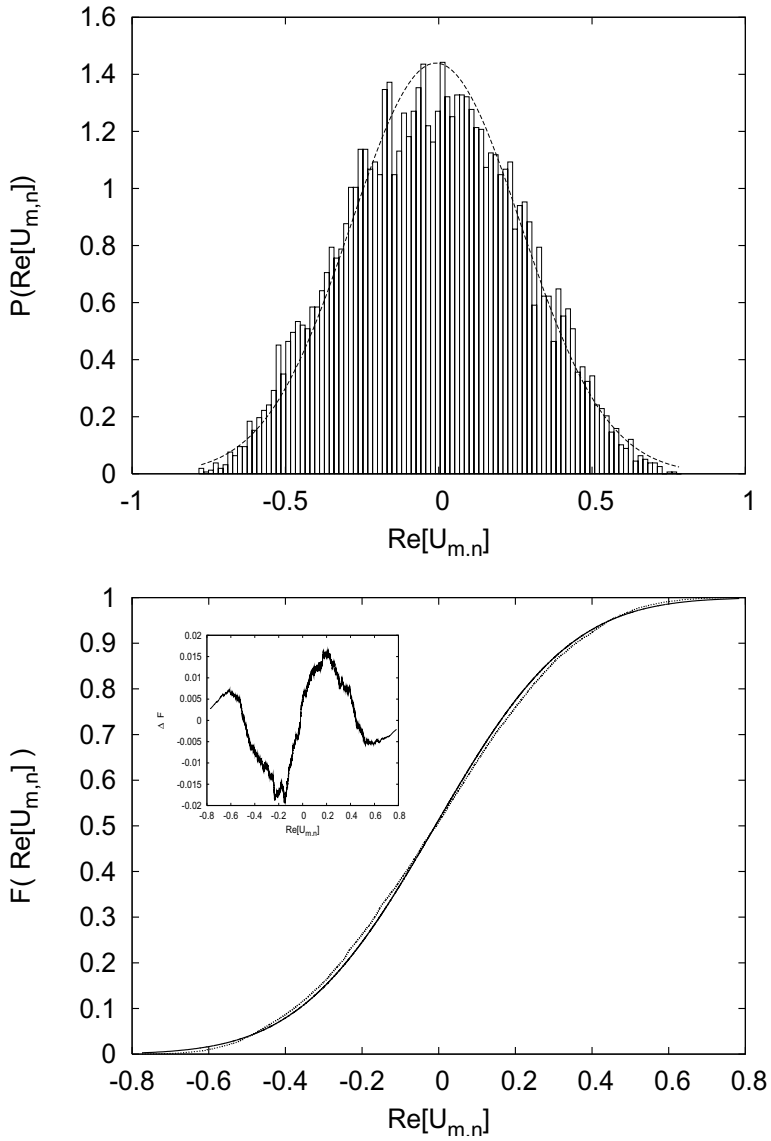

Figure 4.12: (Upper) A histogram of the probability density function (PDF) for the real part of the off-diagonals $Re[U_{m,n}]$ for $n = 0$, $m = 1$. 100 bins are used in the construction of the histogram. Also plotted is the probability density function for a Gaussian distribution with mean and variance taken from the set of values $Re[U_{m,n}]$. (Lower) Approximation to the cumulative density function (CDF) $F(Re[U_{m,n}])$ of the real part of the off-diagonals $Re[U_{m,n}]$ for $n = 0$, $m = 1$. Also plotted is the cumulative density function for a Gaussian distribution with mean and variance taken from the set of values $Re[U_{m,n}]$. The inset shows the error between the approximate cdf and the Gaussian cdf. The shape of the error is typical of that for sampling convergence with N to a distribution.The diagonal elements $U_{n,n}$ are calculated after propagation to $r = 50$ km and $N = 10000$ values (corresponding to different internal wave seeds). This was done for a wavenumber k corresponding to a source frequency of 75 Hz.

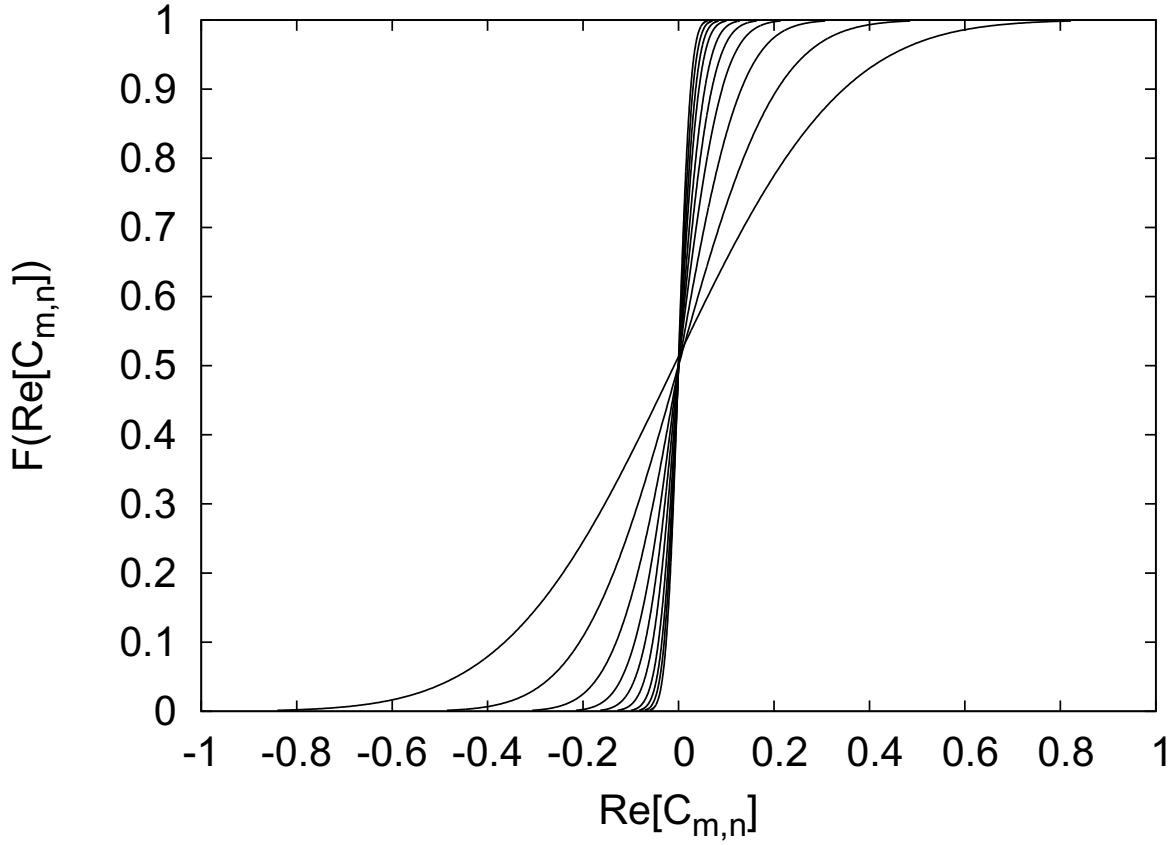

Figure 4.13: The distribution function $F(Re[U_{m,n}])$ is plotted as a function of $Re[U_{m,n}]$, the real part of $U_{m,n}$, for $n = 0$ and $m = 1, 2, ..., 10$. $U_{m,n}$ is calculated after propagation to $r = 50$ km. The distribution functions are calculated using $N = 10,000$ internal wave seeds so they are accurate to about $\frac{1}{\sqrt{N}} = 0.01$. The means of $Re[U_{m,n}]$ are statistically consistent with zero, which is consistent with the location of the center of the distribution function.

However, the true distribution of the real and imaginary parts of the off-diagonal elements cannot be a Gaussian random variable. Recall that $U_{m,n}$ is a probability amplitude so that $|U_{m,n}| < 1$ and the real and imaginary parts of $U_{m,n}$ are constrained to lie within the unit circle, a finite domain. A Gaussian random variable has an infinite domain. The true distribution of the real and imaginary parts may be related to a Gaussian random variable (i.e. a circular normal distribution) or another distribution which has dominant first and second moments. Regardless, the figures suggest that whatever the distribution of the real and imaginary parts, this distribution could be well approximated with a distribution that has only two moments (i.e. a mean and a variance) such as that of a Gaussian distribution.

Variance of Off-Diagonal Elements

The distribution of the variance of the off-diagonal elements $U_{m,n}$ is found to obey a symmetry with constant value of $n + m$ and $n - m$. A transformation from the matrix coordinates (n, m) to the rotated coordinate system of $((n + m)/\sqrt{2}, (n - m)/\sqrt{2})$ is helpful for identifying the dependence of the variance. This rotated coordinate system is shown in Fig. (4.14).

The variance of the real and imaginary parts is a function of mode numbers n, m and wavenumber k. The variance of the real part is shown in Fig. (4.15) to decrease with the difference $n - m$. The variance of the real and imaginary parts do not vary greatly with $(n + m)$, but the small variation seen even in a sample matrix such as in Fig. (4.3) may be important. The imaginary part of the off-diagonal elements $U_{m,n}$ is similar to the real part. The differences are most evident with wavenumber k as shown in Fig. (4.16). The variance

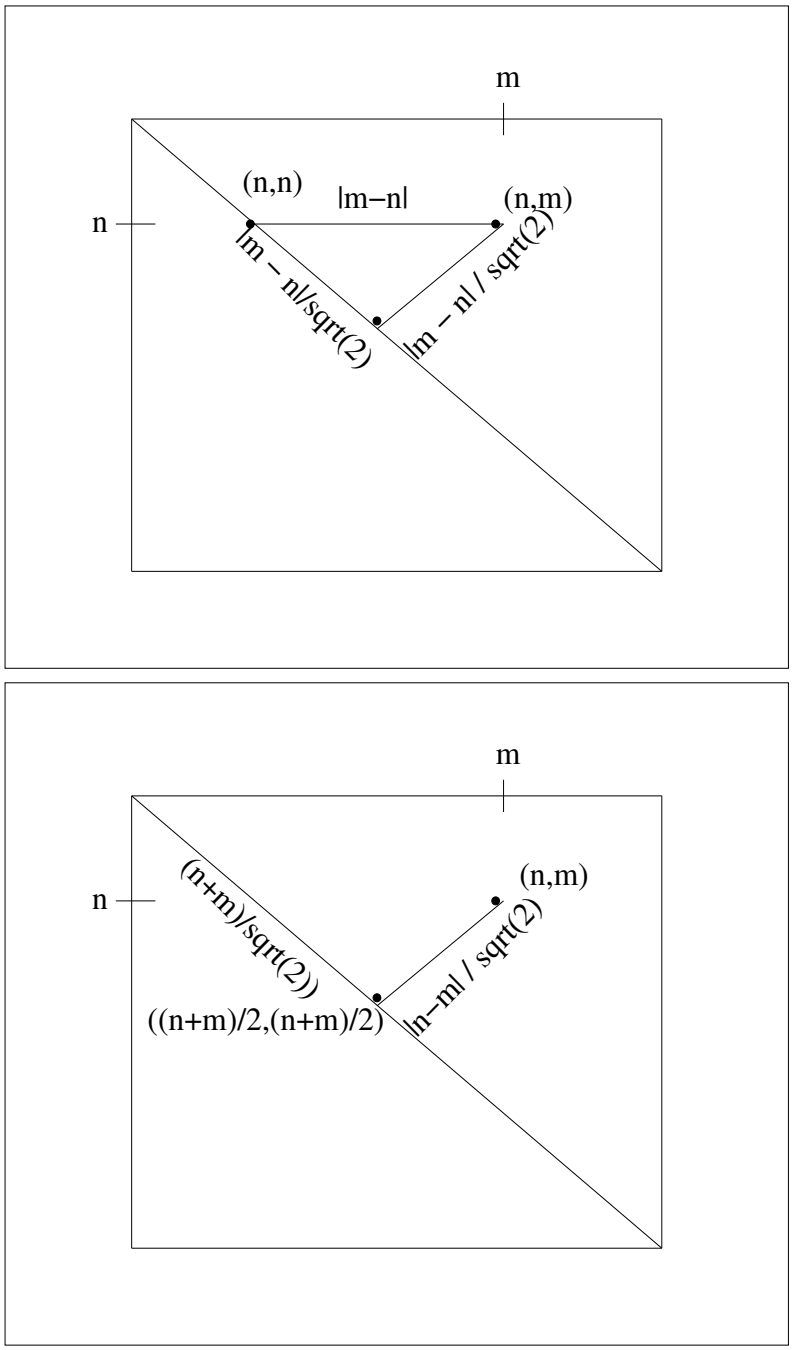

Figure 4.14: The matrix elements (n, m) can be viewed as points in the rotated coordinate system $((n + m)/\sqrt{2}, (n - m)/\sqrt{2})$, where $(n + m)/\sqrt{2}$ is the distance of the point along the diagonal and $(n - m)/\sqrt{2}$ is the distance off of the diagonal, which is also the number of rows off of the diagonal.

of the complex off-diagonal elements, $\sigma^2 = \sigma^2_{Re[U_{m,n}]} + \sigma^2_{Im[U_{m,n}]}$ exhibits smoother behavior in wavenumber than either the real or imaginary parts. An approximate relationship for the variance of the real part of $U_{m,n}$ derived from these figure is

$$\sigma^2_{Re[U_{m,n}]} \approx \begin{cases} e^{-2.5}|n-m|^{-1.4}e^{-.353(ln|n-m|)^2} & \text{for } 0 \leq n \leq 53 \\ e^{33.5}n^{-12} & \text{for } n > 53 \end{cases} . \tag{4.18}$$

Variance as Measure of Bandedness

The sample unitary propagation matrices are banded. The width of the band is an important characteristic of the statistics of these matrices. The variance of the magnitudes of the off-diagonal unitary propagation matrix elements can be used to gain insight into the level of bandedness of the unitary propagation matrix for 50 km, U. Note that

$$\begin{aligned} < |U_{m,n}|^2 > &= < Re[U_{m,n}]^2 > + < Im[U_{m,n}]^2 > \\ &\approx 2 < Re[U_{m,n}]^2 >= 2\sigma^2_{Re[U_{m,n}]} , \end{aligned}$$

so that the variance $\sigma^2_{Re[U_{m,n}]}$ in Fig. (4.15) illustrates the variance of $|U_{m,n}|$ up to a factor of 2. From this figure, matrix elements $U_{m,n}$ have significant contributions only for $|n-m| = 10$, band of 10 about the diagonal.

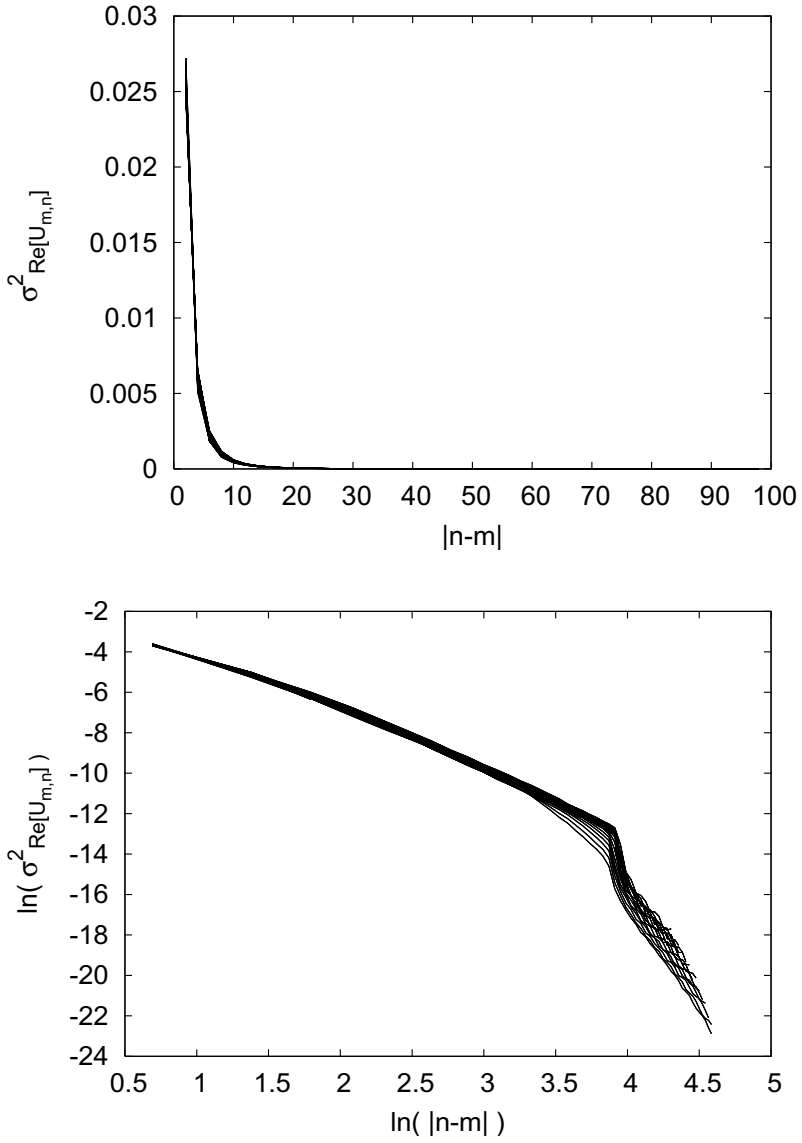

Figure 4.15: (Upper) Variance σ^2 of $Re[U_{m,n}]$ for $n \neq m$ is plotted as a function of the difference $n-m$ for fixed $\frac{1}{2}(n+m) = 1, 2, ..., 50$ values with $n = 0, 1, ..., 13, 15, 20, ..., 70$. (Lower) $ln(\sigma^2)$ of $Re[U_{m,n}]$ is plotted with $\ln|n-m|$. For small n, the relationship is approximately linear implying that the variances are exponentially decaying in the difference $|n-m|$. $U_{m,n}$ is calculated after propagation to $r = 50$ km. The distribution functions are calculated using $N = 10,000$ internal wave seeds so they are accurate to about $\frac{1}{\sqrt{N}} = 0.01$. The variances are symmetric about the diagonal so that $\sigma^2(n-m) = \sigma^2(m-n)$. An approximate relationship is Eq. (4.18). The variances were calculated using $N = 10,000$ internal wave seeds so they are accurate to about $\frac{1}{\sqrt{N}} = 0.01$. This is for a constant wavenumber k corresponding to a source frequency of 75 Hz. Note that the variance of the imaginary part is statistically equal to that of the real part shown here.

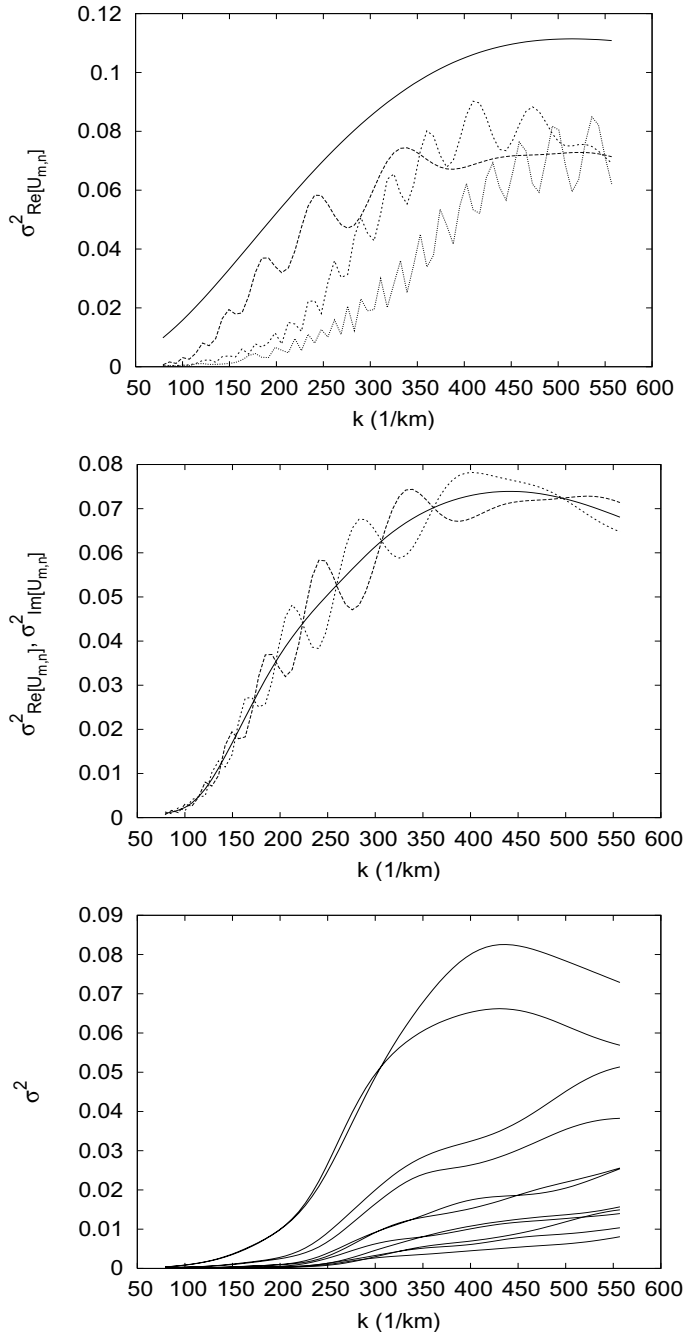

Figure 4.16: (Upper) Variance σ^2 of $Re[U_{m,n}]$ of as a function of wavenumber k. Variances for matrix elements $n = 0, m = 1,\ n = 20, m = 21,\ n = 40, m = 41$ and $n = 60, m = 61$ are plotted. (Middle) Variance σ^2 for $Re[U_{m,n}]$ and $Im[U_{m,n}]$ (dotted lines) are plotted for $n = 20, m = 21$ along with their average(thick line) as a function of wavenumber k. (Lower) Average variance $\sigma^2 = \sigma^2_{Re[U_{m,n}]} + \sigma^2_{Im[U_{m,n}]}$ of the real and imaginary parts of the off-diagonal elements $U_{m,n}$ are plotted for $n = 40$ and $m = 35, 36, ..., 45$ as a function of wavenumber k. The variances were calculated using $N = 100$ internal wave seeds so they are accurate to about $\frac{1}{\sqrt{N}} = 0.1$.

4.3.2 Statistics of Diagonal Elements $U_{m,n}$

The diagonal elements $U_{n,n}$ of the unitary propagation matrix for 50 km hold information on the amount of mixing between modes. The diagonal elements are in general complex numbers. They are functions of range r and source wave number k, as well as the mode number n. The diagonal elements $U_{n,n}$ have a mean rotating phase e^{-ikrE_n} due to propagation in the waveguide, where any additional mean phase is due to the scattering from the internal wave potential.

Numerical simulations of the unitary propagation matrix elements U for propagation to 50 km were calculated using $2,500$ and $10,000$ internal wave seeds for the sound speed fluctuations and 114 different wavenumbers k. The computational resources of the Teragrid [1] were utilized for these simulations.

Distribution of Phases of Diagonal Elements

A histogram of the phases $\phi = Arg\,(U_{n,n})$ of the diagonal elements $U_{n,n}$ over the ensemble of sound speed fluctuations is illustrated in Fig. (4.17). Visually, these plots suggest that the phase of the diagonal elements $U_{n,n}$ is distributed approximately as a Gaussian random number. Since the phase is constrained to lie between $[-\pi, \pi]$ due to the branch cut of the Arg function, and a Gaussian has an infinite domain, the true distribution may related to a Gaussian distribution (i.e. a circular Gaussian distribution where a random number from a normal distribution is mapped onto this interval). A Komogorov-Smirnov test [71] is performed to test if the diagonal phases are Gaussian distributed random variables. The significance

level of this test as a function of n is shown in Fig. (4.18). Small values of the significance show that the cumulative distribution of the diagonal phases is significantly different than that of the cumulative distribution for Gaussian random variables. For some values of n (ie. $n = 7, 45$) , the conclusion that the diagonal phases are distributed as Gaussian distributed random variables cannot be rejected with much confidence, while for other values of n (ie. $n = 10, 25, 30$), this conclusion must be rejected. Regardless if the phase of the diagonal elements is distributed as a truncated Gaussian random variable or not, the figures suggest that whatever the distribution, the phases could be well approximated with a distribution that has only two moments (i.e. a mean and a variance) such as a Gaussian distribution mapped onto the interval $[-\pi, \pi]$.

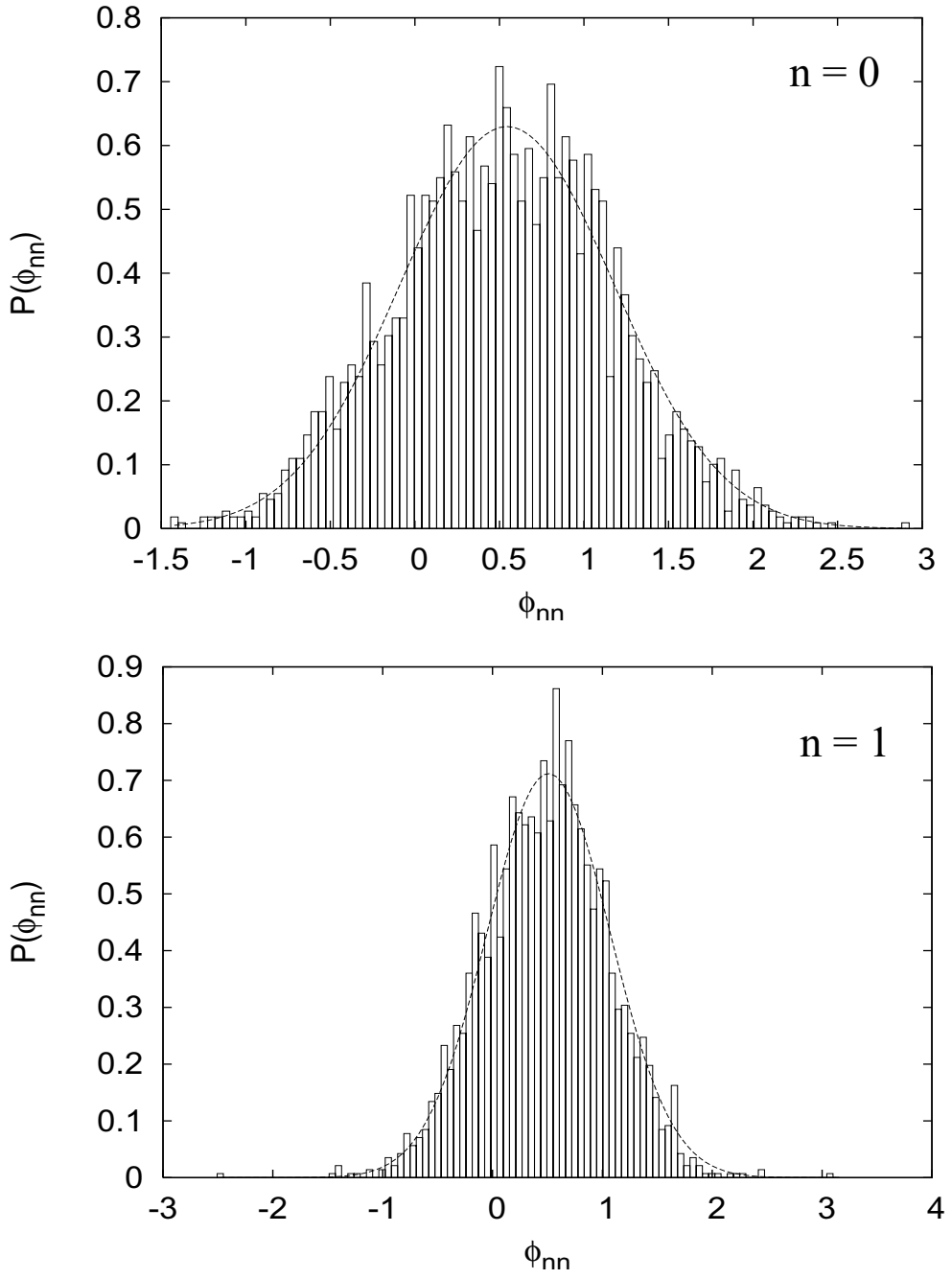

Figure 4.17: A histogram of the phases $\phi_{n,n}$ of $U_{n,n}e^{ikrE_n}$ for (Upper) $n = 0$ and (Lower) $n = 1$ is plotted. The diagonal elements $U_{n,n}$ are calculated after propagation to $r = 50$ km and $N = 2500$ values (corresponding to different internal wave seeds) and 100 bins are used in the construction of the histogram. Also plotted is the probability density function for a Gaussian distribution with mean and variance taken from the set of values $U_{n,n}e^{ikrE_n}$. The good agreement between the histogram and the pdf indicates that the phases are distributed approximately normal. Note that the variance decreases with mode number, so these represented the largest spread in phases.

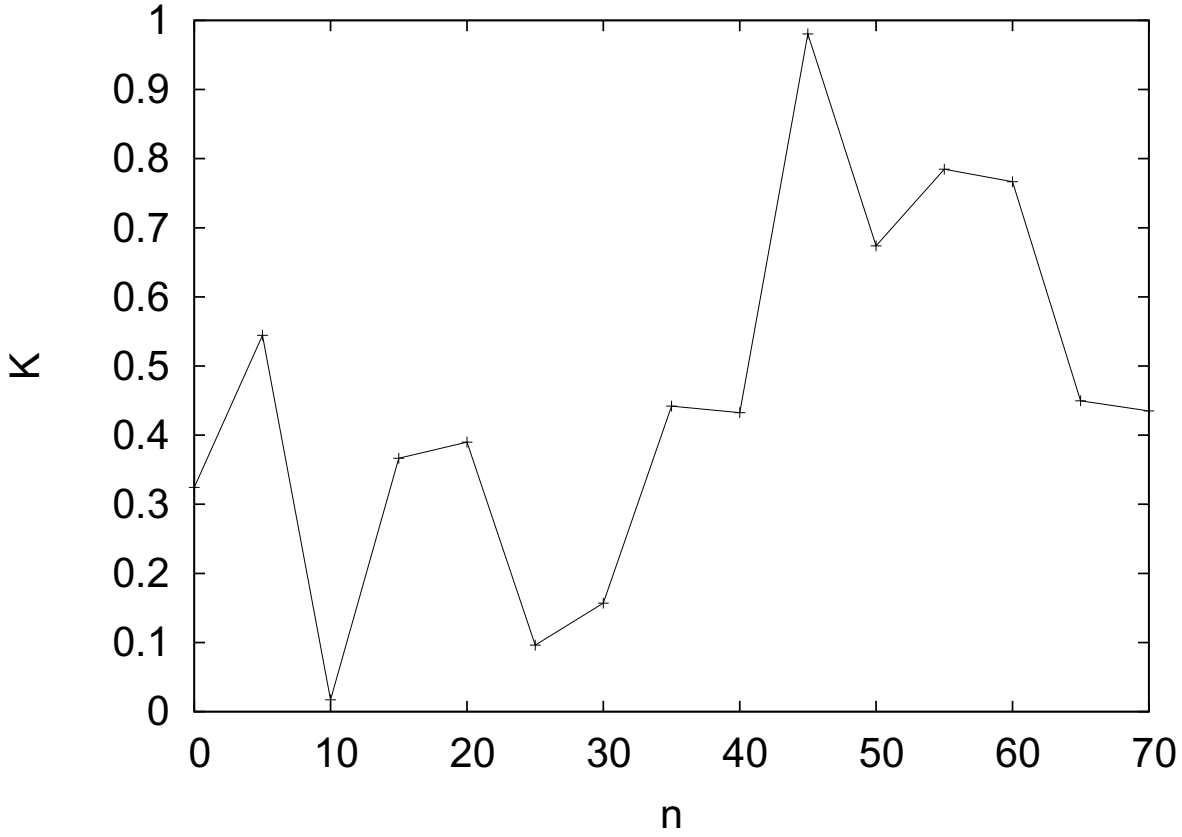

Figure 4.18: A Komogorov-Smirnov Test yielded significance values K for different diagonal phases $\phi_{n,n}$. The significance K is plotted with mode number n.

Method for Determining Mean and Variance of Phases of Diagonal Elements

A direct method of finding the mean and phase of the diagonal elements $U_{n,n}$ would be to find the mean and variance of either $Arg[U_{n,n}]$ or $Arg\left[U_{n,n}e^{-ikrE_n}\right]$. Due to the branch cuts of the Arg function, there is wrap around of the phase in the range $[-\pi, \pi]$. Though the phases are localized in this interval, the presence of outliers and the size of the variance for certain mode number n make this direct method not a reliable way of finding the mean and variance of the phases.

A better method for determining the mean and variance is to use the property that if the phases Φ are Gaussian distributed then the following relation holds:

$$< e^{i\Phi} >= e^{i<\Phi>}e^{-\sigma_\Phi^2/2} \, . \tag{4.19}$$

Using this equation, the means would be calculated by finding $Arg\left[\frac{<e^{i\Phi}>}{|<e^{i\Phi}>|}\right]$ and the variances would be calculated by using $\sigma^2 = -2\ln(|< e^{i\Phi} >|)$. The means and variances from using this equation were compared to that from calculating these quantities directly. It was found that this method is superior because it is not affected by the wrap around of the phase in the range $[-\pi, \pi]$, but otherwise agrees with the direct method. Figure (4.19) illustrates the excellent agreement between using the Gaussian assumption to find the variance using Eq. (4.19) versus calculating the variance of $Arg\left[U_{n,n}e^{-ikrE_n}\right]$ directly.

Mean of Phases of Diagonal Elements

The means of the phases $\Phi_{n,n}$ were calculated using $< \Phi_{n,n} >= Arg\left[\frac{<e^{i\Phi}>}{|<e^{i\Phi}>|}\right]$, which is a result of using Eq. (4.19). The means are shown as a function of mode number n in Figs. (4.20-4.23). A best fit functional form for the means of the phases can be obtained by considering the logarithm of $\mu_{\Phi_{n,n}}(k) + kRE_n$, which is shown in Fig. (4.21) as a piecewise linear function. The difference of $ln\left(\mu_{\Phi_{n,n}}(k) + kRE_n\right)$ from the logarithm of $ln\left(\mu_{\Phi_{n,n}}(k_0) + k_0RE_n\right)$ is shown in Fig. (4.22) and best fit quadratics in $k - k_0$ are found to be $b(n)(k-k_0) + c(n)(k-k_0)^2$, where functional forms for $b(n)$ and $c(n)$ are shown in Fig (4.23). Using these relationships, a best fit approximation for the n and k dependence of $\mu_{\Phi_{n,n}}(k)$ is found to be

$$\mu_{\Phi_{n,n}}(k) \approx \mu_{\Phi_{n,n}}(k_0) + b(n)(k-k_0) + c(n)(k-k_0)^2\,, \tag{4.20}$$

where

$$\mu_{\Phi_{n,n}}(k_0) \approx \begin{cases} 0.55 & \text{for } n = 0 \\ e^{-.68}n^{-.07} & \text{for } 0 < n \leq 28 \\ e^{3.4}n^{-1.3} & \text{for } n > 28 \end{cases}, \tag{4.21}$$

$$b(n) \approx \begin{cases} 0.0015 & \text{for } 0 \leq n < 28 \\ -0.0002 + 1.2 \times (10)^{-6}(n-65)^2 & \text{for } n \geq 28 \end{cases}, \tag{4.22}$$

$$c(n) \approx \begin{cases} 0 & \text{for } 0 \leq n < 28 \\ 2.35 \times (10)^{-6} - 2.25 \times (10)^{-9}(n-60)^2 & \text{for } n \geq 28 \end{cases} \tag{4.23}$$

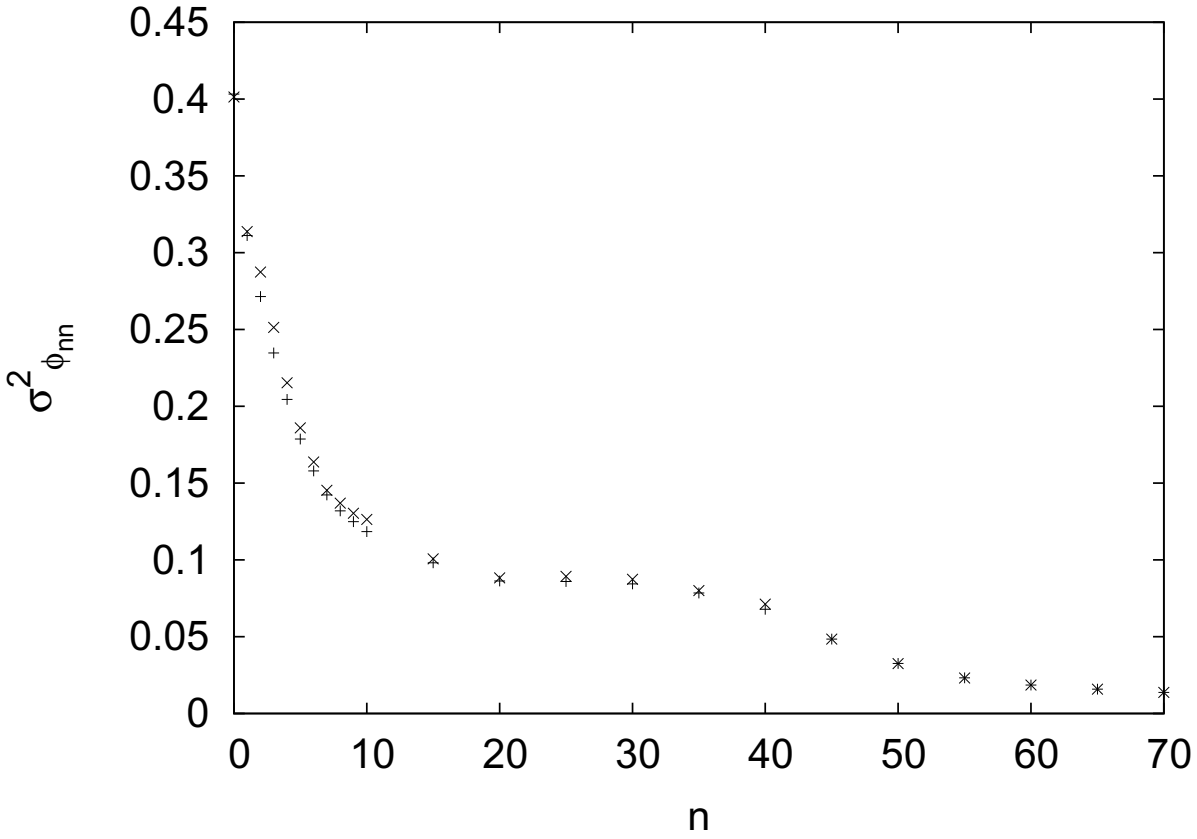

Figure 4.19: The variance $\sigma^2_{\phi_{n,n}}$ of the phase $\phi_{n,n}$ of the diagonal elements $U_{n,n}$ is plotted with mode number n. (Square points) The variance is calculated directly using $Arg\left[U_{n,n}e^{-ikrE_n}\right]$. (X points) The variance is calculated using Eq. (4.19), which assumes that the phases are distributed as Gaussian random variables.

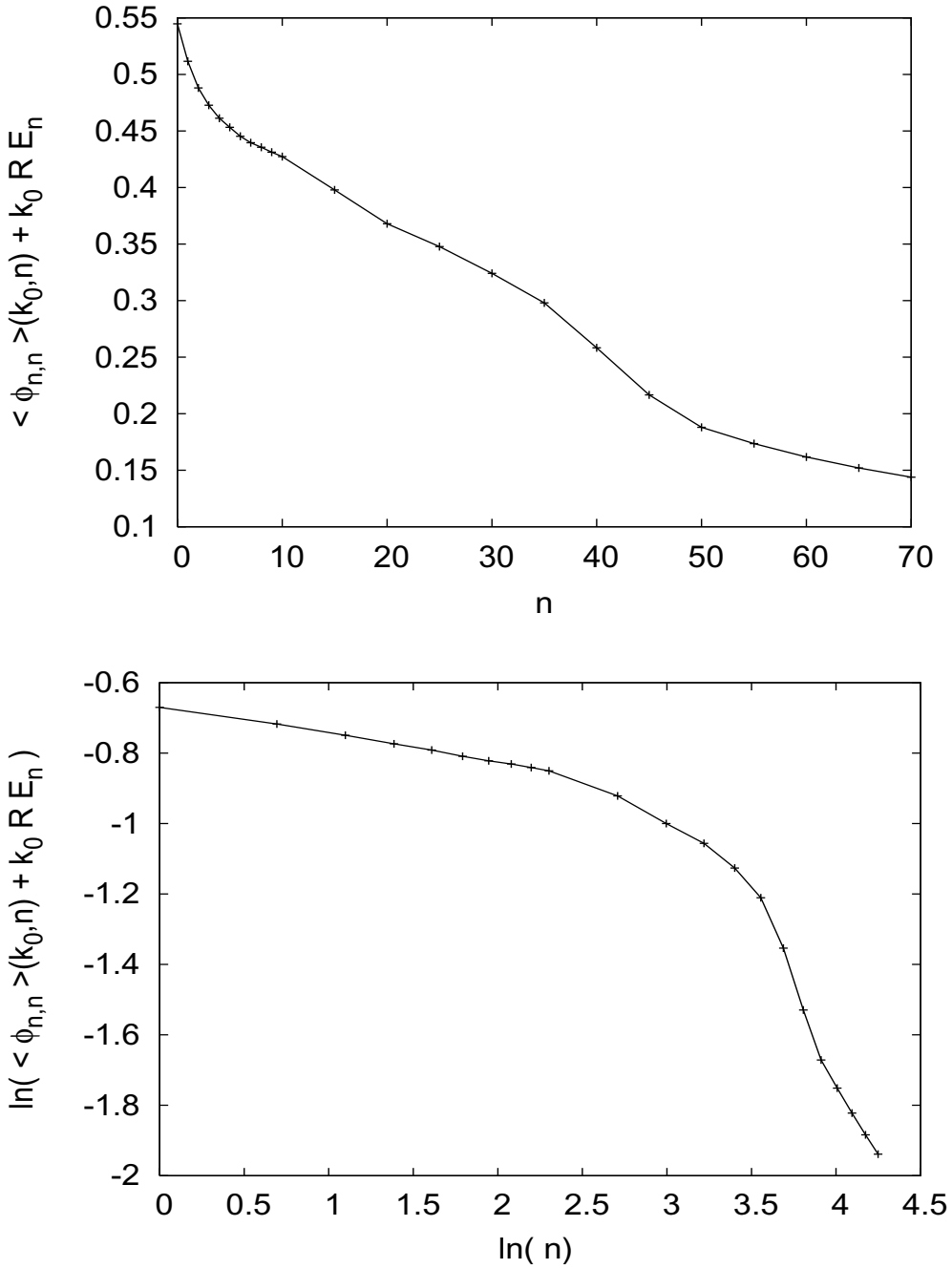

Figure 4.20: (Upper) Mean of the phase $< \Phi_{n,n} >$ of diagonal elements $U_{n,n}$ adjusted by the global phase krE_n as a function of mode number n for $n = 0, 1, ..., 10, 15, 20, ..., 70$ are plotted as points connected by a line. (Lower) Natural logarithm of the mean of the phase $< \Phi_{n,n} >$ of diagonal elements $U_{n,n}$ adjusted by the global phase krE_n as a function of mode number n. The means were calculated using $N = 2500$ internal wave seeds so they are accurate to about $\frac{1}{\sqrt{N}} = 0.02$. This was done for a single wavenumber $k_0 = 2\pi f/c_0$ corresponding to a source frequency of $f = 75$ Hz.

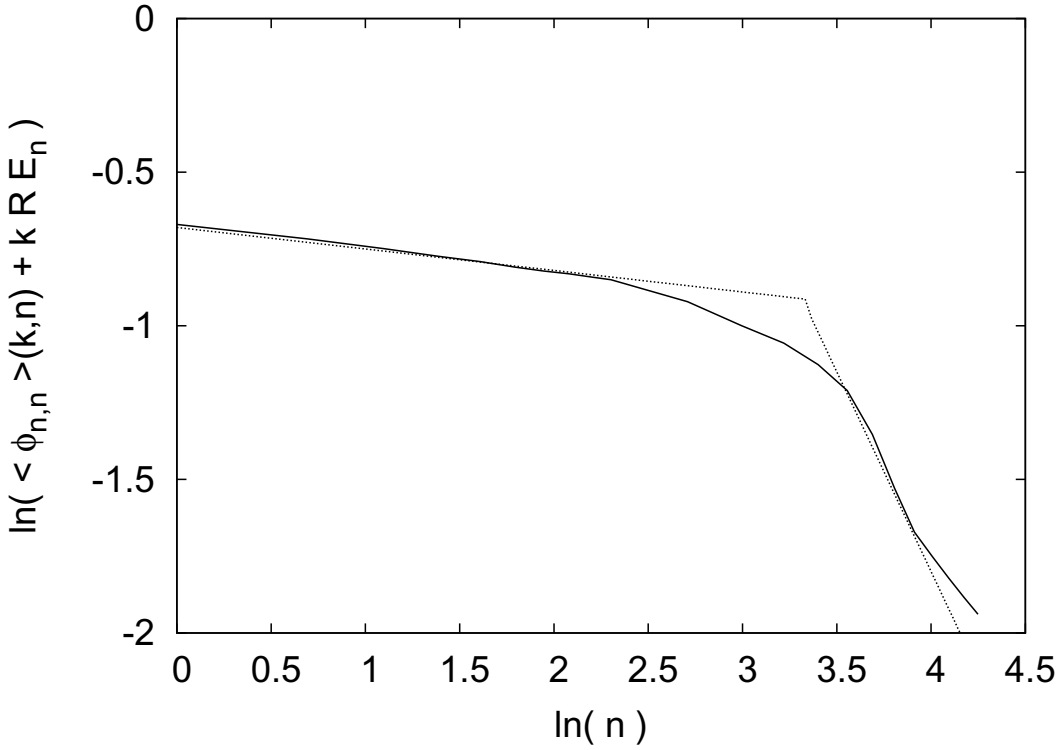

Figure 4.21: Natural logarithm of the mean of the phase $< \Phi_{n,n} >$ of diagonal elements $U_{n,n}$ adjusted by the global phase krE_n as a function of mode number n for $n = 0, 1, ..., 10, 15, 20, ..., 70$ are plotted as points connected by a solid line. The means were calculated using $N = 2500$ internal wave seeds so they are accurate to about $\frac{1}{\sqrt{N}} = 0.02$. This was done for a single wavenumber $k_0 = 2\pi f/c_0$ corresponding to a source frequency of $f = 75$ Hz. The dashed line is the approximate relationship in Eq. (4.20).

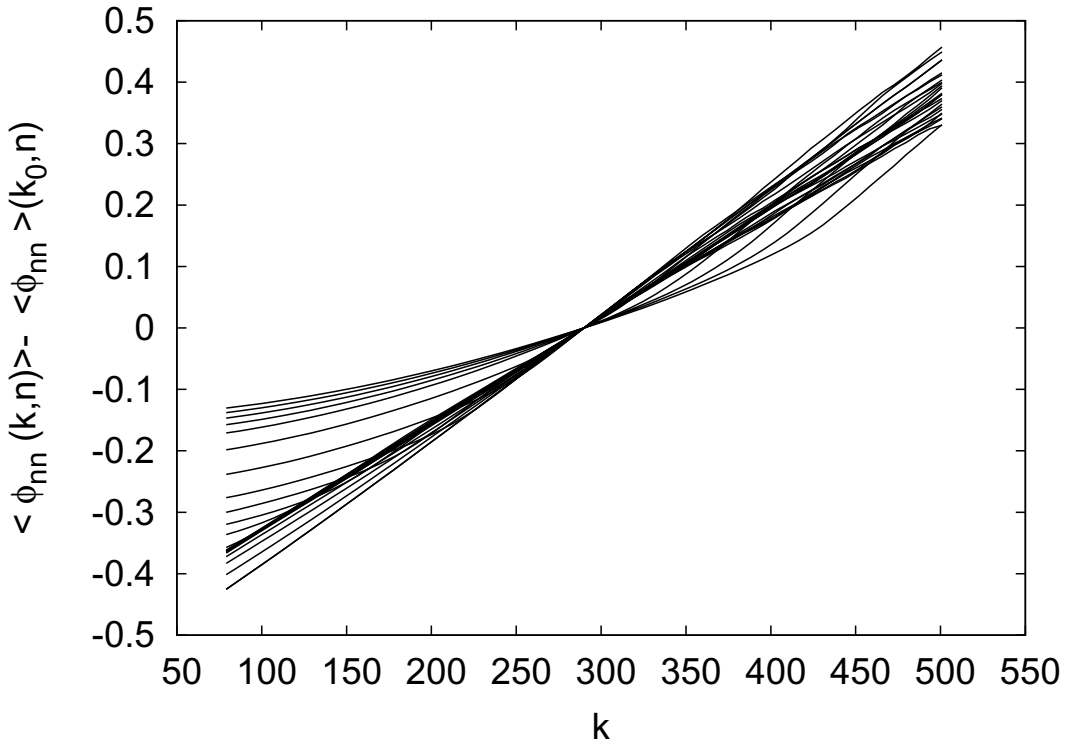

Figure 4.22: Difference between the mean of the phase $\Phi_{n,n}$ of diagonal elements $U_{n,n}$ and the global phase krE_n as a function of wavenumber k for $n_0 = 0, 1, ..., 10, 15, ..., 70$. For smaller mode numbers, the difference is very nearly linear in k. The variances were calculated using $N = 2500$ internal wave seeds so they are accurate to about $\frac{1}{\sqrt{N}} = 0.02$.

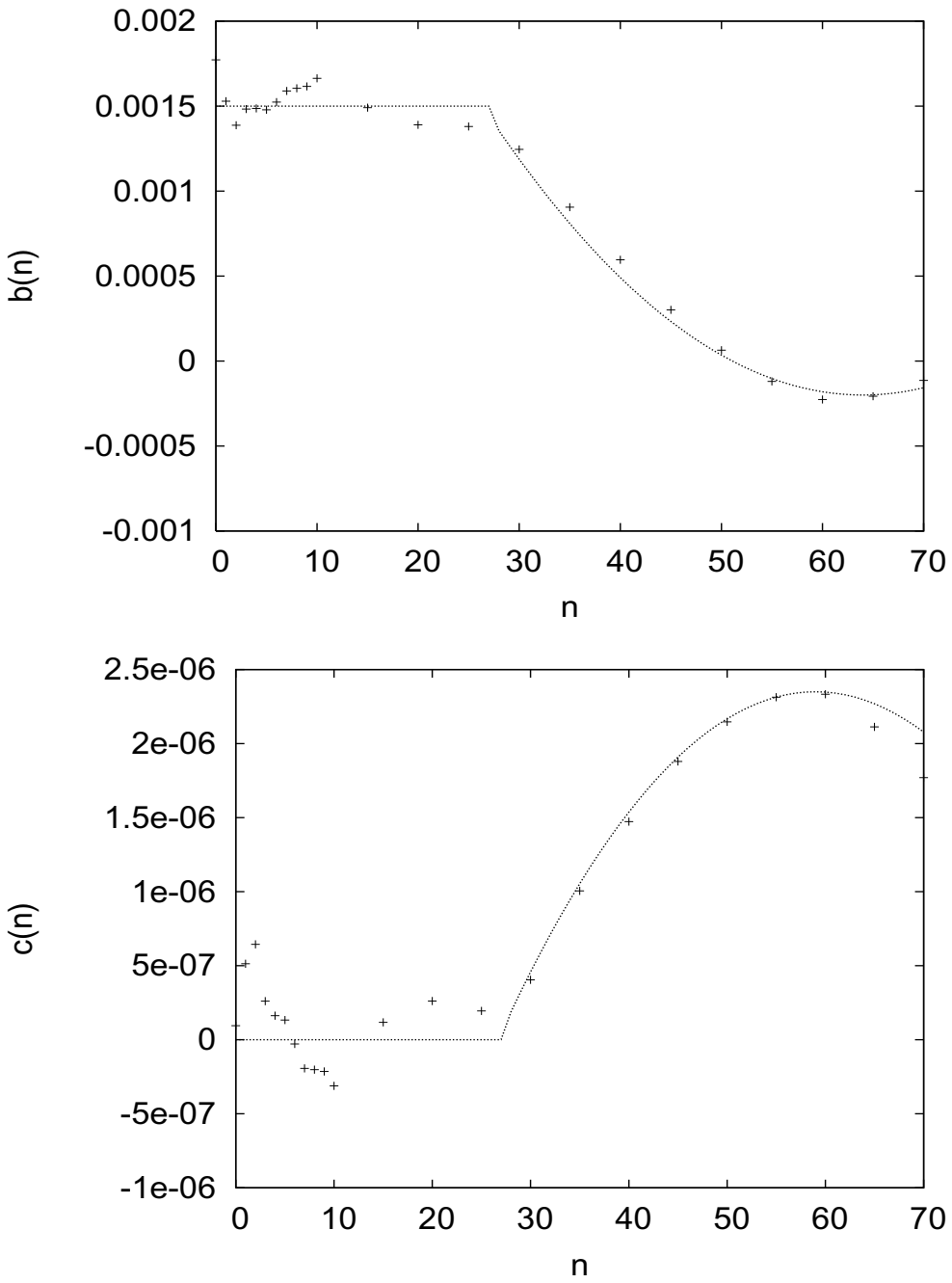

Figure 4.23: A least squares fit of Eq. (4.20) on the data in Fig. (4.22) yields best fit coefficients $b(n)$ and $c(n)$. (Upper) The calculated best fit coefficient $b(n)$ is the solid line plotted with mode number n. An approximation of this function is given in Eq. (4.22) and is plotted as the dashed line. (Lower) The calculated best fit coefficient $c(n)$ is the solid line plotted with mode number n. An approximation to this function is given in Eq. (4.23) and is plotted as the dashed line.

Variance of Phases of Diagonal Elements

The variance σ^2 of the phases $\Phi_{n,n}$ is calculated using $\sigma^2 = -2\ln(|< e^{i\Phi} >|)$, which is a result of using Eq. (4.19). The variance of the phases is shown as a function of n and k in Figs. (4.24)- (4.27). A best fit functional form for the variance of the phases can be obtained using the observations that the variance as a function of n and k have the same functional shape, but seem to differ only by a scale factor $e^{f(n,k)}$. Figure (4.28) illustrates the shape of $f(n,k)$. An approximation for the n and k dependence of the variance of the diagonal phases is found.

$$\sigma^2_{\Phi_{n,n}}(k) \approx e^{f(n,k)}\sigma^2_{\Phi_{n,n}}(k_0) \tag{4.24}$$

$$f(n,k) \approx d(k-k_0) + e(k-k_0)^2\,, \tag{4.25}$$

where the functions are

$$\sigma^2_{\Phi_{n,n}}(k_0) \approx \begin{cases} 0.4 & \text{for } n = 0 \\ e^{-1.2} n^{-.371} & \text{for } 0 < n \leq 36 \\ e^{7.29} n^{-2.73} & \text{for } n > 36 \end{cases} , \tag{4.26}$$

$$d \approx \begin{cases} 8.59 \times (10)^{-3} + 9.09 \times (10)^{-4} n - 6.01 \times (10)^{-5} n^2 & \text{for } 0 \leq n \leq 9 \\ 1.58 \times (10)^{-2} - 5.27 \times (10)^{-4} n + 1.41 \times (10)^{-5} n^2 & \text{for } 10 \leq n \leq 25 \\ -6.19 \times (10)^{-3} + 9.13 \times (10)^{-4} n - 8.97 \times (10)^{-6} n^2 & \text{for } 20 < n \leq 70 \end{cases}$$

$$, \tag{4.27}$$

$$e \approx \begin{cases} 8.59 \times (10)^{-3} + 9.09 \times (10)^{-4} n - 6.01 \times (10)^{-5} n^2 & \text{for } 0 \leq n \leq 9 \\ 1.58 \times (10)^{-2} - 5.27 \times (10)^{-4} n + 1.41 \times (10)^{-5} n^2 & \text{for } 10 \leq n \leq 25 \\ -6.19 \times (10)^{-3} + 9.13 \times (10)^{-4} n - 8.97 \times (10)^{-6} n^2 & \text{for } 20 < n \leq 70 \end{cases} .$$

Figure (4.29) illustrates the shape of the coefficients $d(n)$ and $e(n)$.

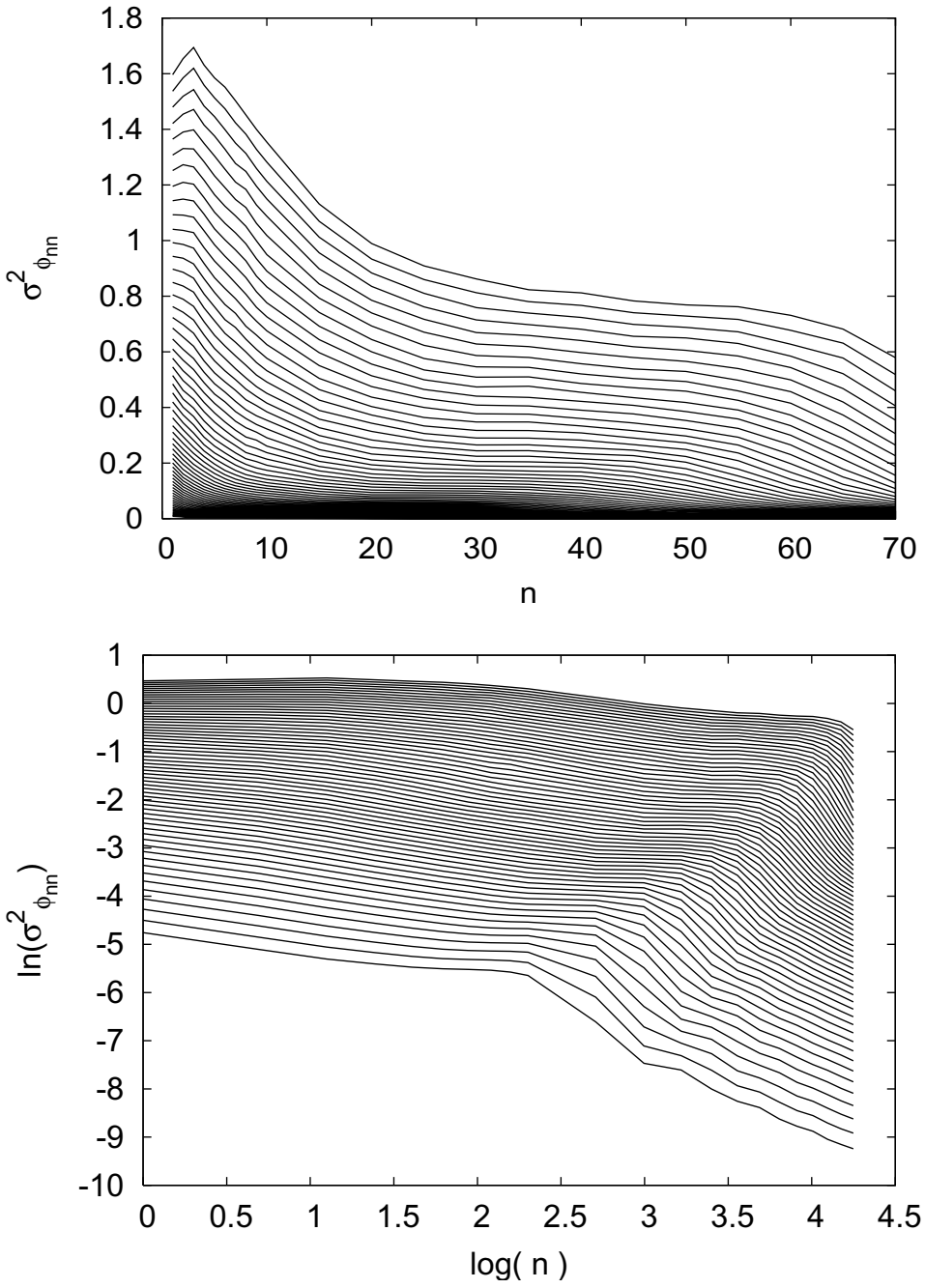

Figure 4.24: (Upper) Variance $\sigma^2_{\Phi_{n,n}}$ of the phase $\Phi_{n,n}$ of the diagonal element $U_{n,n}$ as a function of mode number $n = 0, 1, ..., 10, 15, ..., 40$ for $k = k_0 \pm \sigma_k$. (Lower) Natural Logarithm of the variance $\sigma^2_{\Phi_{n,n}}$ plotted versus wavenumber k. The variances were calculated using $N = 2500$ internal wave seeds so they are accurate to about $\frac{1}{\sqrt{N}} = 0.02$.

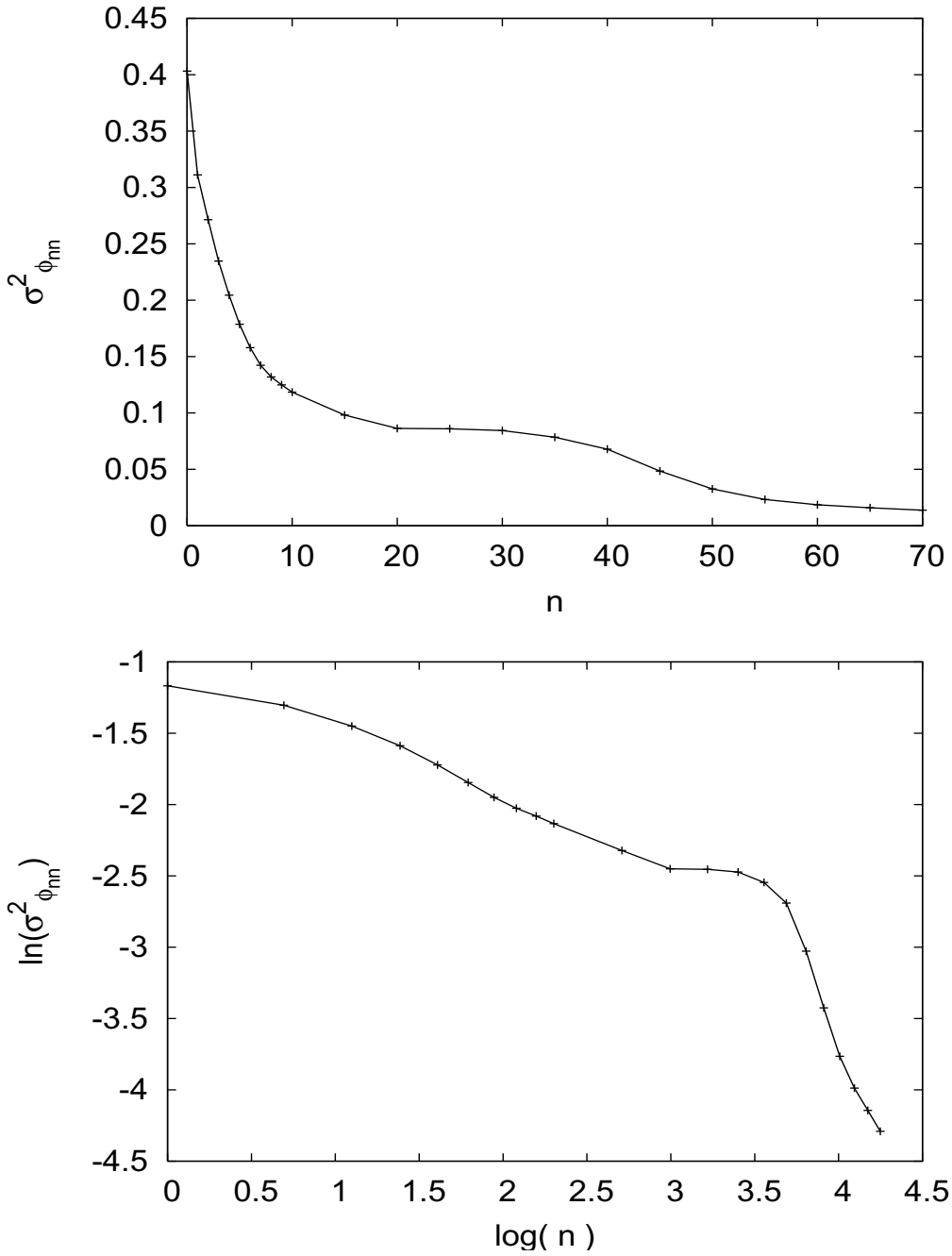

Figure 4.25: The logarithm of the variance σ_ϕ^2 of the phase ϕ of the diagonal elements $U_{n,n}$ is plotted versus mode number n for $n = 0, 1, ..., 10, 15, ..., 70$. Based on the linearity of the graph, a good model for the variance is Eq. (4.24). $U_{n,n}$ is calculated after propagation to $r = 50$ km. These distribution functions are calculated using $N = 2500$ internal wave seeds so they are accurate to about $\frac{1}{\sqrt{N}} = 0.02$. This was done for a wavenumber k corresponding to a source frequency of 75 Hz.

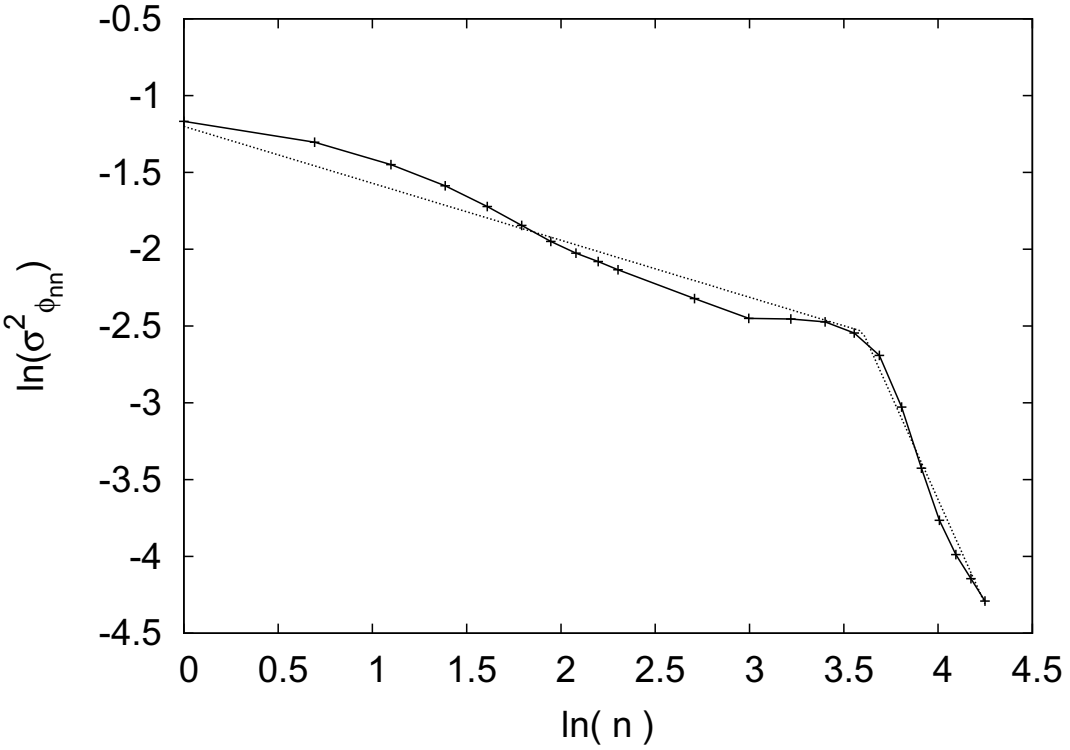

Figure 4.26: The logarithm of the variance σ_ϕ^2 of the phase ϕ of the diagonal elements $U_{n,n}$ is plotted versus mode number n for $n = 0, 1, ..., 10, 15, ..., 70$ as a solid line. The dashed line is the approximation given by Eq. (4.24). $U_{n,n}$ is calculated after propagation to $r = 50$ km. These distribution functions are calculated using $N = 2500$ internal wave seeds so they are accurate to about $\frac{1}{\sqrt{N}} = 0.02$. This was done for a wavenumber k corresponding to a source frequency of 75 Hz.

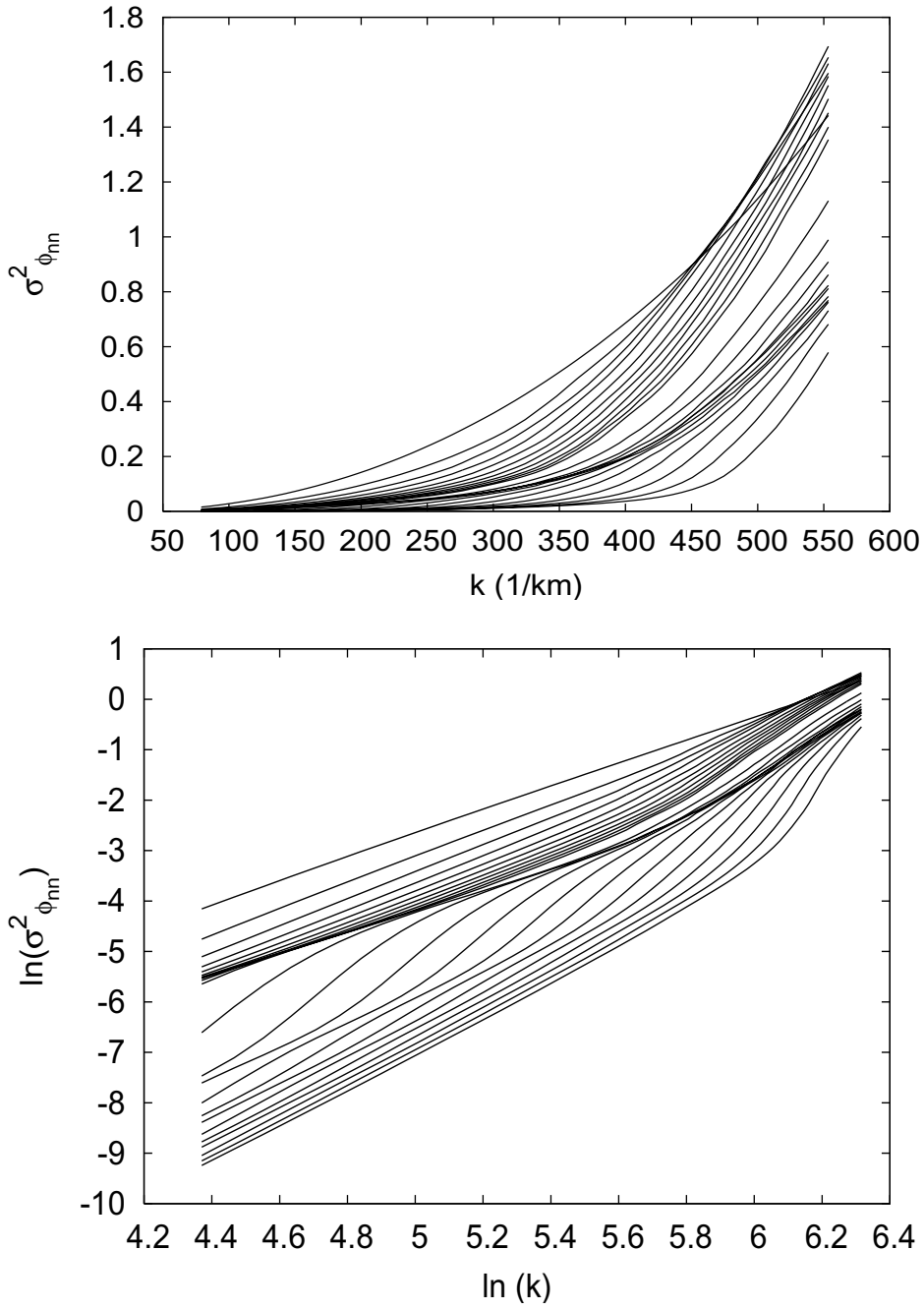

Figure 4.27: (Upper) Variance $\sigma^2_{\Phi_{n,n}}$ of the phase $\Phi_{n,n}$ of the diagonal element $U_{n,n}$ as a function of wavenumber k for $n = 0, 1, ..., 10, 15, ..., 40$. (Lower) Natural logarithm of the variance $\sigma^2_{\Phi_{n,n}}$ plotted versus wavenumber k. The variances were calculated using $N = 2500$ internal wave seeds so they are accurate to about $\frac{1}{\sqrt{N}} = 0.02$.

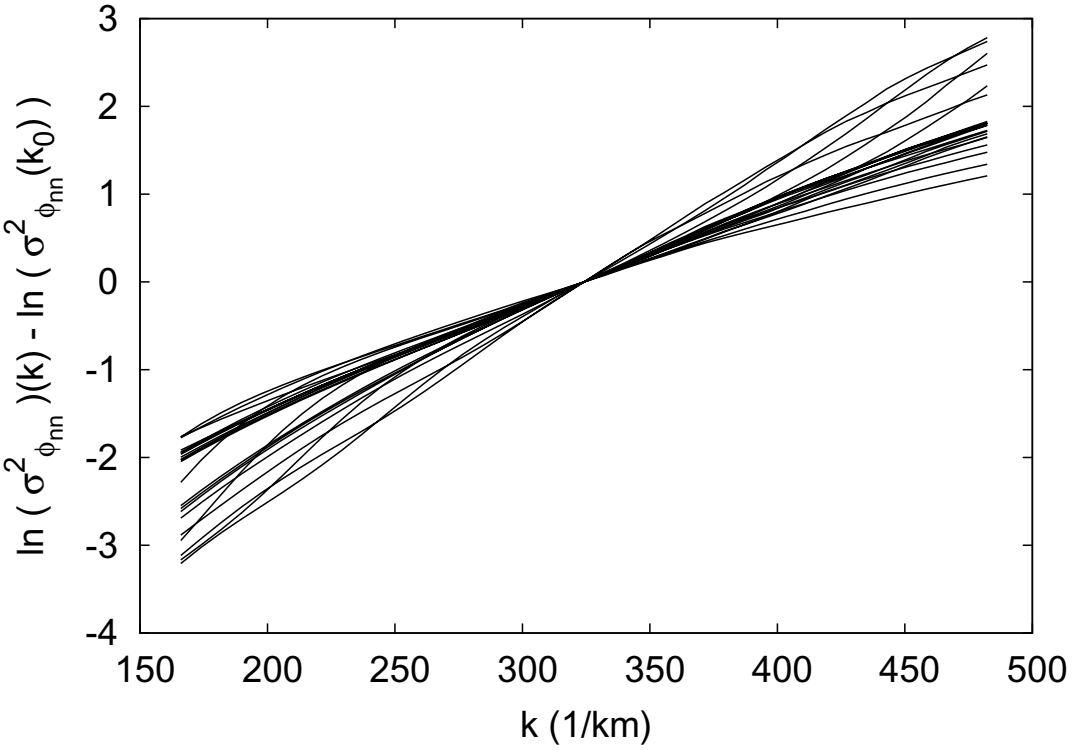

Figure 4.28: (Upper) Difference between the natural logarithm of the variance $\sigma^2_{\Phi_{n,n}}$ of the phase $\Phi_{n,n}$ of the diagonal element $U_{n,n}$ and the natural logarithm of the variance $\sigma^2_{\Phi_{n,n}}$ of the phase $\Phi_{n,n}$ of the diagonal element $U_{n,n}$ at the central wavenumber k_0. as a function of wave number k for mode numbers $n = 0, 1, ..., 10, 15, ..., 40$. The variances were calculated using $N = 2500$ internal wave seeds so they are accurate to about $\frac{1}{\sqrt{N}} = 0.02$.

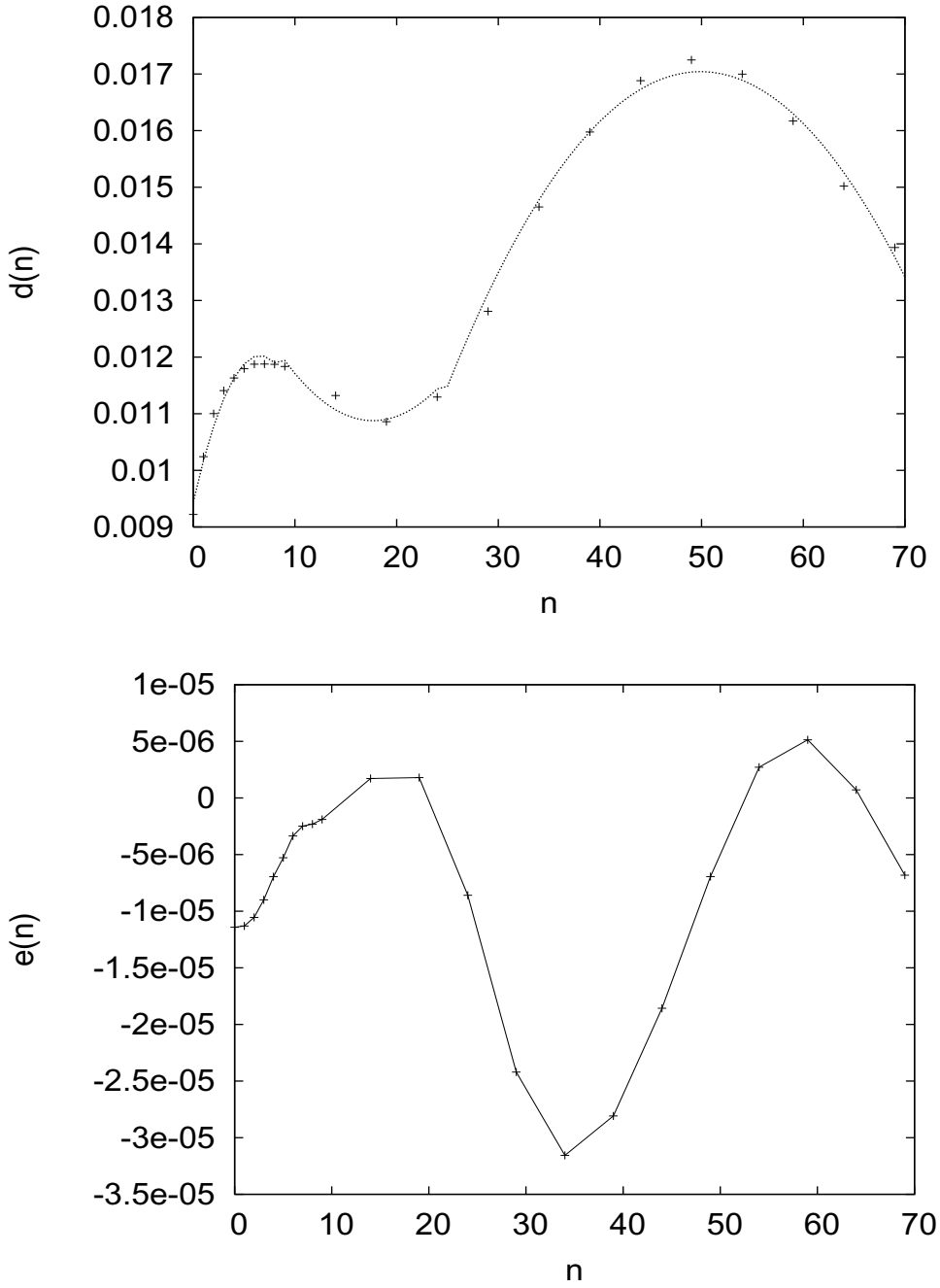

Figure 4.29: A least squares fit of Eq. (4.25) on the data in Fig. (4.28) yields best fit coefficients $d(n)$ and $e(n)$. (Upper) The calculated best fit coefficient $d(n)$ is the solid line plotted with mode number n. An approximation of this function is given in Eq. (4.27) and is plotted as the dashed line. (Lower) The calculated best fit coefficient $e(n)$ is the solid line plotted with mode number n. An approximation to this function is given in Eq. (4.28) and is plotted as the dashed line.

Distributions of Amplitudes of Diagonal Elements

A histogram of $|U_{n,n}|$ and $ln[1 - |U_{m,n}|]$ for $n = 0$ is shown in Fig. (4.30). A sample cumulative density function of $ln[1 - |U_{m,n}|]$ for $n = 0$ is shown in Fig. (4.31). Visually, the distribution of $ln[1 - |U_{m,n}|]$ appears to be distributed as a Gaussian random number, suggesting that $1 - |U_{m,n}|$ is distributed as a log-normal random number. Again, since values of $1 - |U_{m,n}|$ are constrained to lie between $[0, 1]$, a finite domain, and a log-normal distribution is on an semi-infinite domain, the true distributions may just be well approximated by a log-normal distribution mapped to the domain.

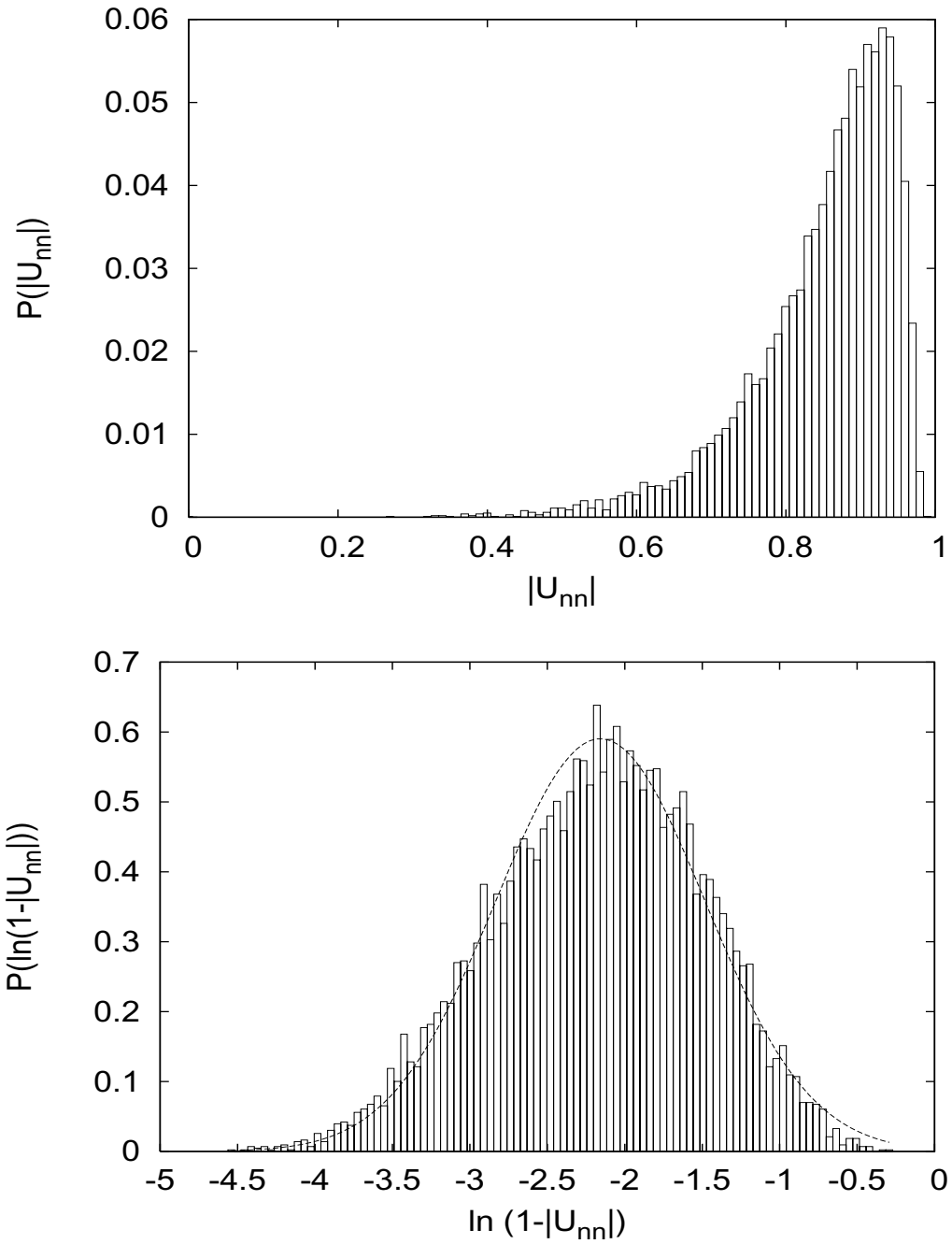

Figure 4.30: (Upper) A histogram of the magnitudes $|U_{n,n}|$ for $n = 0$ and (Lower) a histogram of the natural logarithm of the difference between the magnitudes $|U_{n,n}|$ and one, $ln(1 - |U_{n,n}|)$ for $n = 0$ is plotted. The diagonal elements $U_{n,n}$ are calculated after propagation to $r = 50$ km and $N = 10000$ values (corresponding to different internal wave seeds) and 100 bins are used in the construction of the histogram. Also plotted is the probability density function for a Gaussian distribution with mean and variance taken from the set of values $ln(1 - |U_{n,n}|)$. The good agreement between the histogram and the pdf indicates that the difference between the magnitudes $|U_{n,n}|$ and 1 is distributed log normal.

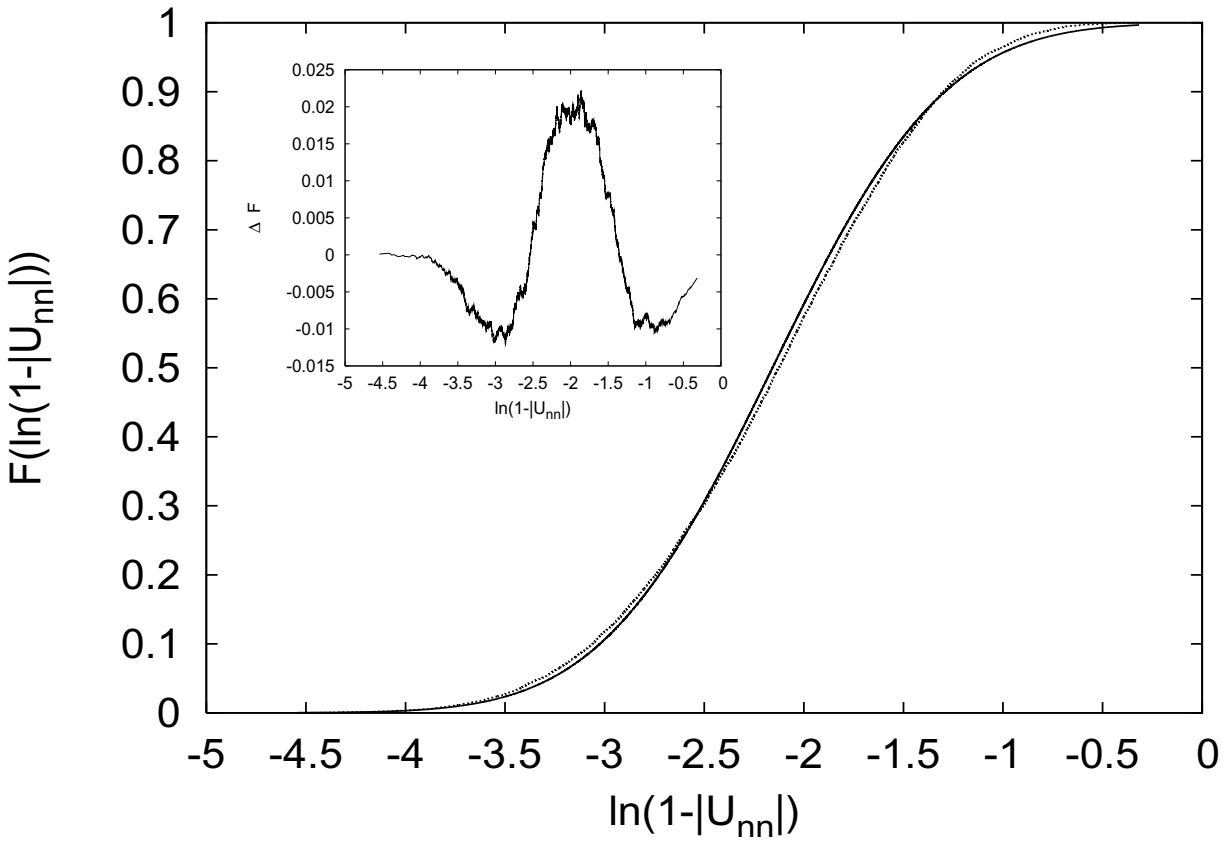

Figure 4.31: Approximation to the cumulative density function (cdf) $F(ln(1-|U_{n,n}|))$ of the natural logarithm of the difference between the magnitudes $|U_{n,n}|$ and one, $ln(1-|U_{n,n}|)$ for $n=0$ is plotted, where the diagonal elements $U_{n,n}$ are calculated after propagation to $r=50$ km and $N=10000$ values (corresponding to different internal wave seeds). Also plotted is the cumulative density function for a Gaussian distribution with mean and variance taken from the set of values $ln(1-|U_{n,n}|)$. The good agreement between the histogram and the pdf indicates that the difference between the magnitudes $|U_{n,n}|$ and 1 is distributed log normal. The inset shows the error between the approximate cdf and the Gaussian cdf. The shape of the error is typical of that for sampling convergence with N to a distribution. This was done for a wavenumber k corresponding to a source frequency of 75 Hz.

4.3.3 Correlations

The correlation between the complex matrix elements $U_{m,n}$ and $U_{m',n'}$ is the complex number $\rho(U_{m,n}U_{m',n'})$.

$$\rho_{U_{m,n}U_{m',n'}} = \frac{< U_{m,n}U^*_{m',n'} > - < U_{m,n} >< U_{m',n'} >^*}{\sigma_{U_{m,n}}\sigma_{U_{m',n'}}},$$

where $*$ denotes the complex conjugate and $\sigma^2_{U_{m,n}} =< U_{m,n}U^*_{m,n} > - < U_{m,n} >< U_{m,n} >^*$ is the variance of the distribution of $U_{m,n}$. Note that the self correlation is one and the magnitude of the correlation decreases to zero as the matrix elements become statistically independent of each other.

Correlations with wavenumber

The correlation of the matrix element $U_{n,m}$ as a function of wavenumber k is

$$\rho_{n,m}(k,k_0) = \frac{< U_{n,m}(k_0)U^*_{n,m}(k) > - < U_{n,m}(k_0) >< U_{n,m}(k) >^*}{\sigma_{U_{n,m}(k_0)}\sigma_{U_{n,m}(k)}}, \quad (4.28)$$

where $*$ denotes the complex conjugate and $\sigma^2_{U_{n,m}(k)} =< U_{n,m}(k)U^*_{n,m}(k) > - < U_{n,m}(k) >< U_{n,m}(k) >^*$ is the variance of the distribution of $U_{n,m}(k)$. Note that the self correlation is one for $k = k_0$ and decreases to zero as the wavenumber deviates from k_0. Figure (4.32) shows some correlations in wavenumber for $k_0 = \frac{2\pi 75}{c_0}$. The magnitude of the correlations are in general oscillatory and decay away from k_0. The rate of oscillation and amount of decay in the amplitude of the magnitude of the correlations depends heavily on the value of n, m. The

rate of decay in the amplitude of the magnitude of the correlations from that for $k = k_0$ is slow.

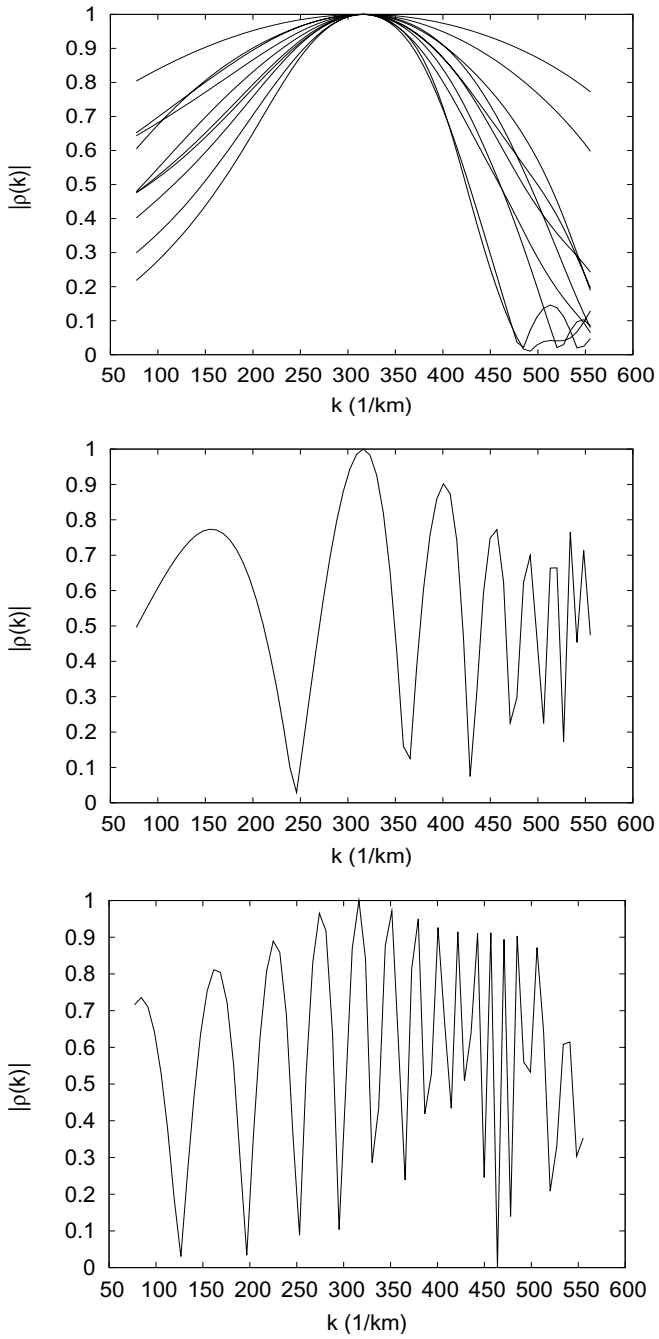

Figure 4.32: The magnitude of the correlation functions $|\rho(k, k_0 = \frac{2\pi 75}{c_0})|$ calculated using Eq. (4.28) are plotted with wavenumber k for the off-diagonal elements (Upper) $n = 0$ and $m = 0, 1, ..., 10$,(Middle) $n = 20$ and $m = 21$ and (Lower) $n = 40$ and $m = 41$. Correlations were calculated using values of $U_{m,n}$ from the propagation through 2500 internal wave realizations using the source frequency of 75 Hz.

Correlation Between Elements

The diagonal elements and off-diagonal elements $U_{m,n}$ are correlated since they must obey the unitary constraints $\sum_n |U_{m,n}|^2 = 1$ for each n and $\sum_m |Um,n|^2 = 1$ for each m. The correlation between the two matrix elements $U_{m,n}$ and $U_{m',n'}$ at fixed wavenumber k_0 is defined to be

$$\rho_{U_{m,n},U_{m',n'}}(k) = \frac{< U_{m,n}(k_0)U^*_{m',n'}(k_0) > - < U_{m,n}(k_0) >< U_{m',n'}(k_0) >^*}{\sigma_{U_{m,n}(k_0)}\sigma_{U_{m',n'}(k_0)}} \quad (4.29)$$

where $\sigma^2_{U_{m,n}(k_0)} =< U_{m,n}(k_0)U^*_{m,n}(k_0) > - < U_{m,n}(k_0) >< U_{m,n}(k_0) >^*$ is the variance of the distribution of $U_{m,n}(k_0)$. Note that the self correlation is one for $n = n'$ and $m = m'$ and decreases to zero as the matrix mode numbers n, n' and m, m' differ.

The correlation between some sample diagonal elements and other matrix elements are shown in the contour plot in Fig. (4.33). As shown in the figures, the dominant correlations of the diagonal elements are with other diagonal elements. The correlations between diagonal elements for some values of n are shown in Fig. (4.35). The correlations decay to $|\rho| < 0.1$ for $|n - m| > 10$, giving a correlation length in mode number. In Fig. (4.35), the correlations appear to decay exponentially with m for $m > n$ and decay Gaussian for $n > m$. The decay rate appears to be the same regardless of n. For $n = 0$, the decay is a pure exponential, $|\rho_{U_{0,0},U_{m,m}}| \approx e^{-.25m}$.

The correlation between some sample off-diagonal elements and other matrix elements is shown in the contour plot in Fig. (4.34). As shown in the figures, the dominant correlations of the off-diagonal elements are with other matrix elements that are equidistant from the

diagonal. This along with with the correlations of the diagonals in Fig. (4.33) supports the conclusion that the elements are most highly correlated with other elements that are along the same band from the diagonal.

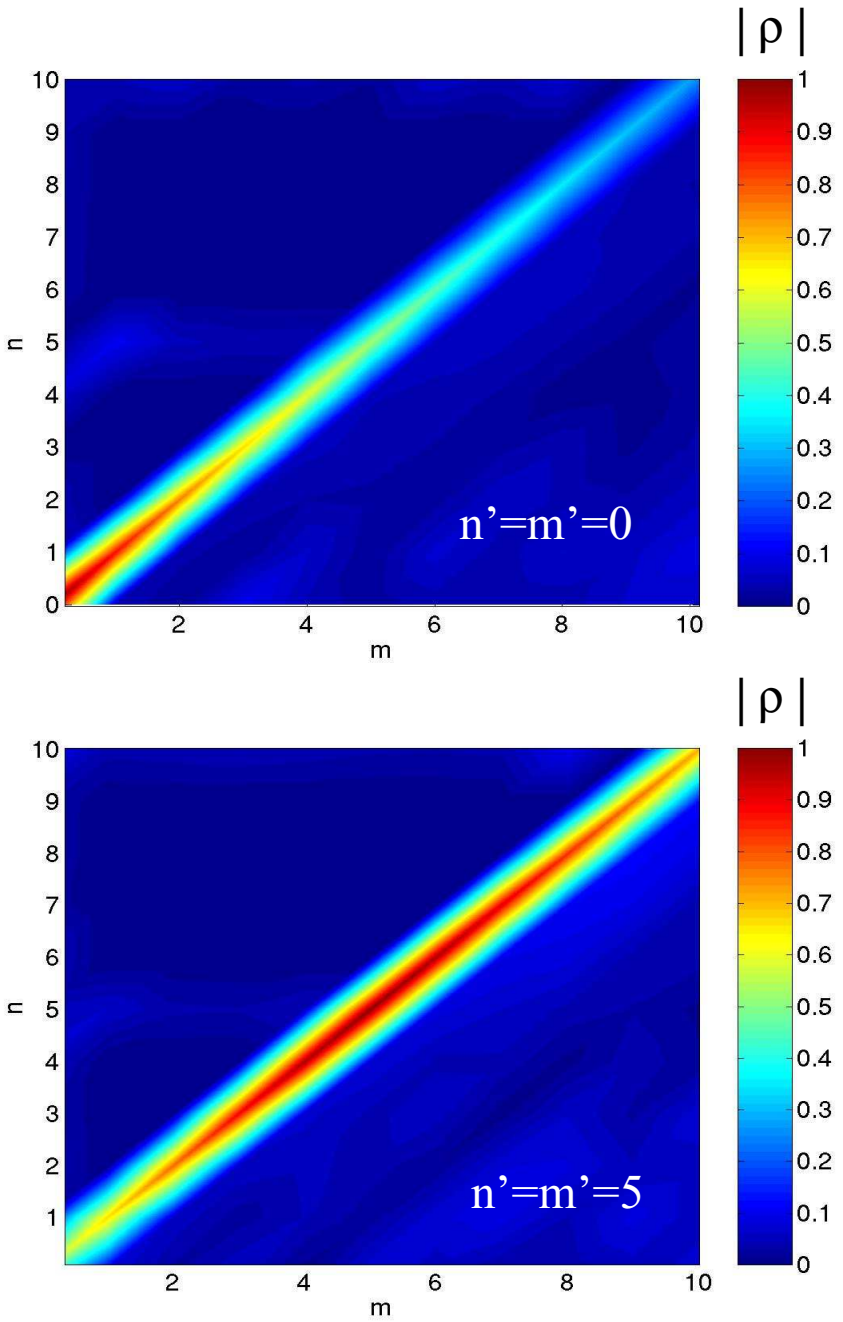

Figure 4.33: The magnitude of the correlation $|\rho_{U_{n',n'},U_{n,m}}|$ between the diagonal element $U_{n',n'}$ and the matrix element $U_{m,n}$ calculated using Eq. (4.29) is plotted as a contour plot with mode number n and m. (Upper) Correlations for $n' = m' = 0$. The correlations are dominant on the diagonal for $|n - 0| < 10$. (Lower) Correlations for $n' = m' = 5$. Correlations were calculated using values of $U_{m,n}$ from the propagation through 2500 internal wave realizations using the source frequency of 75 Hz.

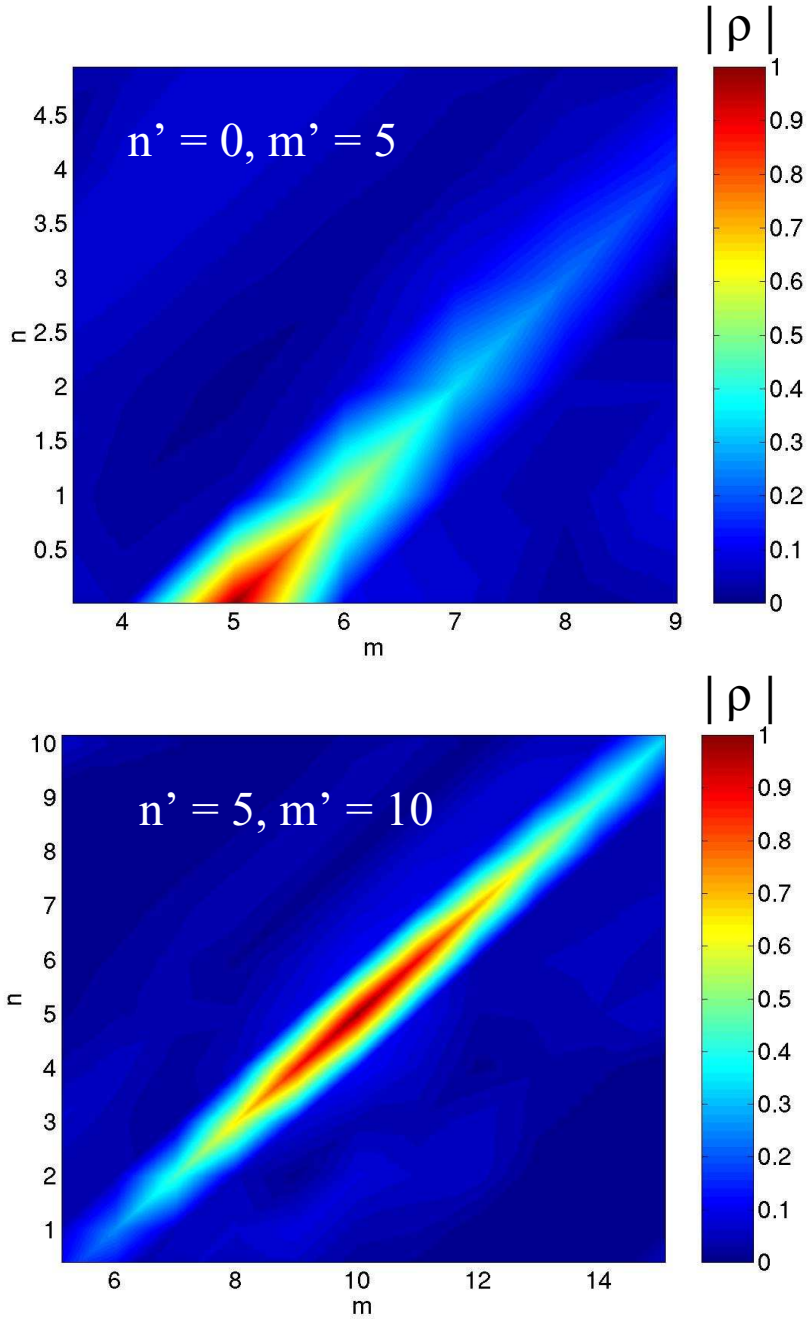

Figure 4.34: The magnitude of the correlation $|\rho_{U_{m',n'},U_{m,n}}|$ between the off-diagonal element $U_{m',n'}$ and the matrix element $U_{m,n}$ is calculated using Eq. (4.29) is plotted as a contour plot with mode number n and m. (Upper) Correlations for $n' = 0$, $m' = 5$ (Lower) Correlations for $n' = 5$, $m' = 10$. Correlations were calculated using values of $U_{m,n}$ from the propagation through 2500 internal wave realizations using the source frequency of 75 Hz.

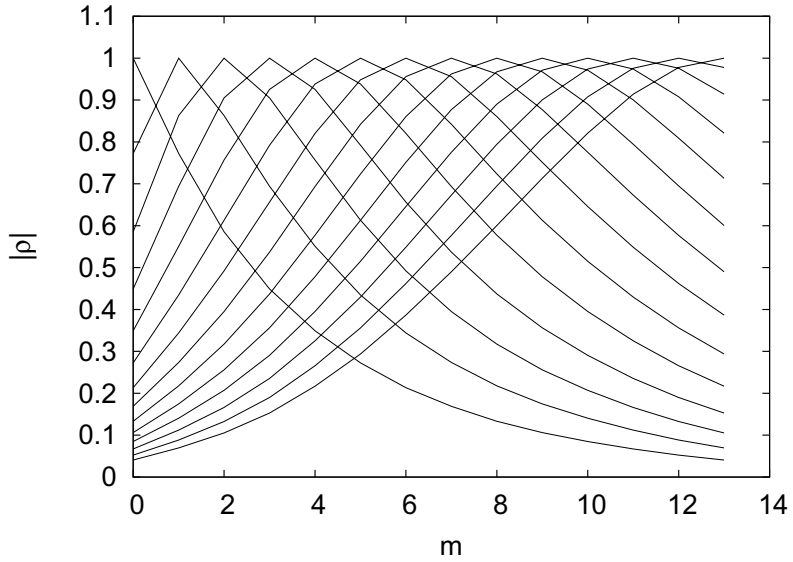

Figure 4.35: The magnitude of the correlation $|\rho_{U_{n,n},U_{m,m}}|$ between the diagonal elements $U_{n,n}$ and $U_{m,m}$ calculated using Eq. (4.29) is plotted for $n = 1, 2, ..., 13$ versus m. Correlations were calculated using values of $U_{m,n}$ from the propagation through 2500 internal wave realizations using the source frequency of 75 Hz.

4.4 Chapter Summary

In this chapter, the properties of the unitary propagation matrix are explored from the numerical calculation of the matrix elements $C_{m,n}$. Several results from this chapter will be utilized in the construction of the ensemble model in Ch. (5).

First, sample matrices were calculated for several ranges, as shown in Figs. (4.3-4.7). These samples illustrate that the phase of the matrices by 50 km have the qualitative appearance of matrices constructed through a random process. Also, the magnitudes of the matrices are clearly banded even up to 1000 km. In Ch. (5), these samples will be compared qualitatively with the statistical ensemble to give a qualitative indication as to how well the model works.

Second, it has been argued that the dynamic multiplication property shown in Eq. (4.9) exists for the matrices. In that case, the matrix for propagation from $r = 0$ to $r = 2R$ can be obtained from the multiplication of the matrix for propagation from $r = 0$ to $r = R$ and the matrix for propagation from $r = R$ to $r = 2R$. In Ch. (5), this property will be used to multiply independent building blocks from the ensemble model (modeling the unitary propagation matrices for 50 km) to obtain an ensemble of unitary propagation matrices for longer ranges.

Third, the first order quantum perturbation theory result in Eq. (4.10) was used to get a rough estimation of a good minimum range at which successive unitary propagation matrices decorrelate. This range was found to be 50 km, which is the average wavelength of one period of oscillation of a classical ray in the potential. In Ch. (5), this range will be used as the building block range for modelling the properties of the unitary propagation matrix for 50 km.

Finally, the statistical properties of $C_{m,n}$ for 50 km (termed $U_{m,n}$ in this chapter) were identified by analysing the matrices obtained from numerical simulations using the parabolic equation. It was found that the real and imaginary parts of the off-diagonal elements and the phase of the diagonal elements were approximately Gaussian random variables. Best fit functional forms for the means and variances of these quantities were found. Correlations among the matrix elements were found to be most significant with matrix elements along the same band of the matrix.

In Ch. (5), Gaussian distributions will be used for construction of the random matrices. The statistical properties of the propagation will be compared to the statistical properties of

the ensemble as a verification that the model is correctly characterizing the scattering from the propagation.

Chapter 5

STATISTICAL ENSEMBLE MODEL: UNITARY PROPAGATION MATRIX

A statistical ensemble is a theoretical tool used to analyze macroscopic systems, such as those in thermodynamics [72]. In thermodynamics, the macroscopic system (i.e. a gas in a volume) consists of many particles. A complete description (i.e. the position and momentum) of every particle in the system is a microstate. The possible microstates which can exist in the system are described by the ensemble. In thermodynamics, it is assumed that each microstate occurs with the same probability. However, in general it is necessary to describe the probability for a certain microstate to occur in the system (the probability density). Each microstate shares certain universal properties of the ensemble called macrostates (i.e. pressure, temperature, volume). The macrostates are obtained by taking the average value of different quantities over all microstates in the system. Similarly, average properties of a general system can be obtained from the statistical moments (i.e. mean, variances) of quantities over all possible

states of the system.

The sound speed fluctuations due to internal waves in the ocean are described by the statistical ensemble in Eq. (3.12). As an ensemble, this equation describes a set of possible models for an entire field of sound speed fluctuations and their appropriate weightings (the probability density) in occurrence. The assumed probability density is described in the derivation in Appendix B and given statistical properties from real observations of internal waves in the ocean. A specific realization for the fluctuations is considered by inputing a single random matrix ϕ_{j,k_r} into the formula to extract a member from the ensemble.

Given a single realization of internal wave sound speed fluctuations, the propagation of the eigenmodes through the resulting sound speed potential allows a calculation of the unitary propagation matrix of $C_{m,n}$'s and a timefront at all desired ranges. Similarly, using all possible realizations of internal wave sound speed fluctuations from the ensemble model, the propagation of the eigenmodes through all possible resulting potentials results in an ensemble of all possible $C_{m,n}$'s and an ensemble of all possible timefronts at all desired ranges. A single timefront or a single matrix resulting from a single experiment only holds information about the propagation through a single internal wave field. It is not possible to extract the parameters of the internal wave field from just a single experiment, since these parameters are statistical parameters of the ensemble of internal wave fields. It is the statistical properties of the ensemble of $C_{m,n}$'s which must give information about the desired parameters of the internal wave field.

The statistical properties of $C_{m,n}$ have been explored as the popularity of a modal decomposition of the propagation has increased in recent years [35, 38, 31, 73, 74]. Previously,

attention had focused on the properties of the timefronts [39, 59, 40, 41], which are the observable quantities from the experiments. However, the timefronts can be obtained from the $C_{m,n}$'s, so that knowing the properties of the $C_{m,n}$'s is equivalent to knowing the properties of the timefronts.

Despite the attention to the timefronts, the relationship between the statistical properties of the timefront and the statistical properties of the internal wave field is still unknown. In fact, the only parameter of the internal wave model which has been investigated using experimental data is the energy parameter E in Eq. (3.12) [39, 40]. Previously, Colosi et. al. [39] explored the dependence of E by simulating timefronts for a few (i.e. 5) realizations of the internal wave field with 2-3 values of E (while keeping all other parameters constant). Incoherent averages of the intensities in the arrival patterns of these timefronts were then compared to experimental timefronts to determine which E was best in modeling the experiments (he concluded the best to be E= 0.5-GM, where the Garrett-Munk energy is 1-GM = 6.3 x 10^{-5}) [22]. The scarcity of simulations for this research is likely due to the time consuming numerical simulations of waves to long ranges, which require high resolution in spatial and temporal grids. Regardless, Colosi's method is clearly not an acceptable method of doing tomography to achieve any reliable information about the ocean from the experiments. Note that more recently, Uffelen et. al. [40] avoided the use of the timefronts completely by extracting an E from comparing the variance of vertical fluctuations from an ensemble of ocean measurements to the variance from a theoretical internal-wave spectrum. They concluded that the best value of E was the Garrett-Munk energy (1-GM), which is the one taken for simulations in this thesis.

Since the ensemble of $C_{m,n}$'s hold information about propagation through an ensemble of internal wave fields, it would be useful to have a statistical ensemble model for the $C_{m,n}$'s. Statistical ensembles provide a method for identifying the surviving information in the propagation and for forming a physical picture of the propagation in a way that numerical simulations of the parabolic equation alone could never make possible. The aim of the statistical ensemble model created and qualitatively verified in this chapter is to capture the minimal information surviving from the propagation.

Statistical ensemble models composed of random matrixes are used to study problems in quantum chaos [26], where the corresponding classical dynamics is chaotic. The minimum information necessary to capture the dynamics of these systems is included in the parameters of the random matrices and studied using random matrix theory [27, 28]. Perez et. al. [21] used a product of random transfer matrices, with statistics capturing only the first and second statistical moments, to represent the surviving information from the dense weak scattering limit. The universality of Perez's model constituted the existence of a generalized central limit theorem.

In probability and statistical theory, the Central Limit Theorem (CLT) states that the sum of a large number of independent and identically distributed random variables (with finite mean and variance) is approximately normally distributed (as Gaussian random variables) [75]. A normal (Gaussian) distribution is characterized by only two parameters, a mean and a variance. The CLT predicts that the universal parameters of the sum are the mean and variance, and these are the sum of the means and variances of the random variables, respectively. The CLT also implies that the product of a large number of independent and identically

distributed random variables (with finite mean and variance) is approximately log-normally distributed (where the logarithm of the product is distributed as a Gaussian random variable).

The universal property described in the CLT can be thought of as a process in which there is a loss of information. The set of random variables in the CLT can be drawn from any distribution with any number of parameters necessary to characterize the distribution. The fact that only two parameters and the Gaussian distribution are left to characterize the sum implies that there has been a great loss of information in summing the variables. Therefore, the loss of information in a system when a large number of random variables are added or multiplied has come to be synonomous with the existence of a generalized CLT for the system, as in Perez's model [21].

In ocean acoustics, experimental and simulated acoustic timefronts seem to indicate that there is limited surviving information about the propagation in the timefronts, suggesting that a generalized central limit theorem might be operating during the propagation so that few physical parameters dominate the properties of the ensemble of timefronts. The late arrivals in the timefront contain little or no structure (due to the destructive interference of multiple pulse arrivals), yet the early arrivals exhibit structure in the presence of identifiable branches of the timefront (due to constructive interference from multiple pulse arrivals). The presence of structure in the timefront indicates that there is information about the propagation stored in the properties of the timefront, whereas the absence of structure in the timefront indicates that the information has been lost. The size of the structured region decreases with increasing range, indicating that the information remaining in the timefronts decreases with range. To date, no one really knows what information survives in the timefront. The work in this thesis

gives a route to coming to terms with this lack of understanding.

In motivating the use of a building block model (as in Perez et. al. [21]) for ocean acoustics to long ranges, there are two observations to consider. First, the matrixes C at any range can be written as a product of unitary propagation matrices from earlier ranges. Specifically, the matrix C, describing the propagation from $r = 0$ to $r = 2R$, can be written as the product of a matrix C_1, for $r = 0$ to $r = R$, and a matrix C_2, for $r = R$ to $r = 2R$. Second, there may exist a range at which the dynamics between successive range segments becomes independent. As the potential decorrelates in range, it is likely that the dynamics occurring in different range segments decorrelates. In the study of classical rays, it is believed that the scattering from the internal wave field is dominant near the upper turning points of the rays and that scattering episodes between the cycles of the rays might be treated as independent (at least for rays with large angles from the horizontal) [12, 22]. This suggests that the period of a typical classical ray may be appropriate for the length of a building block range. Indeed, the building block model of considering the unitary propagation matrices as products of a large number of independent matrices would provide a physical picture as to why a generalized CLT seems to exist in the acoustic timefronts from ocean acoustic propagation.

Several properties discovered in Ch. (**??**) motivate the construction of a statistical ensemble for the building blocks of $C_{m,n}$ at 50 km. It was found that the phase of the diagonal elements and the real and imaginary parts of off-diagonal elements have distributions that look very close to Gaussian distributions. Additionally, several members of the ensemble of phases of the matrices $C_{m,n}$ look to be drawn from a random process, as shown in Fig. (4.3). This suggests that a good model for the building block ensemble model is a statistical ensem-

ble model and this model can be built with random matrices of Gaussian random variables.

The collection of ideas discussed so far leads to the present construction of an ensemble model for the long range acoustic propagation in the ocean described in this chapter. This long range ensemble model is created by multiplying members of the building block ensemble (modeling propagation to 50 km). The building block ensemble is constructed to have members which are unitary by utilizing a transformation involving a Hermitian matrix A and a diagonal matrix Λ of average phases for the diagonal elements. The elements of the matrix A are formed from a random matrix of independent Gaussian random variables of zero means and with variances dependent on the band of the matrix. The variances are obtained from the variances of first order perturbation theory for $C_{m,n}$. The strong correlations between elements and the correlations in wavenumber k discovered in Sec. (4.3.3) of Ch. (**??**) have been neglected in this model, as was done in Perez et. al. [21].

This long range ensemble model has only the minimal information captured by the propagation to 50 km. This information is contained in a variance matrix and a diagonal matrix of average phases. The variance matrix is created from analytic formulas derived from first order perturbation theory which depict the dependencies on wavenumber, range, mode number and parameters of the potential. This dependency provides the potential for analytic work to connect the statistical properties of the model to the timefront. The paramount benefit of the ensemble model is that the important physics of ocean acoustic propagation is captured in this model. However, an additional benefit is that these physics can be extracted in a reasonable amount of time, since the building block matrix elements can be generated and multiplied together quickly to generate a statistical ensemble for $C_{m,n}$ at long range allowing

the calculation of accurate statistics for comparison to the true propagation.

5.1 Building Block Model

The building block model is a set of matrices U modeling the unitary propagation matrices for propagation to 50 km. The first order perturbation theory prediction for these matrices in Eq. (4.9) are not unitary matrices. Therefore a goal of this chapter is to construct a unitary matrix U which contains information predicted by perturbation theory. It turns out that the probability density function and the first and second moments predicted by first order perturbation theory are all that are needed to motivate the construction of the ensemble of building blocks. The distributions, means, variances and correlations of the building block ensemble are compared to those arising from the propagation to 50 km.

5.1.1 Ensuring Unitarity

In the analogy of the parabolic equation with the one dimensional Schrödinger equation of quantum mechanics, the propagation of the acoustic wave field is norm preserving and the unitary propagation matrices U are unitary matrices. Therefore, the unitary propagation matrices satisfy the unitarity constraints, $UU^\dagger = U^\dagger U = I$, where I is the identity matrix and $U^\dagger$ is the Hermitian conjugate (the complex conjugate transpose of matrix U). One of the resulting unitarity constraints is that $\sum_m |U_{m,n}|^2 = 1$, which states that the sum of the probabilities of transitioning from an initial state n to a final state m, summed over all final states m is unity. Another similar constraint is that $\sum_n |U_{m,n}|^2 = 1$, which states that the sum of

the probabilities of transitioning from an initial state n to a final state m, summed over all initial states n is also unity.

For propagation in only the unperturbed potential in Eq. (3.11), the matrices are diagonal and unitary with $U_{m,n} = e^{-ikrE_m}\delta_{m,n}$, indicating no mode mixing. With the addition of the perturbative internal wave potential in Eq. (3.12), mixing is now allowed and the matrices deviate from the diagonal matrix but still remain unitary and are banded about the diagonal.

Cayley Transform in Matrix A

Every unitary matrix U can be written as a Cayley transform of a Hermitian matrix A as $U = (I + iA)^{-1}(I - iA)$ [76]. By using this Cayley transform with an appropriate matrix A, the resulting matrix U is guaranteed to be unitary. Since A is a complex Hermitian matrix, $A^\dagger = A$. This implies that the diagonal elements of A need to be real and the offdiagonal elements need to satisfy $A_{m,n} = A^*_{n,m}$, where * represents the complex conjugate.

Global Phase Matrix Λ

As the elements of the Hermitian matrix diminish to zero, ie. $A \to 0$, the Cayley transform approaches the identity matrix, I. Yet, as the internal wave potential diminishes to zero, the unitary propagation matrix elements approach $e^{-ikrE_n}\delta_{m,n}$, where E_m are the energies of the Munk potential V. The unitarity is preserved if the Cayley transform is multipled by a unitary diagonal matrix Λ . Therefore, the global oscillating phase can be captured in a model for U

by multiplying the Cayley transform by a diagonal matrix Λ

$$U = \Lambda(I + iA)^{-1}(I - iA) \, , \tag{5.1}$$

where matrix A captures the scattering physics of mode mixing and the elements of matrix Λ capture the average accumulation of phases in the diagonal elements

$$\Lambda_{m,n} = e^{-ikrE_n + i\mu_{n,n}}\delta_{m,n} \, , \tag{5.2}$$

where $\mu_{n,n} = \langle Arg[U_{n,n}] \rangle$ is the average phase accumulated by the diagonal elements of the unitary propagation matrix due the perturbation. Note that $\mu_{n,n} \rightarrow 0$ as $A \rightarrow 0$.

Approximation to the Unitary Construction

The scale of A is related to the size of the internal wave effects since the internal wave sound speed perturbations influence the amount of mixing of modes during the propagation, much as the scale of A controls the amount of mixing of modes in the unitary model in Eq. (5.1). Since the internal waves are 'small' compared to the background sound speed potential, the entries in the matrix A are likely to be 'small' also.

A simple connection between the statistical properties of A and the statistical properties of U can be made by using a perturbation theory approximation in the small elements A. To a second order approximation in the matrix A, the Cayley transform is approximately $(I + iA)^{-1}(I - iA) \approx (I - iA - 2A^2)(I - iA) \approx I - 2iA - 2A^2$ and the unitary transform

is approximately

$$U \approx \Lambda(I - 2iA - 2A^2) \tag{5.3}$$

$$U_{m,n} = e^{-ikrE_m + i\mu_{m,m}} \left(\delta_{m,n} - 2iA_{m,n} - 2\sum_l A_{m,l}A_{l,n} \right) . \tag{5.4}$$

In this form, it is seen that the Cayley transform improves upon the first order approximation $\delta_{m,n} - 2iA_{m,n}$ through the addition of higher order terms. The addition of the second order term $-2\sum_l A_{m,l}A_{l,n}$ bring the resultant from the first order terms closer to the unit circle.

The complex numbers $\sum_l A_{m,l}A_{l,n}$ are second order in the perturbation, so to first order the phase is $Arg(U_{n,n}) \approx -krE_n + \mu_{n,n} - 2A_{n,n}$. Then, $A_{n,n} = -\frac{1}{2}\left(Arg(U_{n,n}) + krE_n - \mu_{n,n}\right)$ for all n. Therefore to first order, the diagonals of the matrix A contain the phase difference from the mean phase of the diagonal elements of the unitary propagation matrix.

The unitary transformation approximation is only good for small matrix elements $A_{m,n}$. The upper figure in Fig. (4.12) shows the range of values for the real part of $U_{m,n}$ for $n = 0$, $m = 1$. Though the range of values is centered on zero, there are significant outliers with $|Re[U_{m,n}]| > 0.4$, where the elements are not 'small'. The off-diagonal element $U_{m,n}$ for $n = 0$, $m = 1$ has one of the largest variances of the off-diagonal elements, with the variances decreasing for higher mode numbers. From these considerations, it is expected that the approximation of $A_{m,n}$ as small is good for the off-diagonal elements for larger mode numbers, but is not as good for the off-diagonal elements with the lowest mode numbers, i.e. near $n = 0$.

Note that the phase differences $A_{n,n}$ are relatively small. This is seen in Fig. (4.25), which

illustrates that the maximum variance $\sigma^2_{A_{n,n}}$ is 0.38 for $n = 0$ and the standard deviation is always less than $\sqrt{.38}\ rad \approx 0.6\ rad \approx 35^0$. For most n, the variance in the phase is relatively 'small'. Since there would be no phase fluctuations if the internal waves were not present, the phase is also first order.

5.1.2 Perturbation Theory Model for Matrix A

Comparing the unitary approximation in Eq. (5.3) to first order perturbation theory in Eq. (4.9) gives an identification for the elements of the matrix A. To first order in ϵ, the unitary approximation in Eq. (5.3) can be simplified as

$$U_{m,n} \;=\; e^{-ikrE_m + i\mu_{m,m}} \left(\delta_{m,n} - 2iA_{m,n}\right) \ .$$

In the comparison to Eq. (5.5), $A_{m,n}$ are first order effects, i.e. $A_{m,n} \approx O(\epsilon)$ and

$$\begin{aligned} A_{m,n} &= -\frac{k\epsilon}{2} \sum_j \frac{V_j^{m,n}(z)}{\sqrt{j^2 + j*^2}} \sum_{k_r} \left(\Delta k_r\right)^{1/2} \sqrt{I_{j,k_r}} \qquad (5.5) \\ &\quad \times \left[\frac{e^{i(\omega_{m,n}+k_r)r/2 + i\Phi_{j,k_r}} \sin((\omega_{m,n}+k_r)r/2)}{\omega_{m,n}+k_r} + \frac{e^{i(\omega_{m,n}-k_r)r/2 - i\Phi_{j,k_r}} \sin((\omega_{m,n}-k_r)r/2)}{\omega_{m,n}-k_r} \right] \\ A_{n,n} &= -k\epsilon \sum_j \frac{V_j^{m,n}(z)}{\sqrt{j^2 + j*^2}} \sum_{k_r} \left(\Delta k_r\right)^{1/2} \sqrt{I_{j,k_r}} \frac{\sin(k_r r/2)\cos(k_r r/2 + \Phi_{j,k_r})}{k_r} \qquad (5.6) \\ \mu_{n,n} &= 0 \ , \qquad (5.7) \end{aligned}$$

where the formula for $A_{m,n}$ is general since the formula for $A_{n,n}$ follows from taking $m = n$. The mean $\langle A_{m,n} \rangle$ and the variances $\sigma^2_{A_{m,n}}$ are found by averaging over the uniform random

variables (see Appendix C.4) in the first order perturbation theory result for A in Eq. (5.5),

$$\begin{aligned}
\langle A_{m,n} \rangle &= 0 \\
\langle A_{n,n} \rangle &= 0 \\
\sigma^2_{A_{m,n}} &= \frac{1}{16} (kr\epsilon)^2 (\Delta k_r) \sum_j \frac{\left(V_j^{m,n}(k)\right)^2}{j^2 + j*^2} \sum_{k_r} I_{j,k_r} \left[\frac{\sin^2(\omega_1 r/2)}{(\omega_1 r/2)^2} + \frac{\sin^2(\omega_2 r/2)}{(\omega_2 r/2)^2} \right] \\
\sigma^2_{A_{n,n}} &= \frac{1}{8} (kr\epsilon)^2 (\Delta k_r) \sum_j \frac{\left(V_j^{n,n}(k)\right)^2}{j^2 + j*^2} \sum_{k_r} I_{j,k_r} \frac{\sin^2(k_r r/2)}{(k_r r/2)^2} ,
\end{aligned} \tag{5.8}$$

where $\omega_1 = (\omega_{m,n} + k_r)$ and $\omega_2 = (\omega_{m,n} - k_r)$ and $\omega_{m,n} = k(E_m - E_n)$ and again the formula for $\langle A_{m,n} \rangle$ and $\sigma^2_{A_{m,n}}$ are general for all m, n.

The first order perturbation theory result for A in Eq. (5.5) has uniform random variables Φ_{j,k_r}, so it describes a statistical ensemble for the values of A. The resulting matrix A is a Hermitian matrix which has diagonal elements $A_{n,n}$ which are real and off-diagonal elements satisfying $A_{m,n} = A^*_{m,n}$, so that the unitary transformation can be used with this A to create a model for $U_{m,n}$. As a comment on the potential of this ensemble model, note that the matrix elements $A_{m,n}$ vary with wavenumber so there are correlations with wavenumber built into this model. Also since certain matrix elements will likely have a similar $\omega_{m,n}$, there are correlations between the matrix elements built into this model. However, this model will not be studied further in this thesis since the correlations will turn out to not be that important to the propagation.

The model that will be pursued in this thesis is motivated by the statistics of A from Eq. (5.5). The distribution of the elements $A_{m,n}$ derived from first order perturbation theory

in Eq. (5.5) is shown in the histograms in Figs. (5.1) and (5.2). The distributions appear to be very close to that of a Gaussian random variable. Further, the real and imaginary parts of the offdiagonal elements appear to have the same mean and variance, as shown in the example of $n = 0, m = 1$ in Fig. (5.3). Lastly, the real and imaginary parts of $A_{n,m}$ were found to be independent (with correlation values consistent with zero within expected statistical fluctuations).

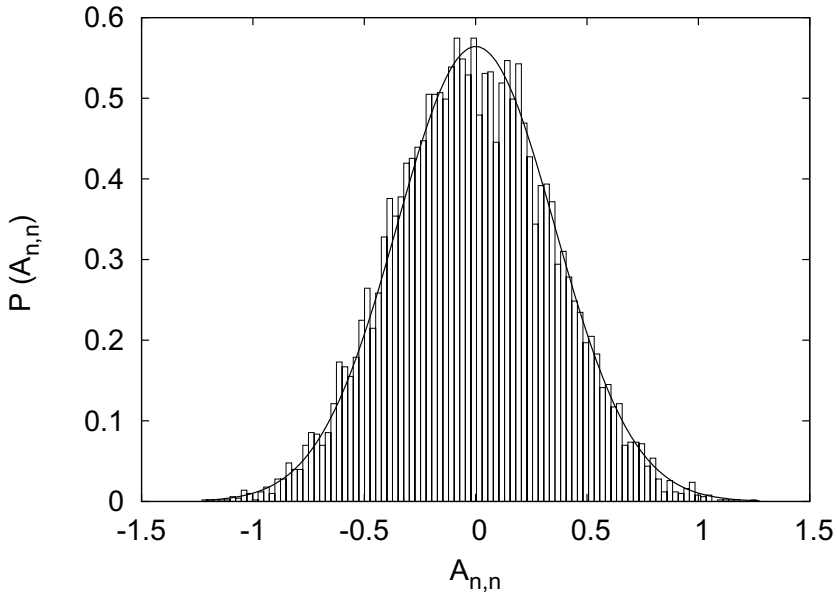

(a) Histogram of $A_{n,n}$ from random phasor sum for $n = 0$

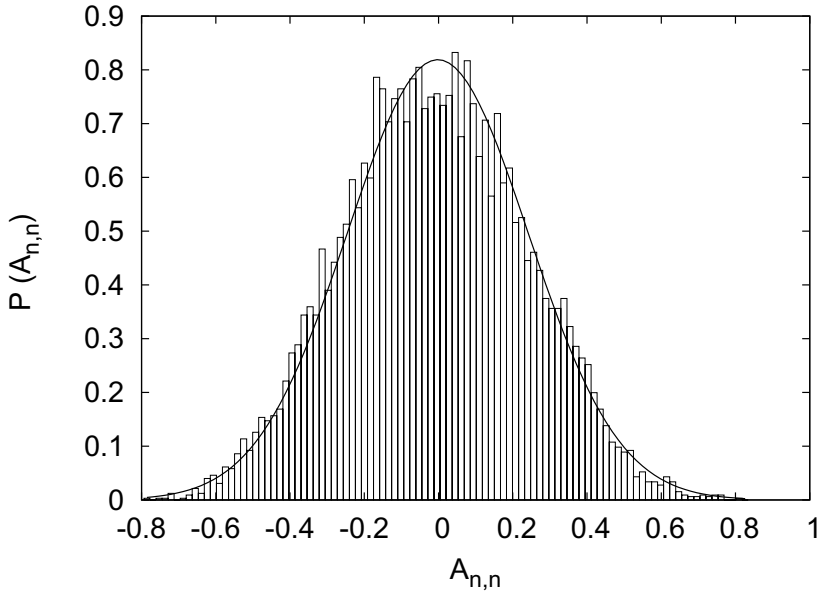

(b) Histogram of $A_{n,n}$ from random phasor sum for $n = 5$

Figure 5.1: Histograms of the probability density function $P(\cdot)$ are plotted with the value of the diagonal phases $A_{n,n}$. Histograms of the diagonal phases of the random phasor sum in Eq. (5.6) for $10,000$ realizations are shown. Overlaid on each histogram is a Gaussian using the mean and variance of the sample distribution.

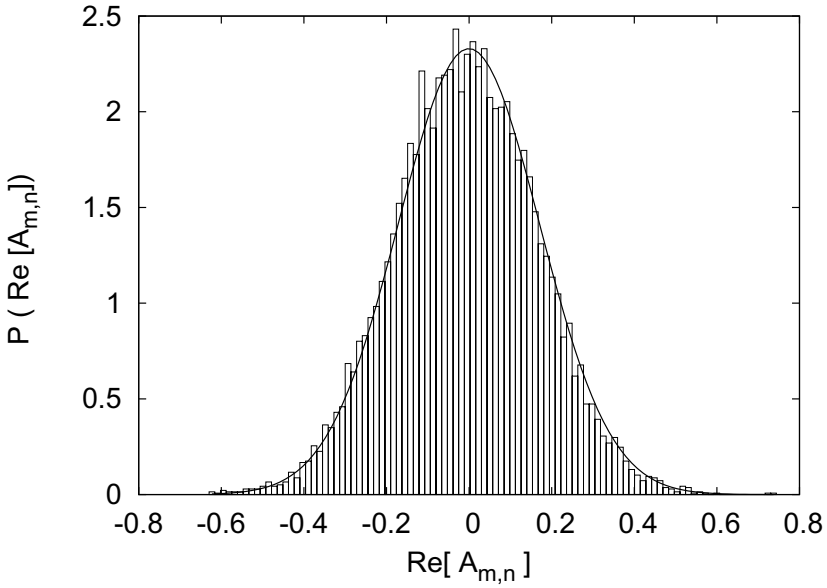

(a) Histogram of the real part of the off-diagonal of the random phasor sum for $n = 0$, $m = 1$

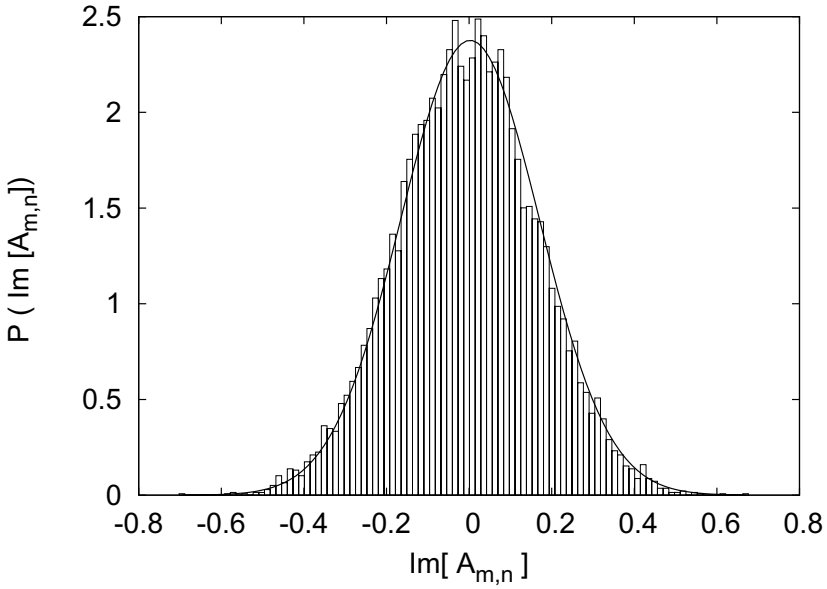

(b) Histogram of the imaginary part of the off-diagonal of the random phasor sum for $n = 0$, $m = 1$

Figure 5.2: Histograms of the probability density function $P(\cdot)$ are plotted with the value $(\cdot)$. Histograms of the off-diagonals of the random phasor sum in Eq. (5.5) for $10,000$ realizations are shown. Overlaid on each histogram is a Gaussian using the mean and variance of the sample distribution.

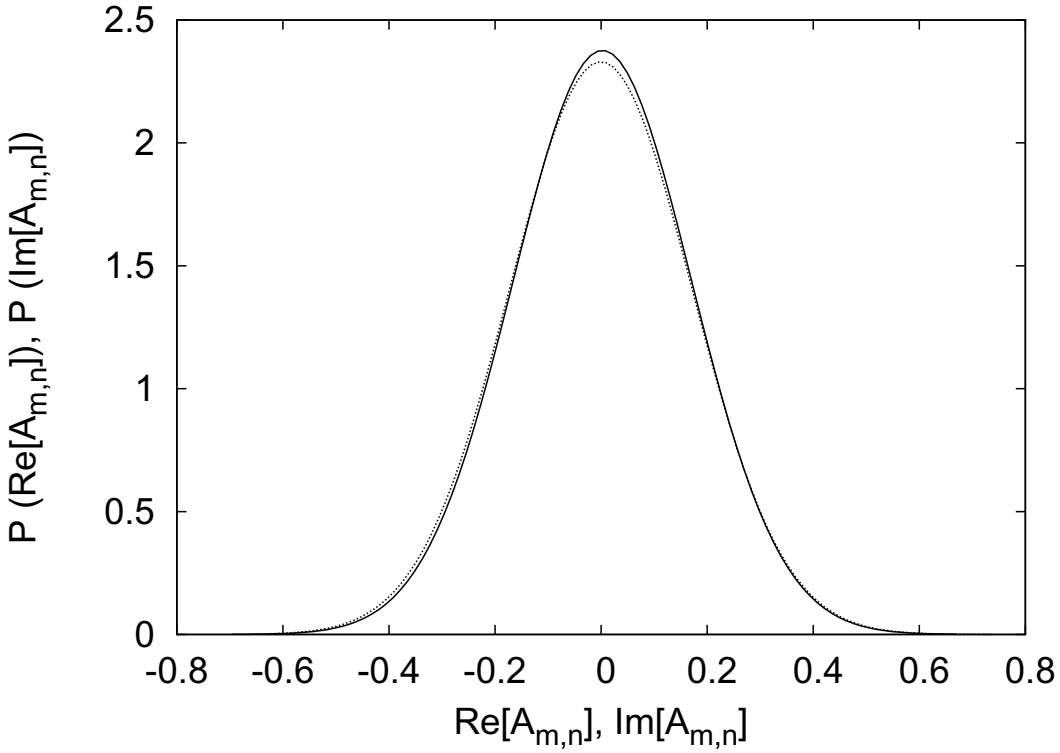

Figure 5.3: Comparison of the distribution of real and imaginary parts of random phasor sum. The approximate Gaussian probability density function $P(\cdot)$ is plotted with values of the (Solid line) real $Re[A_{m,n}]$ and (Dotted line) imaginary $Im[A_{m,n}]$ parts of the random phasor sum. The Gaussian uses the mean and variance of the real and imaginary parts of an ensemble of $10,000$ values of $A_{n,m}$ from Eq. (5.5) are shown.

Matrix A as a Random Phasor Sum

The perturbation theory model in Eq. (5.5) and (5.6) can be viewed as the sum of two random phasor sums, $A_{m,n} = a^{+}_{m,n} + a^{-}_{m,n}$, where

$$a^{+}_{m,n} = \sum_{j,k_r} \alpha^{+}_{m,n,j,k_r} e^{i((\omega_{m,n}+k_r)r/2+\phi_{j,k_r})} \tag{5.9}$$

$$a^{-}_{m,n} = \sum_{j,k_r} \alpha^{-}_{m,n,j,k_r} e^{i((\omega_{m,n}-k_r)r/2-\phi_{j,k_r})} \tag{5.10}$$

$$\alpha^{+}_{m,n,j,k_r} = \frac{k\epsilon}{2} \frac{V^{m,n}_{j}(z)}{\sqrt{j^2+j*^2}} \sqrt{\Delta k_r} \sqrt{I_{j,k_r}} \frac{\sin((\omega_{m,n}+k_r)r/2)}{\omega_{m,n}+k_r} \tag{5.11}$$

$$\alpha^{-}_{m,n,j,k_r} = \frac{k\epsilon}{2} \frac{V^{m,n}_{j}(z)}{\sqrt{j^2+j*^2}} \sqrt{\Delta k_r} \sqrt{I_{j,k_r}} \frac{\sin((\omega_{m,n}-k_r)r/2)}{\omega_{m,n}-k_r} \, . \tag{5.12}$$

In the theory of random phasor sums [77, 78], a central limit theorem may be applied to the sums in Eq. (5.5) and (5.6) to conclude that they are Gaussian distributed if 1) the amplitudes and phases are statistically independent of each other and of all other magnitudes and phases, 2) the phases ϕ_{j,k_r} are all uniformly distributed on $[0, 2\pi)$, 3) the amplitudes $\alpha^{\pm}_{m,n,j,k_r}$ are identically distributed for all j, k_r with the same mean α and variance σ^2_{α}, and 4) the sum is 'large'. In some practical examples where the amplitudes $\alpha^{\pm}_{m,n,j,k_r}$ are not identically distributed as in criteria 3), the central limit theorem can still apply well to the sums [78].

For the random phasor sums in Eq. (5.5) and (5.6), the sums are over k_r and j, which have 512 and 90 terms respectively, so that there are over $512 \times 90 = 46,080$ terms in the random phasor sum. The amplitudes $\alpha^{\pm}_{m,n,j,k}$ are constant, so the amplitudes and the phases ϕ_{j,k_r} are statistically independent of each other (and of the amplitudes and phases of other elementary phasors). The phases ϕ_{j,k_r} are all uniformly distributed on $[0, 2\pi)$. The correlation between

$e^{(\omega_{m,n}+k_r)r/2+\phi_{j,k_r}}$ and $e^{(\omega_{m,n}-k_r)r/2-\phi_{j,k_r}}$ is zero (since $\langle e^{i\phi_{j,k_r}} e^{i\phi_{j,k_r}} \rangle - \langle e^{i\phi_{j,k_r}} \rangle \langle e^{i\phi_{j,k_r}} \rangle = 0$) so the two random phasor sums are independent. Since the amplitudes $\alpha^{\pm}_{m,n,j,k_r}$ have different constant values for each j, k_r, criteria 3) does not hold. However, as seen in Figs. (5.1) and (5.2), the random phasor sum is well approximated by a Gaussian distribution. Therefore, it is likely that in this practical example, the amplitudes may have different distributions and the central limit may still hold approximately [78].

From the theory of random phasor sums, the resultant phasor for $A_{m,n}$ is composed of Gaussian random variables. The offdiagonal element $A_{m,n}$ is predicted to be a complex Gaussian random variable with zero mean and equal variances for the real and imaginary parts. The sum of the variances of the real and imaginary parts is predicted to be

$$< \alpha^2_{m,n} >= \sum_{j,k_r} \left(\alpha^+_{m,n,j,k_r}\right) \left(\alpha^+_{m,n,j,k_r}\right)^* + \left(\alpha^-_{m,n,j,k_r}\right) \left(\alpha^-_{m,n,j,k_r}\right)^* \ . \tag{5.13}$$

The diagonal element $A_{n,n}$ is predicted to be a real Gaussian random variable with zero mean and a variance of

$$< \alpha^2_{n,n} >= \sum_{j,k_r} \left(\alpha^+_{n,n,j,k_r}\right) \left(\alpha^+_{n,n,j,k_r}\right)^* + \left(\alpha^-_{n,n,j,k_r}\right) \left(\alpha^-_{n,n,j,k_r}\right)^* \ . \tag{5.14}$$

Using Eqs. (5.11-5.12), gives the results that $< \alpha^2_{m,n} >= \sigma^2_{A_{m,n}}$ and $< \alpha^2_{n,n} >= \sigma^2_{A_{n,n}}$, and

the variances are

$$\begin{aligned}
\sigma^2_{A_{m,n}} &= \frac{1}{16}\left(kr\epsilon\right)^2 \sum_j \frac{\left(V_j^{m,n}(k)\right)^2}{j^2+j*^2} \sum_{k_r} \left(\Delta k_r\right) I_{j,k_r} \left[\frac{\sin^2\left(\omega_1 r/2\right)}{\left(\omega_1 r/2\right)^2} + \frac{\sin^2\left(\omega_2 r/2\right)}{\left(\omega_2 r/2\right)^2}\right] \\
\sigma^2_{A_{n,n}} &= \frac{1}{8}\left(k\epsilon r\right)^2 \sum_j \frac{\left(V_j^{n,n}(k)\right)^2}{j^2+j*^2} \sum_{k_r} \left(\Delta k_r\right) I_{j,k_r} \frac{\sin^2\left(k_r r/2\right)}{\left(k_r r/2\right)^2} \ ,
\end{aligned} \tag{5.15}$$

where $\omega_1 = (\omega_{m,n} + k_r)$ and $\omega_2 = (\omega_{m,n} - k_r)$. Note that these variances are the same as that in Eq. (5.8).

The variance predictions of the central limit theorem were tested by computing the means and variances of the elements $A_{m,n}$ from the random phasor sums in Eq. (5.5) and (5.6) and comparing to the formula in Eq. (5.8). The means were approximately zero to within expected statistical variation. The variances of the diagonal and offdiagonal elements are plotted in Fig. (5.4) along with the variance calculated using Eq. (5.8). Together with the approximate Gaussian form for the histograms in Figs. (5.1) and (5.2), the agreement of the computed variances with Eq. (5.8) suggest that the random phasor sums for $A_{m,n}$ can be approximated with a Gaussian random variable.

The central limit theorem applied to the phasor sums predicts that the real and imaginary parts of the offdiagonal elements are independent. This was tested using a large ensemble of $N = 1000$ real and imaginary components from Eq. (5.5). The real and imaginary parts were found to have a correlation consistent with zero (within expected statistical variation) so that the real and imaginary parts of the offdiagonal elements are independent.

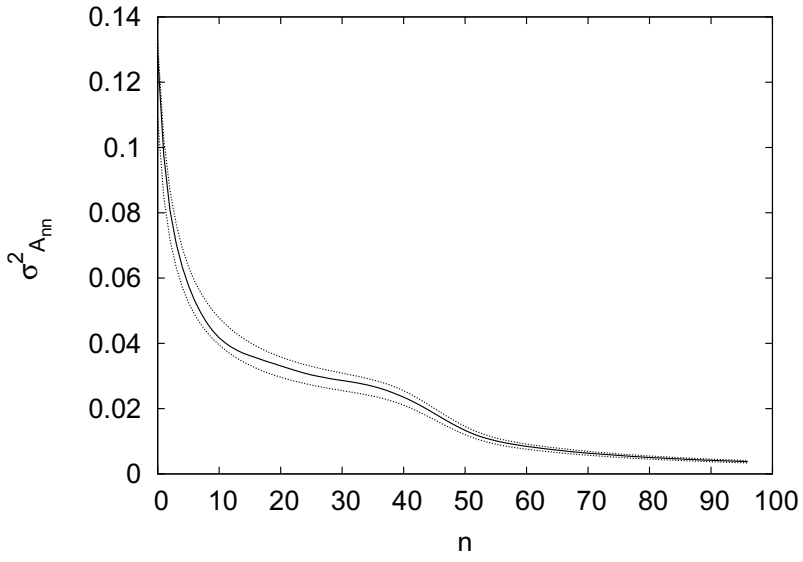

(a) Variances $\sigma^2_{A_{n,n}}$ calculated from random phasor sum versus mode number n

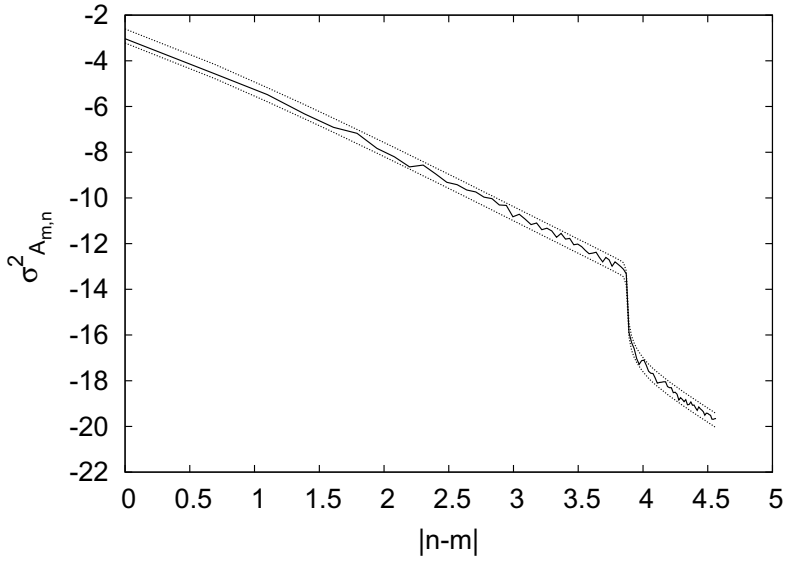

(b) Variances $\sigma^2_{A_{m,n}}$ calculated from random phasor sum versus difference in mode number $|n-m|$ for $n=0$

Figure 5.4: (Solid line) Variances calculated from an ensemble of values of $A_{m,n}$ and $A_{n,n}$ from the random phasor sum in Eq. (5.6). An ensemble of $N = 1,000$ values is used for $A_{n,n}$ and an ensemble of $N = 100$ values is used for $A_{m,n}$. (Dashed lines) Acceptable statistical fluctuations in the variance calculated from Eq. (5.8) with an allowable relative error of $\frac{3}{\sqrt{N}}$ for statistical fluctuations due to finite sampling.

The central limit theorem applied to the phasor sums predicts that the offdiagonal and diagonal elements are all uncorrelated. This has not been tested, but it is likely that several offdiagonal elements from Eq. (5.5) will have similar energy differences (and therefore a similar $\omega_{m,n}$) so that there will be correlations between the matrix elements.

Statistical Model for Matrix A

Using the predictions of the central limit theorem for the random phasor sums in Eqs. (5.9) - (5.10), the off-diagonal elements $A_{m,n}$ can be written as a complex Gaussian random variable $A_{m,n} = \sigma_{A_{m,n}} \frac{1}{\sqrt{2}} (z_1 + iz_2)$ and the diagonal phases $A_{n,n}$ can be written as a real Gaussian random variable $A_{n,n} = \sigma_{A_{n,n}} z_3$. Though there are correlations between the matrix elements, the random variables z_1, z_2, z_3 are chosen to be independent standard normal variables with zero mean and unit variance so that $< A_{m,n}^2 >= \sigma_{A_{m,n}}^2$ and $< A_{n,n}^2 >= \sigma_{A_{n,n}}^2$. Though there are both correlations between elements in the perturbation theory model for $A_{m,n}$ in Eq. (5.5) and there are correlations between elements in the transition matrices from the propagation, these correlations will be found not to be important to long ranges. This is the reason they are left out of this model for A.

Since the mean phase shift $\mu_{n,n}$ for the diagonal elements $U_{n,n}$ is important to the time bias but cannot be captured by the perturbation theory expression in Eq. (4.9), an approximation to the mean phase shift $\mu_{n,n}$ from the propagation results can be utilized with the model.

Then a model for the matrix Λ is

$$\Lambda_{m,n} = \begin{cases} \exp\left[-ikrE_n + i\mu_{n,n}\right] & \text{for } n = m \\ 0 & \text{for } n \neq m \end{cases} , \tag{5.16}$$

where the mean phase $\mu_{n,n}$ is from fits to the propagation analysis as in Eq. (4.20)

and a Hermitian model for A is

$$A_{m,n} = \begin{cases} \sigma_{A_{m,n}}\, z_{m,n} & \text{for } n \geq m \\ A^*_{n,m} & \text{for } n < m \\ \sigma_{A_{n,n}}\, z_{n,n} & \text{for } n = m \end{cases} , \tag{5.17}$$

where $\sigma_{A_{m,n}}$ and $\sigma_{A_{n,n}}$ are from Eq. (5.15) and z is a matrix of random numbers

$$z_{m,n} = \begin{cases} \frac{1}{\sqrt{2}} \left(N(0,1) + iN(0,1) \right) & \text{for } n \neq m \\ N(0,1) & \text{for } n = m \end{cases} , \tag{5.18}$$

with $N(0,1)$ independent Gaussian variables with zero mean and unit variance and the matrix z is chosen constant for all wavenumber k. Note that in the theory of random matrices, the variances of the diagonal and off-diagonal elements are equal for ensembles of random banded matrices [27].

5.1.3 Approximate Statistical Properties

The connection between the statistical properties of A and those of U can be approximated by Eq. (5.3), as long as the resulting elements of A are indeed 'small'. Solving for $A_{m,n}$ in the approximation in Eq. (5.4) and keeping only first order terms gives $A_{m,n} = \frac{i}{2} U_{m,n} e^{ikrE_m - i\phi_{n,n}}$. Therefore the relationship between the variance of the off-diagonal elements of A and of U is

$$\sigma^2_{A_{m,n}} \;=\; < A_{m,n} A^*_{m,n} > = \frac{1}{4} < U_{m,n} U^*_{m,n} > = \frac{1}{4} \left(\sigma^2_{Re[U_{m,n}]} + \sigma^2_{Im[U_{m,n}]} \right) . \tag{5.19}$$

From Eq. (5.3), the phases $A_{n,n}$ are the differences in the phases $Arg[U_{n,n}]$ of the diagonal elements $U_{n,n}$ from $-krE_n - \mu_{n,n}$, so

$$\sigma^2_{A_{n,n}} = \frac{1}{4}\sigma^2_{Arg[U_{n,n}]} . \tag{5.20}$$

Though, information about the real and imaginary parts of the offdiagonal elements of U and the phase of the diagonal elements of U are captured in the statistics of the matrices A and Λ, information about the magnitude of the diagonal elements of U is captured by the constraint of unitarity from the unitary transformation on A in Eq. (5.1). Using the approximation to the unitary model, $|U_{n,n}| = \left(1 - \sum_{l\neq n} A_{n,l}A_{l,n}\right)$. Since the model for A is created from Gaussian random variables $A_{m,n}$ for $m \neq n$, the terms $A_{n,l}A_{l,n} = \sigma_{A_{n,l}}\sigma_{A_{n,l}} z_{n,l}z_{l,n}$ are a product of two approximate Gaussian random variables or a Chi Square random variables. The differences in the magnitudes from unity seen from the propagation results in Fig. (4.30) are more consistent with a sum of Chi Square random variables than a Gaussian random variable. The mean value for the magnitude of the diagonal elements is

$$\langle |U_{n,n}| \rangle = \left(1 - \sum_{l\neq n} \sigma_{A_{n,l}}\sigma_{A_{l,n}}\right) \tag{5.21}$$

where $\langle |U_{n,n}| \rangle \in [0, 1]$.

5.1.4 Verification of Statistics

In this section, the statistics of the Ensemble Model are compared to 1) the predicted statistics of the model and 2) to the propagation statistics for 50 km. A large sample from the Ensemble Model consists of transition matrices U for propagation to 50 km is generated by using the ensemble model described in Eq. (5.1) and Eqs. (5.17-5.18).

Accuracy of Predicted Model Statistics

Several approximations have been made in constructing the Ensemble Model. To ascertain how well these approximations perform in the creation of the model, it is desired to compare the actual model statistics to the predicted model statistics. The only inputs which change the Ensemble Model are the variances $\sigma^2_{A_{m,n}}$ and $\sigma^2_{A_{n,n}}$ in Eq. (5.17-5.18). Based on these input statistics, it is predicted that the variances for the resulting transition matrices of the Ensemble Model have the simple relationships in Eq. (5.19) and (5.20).

The variances of the off-diagonal elements $U_{m,n}$ and the diagonal phase differences $A_{n,n}$ are calculated from a large sample from the ensemble model. The calculated variances are found to be in close agreement with the variances in Eqs. (5.15). The agreement in the variances is illustrated in Fig. (5.5). The agreement shows that the variances input to the Ensemble Model through $\sigma^2_{A_{m,n}}$ and $\sigma_{\phi_{n,n}}$ in Eq. (5.17-5.18) have the simple relationships in Eq. (5.19) and (5.20) to the output of the Ensemble Model for U.

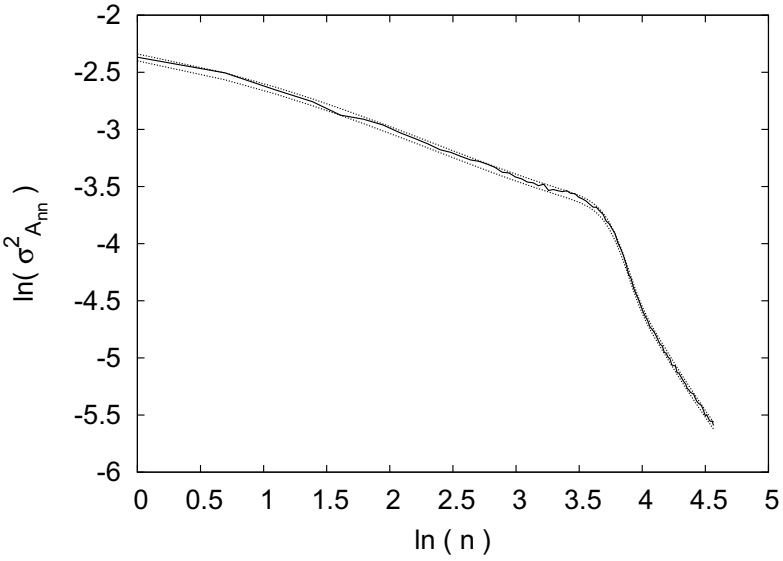

(a) Variances of diagonal phases $A_{n,n}$ using Ensemble Model

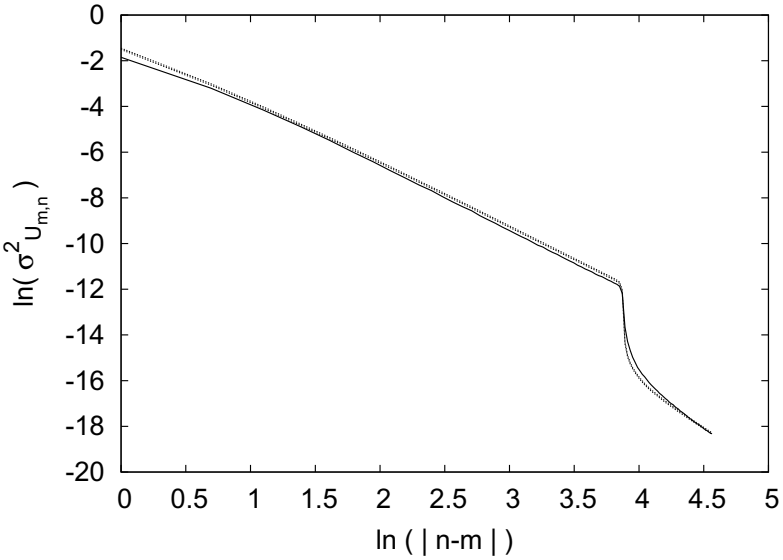

(b) Variances of off-diagonals $U_{m,n}$ for $n = 0$ using Ensemble Model, where $\sigma^2_{U_{m,n}} = \sigma^2_{Re[U_{m,n}]} + \sigma^2_{Imag[U_{m,n}]}$

Figure 5.5: Calculated and predicted variances of off-diagonal and diagonal elements U. The natural logarithm of the variance is plotted with natural logarithm of (a) mode number n (b) difference in mode number $|n - m|$. (Solid line) Variances are generated with values from $10,000$ realizations of the ensemble model using Eq. (5.1) and Eqs. (5.17-5.18). (Dotted line) Overlaid on each plot is the predicted variance from Eqs. (5.15).

Agreement of Model Statistics with Propagation Statistics

The matrix elements $A_{m,n}$ input into the Ensemble Model are distributed as complex Gaussian random variables. After the unitary transformation, the distributions of the off-diagonal elements $U_{m,n}$ and the diagonal phases $Arg[U_{n,n}]$ were found to be approximately Gaussian distributed also so that the unitary transformation appears to preserve the distribution of the elements. The distributions for a sample off-diagonal elements and a sample diagonal phase are shown in Fig. (5.6). This is in qualititative agreement with the distributions for the off-diagonal elements $U_{m,n}$ and the diagonal phases $Arg[U_{n,n}]$ for the propagation to 50 km. As shown in Sec. (4.3.2) and (4.3.1), the off-diagonal elements $U_{m,n}$ and the diagonal phases $Arg[U_{n,n}]$ from the propagation are approximately Gaussian distributed.

The variances of the off-diagonal elements $U_{m,n}$ and the diagonal phases $Arg[U_{n,n}]$ are calculated from a large sample from the ensemble model. The calculated variances are found to be in close agreement with the variances in Eqs. (5.15), but there are differences in both the diagonal and off-diagonal variances as seen in Fig. (5.7). The calculated variance for the diagonal phases differ by roughly a factor of $\sqrt{2}$ (an 18% difference in the standard deviation), with the variance of the Ensemble Model larger than the variance of the propagation. The calculated variance for the off-diagonal elements also differ by roughly a factor of $\sqrt{2}$, but with the variance of the Ensemble Model smaller than the variance of the propagation.

The magnitudes of the diagonal elements $|U_{n,n}|$ are calculated from a large sample from the ensemble model. The distribution of the magnitudes are found to be in close agreement with the distribution of the magnitudes from the propagation. The qualitative agreement is

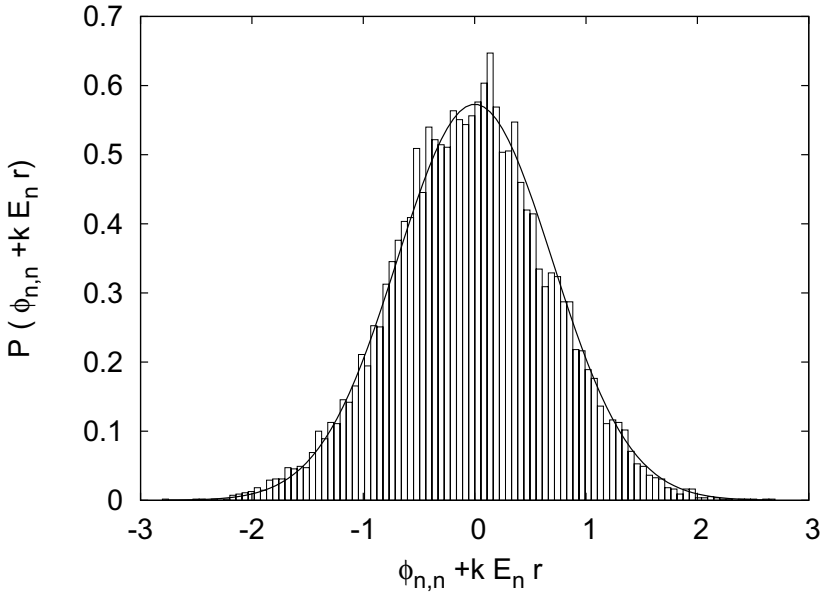

(a) Histogram of diagonal phases $\phi_{n,n}$ for $n = 0$ using Ensemble Model

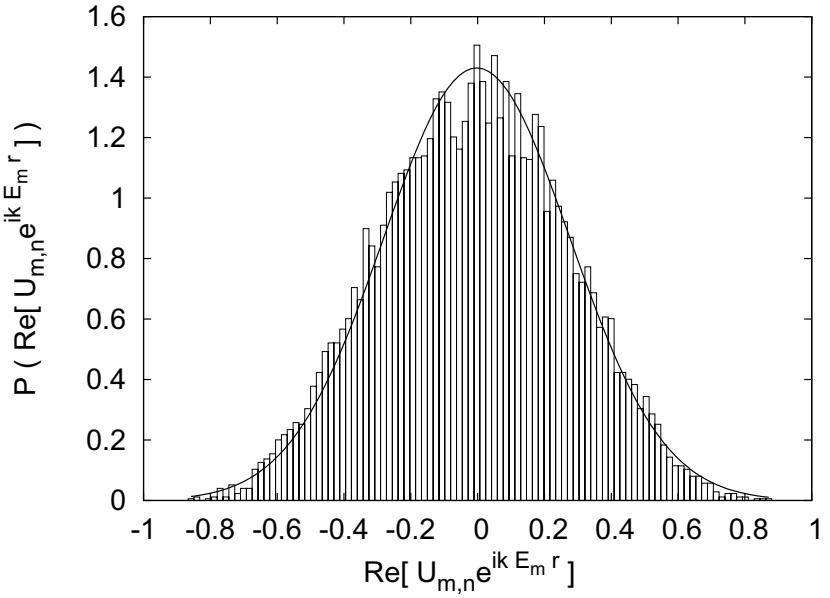

(b) Histogram of off-diagonals $U_{m,n}$ for $n = 0$, $m = 1$ using Ensemble Model

Figure 5.6: Histograms of the probability density function $P(\cdot)$ are plotted with the value $(\cdot)$. Histograms are generated with values from $10,000$ realizations of the ensemble model using Eq. (5.1) and Eqs. (5.17-5.18). Overlaid on each histogram is a Gaussian using the mean and variance of the sample distribution.

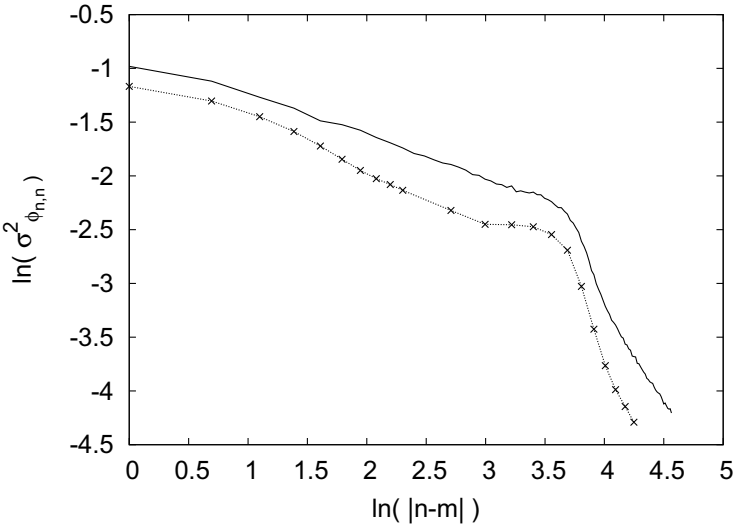

(a) Calculated variances of diagonal phases $\phi_{n,n}$ for Ensemble Model(line) compared to propagation(points)

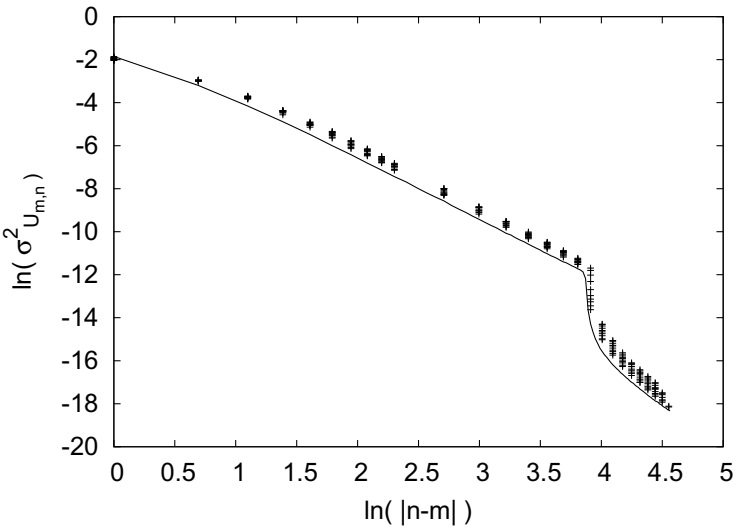

(b) Calculated variances of off-diagonals $U_{m,n}$ for $n = 0$ for Ensemble Model(line) compared to propagation(points), where $\sigma^2_{U_{m,n}} = \sigma^2_{Re[U_{m,n}]} + \sigma^2_{Imag[U_{m,n}]}$

Figure 5.7: Comparison of the calculated variances from propagation and the calculated variances from Ensemble Model. The natural logarithm of the variance $\sigma^2_{(\cdot)}$ is plotted with natural logarithm of (a) mode number n (b) difference in mode number $|n-m|$. (Dotted line/points) Variances are generated with values from propagation to 50 km through $2,500$ independent realizations of the internal wave sound speed field. (Solid line) Variances are generated with values from $10,000$ realizations of the ensemble model using Eq. (5.1) and Eqs. (5.17-5.18).

illustrated in Figs (5.8) and (5.9). The distribution of $ln\,(1-|U_{n,n}|)$ is compared to that of a Gaussian random variable in Fig. (5.9) to surprising agreement suggesting that the magnitudes $|U_{n,n}|$ are distributed as log normal random variables. The mean and variance of $|U_{n,n}|$ are compared to that from the propagation in Fig. (5.10) to close agreement.

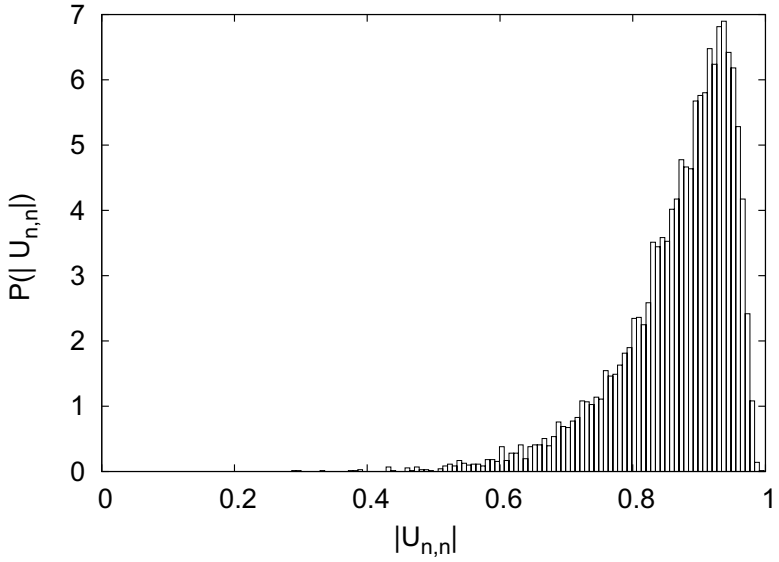

(a) Histogram from Ensemble Model

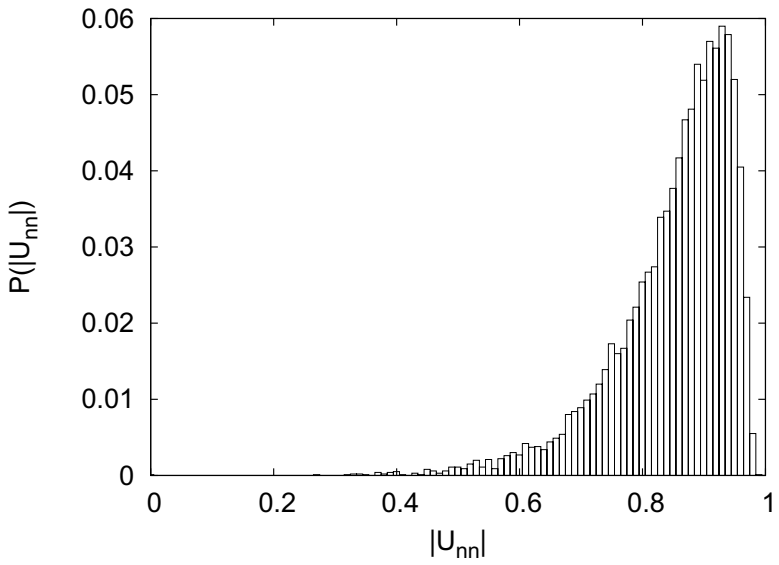

(b) Histogram from propagation

Figure 5.8: Comparison of the histograms of the probability density function $P(\cdot)$ as a function of the the magnitude of the diagonal elements $|U_{n,n}|$ for $n = 0$. The histogram generated with $10,000$ realizations of the ensemble model using Eq. (5.1) and Eqs. (5.17-5.18) is compared to the histogram generated with 2500 realizations of the propagation to 50 km. The means and variances of $|U_{n,n}|$ is shown in Fig.(5.10). The disagreement is most prominent for lower mode numbers. The mean is overestimated by the Ensemble Model mainly for mode number $5 < n < 45$, while the variance is underestimated by the Ensemble Model.

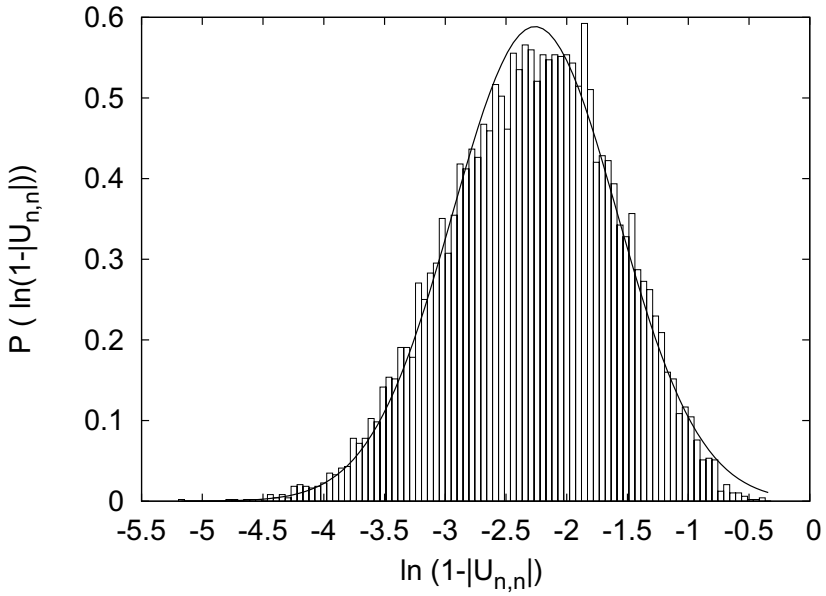

(a) Histogram from Ensemble Model

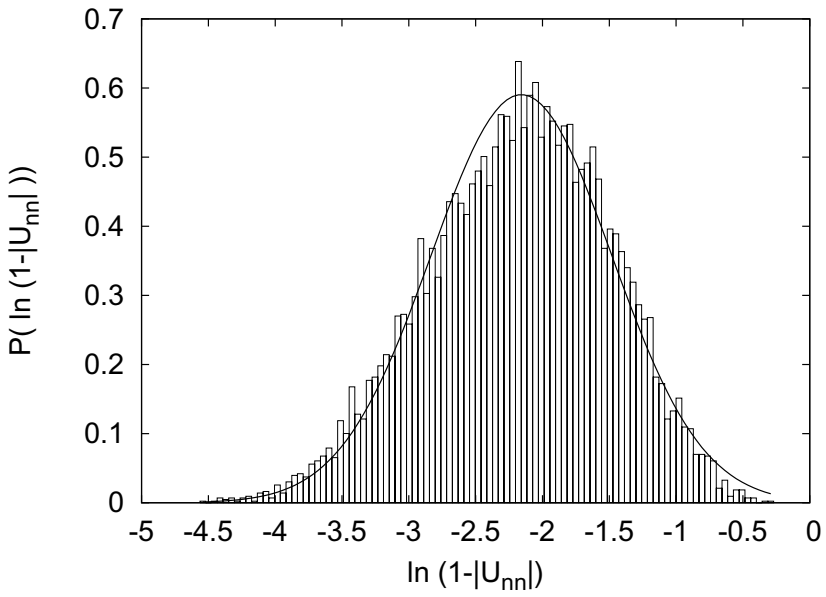

(b) Histogram from propagation

Figure 5.9: Comparison of the histograms of the probability density function $P(\cdot)$ as a function of the natural logarithm of the difference from one of the magnitude of the diagonal elements $ln\,(1-|U_{n,n}|)$ for $n=0$. The histogram generated with $10,000$ realizations of the ensemble model using Eq. (5.1) and Eqs. (5.17-5.18) is compared to the histogram generated with 2500 realizations of the propagation to 50 km.

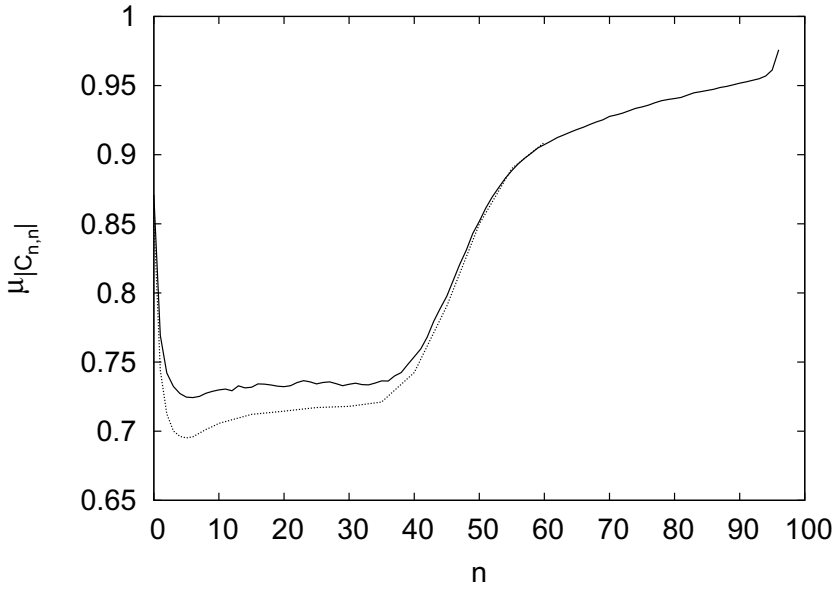

(a) Mean of $|U_{n,n}|$ from Ensemble Model(solid line) and propagation (dashed line)

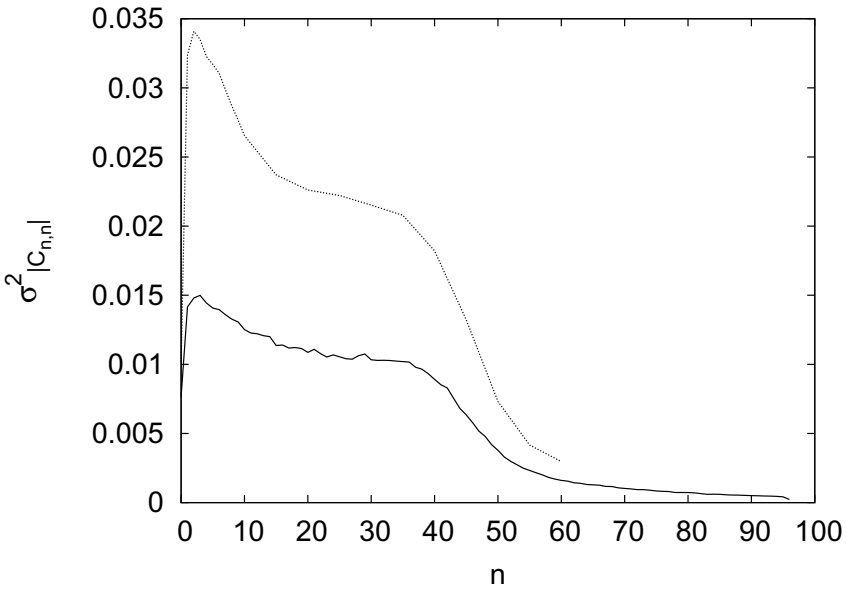

(b) Variance of $|U_{n,n}|$ from Ensemble Model(solid line) and propagation (dashed line)

Figure 5.10: Comparison of the mean and variance of $|U_{n,n}|$ from the Ensemble Model and the propagation to 50 km. The means and variances are calculated from values of $|U_{n,n}|$ from $10,000$ realizations of the ensemble model using Eq. (5.1) and Eqs. (5.17-5.18) and from 2500 realizations of the propagation to 50 km.

5.1.5 Comparison of Sample Ensemble and Propagation Matrices

In this section, a sample of building block matrices from the Ensemble Model is compared qualitatively to a sample of transition matrices from propagation to $r = 50$ km.

A single realization of a building block matrix U generated from the Ensemble Model is compared qualitatively to a single realization of a transition matrix U for propagation to 50 km by comparing the phases and magnitudes of the matrix as a contour plot in mode number n and m. The matrices generated are for a source frequency of 75 Hz. In Fig. (5.12-5.13), the magnitudes $|U_{m,n}|$ and logarithm of the magnitudes $ln\left(|U_{m,n}|\right)$ are compared, while in Fig.(5.11), the phases $Arg[U_{m,n}]$ of the transition matrix elements are compared. The Ensemble Model captures the randomness of the phases convincingly and captures the width of the banding along the diagonal very well also.

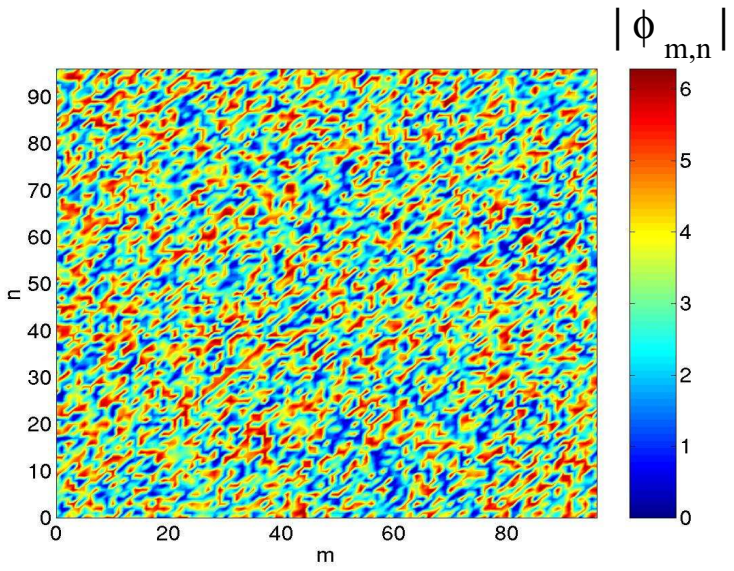

(a) Phase of sample building block matrix from Ensemble Model

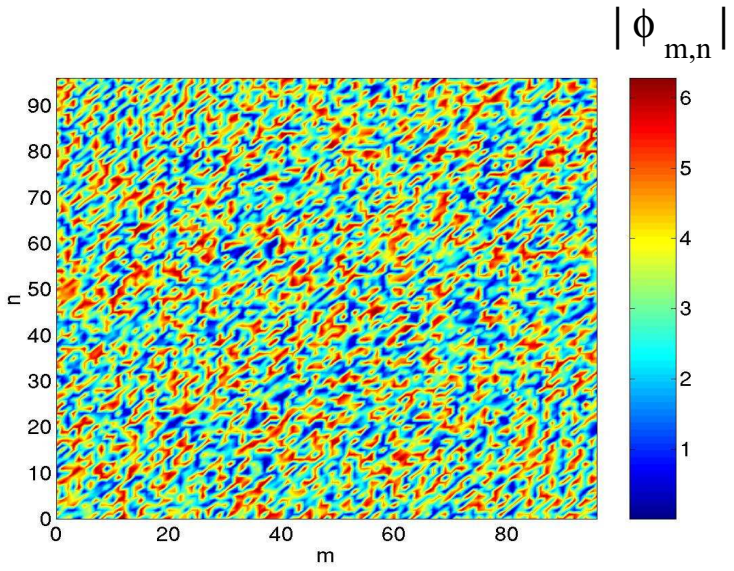

(b) Phase of sample transition matrix from propagation to 50 km

Figure 5.11: Comparison of phase of sample matrices from Ensemble Model and propagation for 50 km. The phases $\Phi_{m,n} = Arg\,[U_{m,n}]$ of the matrix elements $U_{m,n}$ are plotted with initial wave number n and final wave number m for the propagation range $r = 50$ km with the source frequency of 75 Hz. (a) A sample transition matrix U is generated from a single member of the Ensemble Model from Eq. (5.1) and Eqs. (5.15-5.18). (b) A sample transition matrix U from propagation through a single internal wave field.

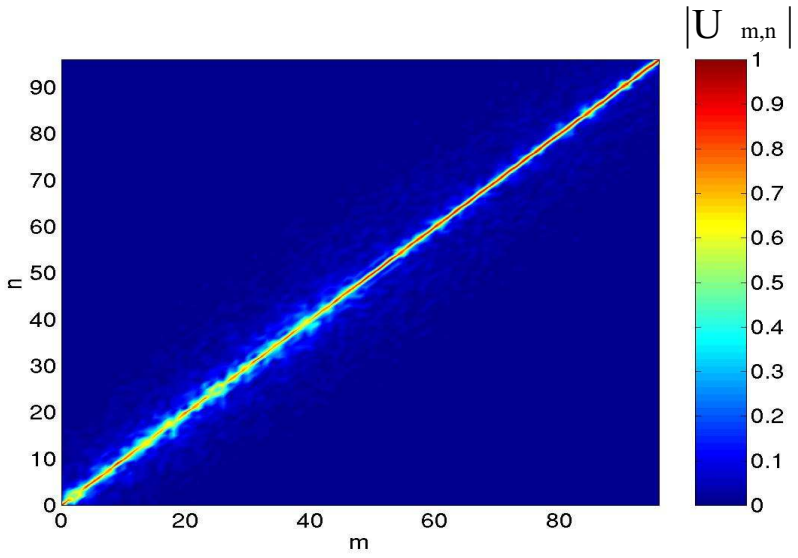

(a) Amplitude of sample building block matrix from Ensemble Model

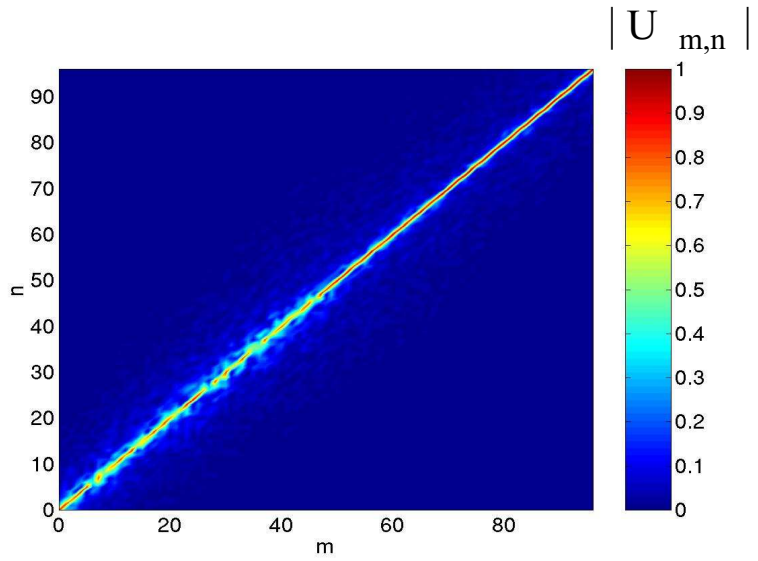

(b) Amplitude of sample transition matrix from propagation to 50 km

Figure 5.12: Comparison of magnitudes $|U_{m,n}|$ of sample matrices from Ensemble Model and propagation for 50 km. The magnitudes $|U_{m,n}|$ are plotted with initial wave number n and final wave number m for the propagation range $r = 50$ km with the source frequency of 75 Hz. (a) A sample transition matrix U is generated from a single member of the Ensemble Model from Eq. (5.1) and Eqs. (5.15-5.18). (b) A sample transition matrix U from propagation through a single internal wave field.

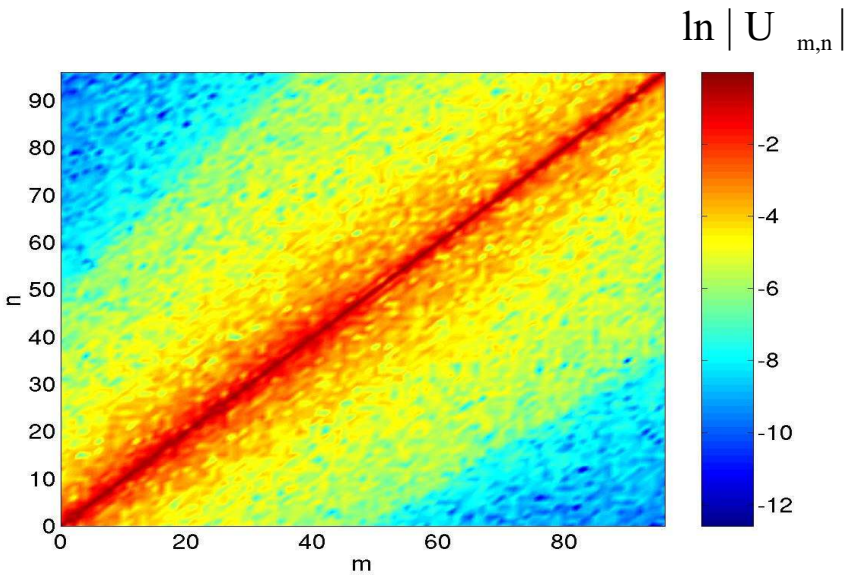

(a) Logarithm of magnitude of sample building block matrix from Ensemble Model

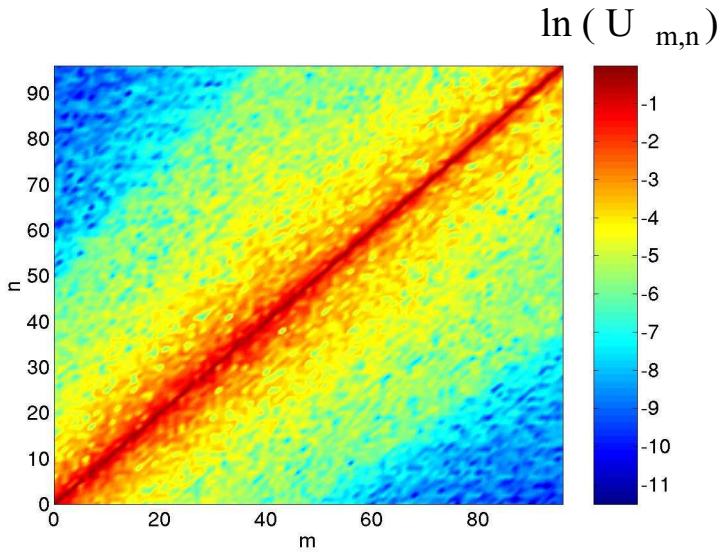

(b) Logarithm of magnitude of sample transition matrix from propagation

Figure 5.13: Comparison of natural logarithm of magnitudes $ln\,(|U_{m,n}|)$ of sample matrices from Ensemble Model and propagation for 50 km. The logarithm of the magnitudes $ln\,(|U_{m,n}|)$ are plotted with initial wave number n and final wave number m for the propagation range $r = 50$ km with the source frequency of 75 Hz. (a) A sample transition matrix U is generated from a single member of the Ensemble Model from Eq. (5.1) and Eqs. (5.15-5.18). (b) A sample transition matrix U from propagation through a single internal wave field.

5.2 Long Range Ensemble Model

A Long Range Ensemble Model for transition matrices for long ranges greater than 50 km is formed through the multiplication of independent building block matrices for 50 km propagation regions. Due to the construction, the Long Range Ensemble Model can only construct transition matrices at ranges which are integer multiples of 50 km.

The validity of the long range model depends greatly on the 'independence' of the successive transition matrix elements for 50 km propagation in the potential, upon which the independent building blocks were constructed.

In this section, qualitative comparisions of the resulting matrices and timefronts from the long range ensemble model are compared to those from the long range propagation. Additionally, using simulations of a large sample from the Long Range Ensemble Model, predictions of the range dependence of certain statistical quantities are made.

5.2.1 Building Block Matrix Multiplication

A transition matrix C for propagation to a long range $R = 50N$ km, for N an integer, is calculated by multiplying statistically independent building blocks U_i from the Ensemble Model for each 50 km segment of the propagation to long range.

$$C = \prod_{i=1}^{i=N} U_i$$

The building block matrices U_i are chosen from the Ensemble Model using Eq. (5.1) and Eqs. (5.17-5.18). The set of matrices U_i create a member of the ensemble for the Long Range Ensemble Model.

5.2.2 Comparison of Sample Ensemble and Propagation Matrices

In this section, a sample building block matrix from the Long Range Ensemble Model is compared qualitatively to a sample transition matrix from propagation to ranges which are integer multiples of 50 km.

A single realization of a transition matrix C generated from the Long Range Ensemble Model is compared qualitatively to a single realization of a transition matrix C for propagation to a range r by comparing the phases and magnitudes of the matrix as a contour plot in mode number n and m. The matrices generated are for a source frequency of 75 Hz. In Fig. (5.16-5.17), the magnitudes $|U_{m,n}|$ and logarithm of the magnitudes $ln\left(|U_{m,n}|\right)$ are compared for a range of 1000 km. The phases of the matrices resulting from the Long Range Ensemble Model appear to be just as random as the phases in Fig. (5.11). Therefore the Long Range Ensemble Model captures the randomness of the phases convincingly and captures the width of the banding along the diagonal very well for long ranges too.

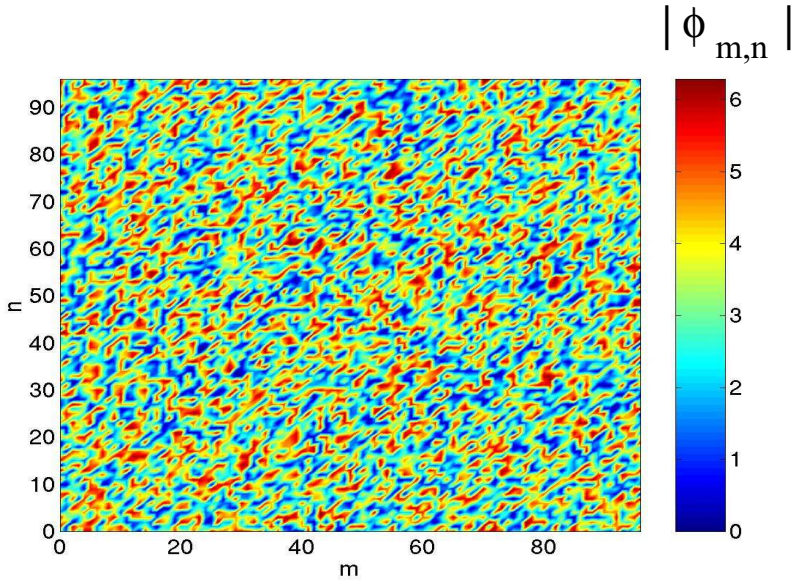

(a) Phase of sample building block matrix from Ensemble Model

Figure 5.14: Phase of sample matrix from Ensemble Model for 1000 km. The phases $\Phi_{m,n} = Arg\,[U_{m,n}]$ of the matrix elements $U_{m,n}$ are plotted with initial wave number n and final wave number m for the range $r = 1000$ km with the source frequency of 75 Hz. (a) A sample transition matrix U is generated from a single member of the Ensemble Model from Eq. (5.1) and Eqs. (5.15-5.18).

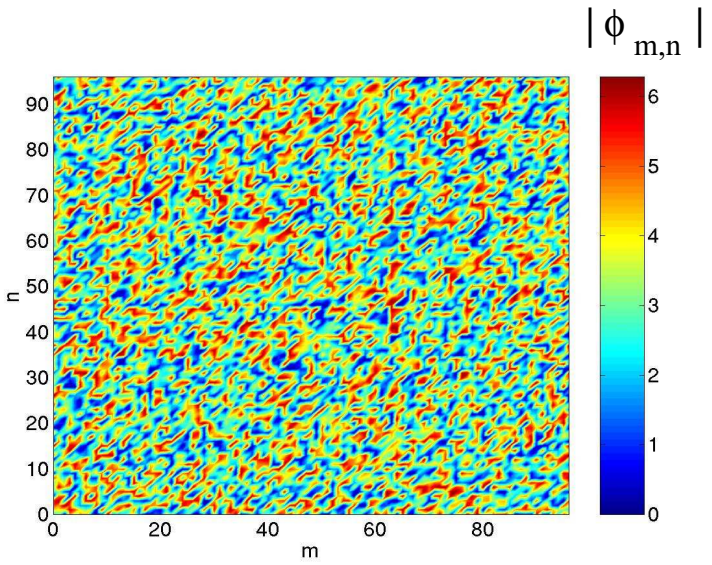

(a) Phase of sample building block matrix from Ensemble Model for $r = 2000$ km

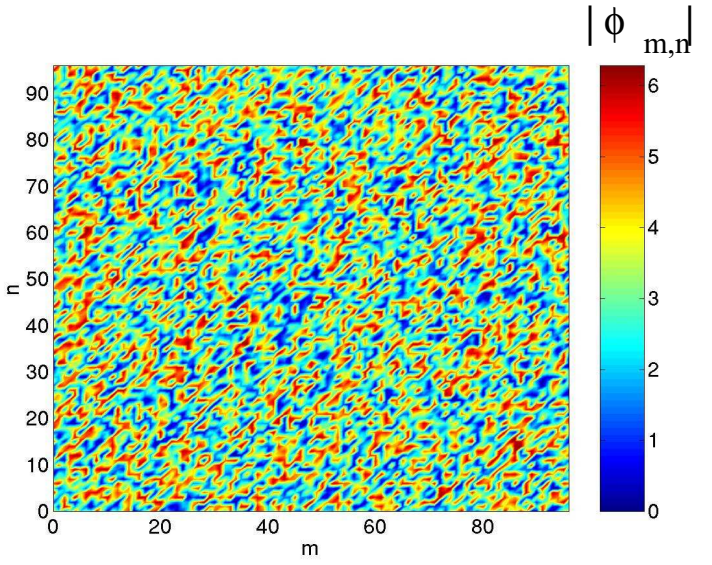

(b) Phase of sample building block matrix from Ensemble Model for $r = 3000$ km

Figure 5.15: Phase of sample matrix from Ensemble Model for 2000 km. The phases $\Phi_{m,n} = Arg\,[U_{m,n}]$ of the matrix elements $U_{m,n}$ are plotted with initial wave number n and final wave number m for the range $r = 2000$ km with the source frequency of 75 Hz. A sample propagation matrix U is generated from a single member of the Ensemble Model from Eq. (5.1) and Eqs. (5.15-5.18) for (a)$r = 2000$ km and (b) $r = 3000$ km.

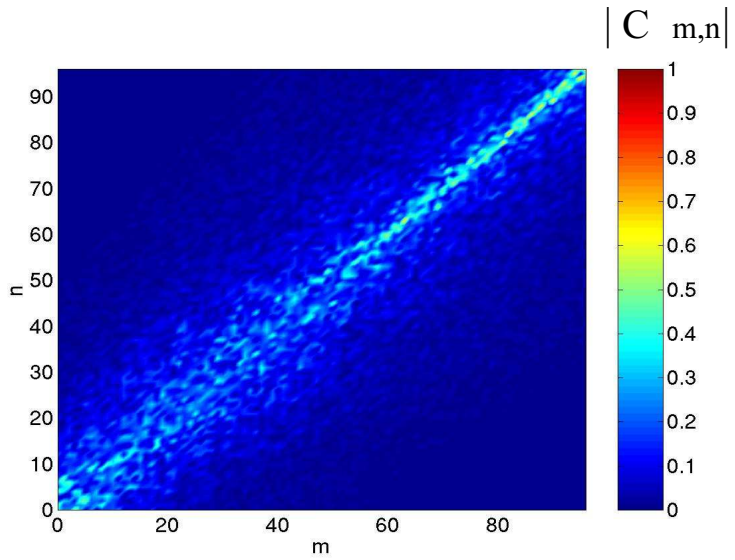

(a) Sample matrix from Long Range Ensemble Model for 1000 km

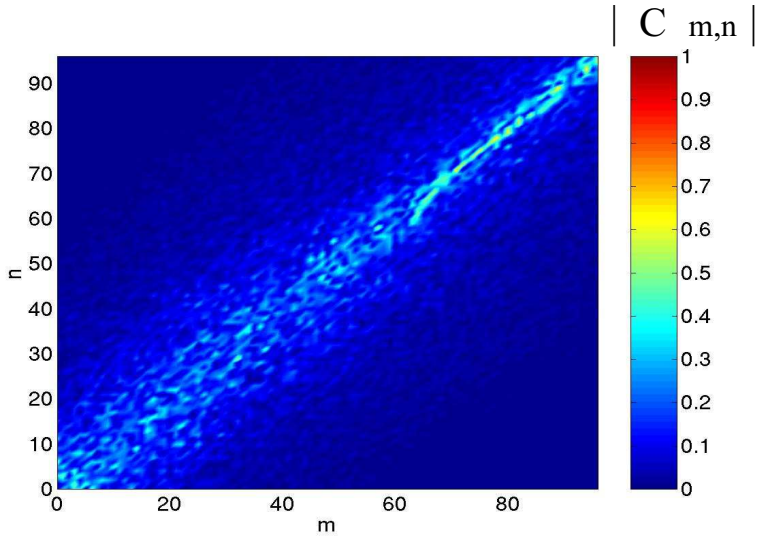

(b) Sample matrix from propagation to 1000 km

Figure 5.16: Contour plot of transition matrix from perturbation theory statistics ensemble. The transition matrix C for propagation through a single internal wave field is illustrated as a contour plot of the magnitudes of the matrix elements $|C_{m,n}|$ plotted with initial wave number n on the vertical axis and final wave number m on the horizontal axis.(Upper) Transition matrix generated from 20 members of the ensemble generated from Eq. (5.1) and Eqs. (5.15-5.18). (Lower) Transition matrix generated from a single seed from the propagation. The propagation ranges are $r = 1000$ km. The source frequency is 75 Hz.

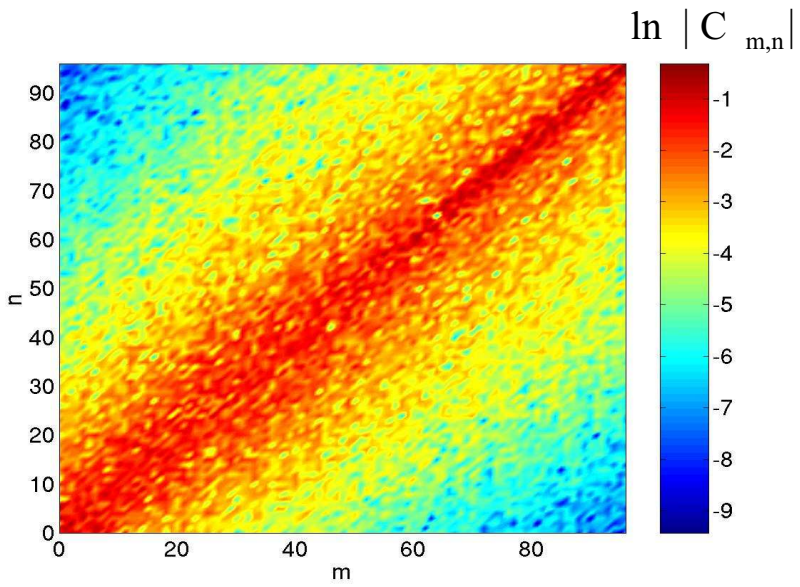

(a) Sample matrix from Long Range Ensemble Model for 1000 km

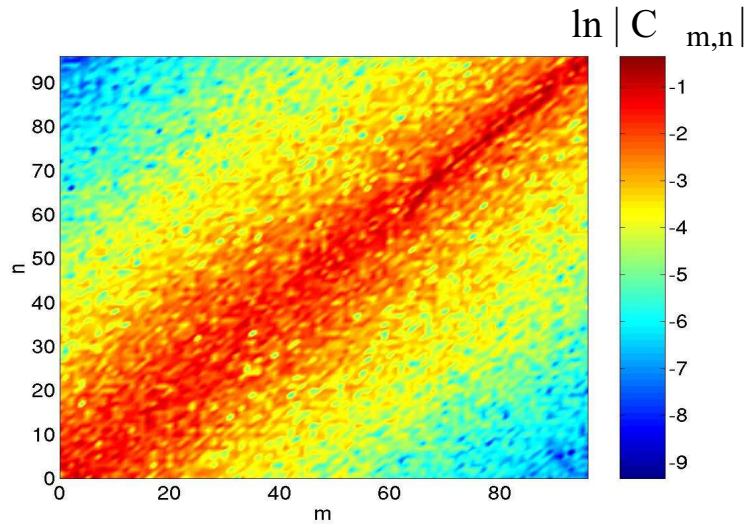

(b) Sample matrix from propagation to 1000 km

Figure 5.17: The transition matrix C for propagation through a single internal wave field is illustrated as a contour plot of the logarithm of the magnitudes of the matrix elements $|C_{m,n}|$ plotted with initial wave number n on the vertical axis and final wave number m on the horizontal axis.(Upper) Transition matrix generated from a single member of the perturbation theory statistics ensemble generated from Eq. (5.1) and Eqs. (5.15-5.18). (Lower) Transition matrix generated from a single seed from the propagation. The propagation ranges are $r = 1000$ km. The source frequency is 75 Hz.

5.2.3 Predictions for Long Range Statistics

Using a large sample from the long range ensemble model to different ranges, the statistical properties predicted by the model can be explored. These predictions cannot be done using the simulated propagation due of the long computational time to generate an ensemble of mode propagation to long ranges. This section is an example of the kinds of predictions that can be made using the ensemble models.

The distributions of some sample diagonal phases and off-diagonal elements are shown in the histograms in Fig. (5.22) for several ranges. The histogram of the diagonal phases have large fluctuations about a seemingly constant value. The histogram of the real and imaginary parts of the off-diagonal elements appear to be approximately Gaussian distributed. The variances of the diagonal phases and off-diagonal elements are shown in Figs. (5.19). The variances in both cases increase with range in a consistent pattern. Since the variance of the phases are calculated in this figure with the assumption that the distribution of phases is Gaussian, the continuation in the pattern with range seems to suggest that the phases remain Gaussian on the infinite domain $(-\infty, \infty)$ with increasing range. This is supported by the flatness of the distribution of the phases since the Gaussian phases on the infinite domain would be mapped to the branch $[-\pi, \pi]$ in a manner consistent with that seen in the figure.

The distributions of the magnitude of the diagonal elements $|C_{n,n}|$ are shown in the histograms in Fig. (5.20) for several ranges. The means and variances of the magnitude of the diagonal elements $\mu_{|C_{n,n}|}$ are shown in Fig. (5.21) for several ranges. The means decrease with range. But the decrease is much greater for the lower order modes than for the higher

order modes, with modes between $5 < n < 40$ having the greatest decrease.

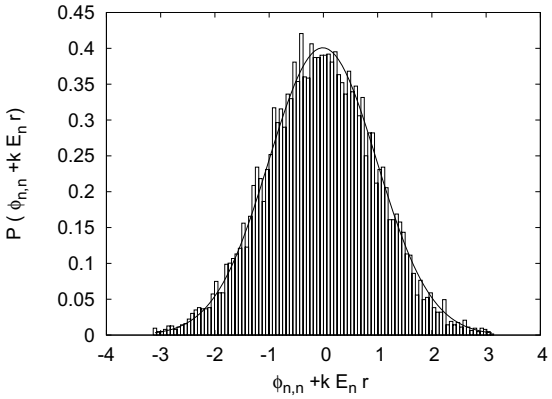

(a) Histogram of $\phi_{n,n}$ for $n = 0$ using long range ensemble model for $r = 100$ km.

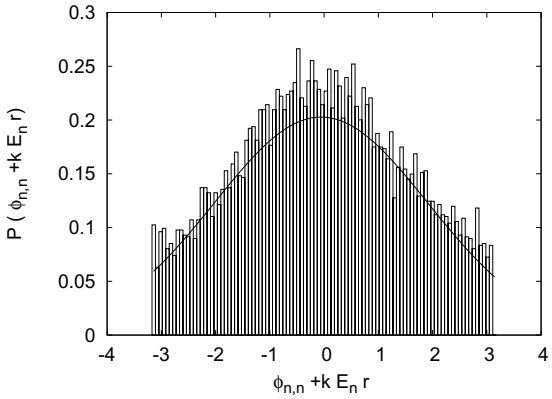

(b) Histogram of $\phi_{n,n}$ for $n = 0$ using long range ensemble model for $r = 250$ km.

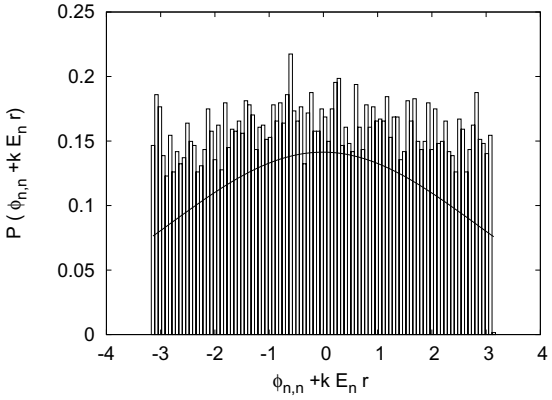

(c) Histogram of $\phi_{n,n}$ for $n = 0$ using long range ensemble model for $r = 500$ km.

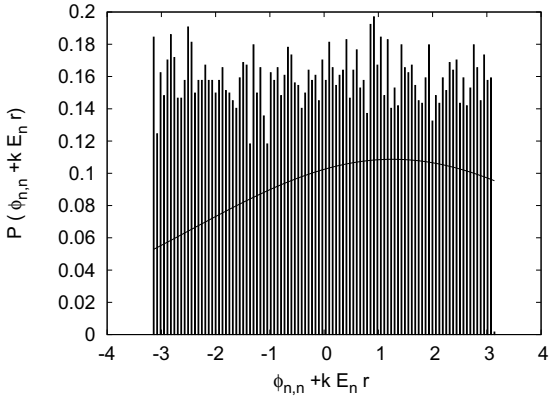

(d) Histogram of $\phi_{n,n}$ for $n = 0$ using long range ensemble model for $r = 1000$ km.

Figure 5.18: Histograms of the probability density function $P(\cdot)$ are plotted with the value of the diagonal phase $\phi_{n,n}$ for $n = 0$. Histograms are generated with values from $10,000$ realizations of the long range ensemble model for $r = 1000$ km. Overlaid on the histograms is a Gaussian using the mean and variance of the sample distribution (assuming the distribution is Gaussian).

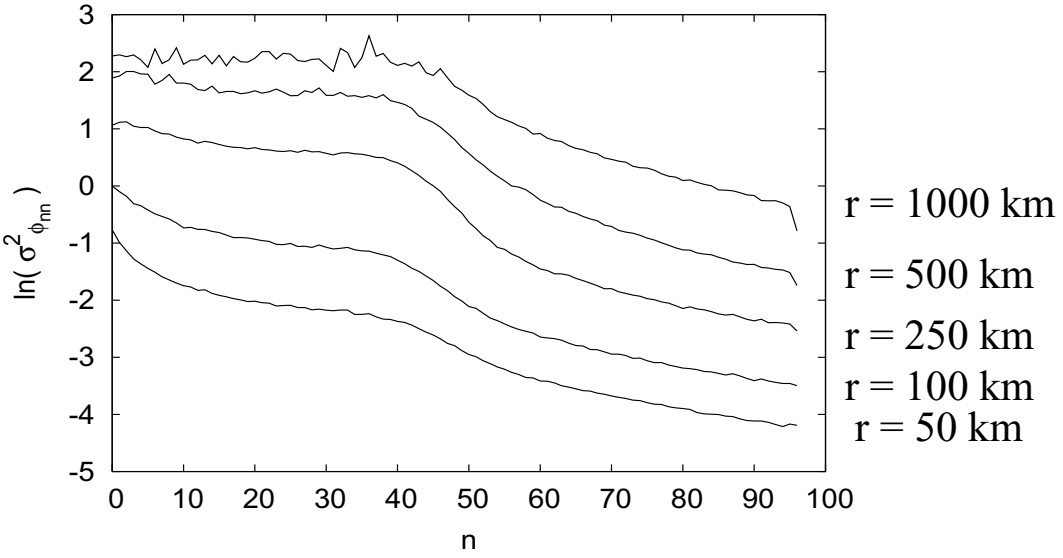

(a) Predicted variances of diagonal phases $\phi_{n,n}$ using long range ensemble model

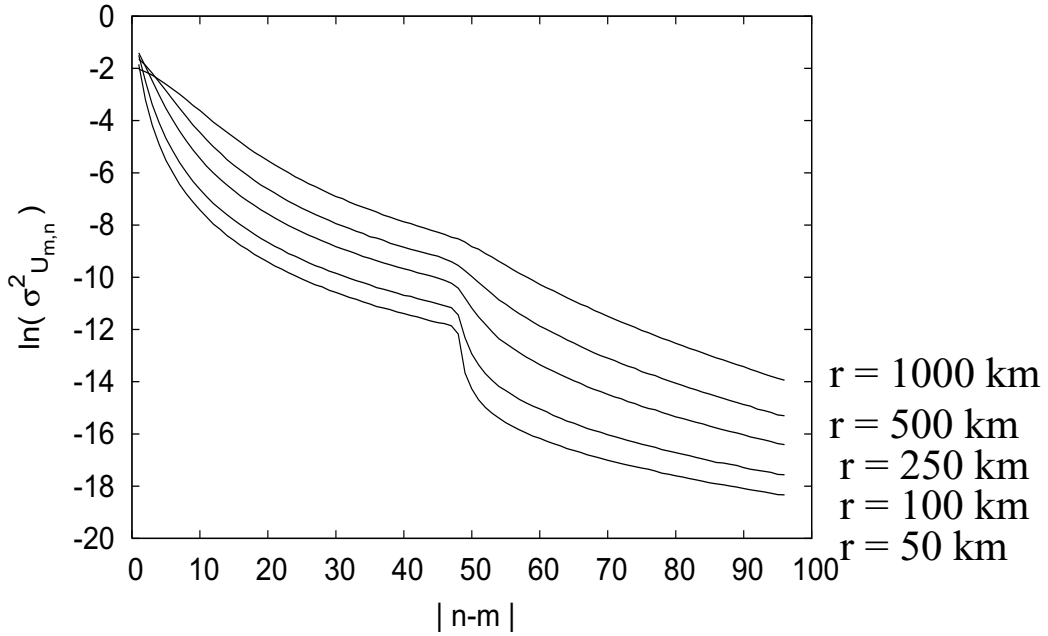

(b) Predicted variances of off-diagonals $U_{m,n}$ for $n = 0$ using long range ensemble model, where $\sigma^2_{U_{m,n}} = \sigma^2_{Re[U_{m,n}]} + \sigma^2_{Imag[U_{m,n}]}$

Figure 5.19: Predicted variances using long range ensemble model. The natural logarithm of the variance is plotted with (a) mode number n (b) difference in mode number $|n-m|$. (Solid line) Predicted variances are generated with values from $10,000$ realizations of the long range ensemble model for $r = 250, 500, 1000$ km.

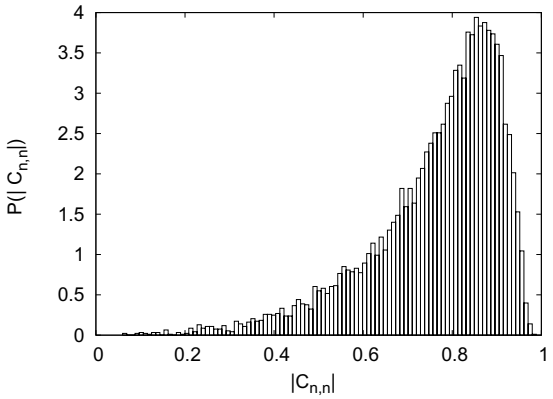

(a) Histogram of $|C_{n,n}|$ from long range ensemble model for $r = 100$ km

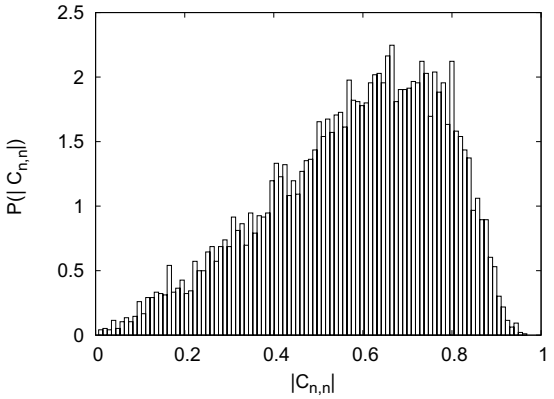

(b) Histogram of $|C_{n,n}|$ from long range ensemble model for $r = 250$ km

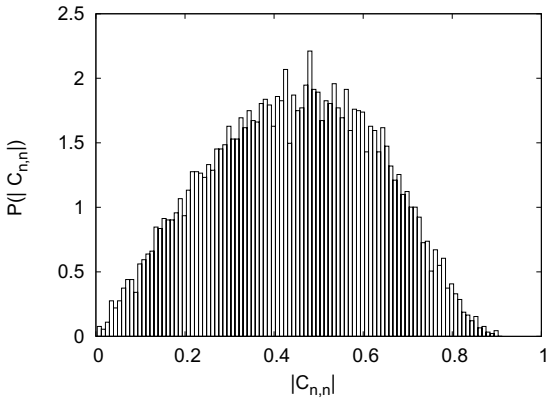

(c) Histogram of $|C_{n,n}|$ from long range ensemble model for $r = 500$ km

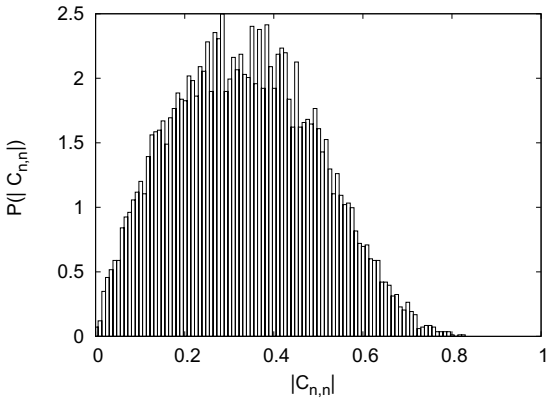

(d) Histogram of $|C_{n,n}|$ from long range ensemble model for $r = 1000$ km

Figure 5.20: Predicted histogram of the probability density function $P(\cdot)$ as a function of the magnitude of the diagonal elements $|C_{n,n}|$ for $n = 0$. The values are generated with $10,000$ realizations of the long range ensemble model.

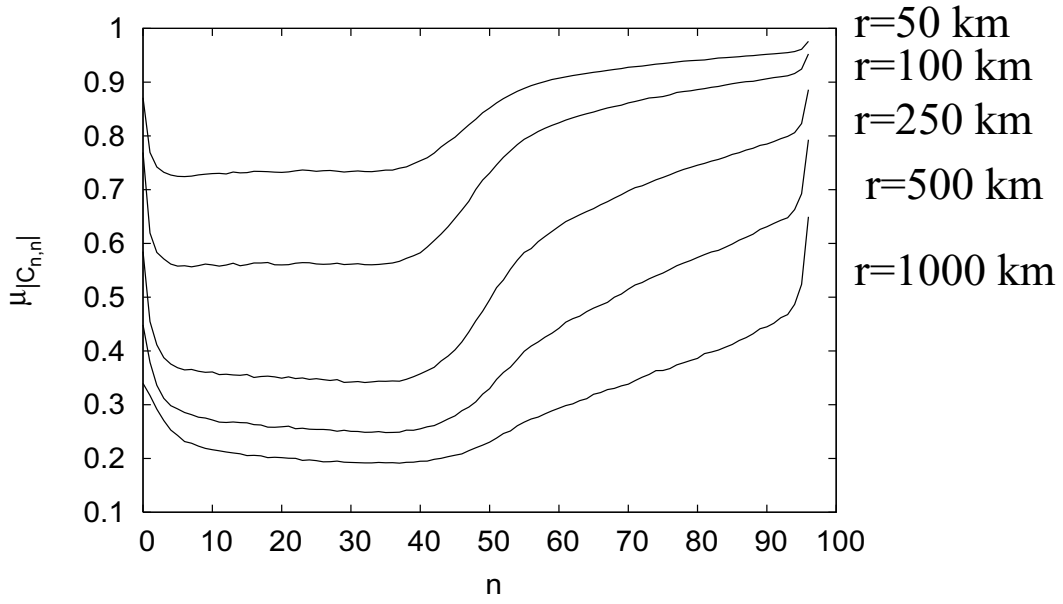

(a) Predicted mean diagonal magnitudes $|C_{n,n}|$ using long range ensemble model

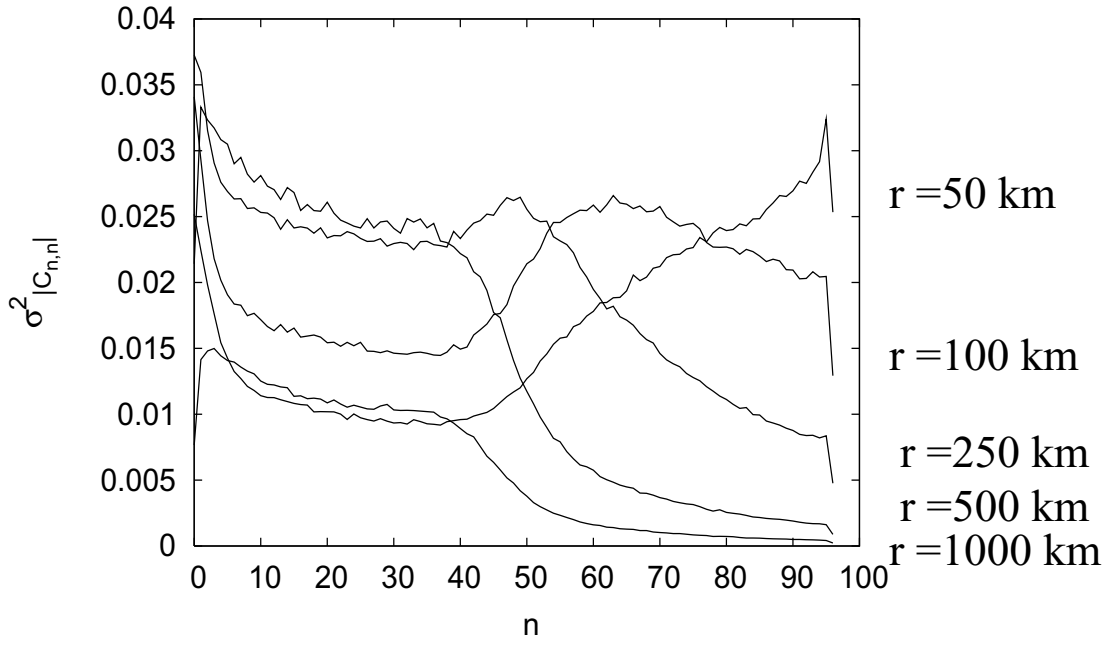

(b) Predicted variance of diagonal magnitudes $|C_{n,n}|$ using long range ensemble model

Figure 5.21: Predicted means diagonal magnitudes $|C_{n,n}|$ using long range ensemble model for $r = 250, 500, 1000$ km. The means are plotted with mode number n. Means are generated with values from $10,000$ realizations of the long range ensemble model.

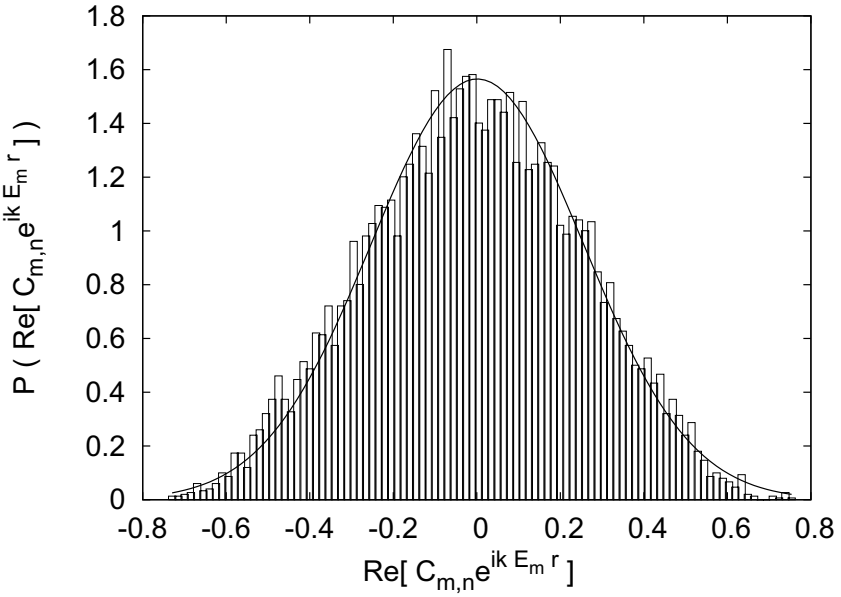

Figure 5.22: Histogram of off-diagonals $U_{m,n}$ for $n = 0$, $m = 1$ using long range ensemble model for $r = 1000$ km. Histograms of the probability density function $P(\cdot)$ are plotted with the value $(\cdot)$.Histograms are generated with values from $10,000$ realizations of the long range ensemble model for $r = 1000$ km. Overlaid on the lower histogram is a Gaussian using the mean and variance of the sample distribution.

5.3 Chapter Summary

In this chapter, a long range ensemble model has been constructed for the unitary propagation matrix by the multiplication of building blocks of random matrices. The building blocks model the unitary propagation matrices at 50 km. Several properties of the ensemble model are investigated and compared to the properties of the ensembles from the propagation. Already, there are some surprises.

First, the statistics of first order perturbation theory agree very well with some of the observed statistics from the propagation. First order perturbaton theory is used to predict the variances of the off-diagonal elements and diagonal phases. These agree with the variances obtained from the propagation to good agreement in the shape of the functional form, but

they are off by a multiplicative factor near 1.2 for the central wavenumber k_0, as seen in Fig. (5.7). First order perturbation theory is also used to predict a Gaussian distribution for the off-diagonal elements and the phases of the diagonal elements. This is also in good qualitative agreement with the observed distributions from the propagation. Though first order perturbation theory has an extremely short range of validity, it seems that the average properties of the propagation predicted by perturbation theory are valid out to much longer ranges.

Second, there is good qualitative agreement between the structure of the amplitudes and phases of sample matrices from sample propagated matrices and those generated by the ensemble model at the central wavenumber k_0. This is surprising because it was seen in Ch. (**??**) that the matrix elements from the propagation have strong correlations with neighboring matrix elements which are on the same band of the matrix. Yet these correlations are not captured by the ensemble model. s indicates that the correlations between matrix elements is not information that survives the propagation, as this information is not physically relevant.

The general conclusion of this chapter is that the ensemble model looks very promising as a quick method of generating the minimal information which survives the propagation to long ranges. Up to this point, no one in ocean acoustics has attempted to create an ensemble model for the acoustic wave propagation. The nearest statistical model has come from the theoretical work of Virovylansky et. al. [55, 38, 79, 80], who have created an statistical description of chaotics rays corresponding to the propagation. Using this model, they have investigated properties of modes and written the quantity $a_n(r, k)$ in Eq. (4.7) in terms of classical actions I of certain classical rays called 'mode rays'[38]. If semiclassical theory

utilizing classical ray information [26] could be used to long ranges, these results would indicate a deep connection between $C_{m,n}$'s and actions I.

The significance of the ensemble model in this chapter to researchers in the field could be great. The experiments are done in order to learn about the average properties of the ocean. Tomography is performed on the experimental timefronts in order to extract these mean properties. If the only information left in the propagation to long ranges is contained in a variance matrix and a phase matrix of the ensemble model, then it needs to be determined if the desired properties of the ocean are captured by this information. If the experiments cannot capture the desired properties, then they should be reevaluated. If the experiments can capture the desired properties, then the relationship between the parameters of the ensemble model and the desired ocean properties needs to be determined. It is likely that semiclassical theory [26] could be utilized in determining this relationship, since 50 km is a range where the classical rays are not fully chaotic yet. Once this relationship is identified, the ensemble model could be used to perform tomograophy more effectively to learn more about the ocean from the experiments.

Though this chapter has only given affirmation of the adequacy of the ensemble model in capturing the information stored in the unitary propagation matrices, the next chapter will provide more qualitative and quantitative information on the agreement of the timefronts generated by the ensemble model with that of the propagation.

Chapter 6

TIMEFRONT OBSERVABLES

In long range ocean acoustic experiments, the time series of acoustic pressures at the receivers are the primary observable which is gathered from the experiments. The collection of all time series at all receiver depths forms a structure in the time-depth plane, which constitutes the acoustic timefront.

The significant properties of the structure of the timefront of acoustic arrivals in time and depth are related to the fluctuations in time, depth and intensity of the arrivals. These properties can be described both qualitatively and quantitatively, where many qualitative descriptions have a corresponding quantitative description. The quantititive description of the timefronts is in terms of 'observables' - measurements which can be made on the structure of a single timefront or statistics which can be calculated from a set of measurements on the timefronts.

The properties of the acoustic timefront store information about the experiments and are thus functions of the parameters of the experiment (i.e. the central wavenumber and spread of

the source, the range of the receivers, and the parameters of the waveguide and internal wave sound speed fluctuations). As the properties are dependent on the parameters, a variation in an experimental parameter would result in a variation in an observable of the timefront structure. If the connection between the observables and the parameters of the experiment were known, this would provide a method for analysing experimentally measured observables to infer parameters of the ocean.

However, since the timefront of acoustic pressures is so important to the process of tomography, the properties of the timefronts will be the final test of the information contained in the ensemble model derived in Ch. (5). By comparing the set of timefronts generated by the ensemble model to the set of timefronts generated from the propagation through the perturbed model described in Ch. (3), it can be ascertained what properties of the timefronts the ensemble model is capturing properly. In determining which properties of the timefront should be compared, the structure of the acoustic timefronts is studied using 1) the insight from several theoretical tools (i.e. perturbation theory, semiclassical theory and mode theory) and 2) the qualitative variations in the acoustic timefront simulated from the acoustic model. Differences will be compared to results from the baseline of the unperturbed propagation to determine their significance.

The building block ensemble model contains only a minimal amount of information about the propagation to 50 km. For ranges which are multiples of 50 km, the long range ensemble model utilizes the building block model to 50 km and the independence of range segments of length 50 km. This model cannot be expected to capture all of the details of the timefronts, but the hope is that it captures the important average properties of the timefronts, which is all that

remains for propagation to long ranges. An average of the intensities in the timefront capture these average properties and have been used for experimental analysis [39, 41]. The average intensity timefront will be used dominantly for the final comparison of sets of timefronts in this thesis.

Quantitative comparisons in this chapter will make use of observables of the timefronts and average intensity timefronts. To characterize the branches of the timefronts, the observables of the spread of the arrivals with time [39], the wander of the mean location of the arrivals with time [39] and the time bias [39] will be calculated. To characterize the late arriving finale of the timefronts, the decay of the finale with depth and time will be compared.

6.1 Insight Into Origins of Timefront Structure

The basic structure of the acoustic timefront for the perturbed system originates from that of the unperturbed system. This structure consists of distinct branches which cross over each other. Insight into this basic structure can be obtained from Semiclassical theory utilizing classical rays. Due to the perturbative nature of the sound speed model, the unperturbed timefront will be utilized for a clear picture of the basic structure of the timefronts.

The origins of the variations in the acoustic timefront of the perturbed system arise predominantly from the properties of the variations in the sound speed from the internal wave perturbations (but are also influenced by the properties of the background sound speed model [81]). Variations in the sound speed result in a phase change between the acoustic wave traveling in different locations. As the waves interfere, both the frequency spread of the wave and it's size are broadened and the intensity varies. The timefronts are complicated and identifying a clear picture of how the properties of the internal waves effect the properties of the acoustic timefronts is difficult. A decomposition of the wave propagation into contributions from the acoustic modes is used to gain insight into the timefront construction.

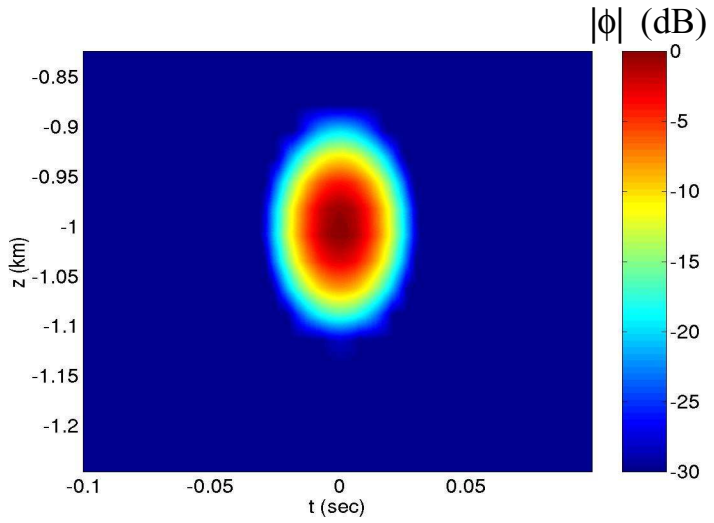

Figure 6.1: Magnitude of the complex acoustic timefront $|\phi|$ of acoustic arrivals at a fixed range of $r = 0$ km is plotted in decibels as a contour plot in time, t, and final depth, z. The decibel value is $3log_2\left(\frac{|\phi|}{max[|\phi|]}\right)$, where $max[|\phi|]$ is the maximum amplitude in the timefront construction.

6.1.1 Initial Timefront at $r = 0$

The complex acoustic timefront at a set of receivers located in depth z, at a range r and received in a time t is given by Eq. (3.20). Initially at $r = 0$, the initial wavefield is $\Psi_0(z, r = 0; k)$ as in Eq. (3.18) so that the initial timefront is

$$\begin{aligned}\Phi(z, r = 0, t) &= \frac{1}{\sqrt{2\pi\sigma_k^2 r}}\left(\frac{1}{2\pi\sigma_z^2}\right)^{\frac{1}{4}} \exp\left(-\frac{(z - z_0)^2}{4\sigma_z^2}\right)\int_{-\infty}^{+\infty} e^{ik(r-c_0t)} \exp\left[-\frac{(k - k_0)^2}{2\sigma_k^2}\right]dk \\ &= \frac{1}{\sqrt{r}}\left(\frac{1}{2\pi\sigma_z^2}\right)^{\frac{1}{4}} \exp\left(-\frac{(z - z_0)^2}{4\sigma_z^2}\right)\exp\left[-\frac{c_0^2k_0^2(t - \frac{r}{c_0})^2}{2} + ic_0k_0\left(t - \frac{r}{c_0}\right)\right],\end{aligned}$$

where the fourier transform integration over wavenumber has been performed. The initial timefront amplitude is a series of Gaussian pulses in depth each centered on $t = 0$ with a variance of $\sigma_t^2 = \frac{1}{c_0^2\sigma_k^2}$. The initial timefront is illustrated as a contour plot in Fig. (6.1).

6.1.2 Semiclassical Theory

Semiclassical theory can be used to connect the information about the classical rays to the properties of the timefront. As derived in Appendix. C, semiclassical theory expresses the wave field $\Psi(z, r; k)$ in the timefront construction in Eq. (3.17) as $\Psi(z, r; k) = \sum_j A_j(k) \exp(iS_j k)$, where $S_j = S_j(z, z_0; r)$ is the action of the jth ray which traverses from initial depth z_0 to a final depth z at a range r and $A_j(k)$ is the semiclassical amplitude.

As derived in Eq. (C.15), the semiclassical amplitude is a function of wavenumber (despite this dependence not being noted in either theoretical paper in Ref. ([12]) or ([22])) and this complicates any analytical integration of the semiclassical timefront. However, if the semiclassical amplitude is approximated $A_j(k) \approx A_j(k_0)$ with the central wavenumber k_0, then the integration can be done analytically to give

$$\phi(z, r; t) = \frac{1}{\sqrt{r}} \sum_j A_j(z, z_0; r, k_0) \exp\left(-\frac{\sigma_k^2 c_0^2}{2} (T_j - t)^2 + ikc_0(T_j - t) \right) , \quad (6.1)$$

where T_j denotes the travel time of the jth ray traveling from $z = z_0$ to a final depth of z. This approximate form also holds for the latest direct arrival in the unperturbed timefront at $z = z_0$, $t = \frac{r}{c_0}$.

The approximation to the timefront in Eq. (6.1) predicts the timefront amplitude to be a superposition of ray arrivals, which are Gaussian in shape with a variance in amplitude of $\sigma_t^2 = \frac{1}{c_0^2 \sigma_k^2}$ and which carry a phase. However, as seen in Sec. (6.1.6) and (6.2.3), this approximation does not get the dependence of the variance correct. However, this approximation does get the location of the peak arrival at $t = T_j$, the ray arrival time correct. The classical

ray propagation is described in Appendix C.1.

The timefront is composed of linear segments, termed 'branches', which crisscross in an 'accordion' pattern. The branch pattern predicted by the classical ray arrivals in the lower plot in Fig. (6.2) is identical to the branching structure of the wave timefront in the upper plot in Fig. (6.2). The branches are distinct throughout most of the timefront for the unperturbed case, with the only exception being for the latest arrivals where the branches are so close together that they interfere. This branch structure can also be identified in the early arrivals of the perturbed timefronts, as shown in Figs. (6.4)-(6.6).

The timefront exhibits an interference pattern where branches cross and where the width of neighboring branches overlap. This is due to the interference between acoustic arrivals with different phases. The semiclassical timefront predicts this interference as the interference of two ray arrivals at that depth and time which have difference phases.

The shape of the accordion in Fig. (6.2) opens to the left of $t = \frac{r}{c_0}$ for the range depicted. This is not always the case. The ray that traverses from $(z_0, r = 0)$ to $(z_0, r = 0)$ in a straight line path has a sound speed c_0, an action $S_j(z_0, z_0; r) = 0$ and an arrival time $T_j(z, z_0; r) = \frac{r}{c_0}$. For all other rays, the path is larger than r and the average sound speed is larger than c_0. For some short ranges, the timefront structure opens to the left of $\frac{r}{c_0}$ and for other short ranges, the timefront structure opens to the right of $\frac{r}{c_0}$. However, for longer ranges, the average speed outweighs the path length so that the timefront structure always opens to the left of $\frac{r}{c_0}$ for all ranges larger than R. Note that locally near $t = \frac{r}{c_0}$, the timefront takes on a parabolic shape which will open to the left or right depending on the range (as discussed for the Harmonic osccillator potential in Sec. (6.1.6)), but the rest of the timefront will open to the left for the

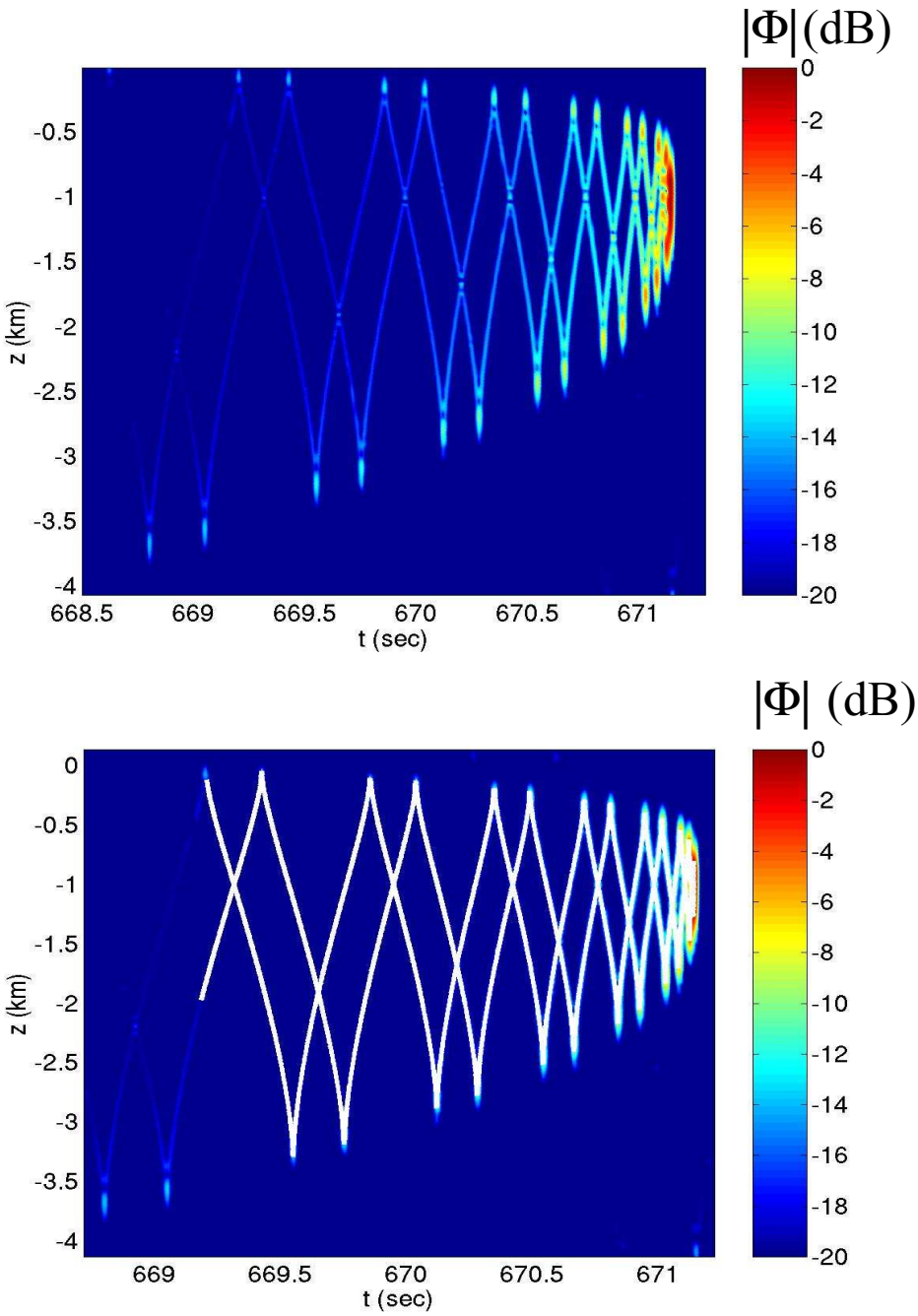

Figure 6.2: Timefront of unperturbed acoustic arrivals for the range $r = 1000$ km. (Upper) A timefront is generated from Eq. (3.20) by propagation through only the Munk potential in Eq. (3.11) to a range $r = 1000$ km. The magnitude of the timefront, $|\phi|$, is plotted with time, t, and final depth, z, of the receiver. (Lower) The classical timefront is overlaid on the wave timefront. The classical timefront is generated from the propagation of classical rays, with an initial ray angle between $-12^o < \theta_0 < 12^o$, through the Munk potential to a range of $r = 1000$ km to a final depth z with a time t from Eq. (C.6).

larger ranges.

The branches of the timefront can be assigned a single, unique branch number since all of the rays making up each branch have some shared topological properties. First, each ray on a branch has encountered the same number of turning points in their oscillation in depth and range. Second, each ray on a branch has the same sign for the initial momenta of the ray (initially propagating upward or downward). These observations can be used to assign a branch number to each branch. The branch number is equal to the number of caustics encountered by the classical ray during the propagation. The sign of the branch number indicates if the ray was initially propagating in the upward (+) or downward (-) direction. For example, the rays in Fig. (6.3) have between 1 - 3 turning points in their propagation to the final range and the corresponding timefront for that range has 5 branches, corresponding to branch numbers -1,-2,-3,+3,+2.

The boundaries of the timefront are formed from connecting the caustics (where classical rays are at a turning point in their motion) at the end of each branch. The turning points have higher intensities than any location along each branch. The semiclassical theory in Eq. (C.16) predicts that the amplitudes A_j in Eq. (C.15) diverge to infinity at the turning points where $\frac{dz}{dp} = 0$, or where $m_{21} = 0$. Though, this infinity indicates a failure of semiclassical theory, a correction can be made using an Airy uniformization [82] which predicts that near the turning points, the timefront is locally an Airy function in depth. The highest amplitudes still occur near the turning points at the end of each branch (and also at the latest direct arrival at $z = z_0$, $t = \frac{r}{c_0}$), as seen in the ends of the branches in Figs. (6.4)-(6.6).

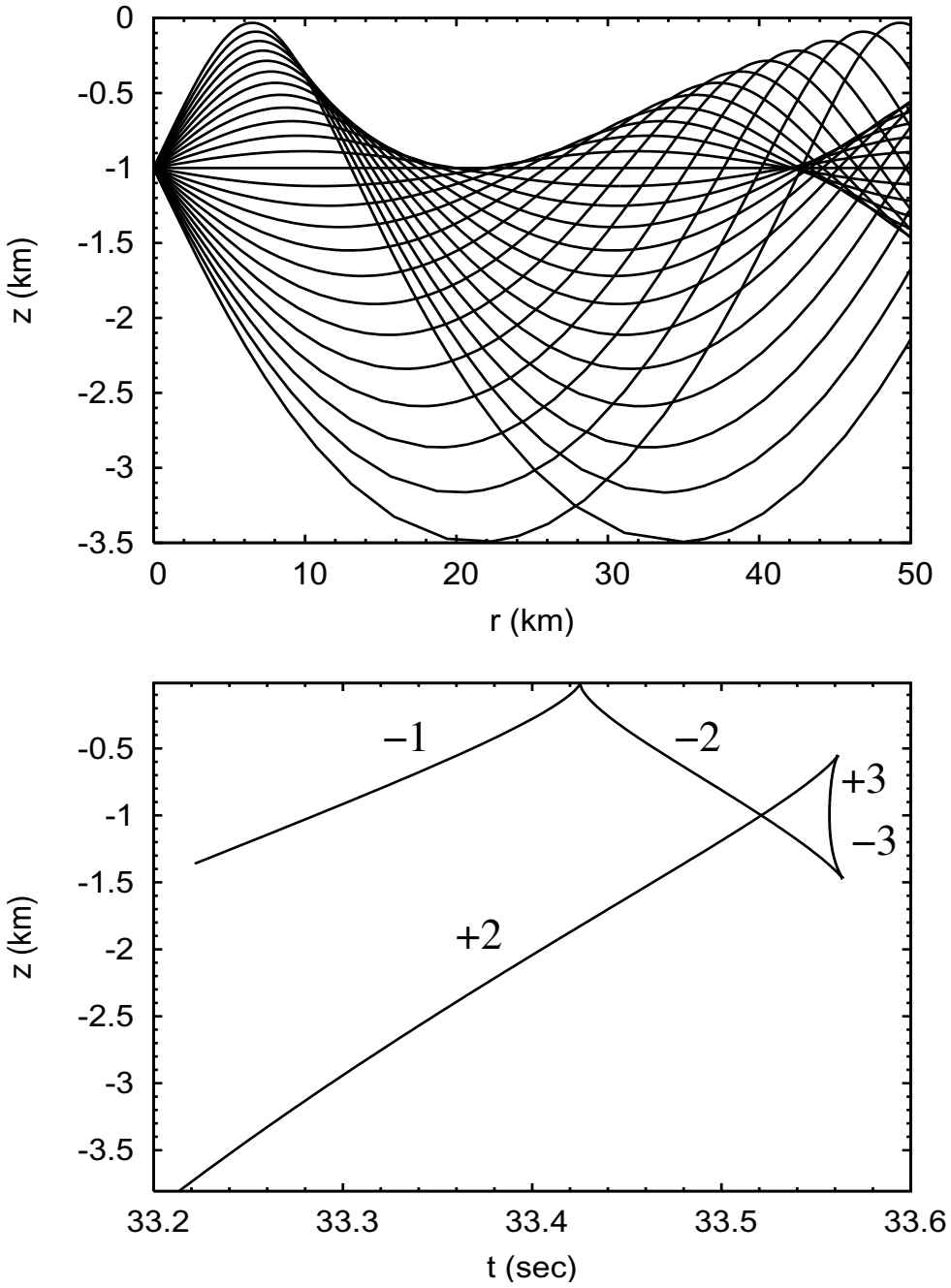

Figure 6.3: Classical rays with initial ray angle of $-12^o < \theta_0 < 12^o$ in increments of 1^o are propagated through the potential consisting of just the Munk potential in Eq. (3.11) to a range of $r = 50$ km. (Upper) Location of the classical ray as a function of depth, z, and range, r. (Lower) Timefront $|\phi|^2$ for classical ray arrivals at a depth, z, and time, t. Each branch of the timefront structure is labeled with a branch number which has a sign corresponding to the initial direction of the ray and an integer amplitude corresponding to the number of turning points encountered in the propagation of the ray.

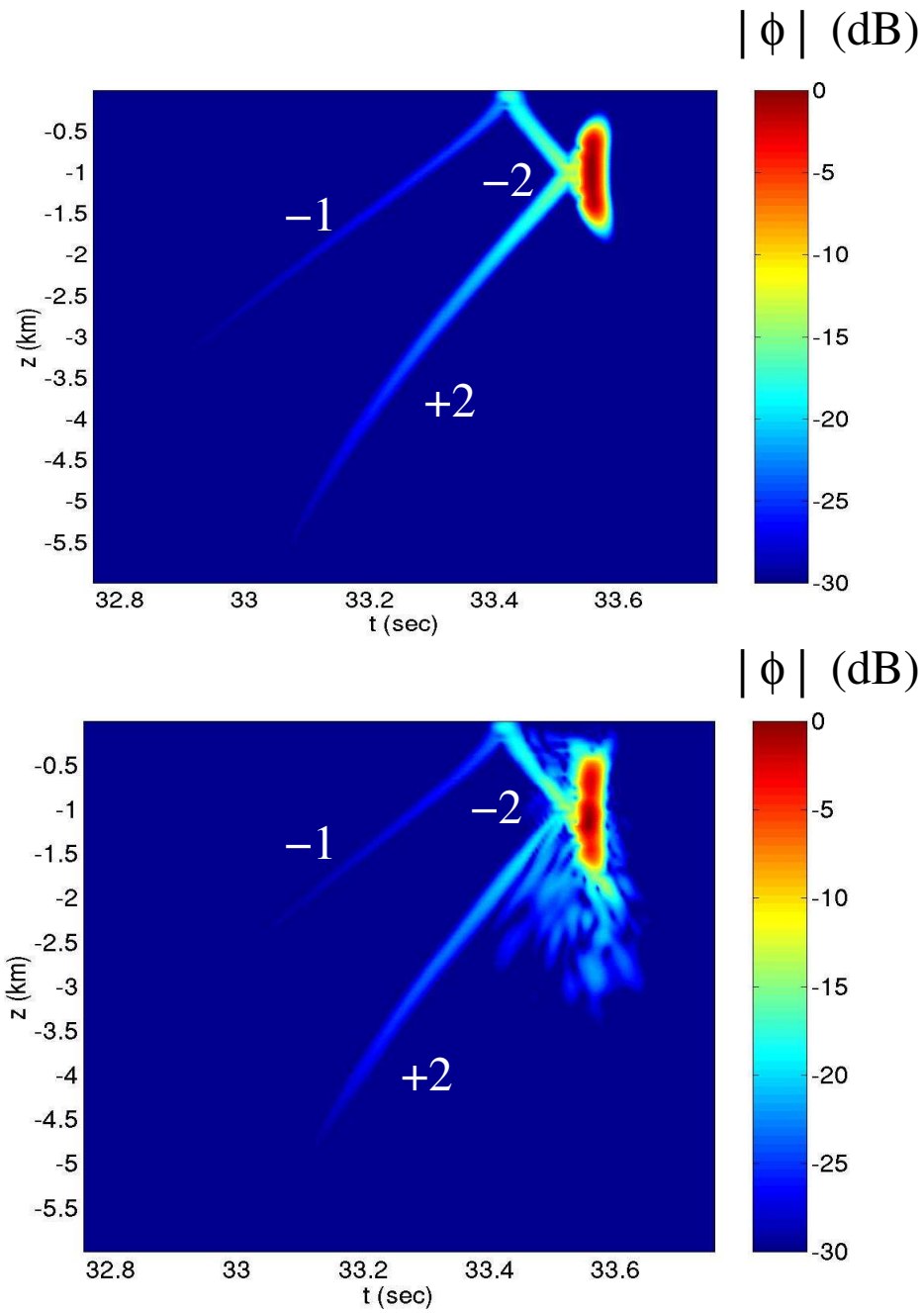

Figure 6.4: Branch numbers are identified for some of the identifiable branches of the time-front of arrivals to 50 km. The magnitude of the timefront $|\phi|$ is plotted as a contour plot with depth z and time t for propagation to 50 km in just (Upper) the Munk potential from Eq. (3.11) and (Lower) in the full potential, with a background from Eq. (3.11) and internal wave fluctuations from Eq. (3.12). Those magnitudes less than -30 dB have been set to -30 dB for the purposes of plotting.

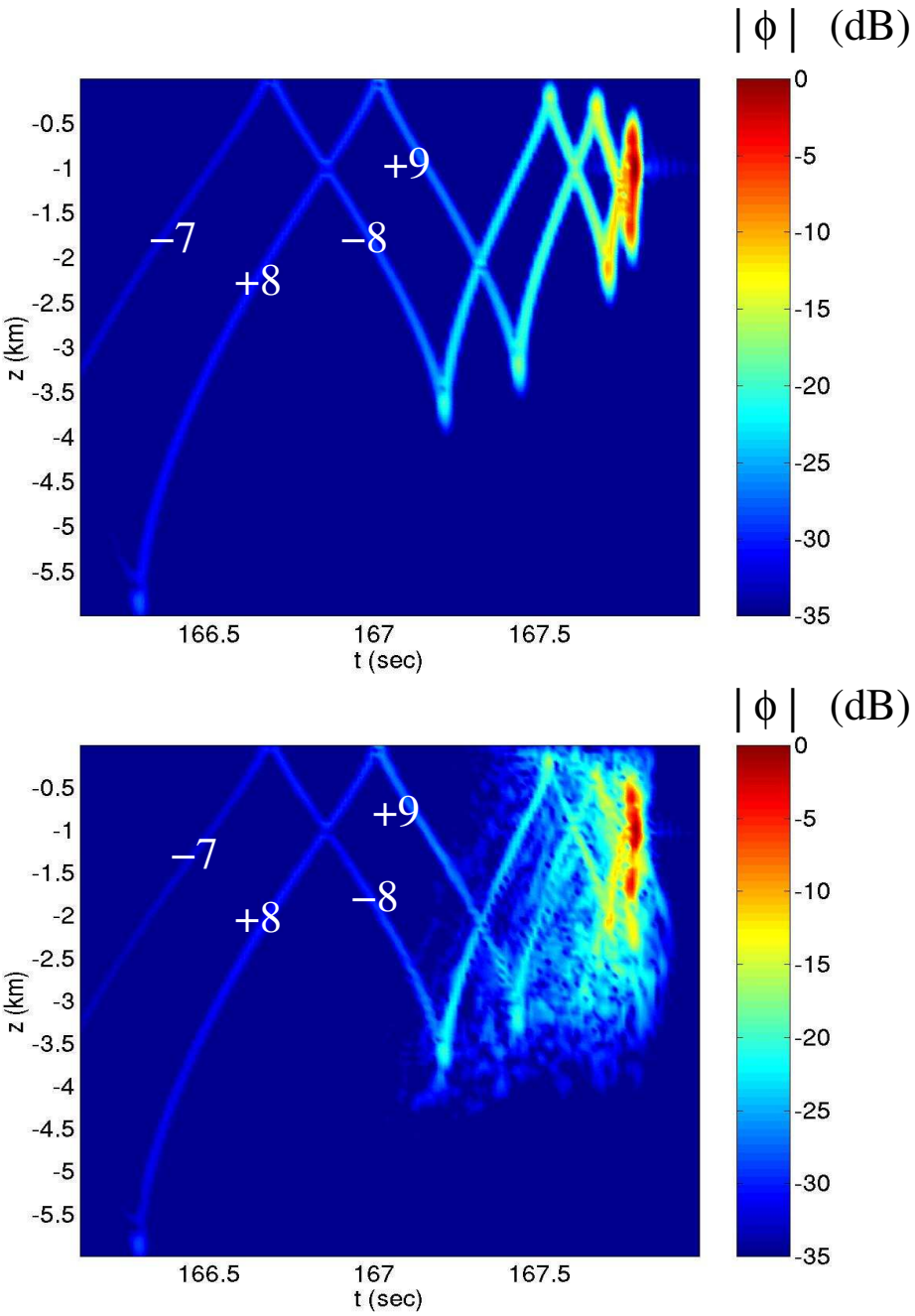

Figure 6.5: Branch numbers are identified for some of the identifiable branches of the timefront of arrivals to 250 km. The magnitude of the timefront $|\phi|$ is plotted as a contour plot with depth z and time t for propagation to 50 km in just (Upper) the Munk potential from Eq. (3.11) and (Lower) in the full potential, with a background from Eq. (3.11) and internal wave fluctuations from Eq. (3.12). Those magnitudes less than -30 dB have been set to -30 dB for the purposes of plotting.

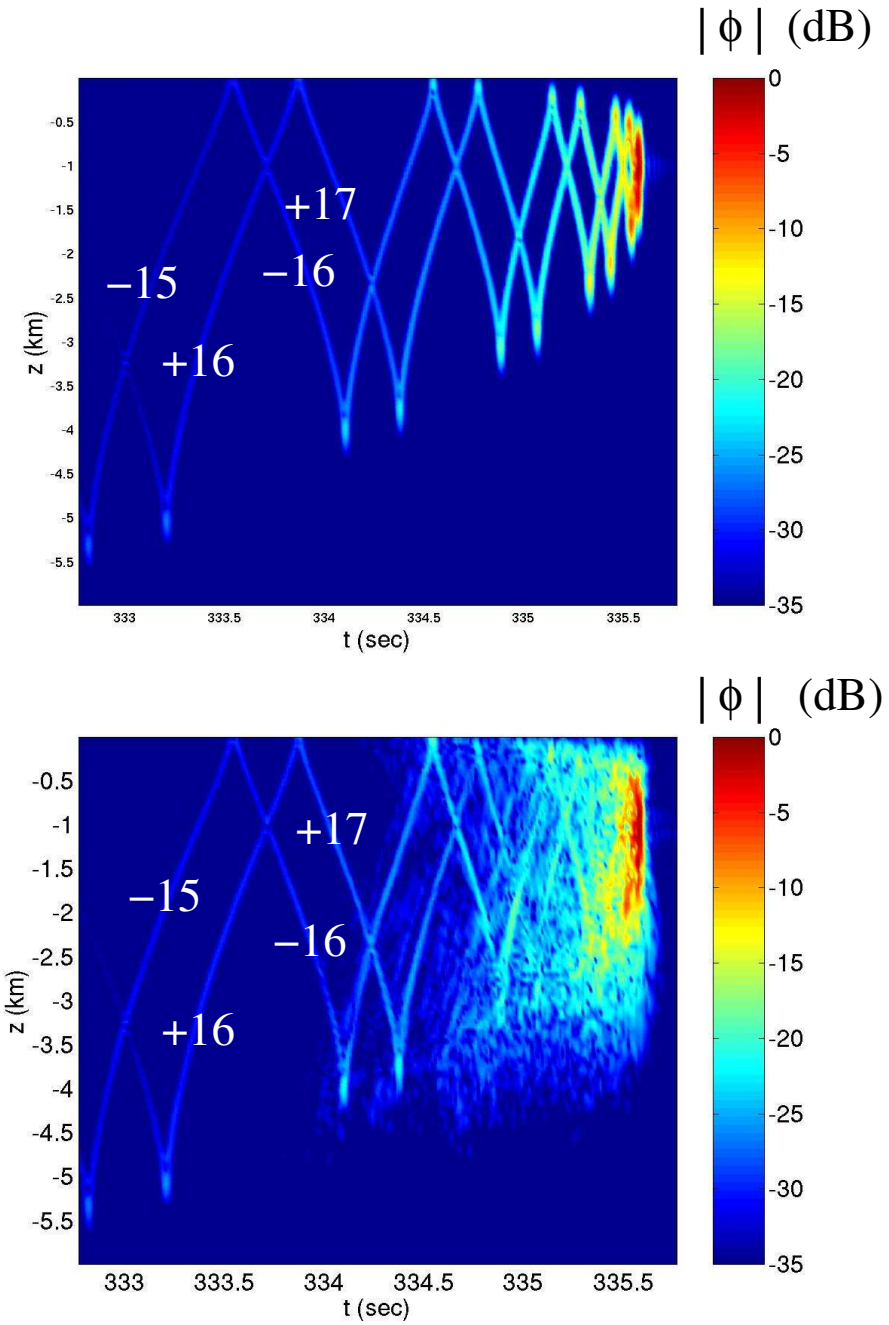

Figure 6.6: Branch numbers are identified for some of the identifiable branches of the timefront of arrivals to 500 km. The magnitude of the timefront $|\phi|$ is plotted as a contour plot with depth z and time t for propagation to 50 km in just (Upper) the Munk potential from Eq. (3.11) and (Lower) in the full potential, with a background from Eq. (3.11) and internal wave fluctuations from Eq. (3.12). Those magnitudes less than -30 dB have been set to -30 dB for the purposes of plotting.

6.1.3 Unperturbed Timefront

The size of the perturbation in the sound speed model from internal waves is small. Therefore, it is not a surprise that the basic structure of the perturbed timefronts is the structure of the unperturbed timefronts, as seen in Figs. (6.4)-(6.6). In looking at a trace of the timefronts at a single depth as in Fig. (6.7), it is seen that the branches are still apparent in the perturbed timefronts and these align very closely with the unperturbed branch arrivals. Additionally, the perturbed timefronts have intensity fluctuations about these branch arrivals, there is some shift in the mean arrival of the pulse arrival in the perturbed timefront arrivals with respect to the unperturbed arrivals, i.e. a non-zero time bias, and the width of the arrivals may be slightly larger, i.e. a non-zero pulse spread.

Due to the different intensity scales along the timefront, a logarithm plot of the traces of the timefront at a fixed depth reveal some additional features of the timefront, as shown in Figs. (6.8)-(6.9). From these figures of perturbed timefronts, there seem to be two dominant structures in the formation of the timefronts. First, the perturbed timefront contains arrivals that very closely match the location of the unperturbed timefront. Second, there is a fluctuation front with a characteristic shape which peaks near $z = z_0$, $t = \frac{r}{c_0}$ and decays in both depth and range. The structure of the fluctuation front at different depths is very similar: the fluctuations peak near $t = \frac{r}{c_0}$, the fluctuations decay quickly for $t > \frac{r}{c_0}$ and decay slowly for $t > \frac{r}{c_0}$.

From these results, this fluctuation front seems to be an effect of the internal wave scattering. However, the presence of this fluctuation front has not been seen before. Additionally,

the existence of this front is not consistent with previous work [12, 22], which has suggested that the multiple scattering from internal waves works in tandem with the structure of the unperturbed timefront so that contributions to the early branch arrivals are only smeared out in a neighborhood of the branches. In contrast, the continuous fluctuation front suggests that the fluctuations due to internal waves are continuous throughout the entire timefront, but diminish in depth from the sound axis and from time from the latest arrival of $t = \frac{r}{c_0}$. Therefore, without some theory to explain the occurrence of this fluctuation front, the author is skeptical about its origin.

The presence of this fluctuation front does explain the smearing of the arrivals seen previously in the late arrival finale section of the timefronts both experimentally and in simulations. Additionally, this front explains why there is a gradual transition in the perturbed timefronts between the clearly identifiable early timefront branches and the smeared together arrivals of the late arrival region of the timefront. Only future work can clarify the origins of this front. The presence of this front will again be noted in average intensity timefronts in Sec. (6.3.1) and in ensemble model predictions in Sec. (6.3.2).

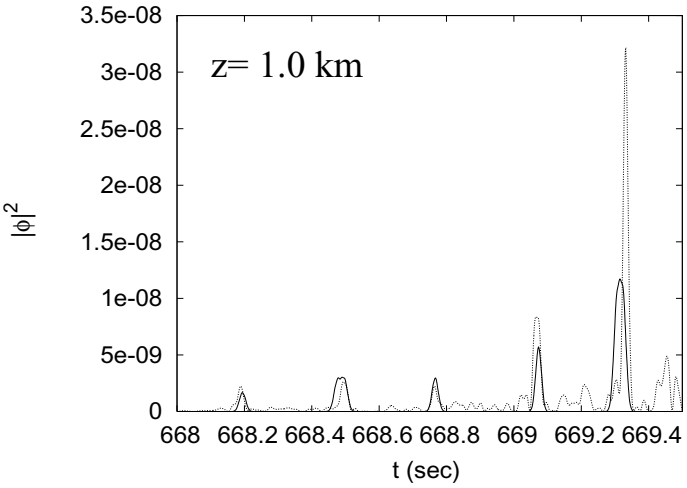

(a) Time interval from timefront trace for $z = 1.0$ km

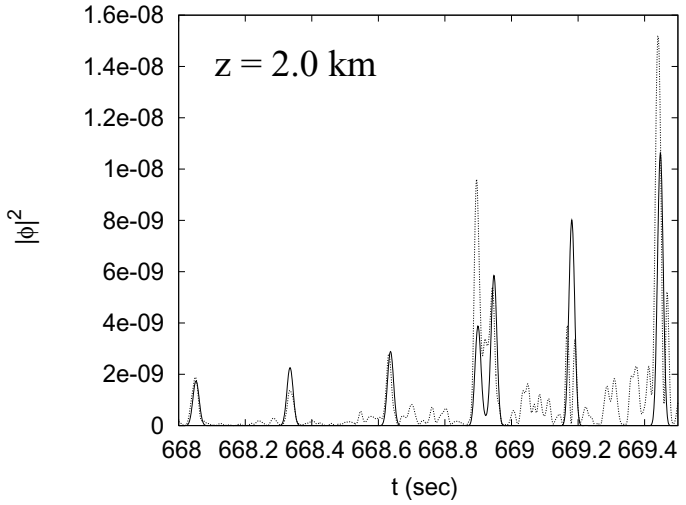

(b) Time interval from timefront trace for $z = 2.0$ km

Figure 6.7: The trace of timefront intensity $|\phi|^2$ at two depths is plotted as a time series in time t for the propagation range 1000 km. The solid line is the trace for the unperturbed timefront and the dotted line is a single realization of a perturbed timefront. The upper plot shows the trace for $z \approx 1$ km and the lower plot shows the trace for $z \approx 2$ km.

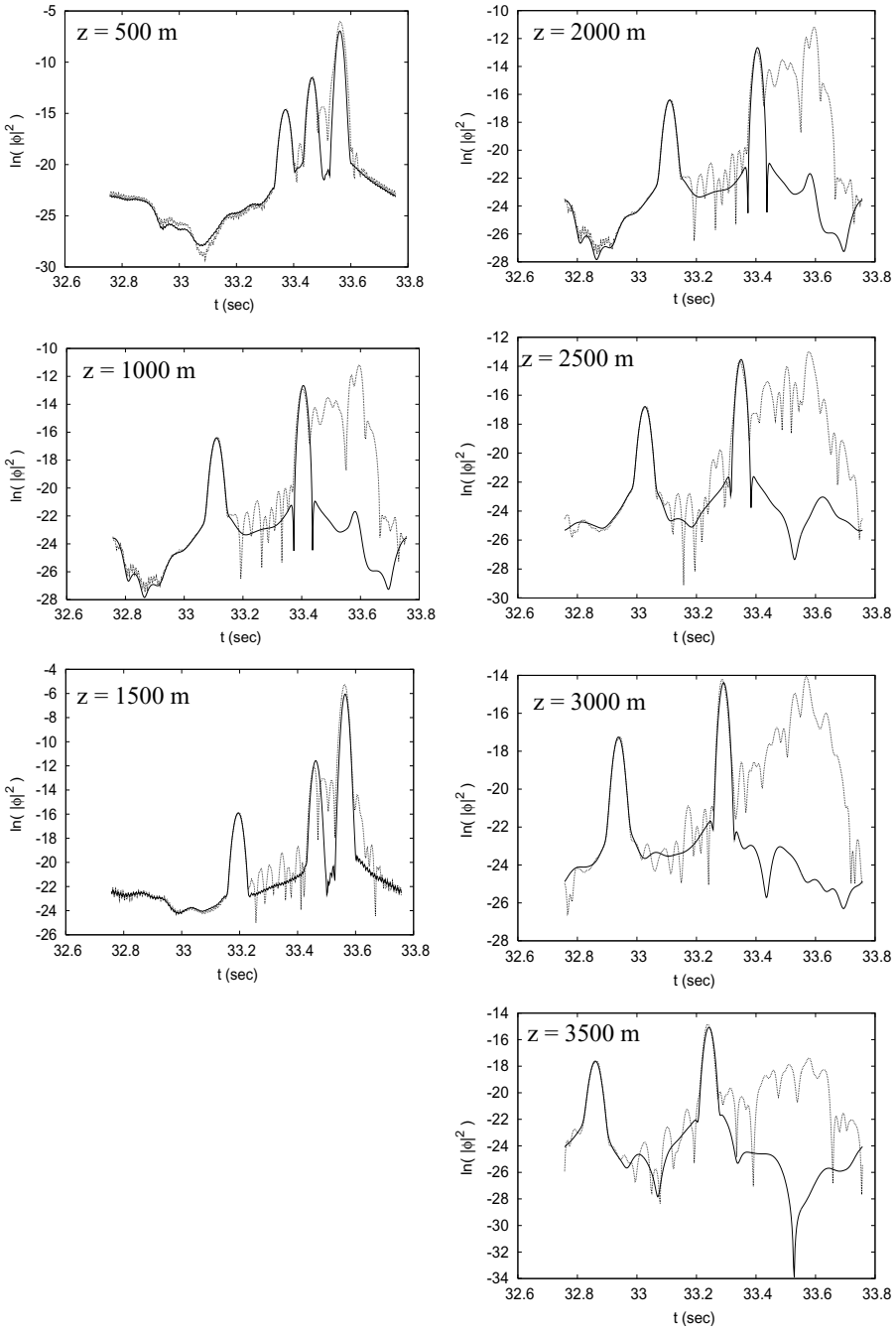

Figure 6.8: The traces at each depth z are plotted as a time series in time t for the propagation range 50 km. The solid line is the trace for the unperturbed timefront and the dotted line is a single realization of a perturbed timefront.

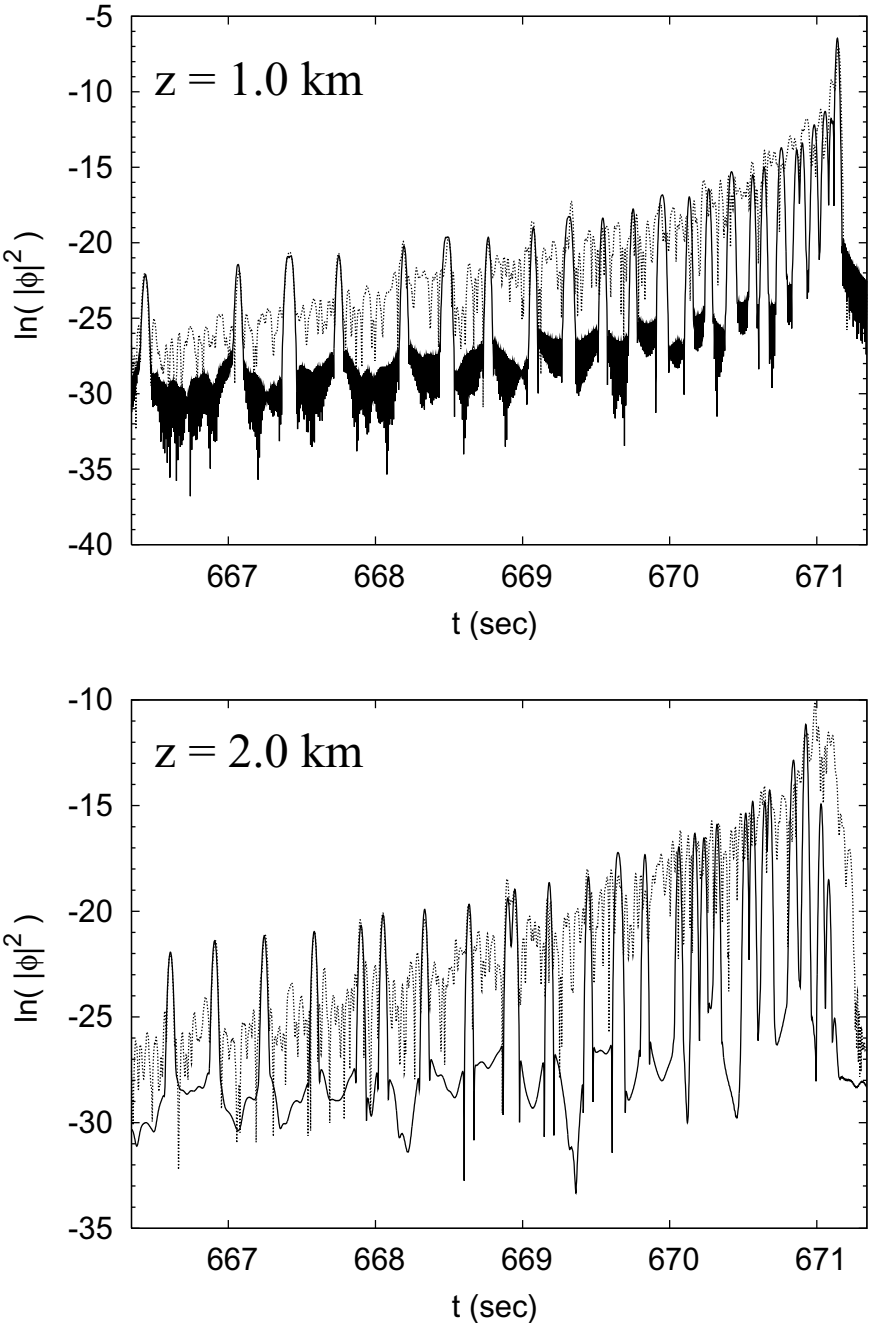

Figure 6.9: The logarithm of the trace of timefront intensity $\ln\left(|\phi|^2\right)$ at two depths is plotted as a time series in time t for the propagation range 1000 km. The solid line is the trace for the unperturbed timefront and the dotted line is a single realization of a perturbed timefront. The upper plot shows the trace for $z \approx 1$ km and the lower plot shows the trace for $z \approx 2$ km.

6.1.4 Sample Perturbed Timefronts

The fluctuations in the ensemble of sound speed fields generate different perturbed timefronts from the propagation. By exhibiting several members of the ensemble of perturbed timefronts, some of the important observables which characterize the ensemble of timefronts are evident.

The timefronts resulting from propagation through sound speed fields with several different seeds to the internal wave fields are shown in Fig. (6.10) - (6.14). For $r = 50$ km, the timefront in Fig. (6.10) is characterized equally by the presence of the clear branches and the smearing of the timefront about the shape of the unperturbed timefront from the upper figure in Fig. (6.10). For $r = 250 - 1000$ km, the timefronts in Fig. (6.11)-(6.13) still show clear branching structure in additional to a large region of smeared finale. For $r = 3000$ km, the timefront in Fig. (6.14) is mainly characterized by the spread in time and depth of the smeared, random region of the finale. As range increases, the branches of the timefront become less clear with destructive interference of arrivals along the branches creating nulls in the branch pressure amplitudes. This interference causes the branch arrivals later in time to become part of the finale region.

In all of these examples, the timefronts are different in detail from seed to seed, but structurally they look very similar. The intensity distribution along the branches and in the finale of the timefronts in all of these sample figures are very similar. The size of the branches undergo very similar changes in size along the branch and nulls in certain locations along other branches. The decay of the intensity with depth in the finale region and with time

from the peak in the finale are also very similar with the different realizations for each range. Since the length of the timefront increases with range, it almost looks as if the finale occupies the same rough proportion of the timefront at each range. Additionally, from Figs. (6.10)-(6.14), it is apparent that with increasing range, there is energy fill in. Energy fill-in has not been discussed in this thesis yet, but is another important observable utilized in experimental analysis of timefronts [40, 41]. Energy fill in refers to the filling in of the entire acoustic timefront due to the presence of arrivals in the shadow zone - the region of the timefront where there are no unperturbed ray arrivals.

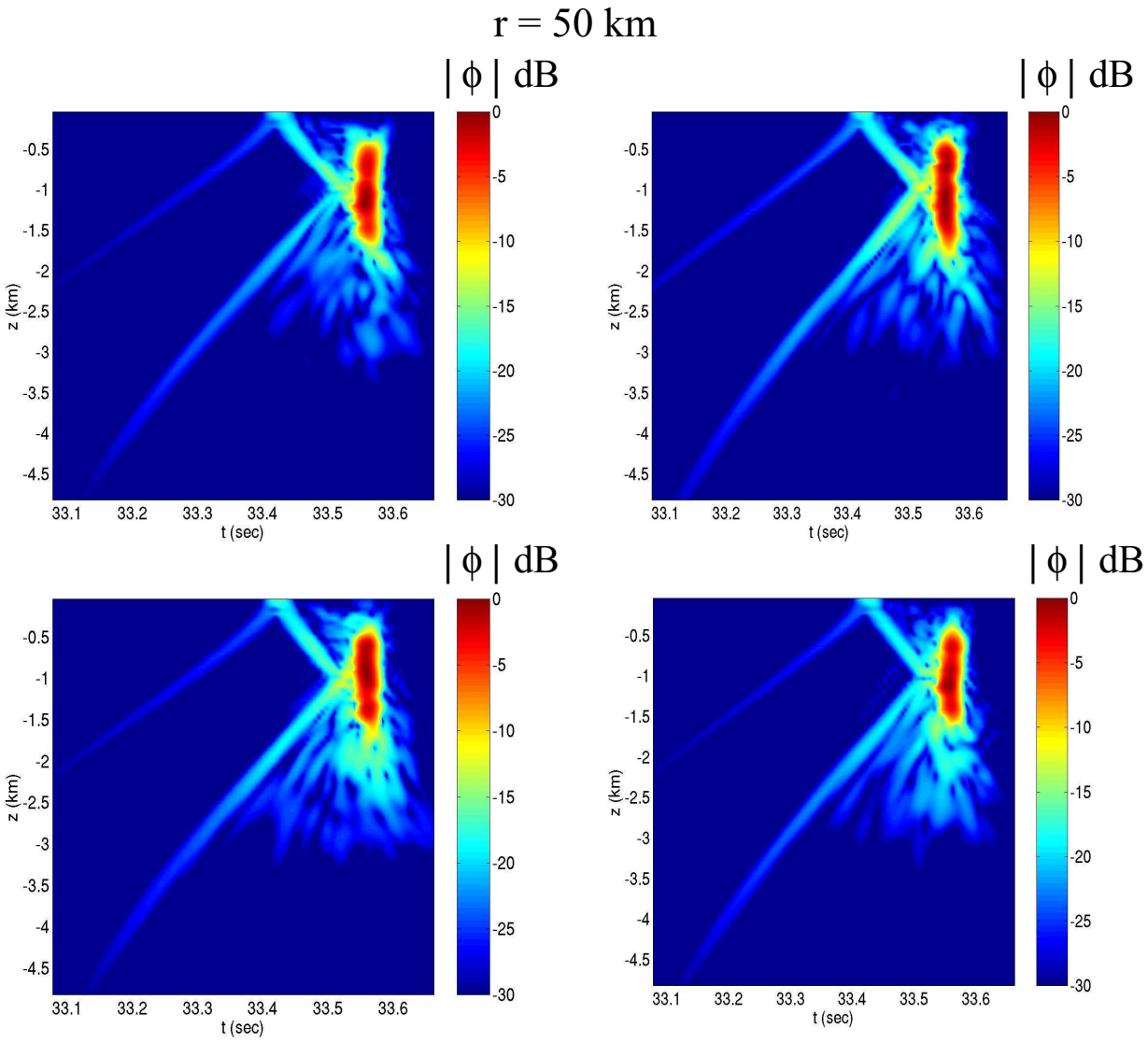

Figure 6.10: Several timefronts for different internal wave seeds are plotted. The magnitude of the timefront $|\phi|$ is plotted as a contour plot with depth z and time t for propagation to 50 km. Propagation is in the full potential, with a background from Eq. (3.11) and internal wave fluctuations from Eq. (3.12). The noise level below 30 dB has been set to 30 dB on the plot.

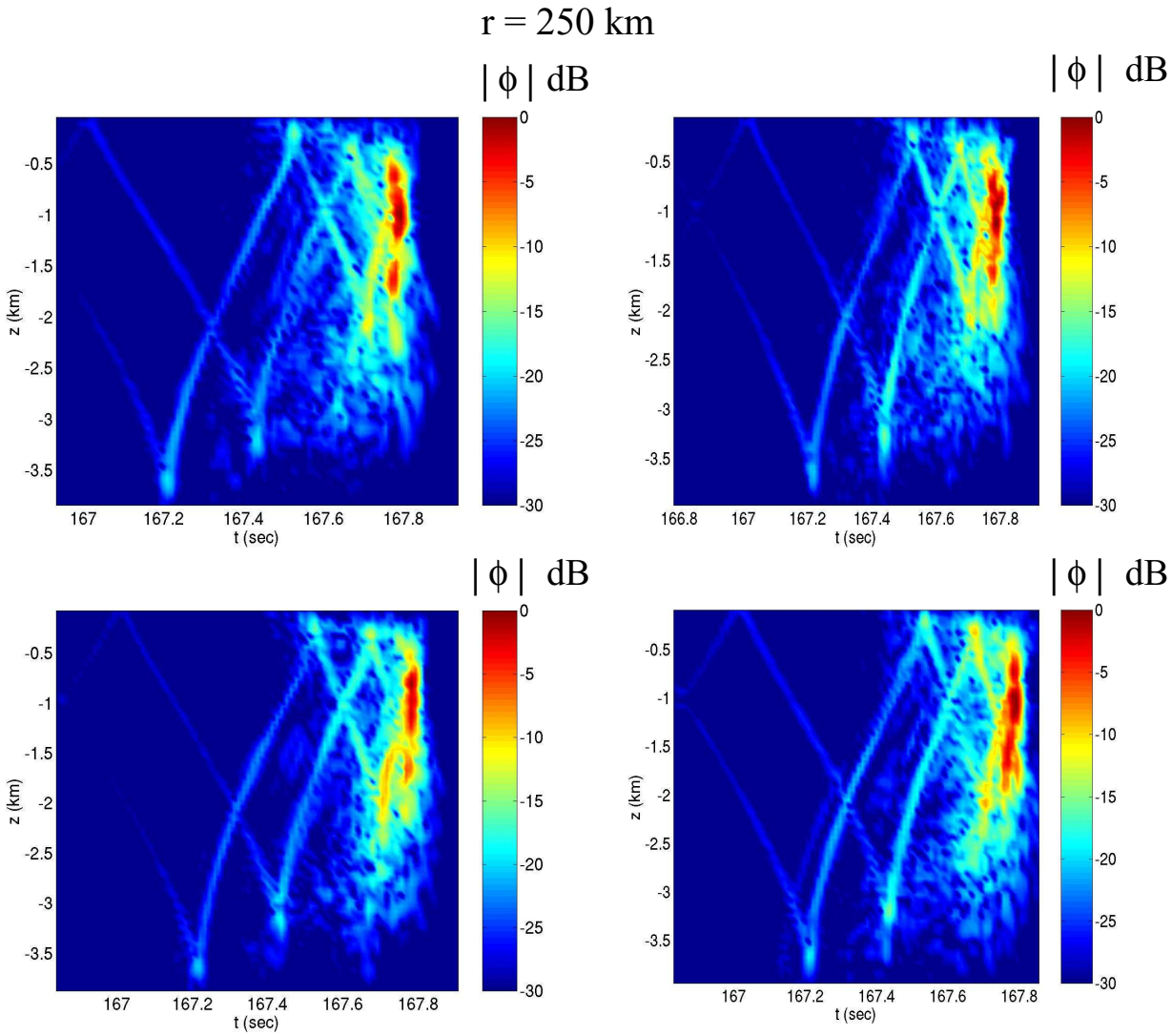

Figure 6.11: Several timefronts for different internal wave seeds are plotted. The magnitude of the timefront $|\phi|$ is plotted as a contour plot with depth z and Propagation is in the full potential, with a background from Eq. (3.11) and internal wave fluctuations from Eq. (3.12). The noise level below 30 dB has been set to 30 dB on the plot.

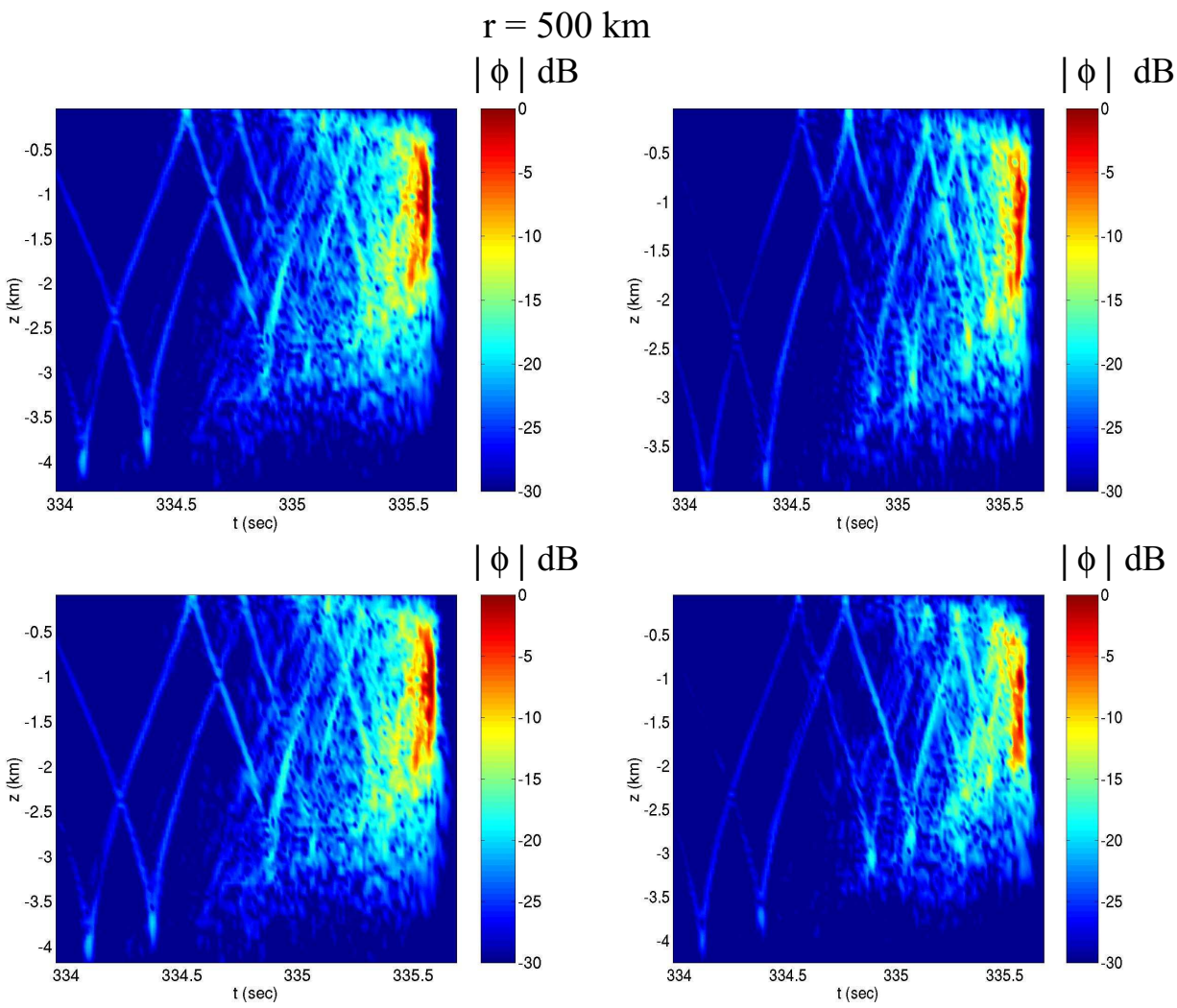

Figure 6.12: Several timefronts for different internal wave seeds are plotted. The magnitude of the timefront $|\phi|$ is plotted as a contour plot with depth z and time t for propagation to 500 km. Propagation is in the full potential, with a background from Eq. (3.11) and internal wave fluctuations from Eq. (3.12). The noise level below 30 dB has been set to 30 dB on the plot.

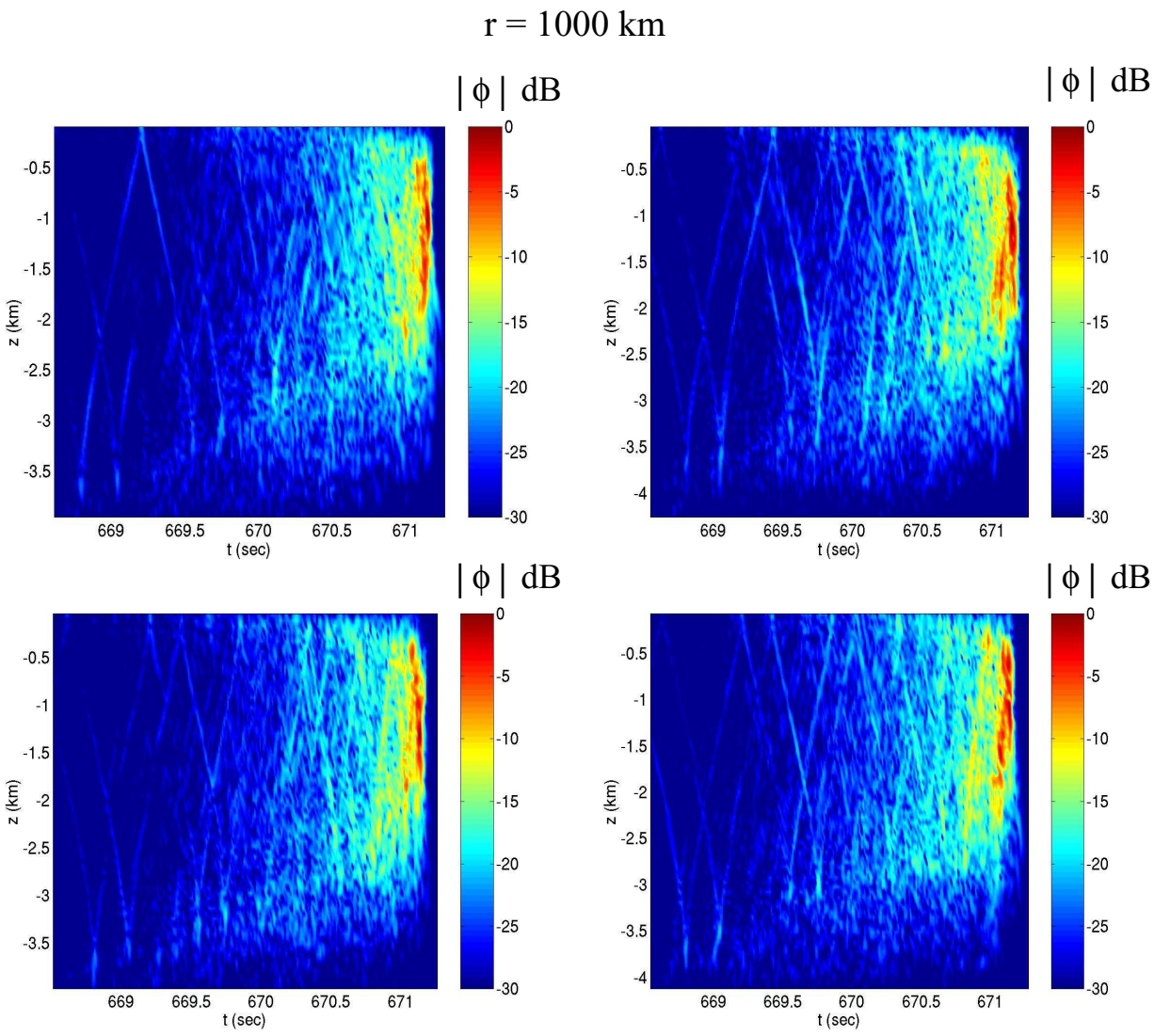

Figure 6.13: Several timefronts for different internal wave seeds are plotted. The magnitude of the timefront $|\phi|$ is plotted as a contour plot with depth z and time t for propagation to 1000 km. Propagation is in the full potential, with a background from Eq. (3.11) and internal wave fluctuations from Eq. (3.12). The noise level below 30 dB has been set to 30 dB on the plot.

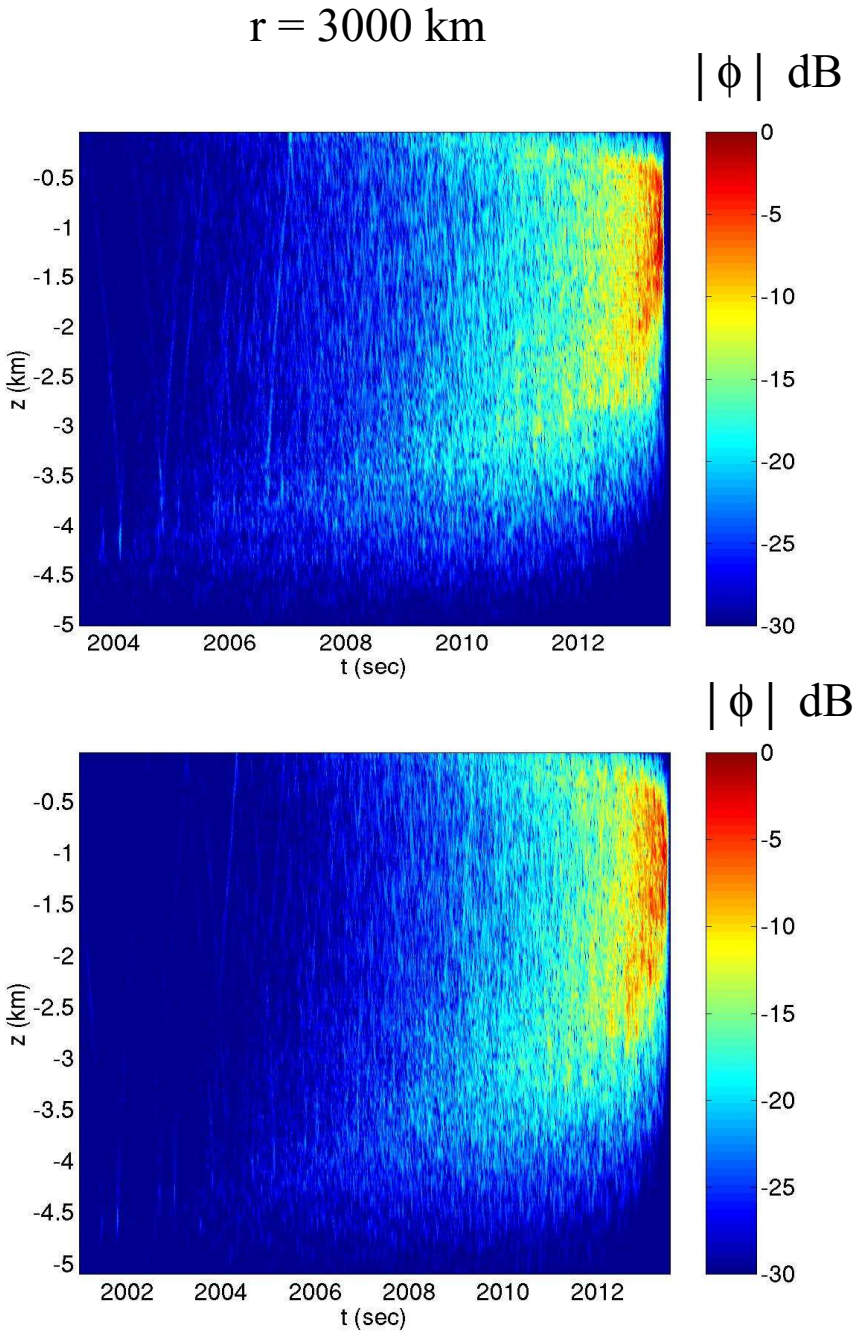

Figure 6.14: Several timefronts for different internal wave seeds are plotted. The magnitude of the timefront $|\phi|$ is plotted as a contour plot with depth z and time t for propagation to 3000 km. Propagation is in the full potential, with a background from Eq. (3.11) and internal wave fluctuations from Eq. (3.12). The noise level below 30 dB has been set to 30 dB on the plot.

6.1.5 Mode Contributions

The timefront is related to the unitary matrices $C_{m,n}$ discussed in Ch. (4) through the wavefield $\Psi(z, r; k)$. The wavefield can be written $\Psi(z, r; k) = \sum_{n,m} a_n C_{m,n} \psi_m(z)$, where ψ_n are the modes of the potential V_0 in Eq. (3.11), $C_{m,n}$ is the complex probability amplitude of transitioning from the nth mode to the mth mode for the propagation range r, and and a_n are the coefficients of each mode in the initial wave packet $\Psi(z, r = 0; k)$ in Eq. (3.18). Then the timefront can be written

$$\Phi(z, r, t) = \frac{1}{\sqrt{2\pi\sigma_k^2 r}} \sum_{n,m} \int_{-\infty}^{+\infty} dk\, a_n(k) C_{m,n}(k) \psi_m(z; k) e^{-ikc_0\left(t - \frac{r}{c_0}\right)} \exp\left[\frac{-(k-k_0)^2}{2\sigma_k^2}\right]. \tag{6.2}$$

For the range independent potential, V_0, energy is conserved during the propagation and there is no mixing of modes so that $C_{m,n} = e^{-ikE_n r}\delta_{m,n}$, where E_n are the energies of the potential V_0. Then the complex timefront is

$$\Phi_{\epsilon=0}(z, r, t) = \frac{1}{\sqrt{2\pi\sigma_k^2 r}} \sum_{n} \int_{-\infty}^{+\infty} dk\, a_n(k) \psi_n(z; k) e^{-ikc_0\left(t - \frac{r}{c_0}(1 - E_n)\right)} e^{\frac{-(k-k_0)^2}{2\sigma_k^2}}. \tag{6.3}$$

Equation (6.3) predicts that the timefront is composed of a sum of mode arrivals n. The vertical extent of the timefront in the different regions of the timefront depend on the vertical extent of $\psi_n(z; k)$ for the mode arrivals in that segment of the timefront. The branches are formed from constructive and destructive interference of the mode arrivals. The intensity along the branches depends on the mode arrivals in that segment of the timefront and the

initial mode weightings in the initial Gaussian wavefield $\psi_0(z)$ captured by the coefficients $a_n(k)$. The maximum intensity of the timefront decays as $\frac{1}{\sqrt{r}}$ with the range of the timefront.

If the fourier transform of the timefront $\phi_{\epsilon=0}(z,r,k)$ in Eq. (6.3) is written as a sum of mode arrivals $\phi_{\epsilon=0}(z,r,k) = \sum_n \alpha_n(r,k)\psi_n(z;k)$ then the frequency dependent coefficients for mode n are [74]

$$\alpha_n(r,k) = \frac{1}{\sqrt{2\pi\sigma_k^2 r}} a_n(k) e^{ikr(1-E_n(k))} \exp\left[\frac{-(k-k_0)^2}{2\sigma_k^2}\right]. \tag{6.4}$$

The contribution of mode n to the timefront is captured in the fourier transform $\alpha_n(t) = \int_{-\infty}^{+\infty} \alpha_n(r,k) e^{-ikc_0 t} dk$. The mode contributions for some unperturbed and perturbed propagations are shown in Fig. (6.15) and (6.16). Since the lower modes represent energy trapped near the sound speed minimum, the lower modes travel slowest. This is consistent with Fig. (6.16), which shows that the higher modes arrive earlier in the timefront, while the lower modes arrive later in the timefront. In Fig. (6.15), it is seen that while the lower modes contribute mainly to the late arrivals of the timefront, the higher modes really only contribute to the branches of the timefront.

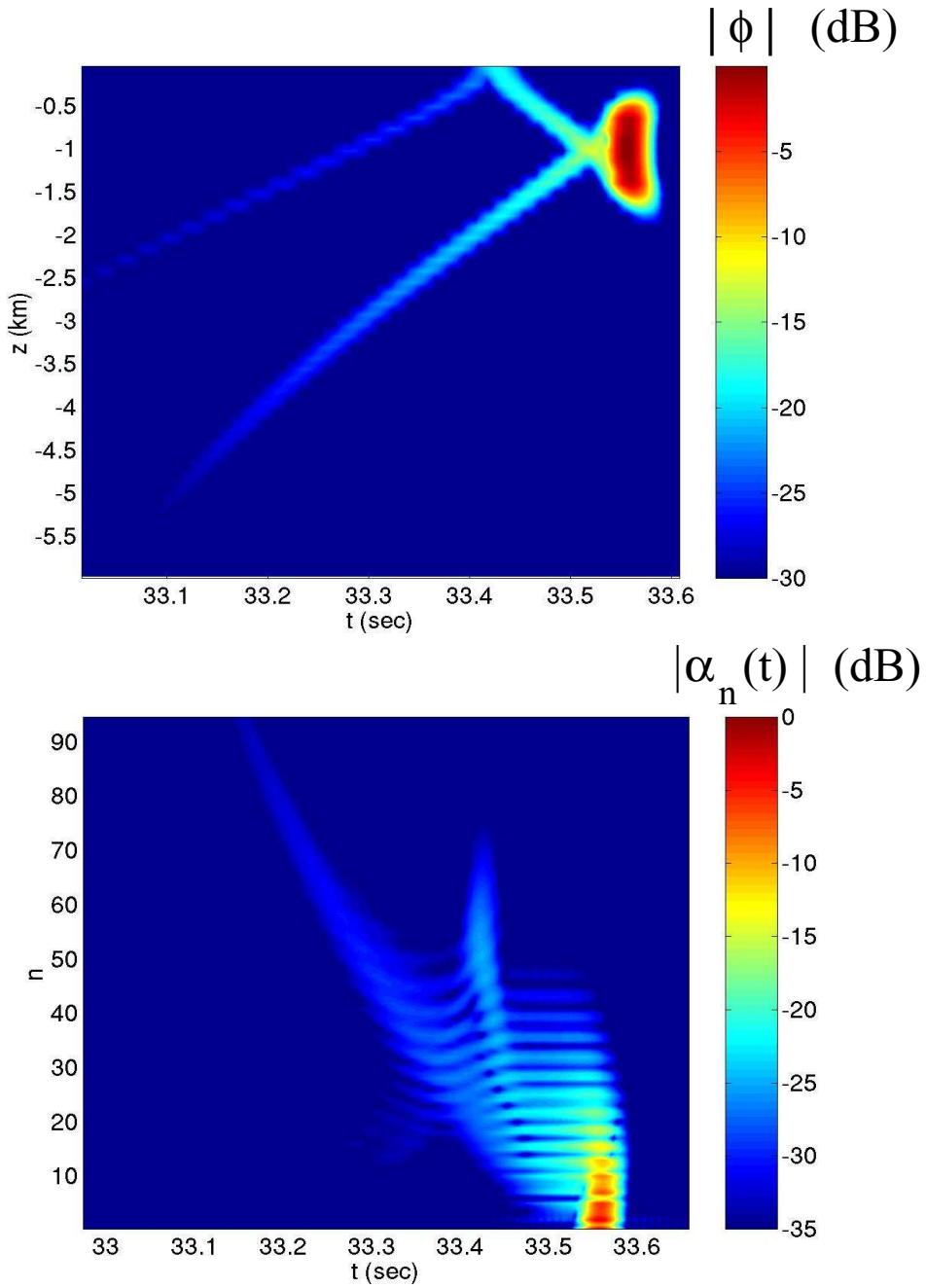

Figure 6.15: Mode Arrivals in Timefront for Unperturbed Propagation to 50 km (Upper) The magnitude of the timefront $|\phi|$ is plotted as a contour plot in depth z and time t with values of the contour in decibels (dB) with respect to the maximum value of $|\phi|$. (Lower) The fourier transform $\alpha_n(t)$ of the frequency dependent coefficients for mode n in Eq.(6.4) are plotted as a contour plot in time t and mode number n in decibels (dB) with respect to the maximum value of $|\alpha_n(t)|$. Note: the decibel scales on each plot are different.

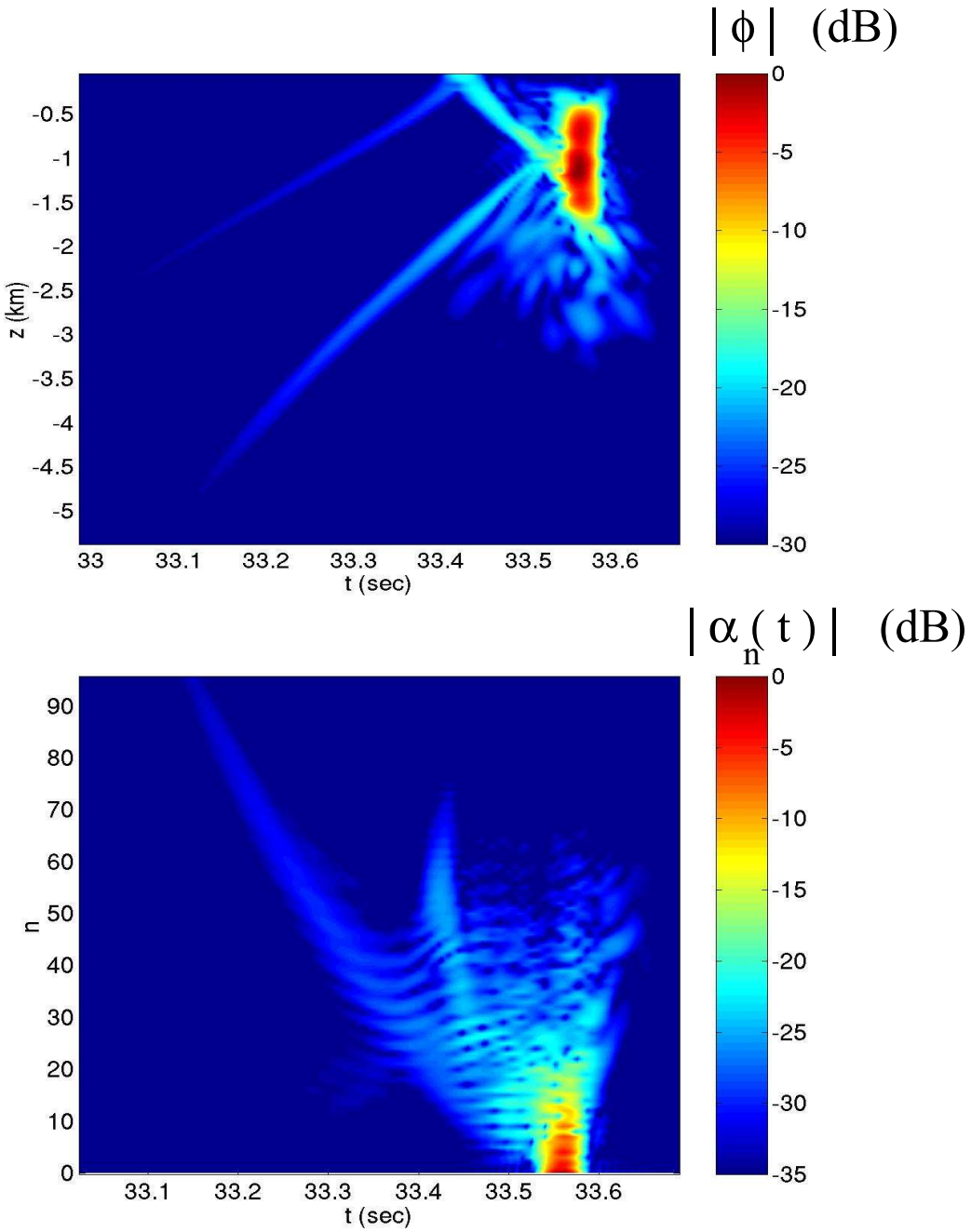

Figure 6.16: Mode Arrivals in Timefront for Perturbed Propagation to 50 km. (Upper) The magnitude of the timefront $|\phi|$ is plotted as a contour plot in depth z and time t with values of the contour in decibels (dB) with respect to the maximum value of $|\phi|$. (Lower) The fourier transform $\alpha_n(t)$ of the frequency dependent coefficients for mode n in Eq.(6.4) are plotted as a contour plot in time t and mode number n in decibels (dB) with respect to the maximum value of $|\alpha_n(t)|$. Note: the decibel scales on each plot are different.

6.1.6 Harmonic Oscillator Timefront

Insight into some of the properties expected of the timefronts can be gained by investigating the properties of the timefront from the propagation through the harmonic oscillator potential

$$V(z) \;=\; \frac{1}{2}\omega(z - z_A)^2 \,, \tag{6.5}$$

where $\omega = \sqrt{2\gamma/B}$. This harmonic oscillator potential is the local approximation of the unperturbed (Munk) potential at the sound speed axis $z = z_A$. For this potential, there is an exact analytic solution for both the wavefield propagation and for the classical ray propagation.

Using the exact solutions to the position, momentum and classical action S for the classical rays propagated through the harmonic oscillator potential [83], the exact classical timefront of final arrival times t and final arrival depths z for propagation through the harmonic oscillator potential to a range R is

$$(z(R) - z_A)^2 \;=\; \frac{2c_0}{\omega}\tan(\omega R)\left(t - \frac{R}{c_0}\right) \,. \tag{6.6}$$

From this general expression, it is understood how the timefront evolves as a function of range, R. For some integer m, when $\omega R = m\pi$, the timefront is a single point at $(R/c_0, z_A$, while for $\omega R = (2m+1)\pi/2$, the timefront is a vertical line, $t = R/c_0$. In between these extremes, the timefront is parabolic with vertex at $(R/c_0, z_A)$. For $\omega R \in [m\pi, (2m+1)\pi/2]$, the value $\tan(\omega R) > 0$ so the parabolic timefront opens to the right, while for $\omega R \in [(2m+1)\pi/2, (m+1)\pi]$, the value $\tan(\omega R) < 0$ so the parabolic timefront opens to the left. These

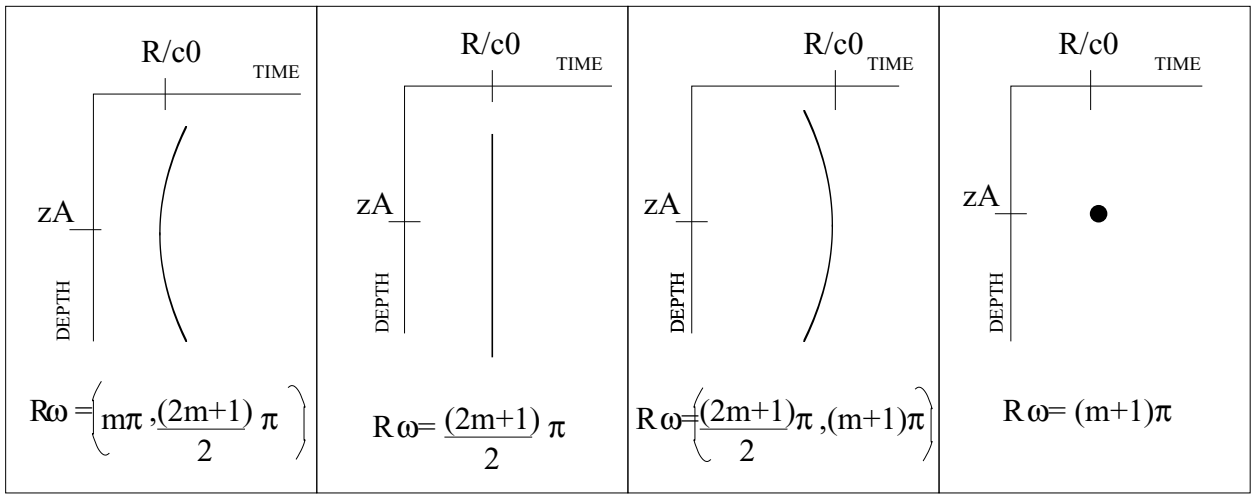

Figure 6.17: The four possible cases for the general shape of the timefront pattern for the harmonic oscillator potential. The cases are distinguished by the different values of $R\omega$, where R is range and ω in the angular frequency of the harmonic oscillator potential. n is any integer greater than 1.

four cases are shown in Fig. (6.17).

The insight comes from noting that for the harmonic oscillator potential, all classical rays have the same period $r = \frac{\pi}{2\omega}$ for their oscillation in range and all of the classical rays achieve the turning point in their oscillation at the same range. However, for the classical rays in the unperturbed potential in Eq. (3.11), only reciprocal classical rays (with the same energy but initial momentum that differ by a sign) have the same period and achieve their turning point at the same range. This is responsible for the creation of branches in the classical timefront for the unperturbed potential as in Fig. (6.3).

For propagation of the initial Gaussian wave field in Eq. (3.18) through the harmonic

oscillator potential in Eq. (6.5), the exact wavefield at a range r is given by [26]

$$\begin{aligned}
\Psi(z',r) &= \left(\frac{\sigma^2}{\pi}\right)^{\frac{1}{4}} \sqrt{\frac{\omega}{ia(r)}} \exp\left[\frac{k\left(c(z,r)+\frac{b^2(z,r)}{4a(r)}\right)}{2\sigma^2\sin(\omega r)}\right] \\
a(r) &= \sin(\omega r)/k - i\omega\sigma^2\cos(\omega r) \\
b(z,r) &= -2i\omega\sigma^2(z-z_A) \\
c(z,r) &= i\omega\sigma^2\cos(\omega r)(z-z_A)^2 \,,
\end{aligned} \tag{6.7}$$

where the branch of the square root taken is

$$\begin{aligned}
\sqrt{ia} &= (\omega\sigma^2\cos(\omega r))^{\frac{1}{2}} + i\sin(\omega r)/k \\
&= Real\left(\sqrt{ia}\right) sign\left(\cos\left(\frac{\omega r}{2}\right)\right) + iImag\left(\sqrt{ia}\right) sign\left(\sin\left(\frac{\omega r}{2}\right)\right) \,.
\end{aligned}$$

With the exact wavefield in Eq. (6.7) for the harmonic oscillator propagation, the harmonic oscillator timefront is constructed using Eq. (3.20) numerically. The wavenumber dependence of the wave field makes analytic integration difficult. The semiclassical derivation for the timefront in Appendix. C is exact for the harmonic oscillator potential, but is also difficult to integrate. For all ranges $r \neq (m+1)\pi/\omega$ where m is an integer, there is only a single pulse arrival at each receiver depth of the timefront. Since there is no interference of multiple pulses at each depth, single peaks can be unambiguously examined and are found to be very close to Gaussian in shape.

By identifying a region around the peaks at each depth, the standard deviation of the single pulse arrivals in intensity at each depth are calculated to estimate the pulse width. The

results are shown in Fig. (6.18) - (6.20) for several ranges illustrating three of the four cases in Fig. (6.17). In all three cases, it is found that the pulse width for intensity varies along the course of the timefront with the smallest variance $\sigma_t^2 = \frac{1}{2c_0^2\sigma_k^2}$ occuring at the vertex of the parabolic timefront (where $z = z_A = 1$ km and $t = \frac{r}{c_0}$) and the variance increasing uniformly along the timefront from the vertex location.

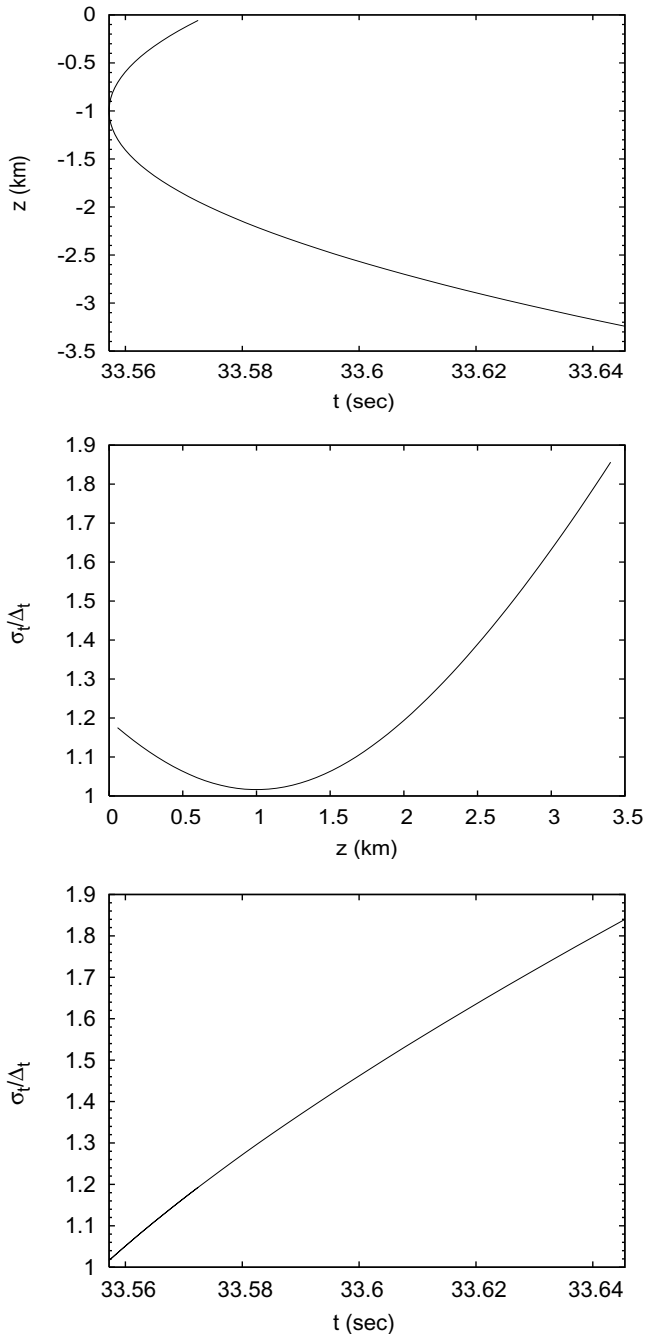

Figure 6.18: (Upper) Classical timefront for rays propagated through harmonic oscillator potential to $r = 50$ km. (Middle) Pulse width σ_t (in units of $\Delta_t = \frac{1}{\sqrt{2}c_0\sigma_k}$) is plotted with final depth z. (Lower) Pulse width σ_t (in units of $\Delta_t = \frac{1}{\sqrt{2}c_0\sigma_k}$) is plotted with arrival time t. Classical rays with initial angles $-20^\circ < \theta_0 < 20^\circ$ uniformly spaced in inital angle are plotted.

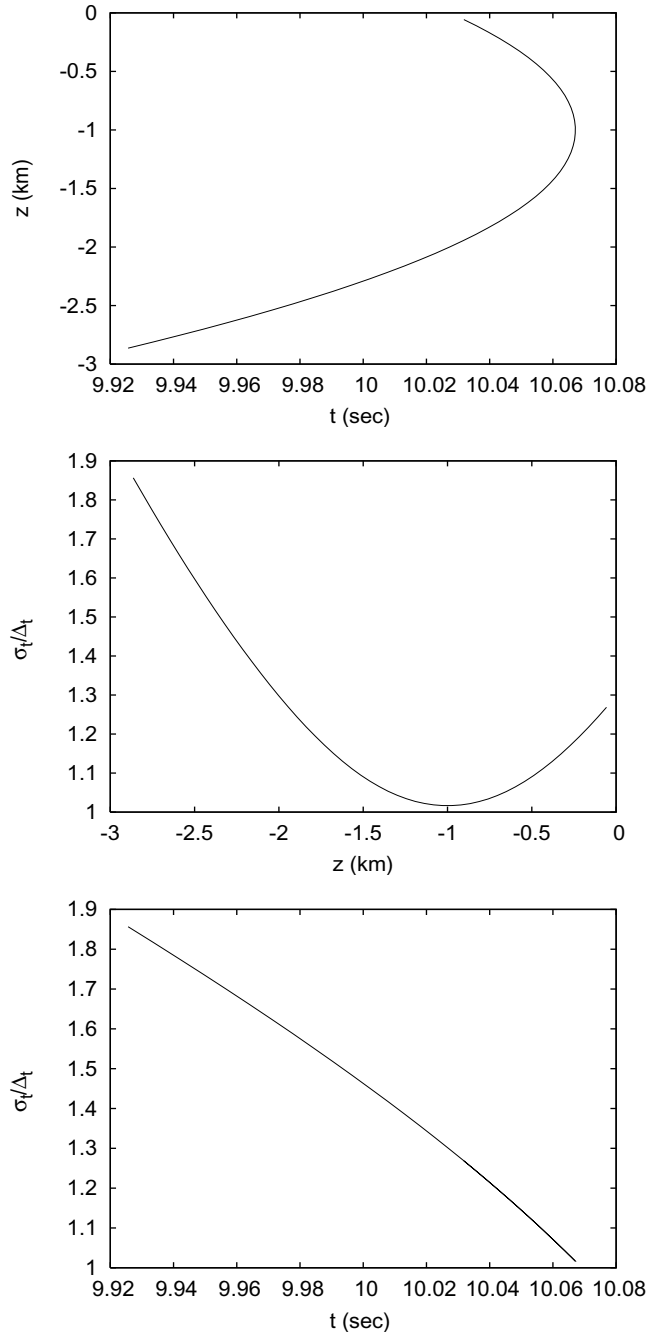

Figure 6.19: (Upper) Classical timefront for rays propagated through harmonic oscillator potential to $r = 15$ km. (Middle) Pulse width σ_t (in units of $\Delta_t = \frac{1}{\sqrt{2}c_0\sigma_k}$) is plotted with final depth z. (Lower) Pulse width σ_t (in units of $\Delta_t = \frac{1}{\sqrt{2}c_0\sigma_k}$) is plotted with arrival time t. Classical rays with initial angles $-20^\circ < \theta_0 < 20^\circ$ uniformly spaced in inital angle are plotted.

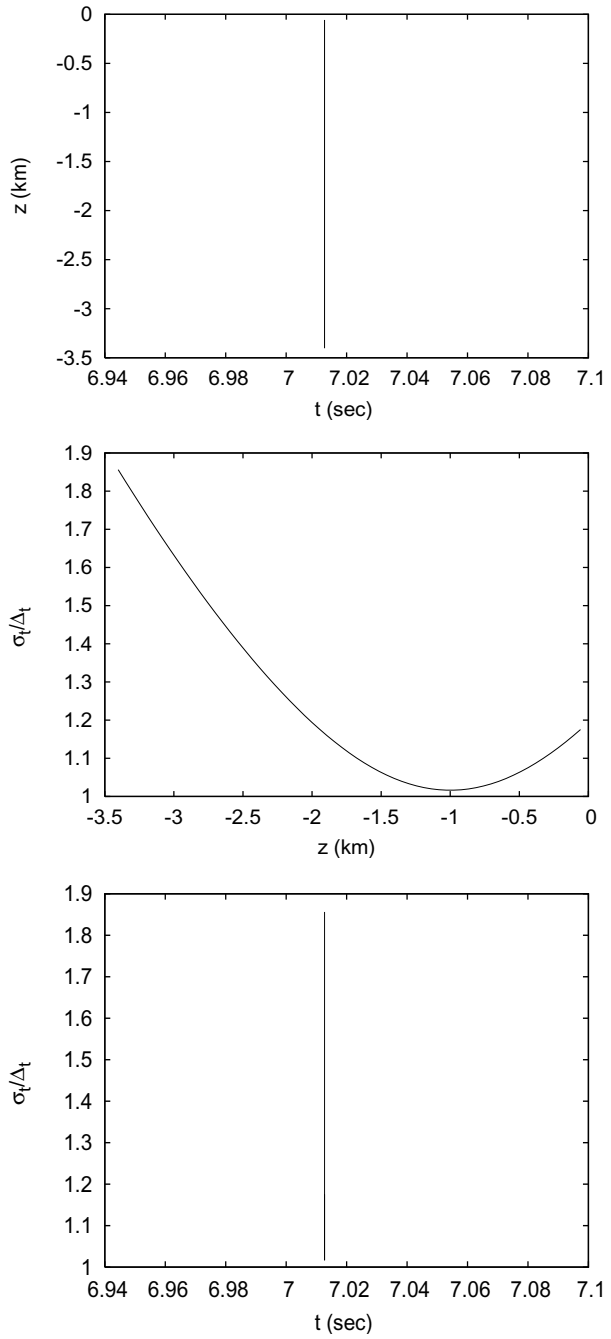

Figure 6.20: (Upper) Classical timefront for rays propagated through harmonic oscillator potential to $r = 10$ km. (Middle) Pulse width σ_t (in units of $\Delta_t = \frac{1}{\sqrt{2}c_0\sigma_k}$) is plotted with final depth z. (Lower) Pulse width σ_t (in units of $\Delta_t = \frac{1}{\sqrt{2}c_0\sigma_k}$) is plotted with arrival time t. Classical rays with initial angles $-20^\circ < \theta_0 < 20^\circ$ uniformly spaced in inital angle are plotted.

6.2 Comparison of Properties of Individual Timefronts

6.2.1 Sample Timefronts

A sample timefront is constructed from the building block ensemble model (with mean phase $\mu_{n,n}$ taken from Eq. (4.20)) and from the propagation and compared qualitatively in Fig. (6.21). Though there are significant differences in the curvature of the branches with the ensemble model, a sample timefront constructed from the building block ensemble model (with $\mu_{n,n} = 0$) and from the propagation compared qualitatively in Fig. (6.22) shows agreement in the curvature of the branches. This suggests that there is a problem with the model for the mean phase $\mu_{n,n}$ in the ensemble model. Perhaps the problem with the model comes from the assumption in Sec. (4.3.2) that the phases of the diagonal elements of the unitary propagation matrix obtained from mode propagation were Gaussian leading to the $\mu_{n,n}$ in Eq. (4.20).

Regardless, the $\mu_{n,n}$ in Eq. (4.20) won't be used in the construction of the ensemble model for final comparisons in this thesis. Instead, $\mu_{n,n} = 0$ for all future references to the ensemble model. This means that the ensemble model in this thesis will investigate only the effect of the variance matrix $\sigma_{A_{m,n}}$ in capturing the fluctuations in the perturbed propagation and not the $\mu_{n,n}$ in shifting the unperturbed timefronts.

The comparison of the timefronts for 50 km Fig. (6.22). The timefront from the ensemble model has branch magnitudes, locations and widths agrees very well qualitatively with a sample timefront from the propagation. However, the vertical extent and temporal extent of the finale region is much larger than that of the timefront resulting from the propagation. This

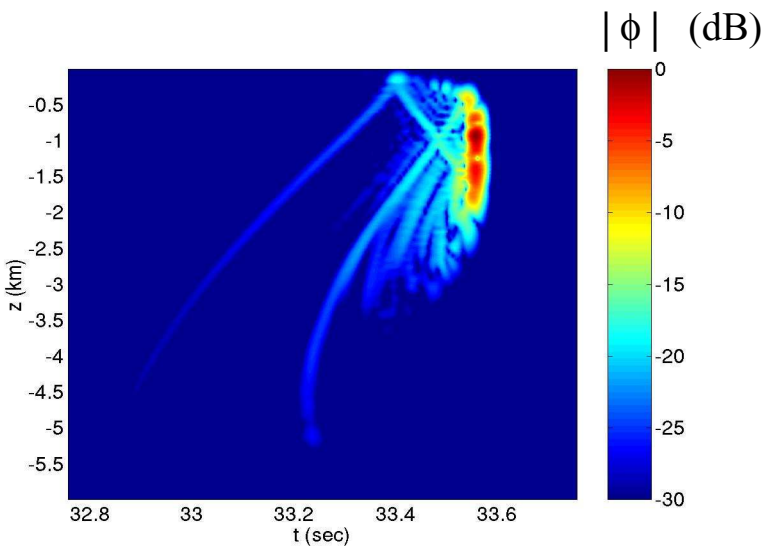

(a) Sample timefront generated from ensemble model (with $\mu_{n,n} \neq 0$)

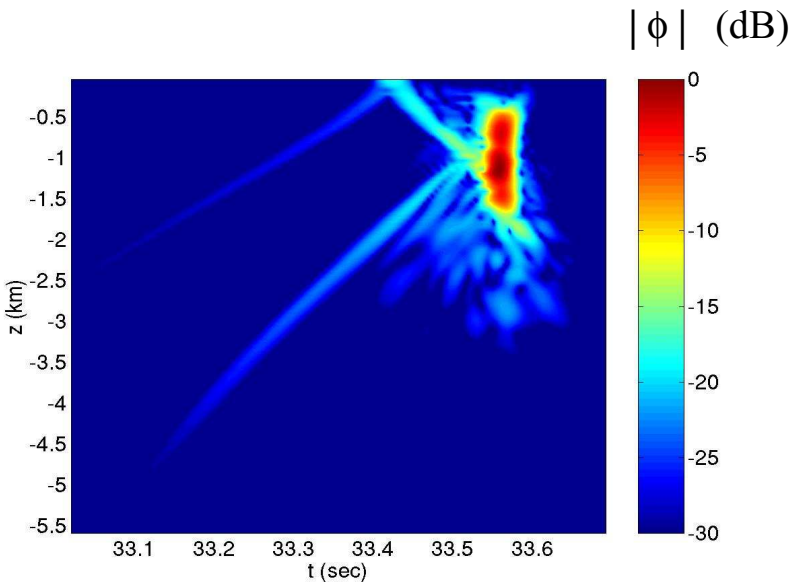

(b) Sample timefront generated from propagation

Figure 6.21: Comparison of sample timefronts from ensemble model and propagation for 50 km. The magnitudes $|\Phi|$ of the timefront are plotted in decibels with respect to the largest value of $|\Phi|$ as a contour plot in depth z and range r. (a) A sample timefront generated from a single member of the ensemble model from Eq. (5.1) and Eqs. (5.15-5.18). (b) A sample timefront from propagation through a single internal wave field. The decibel value is calculated as $3log_2\left(|\Phi|/|\Phi|_{max}\right)$ which is approximately $log_{10}\left(|\Phi|/|\Phi|_{max}\right)$.

seems to indicate that the ensemble model has too much scattering built into the lower order modes.

A sample timefront is constructed from the long range ensemble model and from the propagation and compared qualitatively in Fig. (6.23). The timefront from the long range ensemble model has branch locations that seem to agree very well qualitatively with a sample timefront from the propagation. However, the branch magnitudes and widths do not agree very well qualitatively and the vertical extent and temporal extent of the finale region is much larger than that of the timefront resulting from the propagation. This seems to indicate that the long range ensemble model has too much scattering both in the lower and higher order modes. Most likely, this is due to the building block ensemble model having too much scattering built into the lower order modes, which then scatter to the higher modes in the long range ensemble model from the multiplication of building blocks.

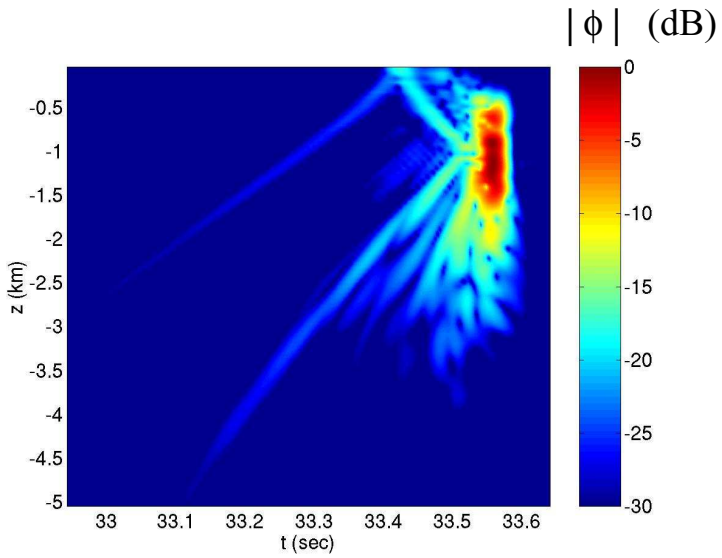

(a) Sample timefront generated from ensemble model

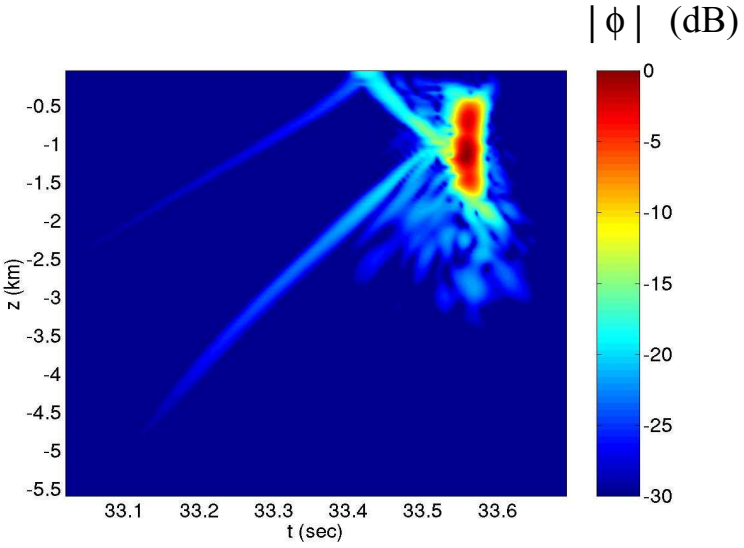

(b) Sample timefront generated from propagation

Figure 6.22: Comparison of sample timefronts from ensemble model and propagation for 50 km. The magnitudes $|\Phi|$ of the timefront are plotted in decibels with respect to the largest value of $|\Phi|$ as a contour plot in depth z and range r. (a) A sample timefront generated from a single member of the ensemble model from Eq. (5.1) and Eqs. (5.15-5.18). (b) A sample timefront from propagation through a single internal wave field. The decibel value is calculated as $3log_2\left(|\Phi|/|\Phi|_{max}\right)$ which is approximately $log_{10}\left(|\Phi|/|\Phi|_{max}\right)$.

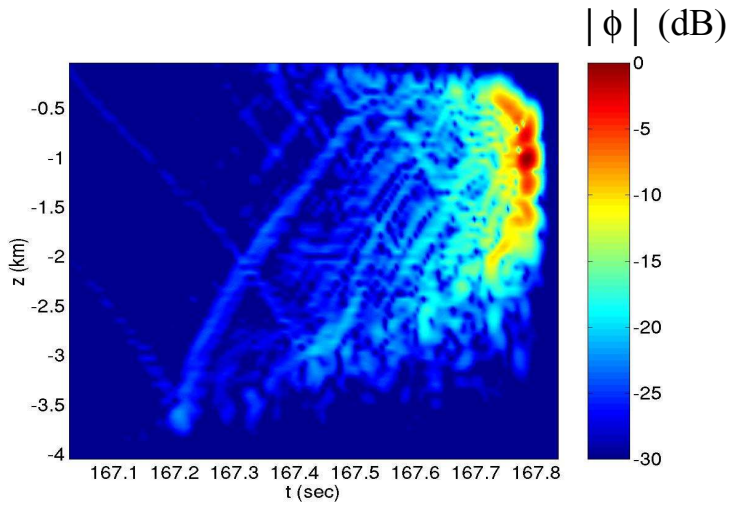

(a) Timefront from long range ensemble model for 250 km

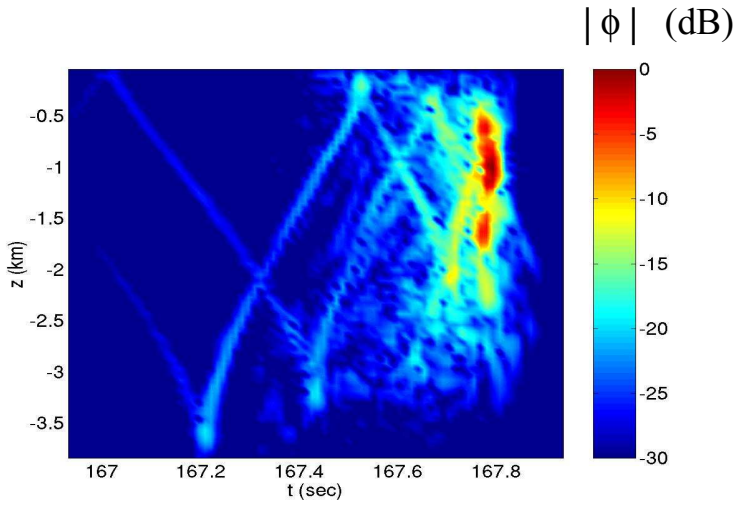

(b) Timefront from propagation to 250 km

Figure 6.23: A timefront generated from the statistics of perturbation theory (Upper) Timefront generated by using values of $U_{m,n}$ generated from the unitary transformation in Eq. (5.1) with values $A_{m,n}$ taken from Eq. (5.17) with variances from the statistics of perturbation theory in Eq. (5.15) for a range of 250 km using 97 modes. (Lower) Timefront generated by propagating the initial Gaussian wavepacket for 250 km in the perturbed potential. Note that the smoothing was done using a smoothing parameter for 75 Hz only (not k-dependent smoothing). Note that the two timefronts are different realizations, so they should not be compared exactly, but rather within the variations seen in Fig. (6.11).

6.2.2 Mode Contributions

The function $\alpha_n(t)$ in Eq. (6.4) captures the modal contributions to the timefronts. This function is shown for a single realization from the perturbed propagation and from the ensemble model to 50 km in Fig. (6.24). The contours of $\alpha_n(t)$ are compared for the perturbed propagation and the ensemble model in Fig. (6.25).

Though the modal contributions do differ slightly in the magnitude of the contributions for the higher modes $n > 50$, the structure of the modal contribution from the ensemble model agrees with the structure of the modal contributions from the propagation to 50 km. This serves to just confirm that the building block ensemble model is performing well in matching the propagation to 50 km.

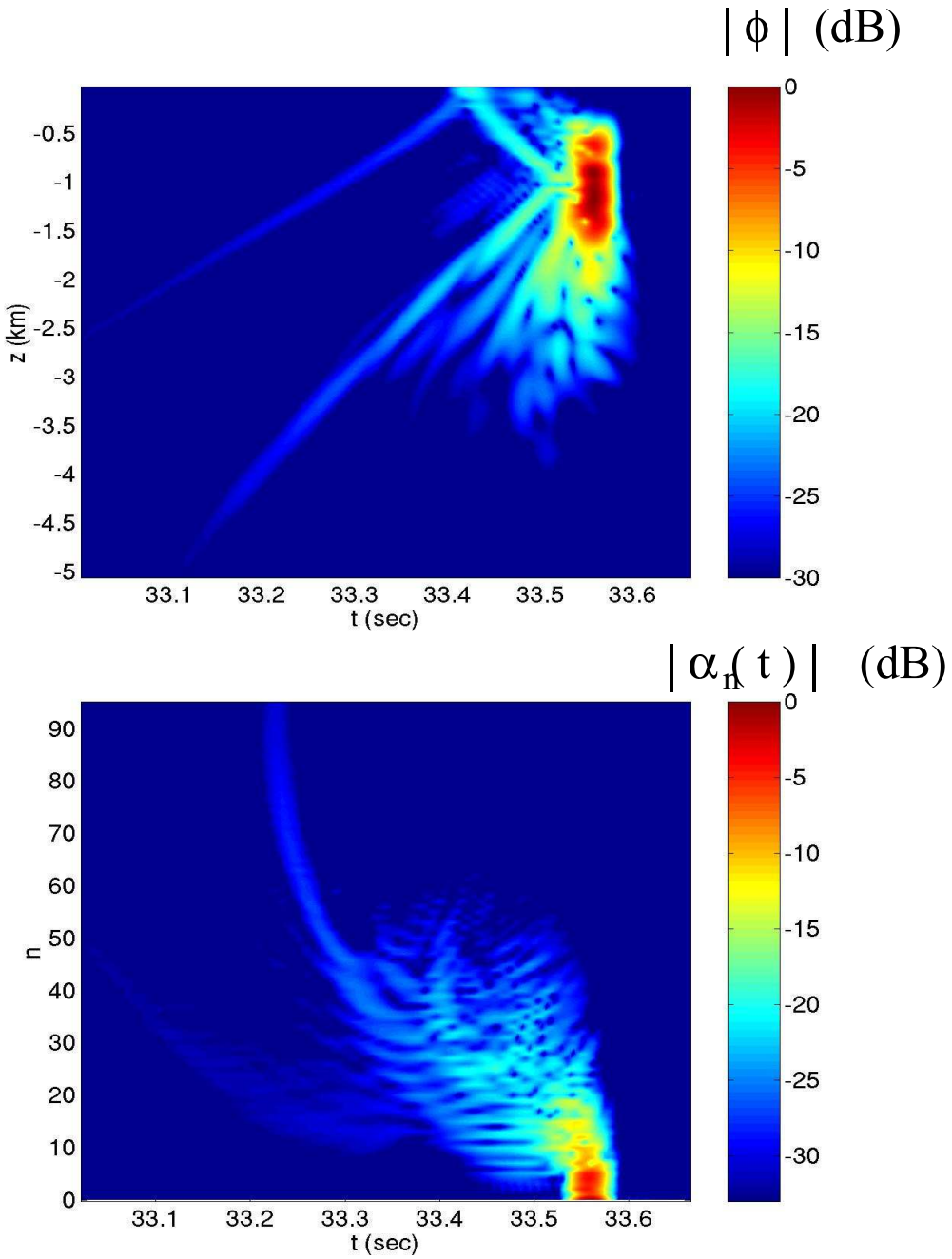

Figure 6.24: Mode Arrivals in Timefront for ensemble model to 50 km. (Upper) The magnitude of the timefront $|\phi|$ is plotted as a contour plot in depth z and time $t$with values of the contour in decibels (dB) with respect to the maximum value of $|\phi|$. (Lower) The fourier transform $\alpha_n(t)$ of the frequency dependent coefficients for mode n in Eq.(6.4) are plotted as a contour plot in time t and mode number n in decibels (dB) with respect to the maximum value of $|\alpha_n(t)|$. Note: the decibel scales on each plot are different.

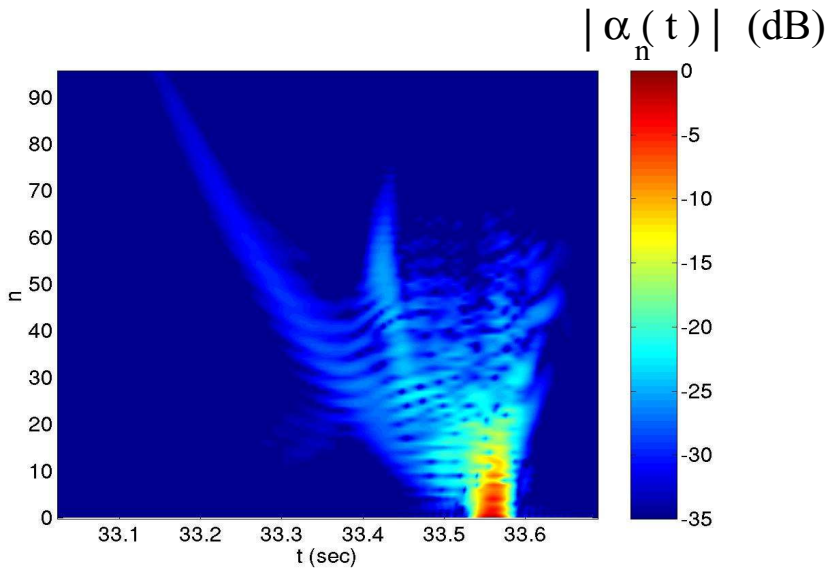

(a) Mode Arrivals in Timefront for Perturbed Propagation to 50 km

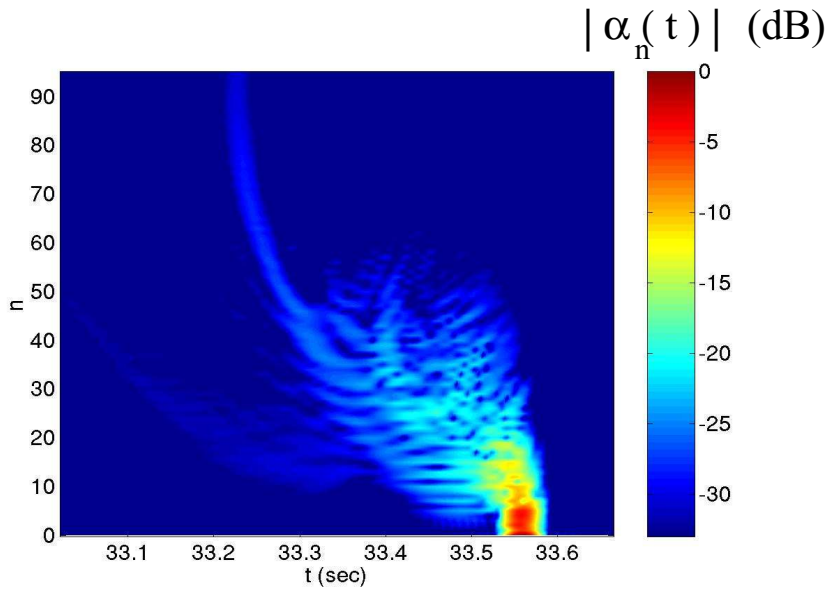

(b) Mode Arrivals in Timefront for ensemble model to 50 km

Figure 6.25: The fourier transform $\alpha_n(t)$ of the frequency dependent coefficients for mode n in Eq.(6.4) are plotted as a contour plot in time t and mode number n in decibels (dB) with respect to the maximum value of $|\alpha_n(t)|$. (Upper) $\alpha_n(t)$ is calculated from propagation through a single sound speed model to 50 km. (Lower) $\alpha_n(t)$ is calculated from propagation through a realization from the ensemble model to 50 km. Note: the decibel scales on each plot are different.

6.2.3 Pulse Spread and Wander

Two observables of interest in analysing sets of experimental timefronts are 1) the variance in the mean location of the arrival time of a branch - the wander, and 2) the average value of the variance of a pulse arrival along a branch, which is related to the spread [12, 22].

Previous experimental analysis of the timefronts to determine the wander was done by taking the average location of the time of the peak arrivals on the branches [39]. Since there are multiple peaks in the experimental timefronts besides those associated with the unperturbed propagation, methods have been developed to associate peaks with branches [39]. However, associating peaks arrivals with branches is a difficult task.

Previous experimental analysis of the timefronts to determine the spread was done by determining the difference in the pulse width of an arrival from that of the initial pulse width of the source [39]. The pulse width of an arrival on a branch was determined by Colosi et. al. [39] by marching down from the peak value $|\phi(z, t_{max}, r)|^2$ to $e^{-0.5}$ of the peak value and estimating the width by taking the difference of the time giving $e^{-0.5}$ of the peak value for a Gaussian pulse from the center. If the pulse intensity is Gaussian in shape, this method gives the standard deviation of the pulse intensity. However, the pulse arrivals are not in general Gaussians.

The approximation in Eq. (6.1) to the semiclassical theory in Eq. (C.16) predicts the timefront will take a form where ray arrivals show up as pulses in time centered about the time of the ray arrival and with an approximate standard deviation in intensity of $\Delta_t = \frac{1}{\sqrt{2}c_0\sigma_k}$. This is only an approximation, but does provide a scale for the pulse widths to be expected.

For the unperturbed timefront, there is only a single ray arrival at each location on a branch. For the perturbed timefronts, there may be several ray arrivals at each location on a branch, which would interfere creating a pulse arrival with a more complicated shape, which generally widens the branch.

In this thesis, the pulse width of the arrival is approximated by the standard deviation of arrival times about the mean arrival time of the pulse. Since there are multiple arrivals at the same depths along a branch and even branches that overlap, the traces of timefront arrivals are littered with interferences from multiple arrivals. For this reason, care is taken to calculate the variance only where branches are deemed 'well-separated'. Classical rays are utilized to identify locations along branches in which pulses are significantly well-separated from pulses on other branches. The procedure for finding the mean and variance ensures that the region in time chosen for the calculation of the variance contains the entire pulse arrival of that branch alone.

Well-Separated Branches

An approximate location of the mean time for the branch is obtained by interpolating a classical ray timefront for unperturbed propagation to the range. 'Phantom rays' are noted at locations in the trace where the Airy tails of the wave corresponding to the classical turning points would produce the tail of an arrival in the trace. The approximate spacing between the pulse arrivals along a trace is obtained by interpolating the intersections of the depth with the classical ray timefront. Branches are deemed well-separated if the travel times along the trace from the classical ray or 'phantom ray' are separated by a separation Δ', taken to be some

multiple of the standard devation of a pulse arrival due to a single ray.

Since the branches are determined to be well-separated pulses using the classical ray timefront, in this thesis only the portion of the timefront corresponding to classical ray arrivals with initial launch angles $|\theta_0| \leq 15^\circ$ will be considered. Rays with initial launch angles larger than 15° represent wave energy that reflects from the surface and is absorbed by the ocean bottom. In the acoustic model, this energy is allowed to propagate above the surface and below the ocean bottom, so that there will be wave arrivals corresponding to angles $|\theta_0| \geq 15^\circ$ in the simulated acoustic timefronts. Therefore the locations where the branches are well-separated will only be chosen from corresponding ray angles with $|\theta_0| \leq 15^\circ$.

The locations of well-separated branches identify regions in which branch arrivals can be consistently identified. The locations in the timefront of the well-separated branches for a range of 50 km with a specific separation criteria Δ' are shown in the unperturbed and perturbed timefront in Fig. (**??**). The well-separated pulses along the unperturbed timefront for some ranges are shown in Fig. (6.26).

Means and Variances of Pulse Arrivals

Once the locations of well-separated branches have been identified, the approximate ray travel time, t_{ray}, is used to locate the target pulse arrival along the trace by considering the interval $(t_{ray} - 2\Delta_t, (t_{ray} + 2\Delta_t)$, where $\Delta_t = \frac{1}{\sqrt{2}c_0\sigma_k}$ is the standard deviation predicted by semi-classical theory in Eq. (C.16) for the intensity of the latest arrival at $z = z_0$, $t = \frac{r}{c_0}$. The maximum intensity $|\phi|^2$ is found in this interval at the time t_{max} .

Though the calculation of the pulse spread for experimental analyses [39] is supposed to

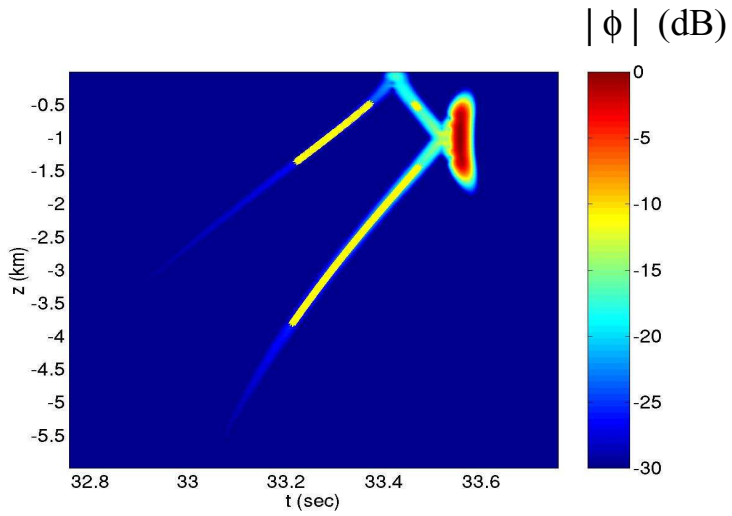

(a) Locations of Well-Separated Branches in Unperturbed Arrivals to 50 km

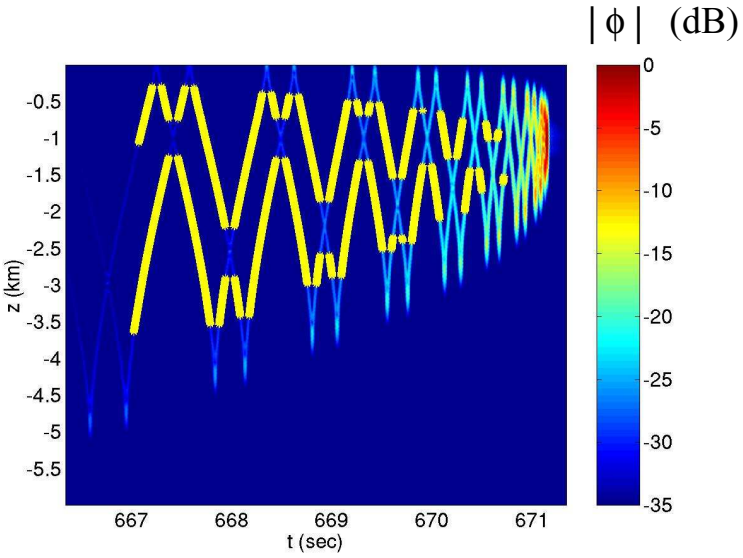

(b) Locations of Well-Separated Branches in Unperturbed Arrivals to 1000 km

Figure 6.26: The locations of wellseparated branches of unperturbed timefront for 50 km corresponding to the classical rays with initial angle $|\theta_0| \leq 15^\circ$ are plotted in yellow and overlaid on the timefront for the unperturbed propagation to 50 km. The unperturbed timefront $|\phi|$ is plotted as a contour plot with time t and depth z. The unperturbed timefront $|\phi|$ is plotted on a decibel scale (dB) with reference to the maximum value of $|\phi|$ in the timefront. Well-separated branches are chosen with $\Delta' = 15\Delta_t$. These locations are the points in the timefront at which the spread/wander of the branch will be calculated.

include all pulse arrivals associated with a branch, the discovery of the continuous fluctuation front in this work does not allow the identification of peak arrivals with branches. Therefore, the pulse width will be calculated only for the single large peak arrival which can be associated with an unperturbed branch. This will likely change the meaning of the quantities calculated.

A region about the peak intensity is determined by taking the central time to be the location of the peak intensity, t_{max}, and determining a width about the mean which captures only a single pulse. Marching down from the left of the value at $t_{max} - 2\Delta_t$ until there is no longer a decrease in intensity gives a location t_{low}. Similarly, marching down from the right of the value at $t_{max} + 2\Delta_t$ until there is no longer a decrease in intensity gives a location t_{high}. This procedure defines a region in time (t_{low}, t_{high}). The width Δ is taken to be $\Delta = \min[|t_{low} - t_{max}|, |t_{high} - t_{max}|]$. Those pulse arrivals which result in values of the intensity at the boundaries which are greater than e^{-2} of the peak intensity (i.e. two standard deviations in a Gaussian pulse) are thrown out since these arrivals either have multiple peaks or are part of the finale. Figure (6.27) illustrates the region of a trace which is captured by this method.

Once an interval about the maximum intensity is found for a pulse arrival, the mean and

variance are calculated with the integral measures in Eq. (6.9) and (6.10),

$$\sigma_t^2(z) = < t^2 > - < t >^2 \tag{6.8}$$

$$< t > = \frac{\int_{t_{max}-\Delta}^{t_{max}+\Delta} t|\phi(z,t;r)|^2 dt}{\int_{t_{max}-\Delta}^{t_{max}+\Delta} |\phi(z,t;r)|^2 dt} \tag{6.9}$$

$$< t^2 > = \frac{\int_{t_{max}-\Delta}^{t_{max}+\Delta} t^2|\phi(z,t;r)|^2 dt}{\int_{t_{max}-\Delta}^{t_{max}+\Delta} |\phi(z,t;r)|^2 dt} , \tag{6.10}$$

where the pulse regions are centered on the location of the maximum t_{max} and Δ is half the pulse region. These measures were also used in Ref. [84]. In this definition, the intensity of the trace, $|\phi(z,t;r)|^2$, is the distribution function and the quantities are normalized by the integrated value of the intensity over the time region. Note that the mean and variance of a pulse arrival are a function of the depth z and branch number n.

The pulse widths $\sigma_t^{\epsilon=0}$ for the branches of the unperturbed timefront for the well-separated arrivals for 50 km in Fig. (6.26(a)) are calculated using Eqs. (6.8)-(6.9) and illustrated in Fig. (6.28). Note that these pulse widths are similar to those obtained for the harmonic oscillator potential in Fig. (6.18)-(6.19). Both sets of pulse widths are linear with travel time and decrease closer to $\frac{1}{\sqrt{2}c_0\sigma_k}$ for times closer to $t = \frac{r}{c_0}$. Pulse widths for the unperturbed arrivals for other ranges are shown shown in Fig. (6.29). These figures illustrate that there is a lot of uncertainty in the calculations of the pulse width for the branches of timefronts for longer ranges, even in the straightforward unperturbed timefronts. Much of this irregularity has been attributed to the slightly different shape of the pulse arrivals along the branch.

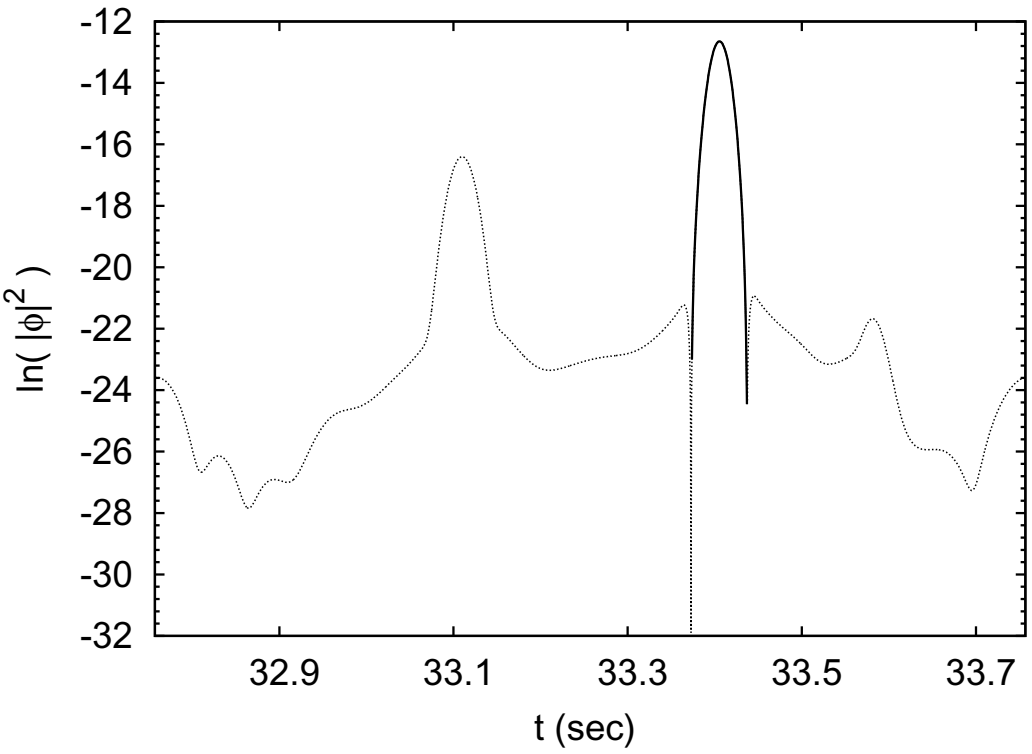

Figure 6.27: A trace of the unperturbed timefront for propagation to 50 km at the depth $z = 2$ km is shown by plotting the logarithm of the intensity $|\phi|^2$ with time t as a dotted line. Overlaid on this trace is solid line denoting the interval in time $(t_{max} - \Delta, t_{max} + \Delta)$ about the unperturbed branch with branch number $+2$ found using the method described in Sec. 6.2.3.

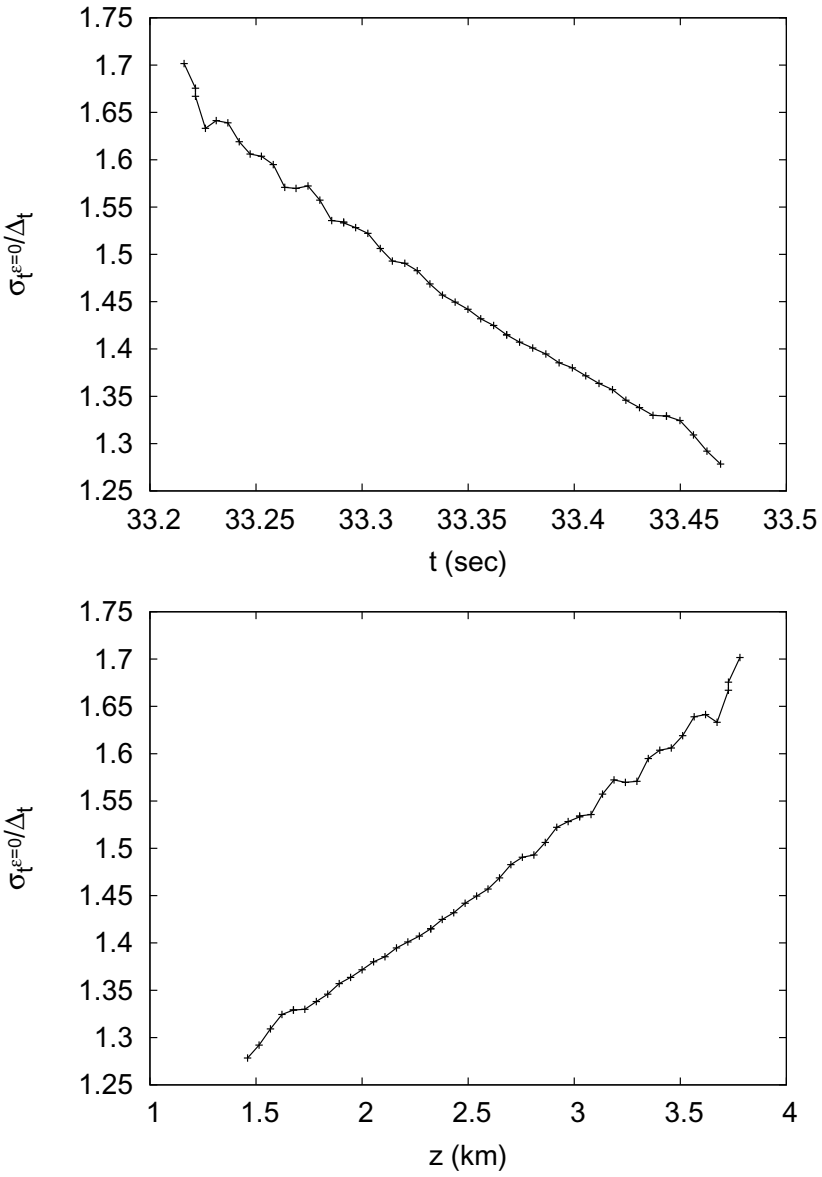

Figure 6.28: The pulse widths $\sigma_t^{\epsilon=0}$ for the branch of the unperturbed propagation with branch number $+2$ is plotted versus the final receiver depth (Upper plot) and versus the mean pulse travel time (Lower plot). The pulse width $\sigma_t^{\epsilon=0}$ is scaled by $\Delta_t = \frac{1}{\sqrt{2}c_0\sigma_k} \approx 6ms$.

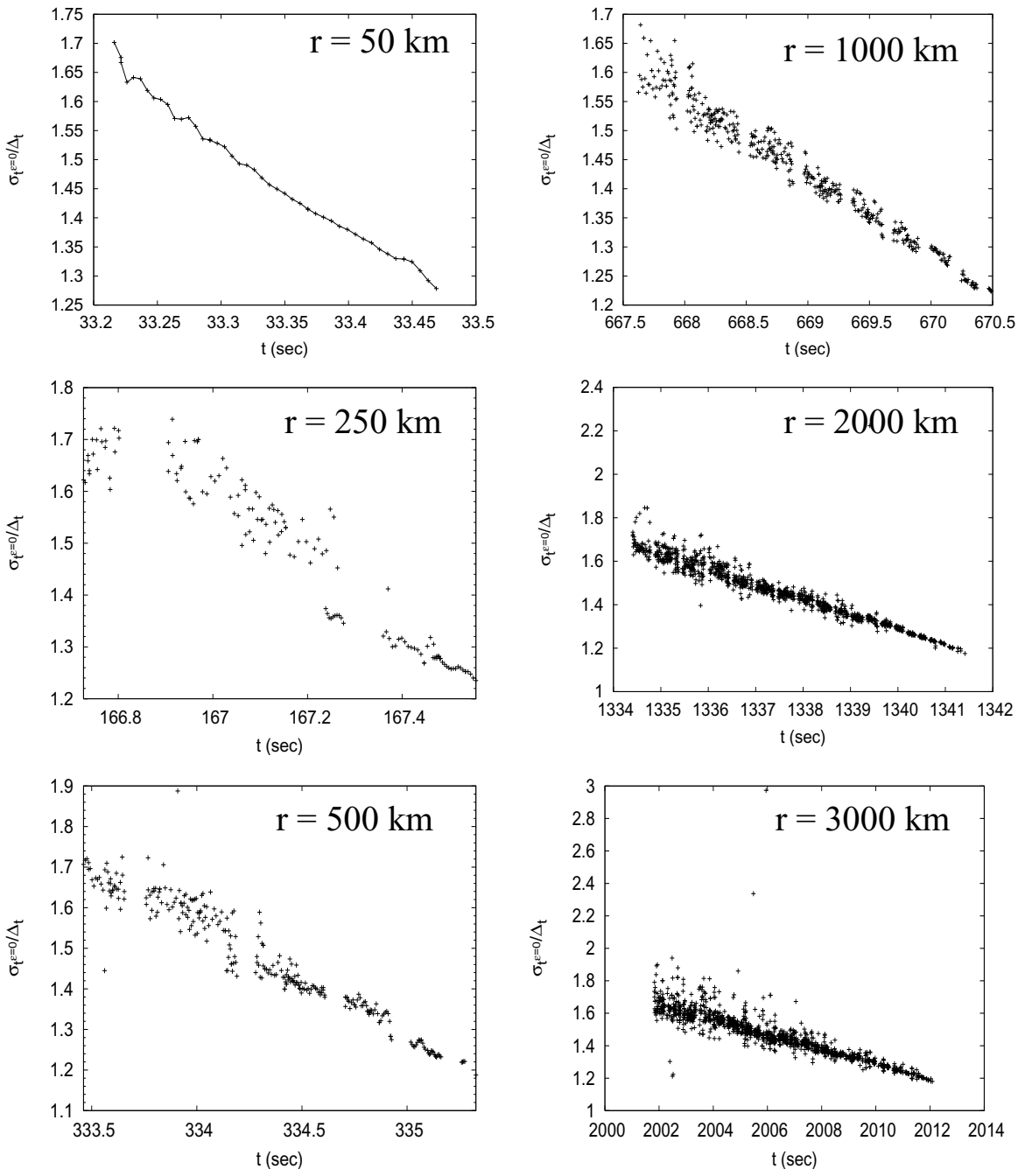

Figure 6.29: The pulse widths $\sigma_t^{\epsilon=0}$ for the unperturbed propagation at the well-separated branch locations corresponding to the classical rays with initial angle $|\theta_0| \leq 15^\circ$ are plotted versus the mean pulse travel time for several ranges, r. The pulse width $\sigma_t^{\epsilon=0}$ is scaled by $\Delta_t = \frac{1}{\sqrt{2}c_0\sigma_k} \approx 6ms$.

Pulse Spread

The pulse spread,μ_{σ_t}, is defined in this thesis to be the mean value of the difference in pulse widths between the perturbed ϵ and unperturbed $\epsilon = 0$ arrivals . If the pulse widths are approximated by the standard deviation of the pulse arrival, then a definition for the pulse spread considers the pulse widths σ_t^ϵ of individual timefronts in the ensemble and then takes the average of the pulse widths over all timefronts in the ensemble as in Eq. (6.11)

$$\mu_{\sigma_t} = \langle \sigma_t^\epsilon(z,n) - \sigma_t^{\epsilon=0}(z,n) \rangle \tag{6.11}$$

where $< \cdot >$ is an average over different timefront realizations.

The pulse spread from experimental analyses [39] is supposed to include all pulse arrivals associated with a branch. Methods for identifying arrivals with branches have been developed [39], however it is unclear if these methods have really captured the intended pulse spread. Due to the continuous fluctuation front on the timefronts constructed in this work, the identification of peak arrivals with branches cannot be accomplished except arbitrarily. Therefore, the pulse widths and pulse spreads calculated in this section may not have any relevance to the pulse spreads discussed in the literature [12, 22].

Using the definition of spread in Eq. (6.11), the average pulse widths $< \sigma_t^\epsilon >$ of the arrivals at locations of well-separated branches are calculated for the perturbed timefronts and the ensemble model timefronts. These results are compared to the pulse widths $< \sigma_t^{\epsilon=0} >$ calculated from the arrivals of the unperturbed timefront in Fig. (6.30, 6.31). From these plots, it is difficult to ascertain the level of agreement of the ensemble model with the Perturbed

propagation due to the great uncertainty in the individual variances of the pulse widths. Colosi et. al.[39] stated that the spread quantity is several orders of magnitude smaller than the wander quantity described in the next section. However, the variations in these plots seem to be more related to the instability of the method for calculating spreads of pulses in individual timefronts.

The author believes that the quantity calculated as 'spread' is very small if at all existent for the present definition of the pulse spread. The identification of the pulse interval used in this thesis has likely not captured the pulse spread in the literature, but rather just the pulse width. This is all that could be calculated considering that there is a fluctuation front on the timefronts, so that peak arrivals can't really be associated with certain branches. The oscillations in the results are likely due to the slightly different asymmetrical shapes of the peak pulse arrivals.

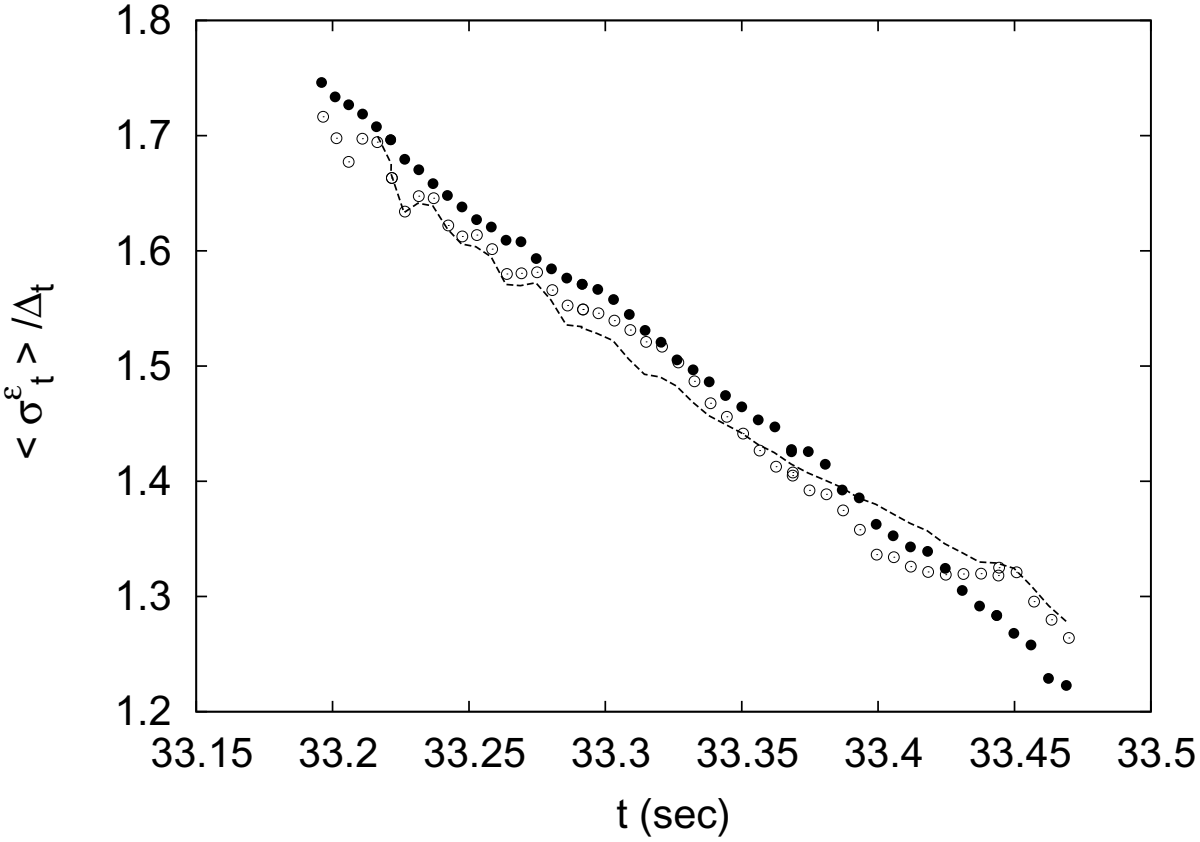

Figure 6.30: Average pulse widths $< \sigma_t >$ are scaled by the factor $\Delta_t = \frac{1}{\sqrt{2}c_0\sigma_k} \approx 6ms$ and plotted versus average pulse travel time t Average pulse widths are shown for the unperturbed timefront (dashed line), perturbed timefronts (solid line) and the ensemble timefronts (dotted line). Average pulse widths are shown only for the well-separated pulses on the branch with branch number $+2$. The calculation of the pulse widths for the perturbed propagation and ensemble model both use 1000 timefront realizations.

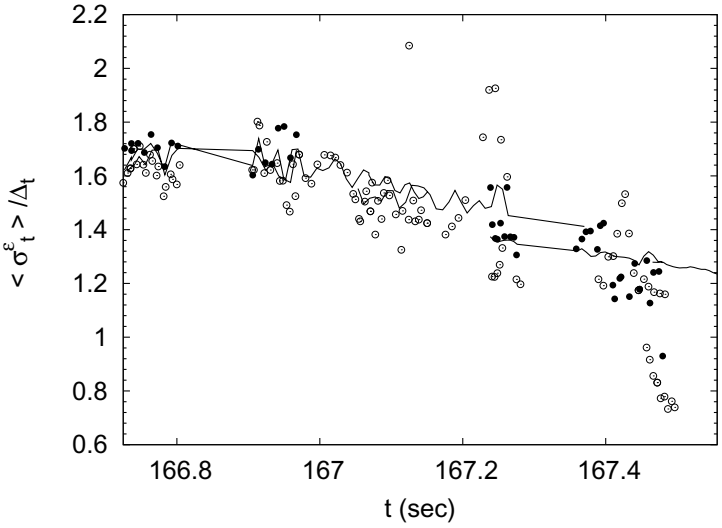

(a) Comparison of Perturbed and Unperturbed Pulse Widthsfor 250 km

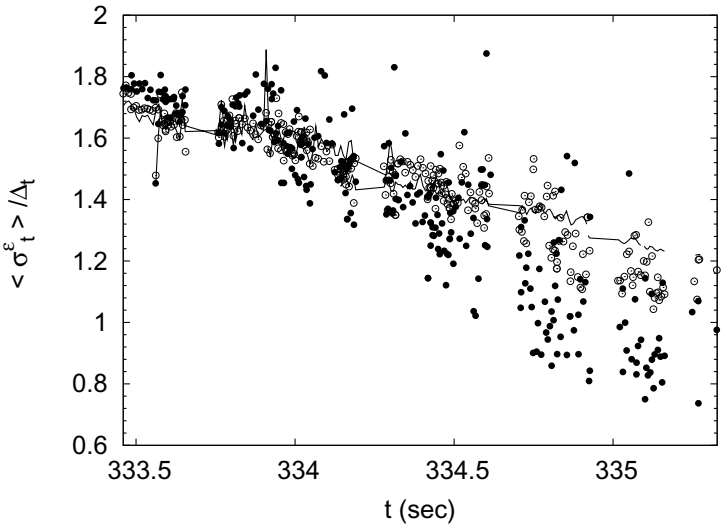

(b) Comparison of ensemble model and Unperturbed Pulse Widths for 500 km

Figure 6.31: Average pulse widths $< \sigma_t >$ are scaled by the factor $\Delta_t = \frac{1}{\sqrt{2}c_0\sigma_k} \approx 6ms$ and plotted versus average pulse travel time t for several ranges. The unperturbed pulse widths(solid line) are displayed along with the average pulse widths for the perturbed timefronts(open circle) and ensemble model(filled circle) timefronts. Average pulse widths are shown only for the well-separated pulses on the branch corresponding to the classical rays with initial angle $|\theta_0| \leq 15^\circ$. The calculation of the pulse width for the perturbed propagation uses 28 timefront realizations, while the calculation of the pulse width for the ensemble model uses 25 timefront realizations.

Pulse Wander

The pulse wander, σ_{μ_t}, is defined to be the standard deviation of the mean location, $\mu_t(z,n)$, of a branch for a single timefront realization ϵ from the average value of $\mu_t(z,n)$ over all ensemble timefronts where

$$\sigma^2_{\mu_t} \quad = \quad \langle (\mu_t - \langle \mu_t \rangle)^2 \rangle \tag{6.12}$$

where $< \cdot >$ is an average over different timefront realizations. The wander is a function of the depth z and the branch number n.

Using the procedure described previously for computing the variances and means of a well-separated pulse arrival, the standard deviation of the center locations of the pulse $< \mu_t >$ are compared for the ensemble model and the perturbed propagation timefronts. The results are compared in Fig. (6.32) and (6.33). Since there is no wander in the unperturbed pulse arrivals, the agreement of the wanders with respect to zero illustrates how well the ensemble model captures the effects of the perturbation. The results for 50 km in Fig. (6.32) show some agreement in the basic trend of the wander along the branch. The results for the other ranges in Fig. (6.33) show good agreement for the early arriving branches, but a lot of scatter in the wanders for the later arriving branches. Again, this seems to be due to some instability in calculating the wander of individual timefronts.

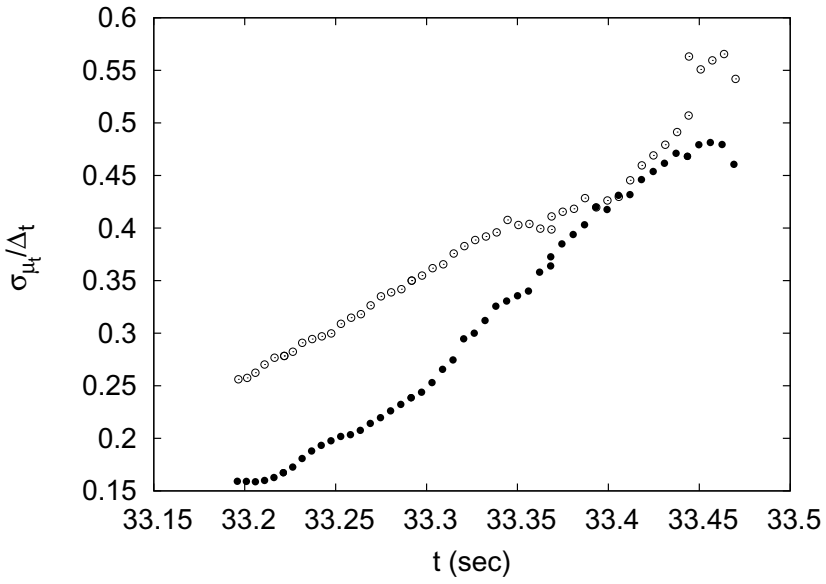

(a) Comparison of Pulse Wanders between ensemble model and Perturbed Propagation to 50 km

Figure 6.32: Pulse wanders σ_{μ_t} are scaled by the factor $\Delta_t = \frac{1}{\sqrt{2}c_0\sigma_k} \approx 6ms$ and plotted versus average pulse travel time t. The pulse wanders for the branches of the perturbed timefronts (open circles) and for the ensemble model timefronts (filled circles) are displayed. Pulse wanders are shown only for the well-separated pulses on the branch with branch number $+2$ corresponding to the classical rays with initial angle $|\theta_0| \leq 15\,^\circ$. The calculation of the pulse width for the perturbed propagation uses 2500 timefront realizations, while the calculation of the pulse width for the ensemble model uses 1000 timefront realizations.

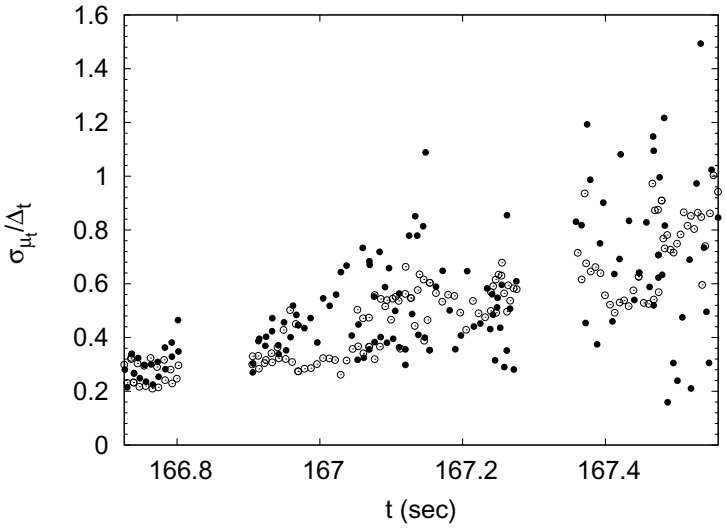

(a) Comparison of Pulse Wanders between ensemble model and Perturbed Propagation to 250 km

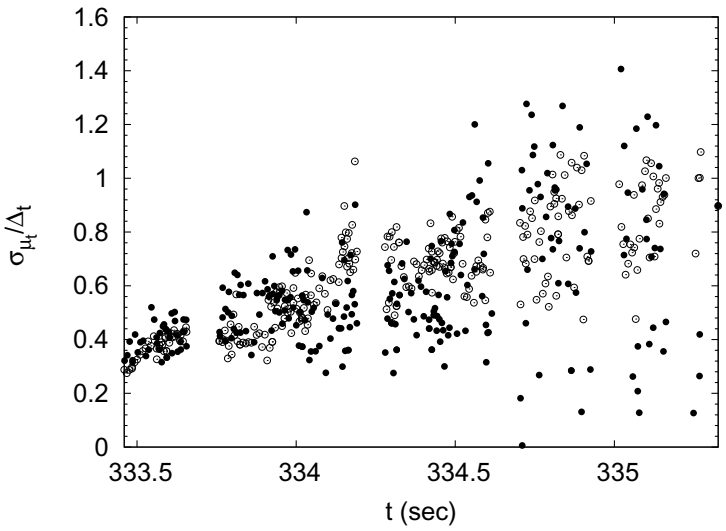

(b) Comparison of Pulse Wanders between ensemble model and Perturbed Propagation to 500 km

Figure 6.33: Pulse wanders σ_{μ_t} are scaled by the factor $\Delta_t = \frac{1}{\sqrt{2}c_0\sigma_k} \approx 6ms$ and plotted versus average pulse travel time t. The pulse wanders for the branches of the perturbed timefronts (open circles) and for the ensemble model timefronts (filled circles) are displayed. Pulse wanders are shown only for the well-separated pulses on the branches corresponding to the classical rays with initial angle $|\theta_0| \leq 15\,^\circ$. The calculation of the pulse width for the perturbed propagation uses 28 timefront realizations, while the calculation of the pulse width for the ensemble model uses 25 timefront realizations.

6.3 Comparison of Properties of Average Intensity Timefronts

An average of the intensity of the timefronts is appealing in the experimental analysis of timefronts because it serves to enhance the peak arrivals along the branches and further reduce the effects of the noise. In a review by Flatte [6], the statistical moments of the intensity of the timefronts were claimed to characterize the ensemble of timefronts. The first moment of intensity was utilized by Uffelen et. al. to analyse the 2004 Spice Experiments [41]. Colosi et. al. utilized a scintillation index - a combination of the first and second intensity moments to analyse the Acoustic Engineering Test experiments [59].

The average intensity is the average value of the intensity $|\phi(z,r,t)|^2$ over a set of N timefronts,

$$\langle I \rangle \quad = \quad \frac{1}{N} \sum_{i=1}^{i=N} |\phi(z,r,t)|^2 \; .$$

For long ranges, only average properties remain in the timefronts, so that the timefront from the average intensity field could characterize the properties of the long range timefronts very well.

6.3.1 Ensemble Model Prediction for Average Intensity Timefront

The ensemble model described in Ch. (5) contains only a minimal amount of information about the propagation and the resulting timefronts. This information can be elucidated by de-

riving the properties of the average intensity timefronts using approximate expressions from the ensemble model. The average value of the intensity $I_\epsilon = |\Phi_\epsilon(z,r,t)|^2$ of the timefront corresponding to the perturbed propagation with parameter ϵ is

$$\begin{aligned}\langle|\Phi_\epsilon(z,r,t)|^2\rangle = \frac{1}{2\pi\sigma_k^2 r}\sum_{n,m,p,q}\int_{-\infty}^{+\infty}\int_{-\infty}^{+\infty} & \quad dkdk'\, e^{-i(k-k')c_0\left(t-\frac{r}{c_0}\right)} \\ & \times \quad \exp\left[\frac{-(k-k_0)^2-(k'-k_0)^2}{2\sigma_k^2}\right] \\ & \times \quad a_n(k)a_q(k')\psi_m(z;k)\psi_p(z;k') \\ & \times \quad \langle C_{m,n}(k)C^*_{p,q}(k')\rangle\,, \end{aligned} \tag{6.13}$$

where the correlations $\langle C_{m,n}(k)C^*_{p,q}(k')\rangle$ are the important quantities.

The ensemble model for 50 km predicts that $C_{m,n} \approx e^{-ikrE_m+i\mu_{m,m}}\left(\delta_{m,n} - 2i\sigma_{A_{m,n}}z_{m,n}\right)$ so that since $\langle z_{m,n}(k)\rangle = 0$ and $\langle z_{m,n}(k)z^*_{p,q}(k')\rangle = \delta_{m,p}\delta_{n,q}$ for any wavenumbers k, k', the correlations predicted by the ensemble model for 50 km are approximately

$$\begin{aligned}\langle C_{m,n}(k)C_{p,q}(k')\rangle \quad \approx \quad & e^{-ikrE_m(k)+ik'rE_p(k')+i(\mu_{m,m}-\mu_{p,p})} \\ & \times\left(\delta_{m,n}\delta_{p,q} + 4\sigma_{A_{m,n}}(k)\sigma_{A_{p,q}}(k')\delta_{m,p}\delta_{n,q}\right)\,. \end{aligned} \tag{6.14}$$

Then the average intensity in Eq. (6.13) simplifies to

$$\langle I\rangle(z,t;r) \quad = \quad I_{\epsilon=0}(z,t;r) + \delta I_\epsilon(z,t;r)\,, \tag{6.15}$$

where

$$
\begin{aligned}
I_{\epsilon=0} = \frac{1}{2\pi\sigma_k^2 r} & \\
\sum_{n,m} \quad & \left(\int_{-\infty}^{+\infty} dk\, e^{-ikc_0\left(t-\frac{r}{c_0}\right)} \exp\left[\frac{-(k-k_0)^2}{2\sigma_k^2}\right] e^{-ikrE_m(k)+i\mu_{m,m}(k)} a_m(k)\psi_m(z;k) \right) \\
\times \quad & \left(\int_{-\infty}^{+\infty} dk'\, e^{-ik'c_0\left(t-\frac{r}{c_0}\right)} \exp\left[\frac{-(k'-k_0)^2}{2\sigma_k^2}\right] e^{-ik'rE_n(k')+i\mu_{n,n}(k')} a_n(k')\psi_n(z;k') \right)^*
\end{aligned}
\tag{6.16}
$$

and δI_ϵ are the deviations in the average intensity,

$$
\begin{aligned}
\delta I_\epsilon = \quad & \frac{\epsilon^2}{2\pi\sigma_k^2 r} \\
& \sum_{m,n} \left| \int_{-\infty}^{+\infty} dk\, e^{-ikc_0\left(t-\frac{r}{c_0}\right)} \exp\left[\frac{-(k-k_0)^2}{2\sigma_k^2}\right] 2\sigma_{A_{m,n}}(k) e^{-ikrE_m+i\mu_{m,m}} a_n(k)\psi_m(z;k) \right|^2 .
\end{aligned}
\tag{6.17}
$$

Note that the unperturbed timefront intensity using Eq. (6.3) is

$$
\begin{aligned}
|\Phi_{\epsilon=0}(z,r,t)|^2 = \quad & \sum_{n,m} \frac{1}{2\pi\sigma_k^2 r} \\
\times \quad & \left(\int_{-\infty}^{+\infty} dk\, e^{-ikc_0\left(t-\frac{r}{c_0}\right)} \exp\left[\frac{-(k-k_0)^2}{2\sigma_k^2}\right] e^{-ikrE_m(k)} a_m(k)\psi_m(z;k) \right) \\
\times \quad & \left(\int_{-\infty}^{+\infty} dk'\, e^{-ik'c_0\left(t-\frac{r}{c_0}\right)} \exp\left[\frac{-(k'-k_0)^2}{2\sigma_k^2}\right] e^{-ik'rE_n(k')} a_n(k')\psi_n(z;k') \right)^*
\end{aligned}
\tag{6.18}
$$

so that the only difference between Eq. (6.16) and Eq.(6.18) is the presence of the mean

phase factor $e^{i\mu_{n,n}(k)}$ in the integrand. The linear wavenumber dependence of $\mu_{m,m}(k)$ causes the resulting fourier transform in Eq. (6.16) to be time shifted from that of the unperturbed timefront $|\Phi_{\epsilon=0}(z,r,t)|^2$. The wavenumber dependence of the average phase of the diagonal elements $\mu_{m,m}$ when modelled with Eq. (4.20) can be approximated by the coefficients in Eq.(4.21). In Eq.(4.21), the linear coefficient $b_n \approx 0.0015km^{-1}$ for $n < 28$. This linear dependence of $\mu_{m,m}$ alone would result in a time shift of $t_0 = b_n/c_0 = 0.001$ s so that $I_{\epsilon=0}(z,t+0.001;r) = |\phi_\epsilon(z,t;r)|^2$, for the unperturbed timefront $|\phi_\epsilon(z,t;r)|^2$. Surprisingly, this is consistent with the time biases estimated by Colosi et. al. [39] for a single cycle of the classical rays. This is consistent with the bias from the building block since the length for the building block is 50 km - an average period for the cycle of the classical rays. Clearly for no perturbations, $\epsilon = 0$, $\sigma_{A_{m,n}} = 0$ and $\mu_{n,n} = 0$, Eq. (6.16) reduces to Eq.(6.18) so that $I_{\epsilon=0} = |\Phi_{\epsilon=0}(z,r,t)|^2$, as it should.

The deviations δI_ϵ in Eq. (6.17) describe the intensity of a timefront created from the sum of all the intensities due to a modal contribution $C_{m,n} = 2\sigma_{A_{m,n}} e^{-ikrE_m + i\mu_{m,m}}$. Since $\sigma^2_{C_{m,n}} = 4\sigma^2_{A_{m,n}}$ in the ensemble model, these intensities represent the differences in the modal contribution from the unperturbed result $C_{m,n} = e^{-ikrE_m}$, where the magnitude of the difference is approximated by one standard deviation over the variation in the magnitudes. The phase $\mu_{n,n}$ in the fluctuations achieves the same time shift as the unperturbed timefront. As ϵ increases from zero, $\sigma_{A_{m,n}}$ and $\mu_{n,n}$ capture information about the changing structure of the timefront.

The deviations δI_ϵ in Eq. (6.17) have the same basic shape with depth, as shown in Fig. (6.34). The similar structure for $z = 0.5$ km and $z = 1.5$ km suggests there is a sym-

metry in the structure about the sound channel axis $z = 1.0$ km. The shape of the fluctuation structure peaks near $t = \frac{r}{c_0}$, $z = 1.0$ km, with a sharp decay for $t > \frac{r}{c_0}$ and a longer decay for $t < \frac{r}{c_0}$. The decay for $t > \frac{r}{c_0}$ looks to be the same with depth. However, the decay for $t < \frac{r}{c_0}$ varies with depth, with longer decay scales for depths farther from the sound channel axis.

The ensemble model gives the timefront at 50 km two characteristic features. First, the mean phases $\mu_{m,m}$ shift the perturbed timefront from the unperturbed timefront. Second, the deviations from the shifted unperturbed timefront are captured by a variance matrix $\sigma_{A_{m,n}}$, which gives an average size to the mode transitions.

This picture of the ensemble of timefronts is consistent with the discussion in Sec. (6.1.3), in which the traces of the perturbed timefront look to be composed of two contributions - the time shifted unperturbed timefront and a fluctuation front.

The deviations δI_ϵ can be split into diagonal and off-diagonal contributions,

$$\delta I_\epsilon(z,t;r) \;=\; \delta I_\epsilon^{n=m}(z,t;r) + \delta I_\epsilon^{n\neq m}(z,t;r)\;, \tag{6.19}$$

where

$$\begin{aligned}\delta I_\epsilon^{m=n} \;=\; & \frac{\epsilon^2}{\pi\sigma_k^2 r}\sum_n \\ & \times\left|\int_{-\infty}^{+\infty} dk\; e^{-ikc_0\left(t-\frac{r}{c_0}\right)}\exp\left[\frac{-(k-k_0)^2}{2\sigma_k^2}\right]\sigma_{A_{n,n}}(k)e^{-ikrE_n+i\mu_{n,n}}a_n(k)\psi_n(z;k)\right|^2\;,\end{aligned} \tag{6.20}$$

and

$$\delta I_{\epsilon}^{m\neq n} = \frac{\epsilon^2}{\pi\sigma_k^2 r} \times \sum_{m,n}^{m\neq n} \times \left| \int_{-\infty}^{+\infty} dk\, e^{-ikc_0\left(t-\frac{r}{c_0}\right)} \exp\left[\frac{-(k-k_0)^2}{2\sigma_k^2}\right] \sigma_{A_{m,n}}(k) e^{-ikrE_m + i\mu_{m,m}} a_n(k)\psi_m(z;k) \right|^2 . \tag{6.21}$$

Figure (6.35) illustrates the contributions of the diagonal elements $m = n$ in Eq. (6.20) to the sum in Eq. (6.17). The diagonal elements capture almost all of the fluctuation structure for the sound channel axis $z = 1.0$ km. For the other depths shown in Fig. (6.35), the off-diagonal elements contribute an approximately constant amount to the intensity across the timefront.

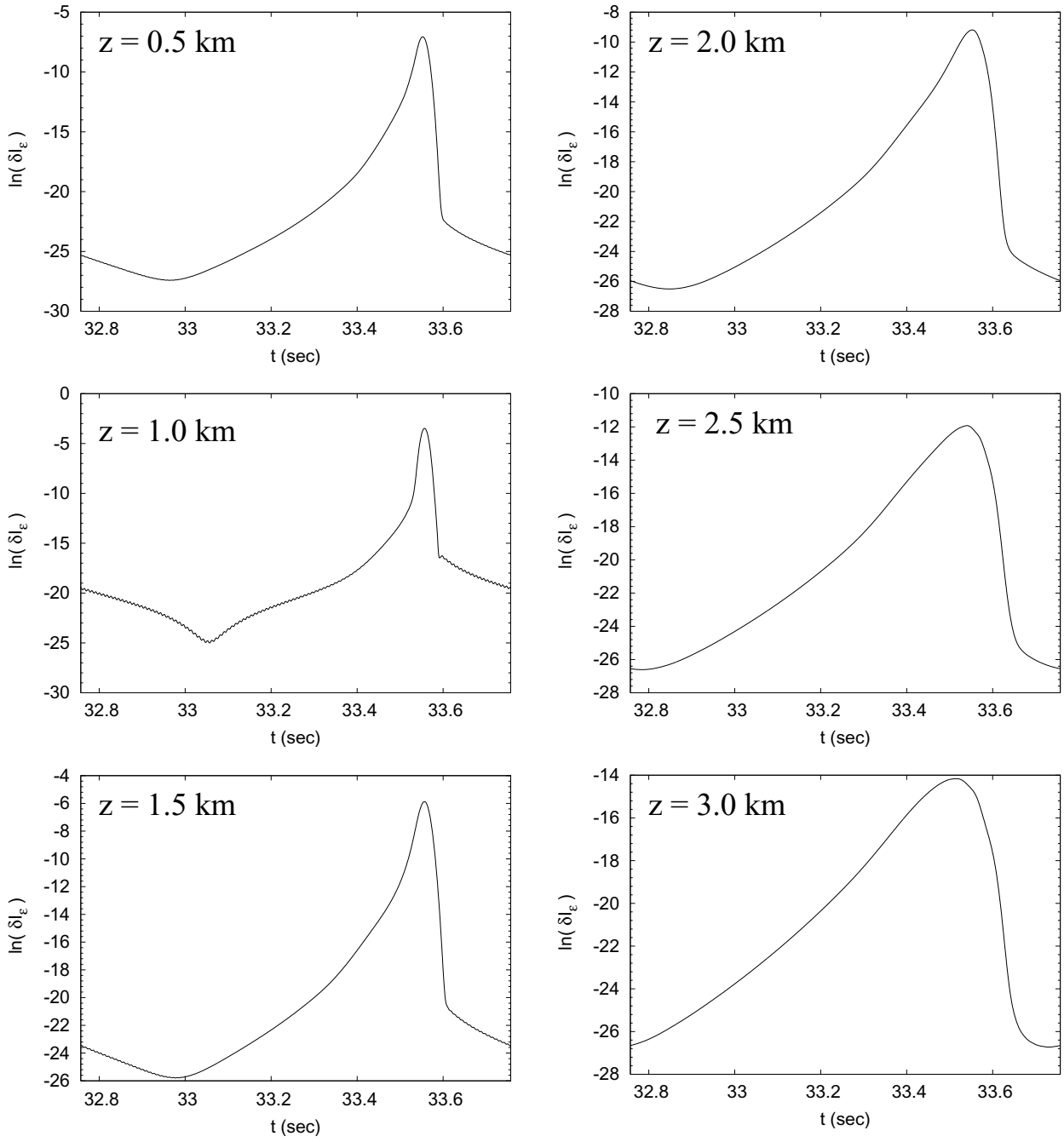

Figure 6.34: The fluctuation front δI_ϵ in Eq. (6.17) (with $\mu_{n,n} = 0$) are plotted with travel time for several depths z. These are the fluctuations predicted by the ensemble model for the average intensity timefronts for 50 km.

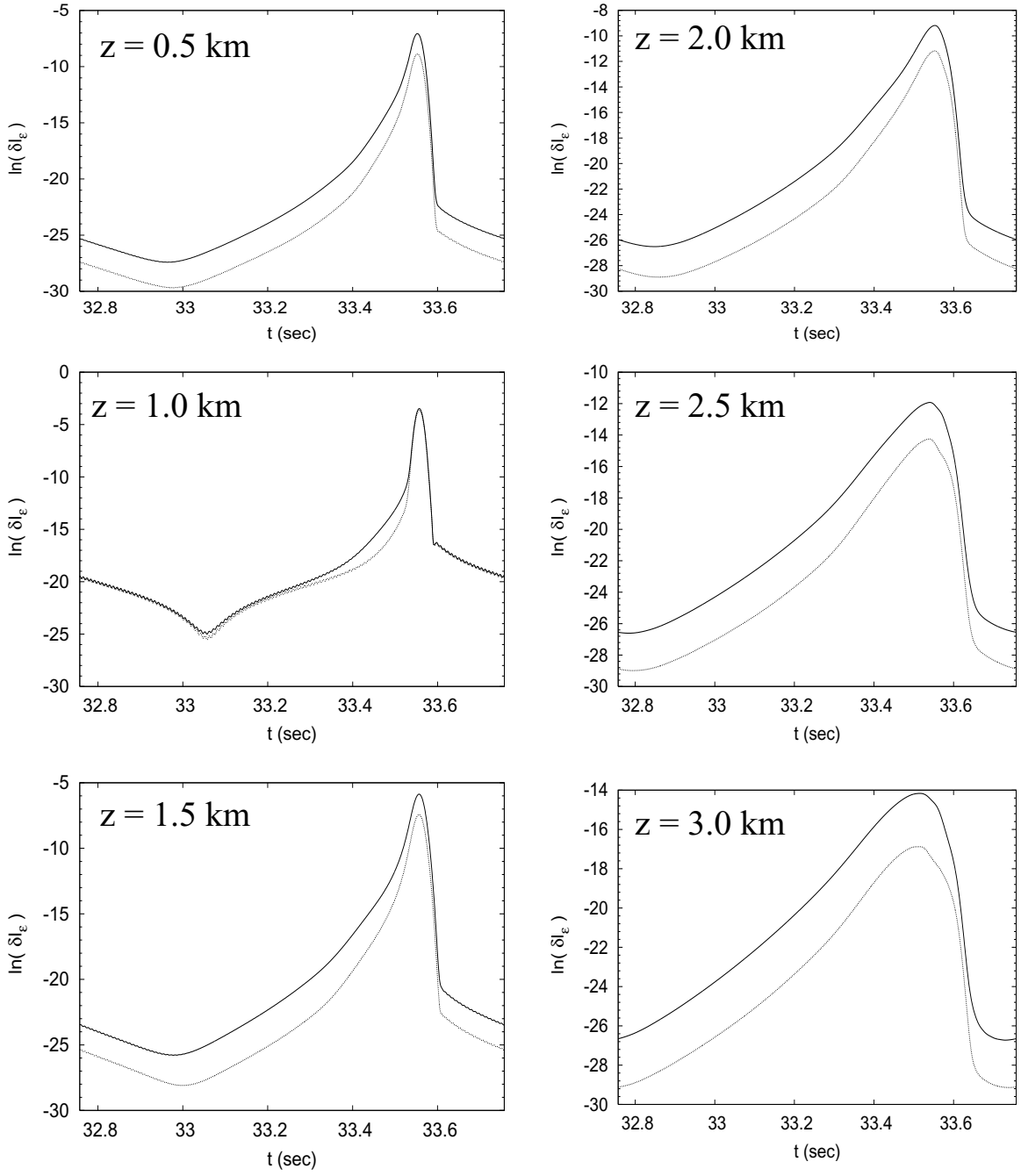

Figure 6.35: The fluctuations front δI_ϵ in Eq. (6.17) (with $\mu_{n,n} = 0$) are plotted (solid line) with travel time for several depths z. The contributions from the diagonal elements in Eq. (6.20) are plotted (dotted line) with travel time for several depths z. These are the fluctuations predicted by the ensemble model for the average intensity timefronts for 50 km.

6.3.2 Sample Average Intensity Timefronts

The average intensity in Eq. (6.13) is calculated for a set of timefront realizations from the ensemble model, the long range ensemble model and from the perturbed propagation. The degree to which the ensemble model is capturing the average intensity for propagation to 50 km is shown in Fig. (6.36). The degree to which the long range ensemble model is capturing the average intensity for longer ranges is shown in Figs.(6.38)-(6.44).

From these figures, one can see that the average intensity field is dominated by two structures. First, the average intensity field has the structure of the unperturbed timefront. Second, the average intensity field has a structure due to the fluctuations which peaks at the location $(z, t) = (1, r/c_0)$ and decays in both depth and time.

The rate of decay in both depth and time of this structure gives a signature for the effect of the fluctuations. The structure due to the fluctuations has the basic shape of the fluctuations δI_ϵ in Eq. (6.17) and shown in Fig. (6.34). However, though the basic structure of the fluctuations predicted by the ensemble model is approximately correct, the fluctuation scale is too large. This is especially pronounced in the depths $z = 2.0, 2.5, 3.0$ km. Also the structure due to the fluctuations in the ensemble model timefronts do not decay as fast as they do in the perturbed timefronts. This leads to poorer resolution of the branches for the ensemble model timefronts, as a larger portion of the timefront for the ensemble model timefronts is dominated (drowned out) by the structure due to the fluctuations. This suggests that the variance matrix in the ensemble model could be rescaled so that the shape of the fluctuations δI_ϵ match up better with the acoustic fluctuations.

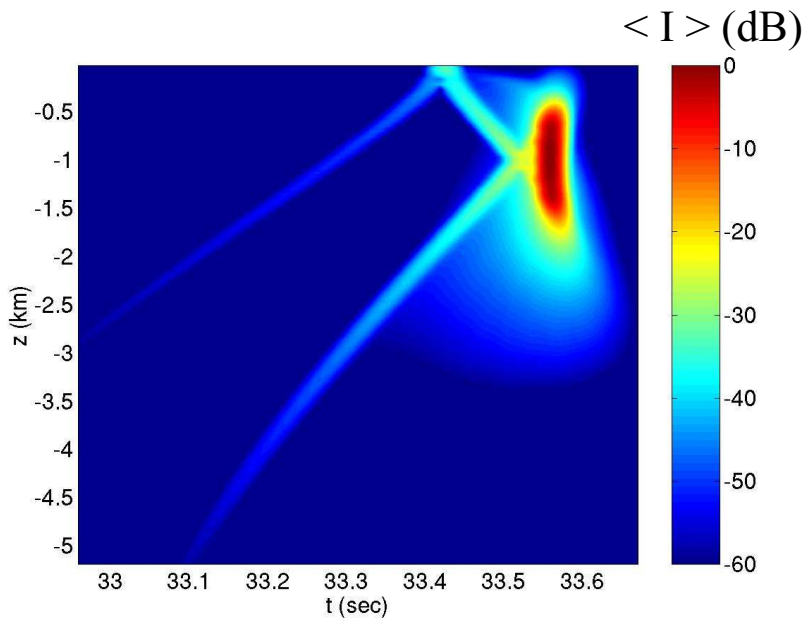

(a) Average Intensity of Timefronts from Propagation for 50 km

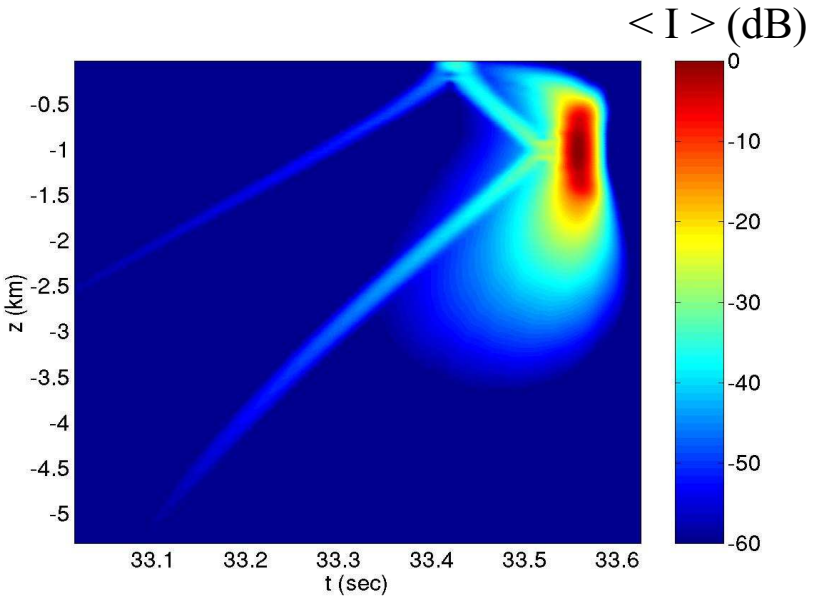

(b) Average Intensity of Timefronts from ensemble model for 50 km

Figure 6.36: The average intensity $\langle I \rangle = \langle |\phi|^2 \rangle$ is shown as a contour plot with depth z and time t of the timefronts. (Upper) The average is taken over timefronts from the propagation through 2500 independent sound speed models to 50 km. (Lower) The average is taken over timefronts resulting from 1000 independent random matrices for 50 km.

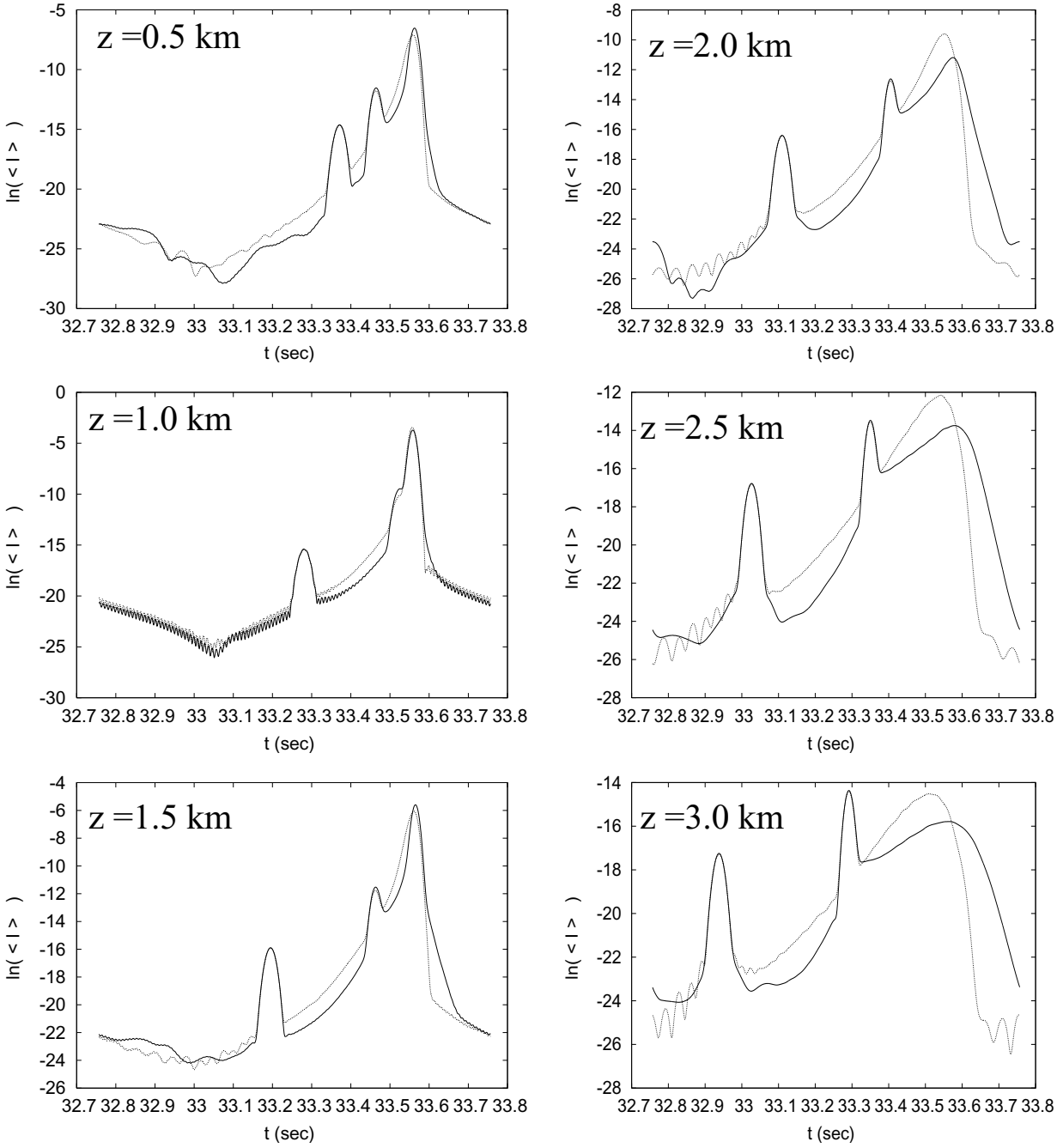

Figure 6.37: Traces of the average intensity $\langle I \rangle = \langle |\phi|^2 \rangle$ are shown for several final depths z as a function of time t. The average of the perturbed timefronts (solid line) is taken over timefronts from the propagation through 2500 independent sound speed models to 50 km. The average of the ensemble model timefronts (dotted line) is taken over timefronts resulting from 1000 independent random matrices for 50 km.

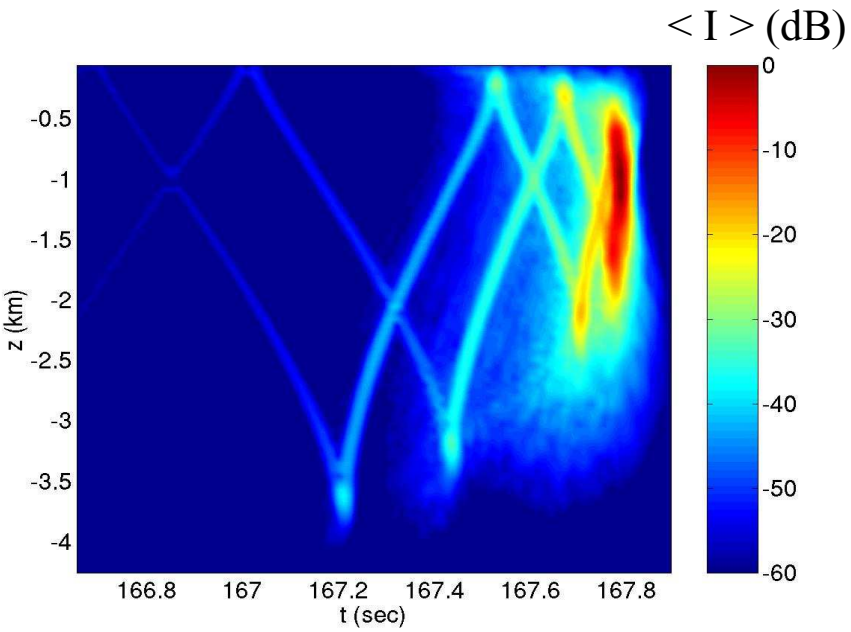

(a) Average Intensity of Timefronts from Propagation for 250 km

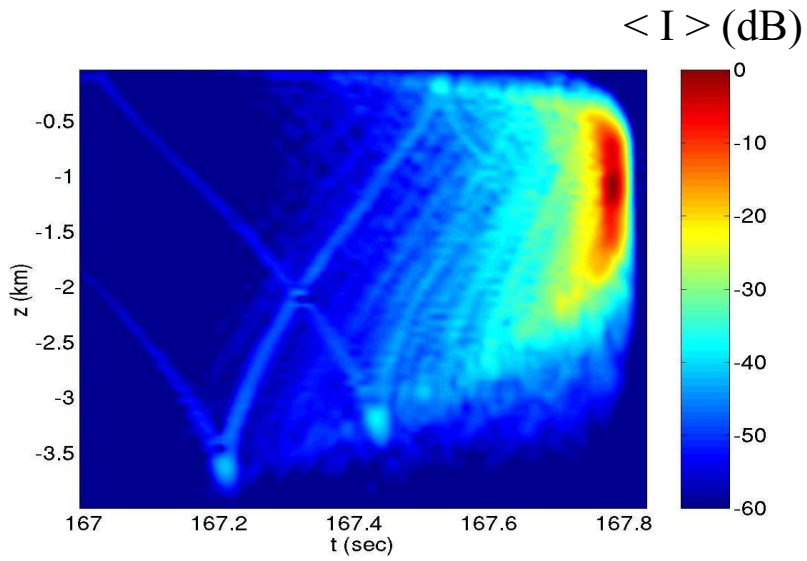

(b) Average Intensity of Timefronts from ensemble model for 250 km

Figure 6.38: The average intensity $\langle I \rangle = \langle |\phi|^2 \rangle$ is shown as a contour plot with depth z and time t of the timefronts. (Upper) The average is taken over timefronts from the propagation through 28 independent sound speed models to 250 km. (Lower) The average is taken over timefronts resulting from 25 independent random matrices for 250 km.

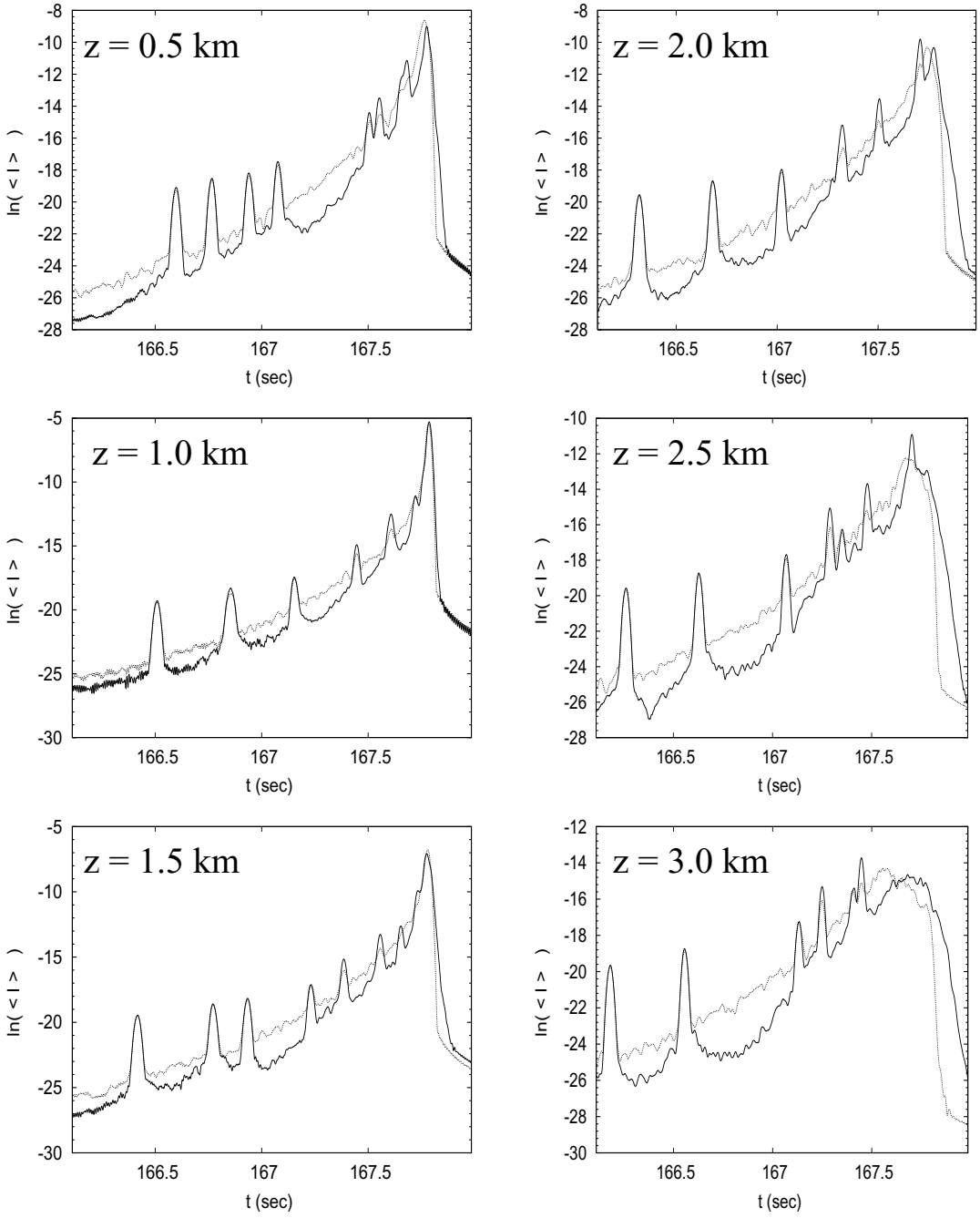

Figure 6.39: Traces of the average intensity $\langle I \rangle = \langle |\phi|^2 \rangle$ are shown for several final depths z as a function of time t. The average of the perturbed timefronts (solid line) is taken over timefronts from the propagation through 2500 independent sound speed models to 250 km. The average of the ensemble model timefronts (dotted line) is taken over timefronts resulting from 1000 independent random matrices for 250 km.

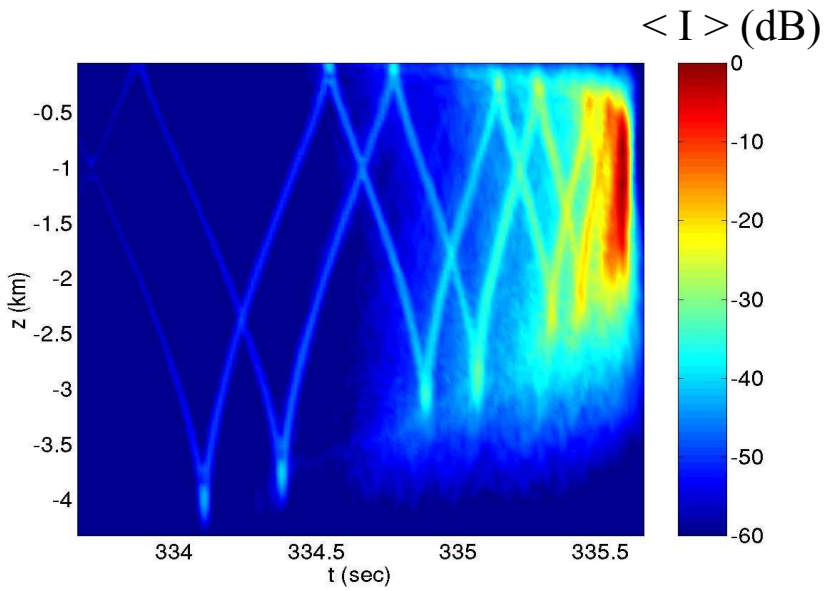

(a) Average Intensity of Timefronts from Propagation for 500 km

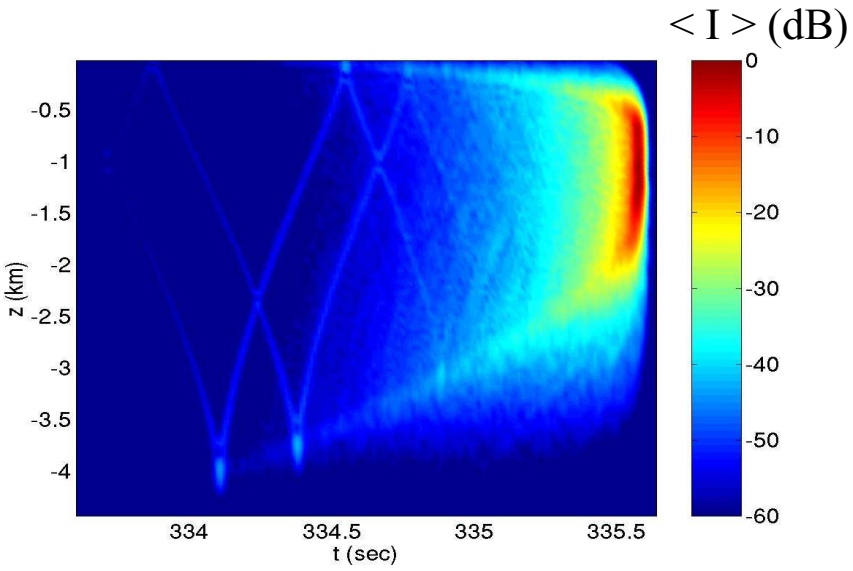

(b) Average Intensity of Timefronts from ensemble model for 500 km

Figure 6.40: The average intensity $\langle I \rangle = \langle |\phi|^2 \rangle$ is shown as a contour plot with depth z and time t of the timefronts. (Upper) The average is taken over timefronts from the propagation through 28 independent sound speed models to 500 km. (Lower) The average is taken over timefronts resulting from 25 independent random matrices for 500 km.

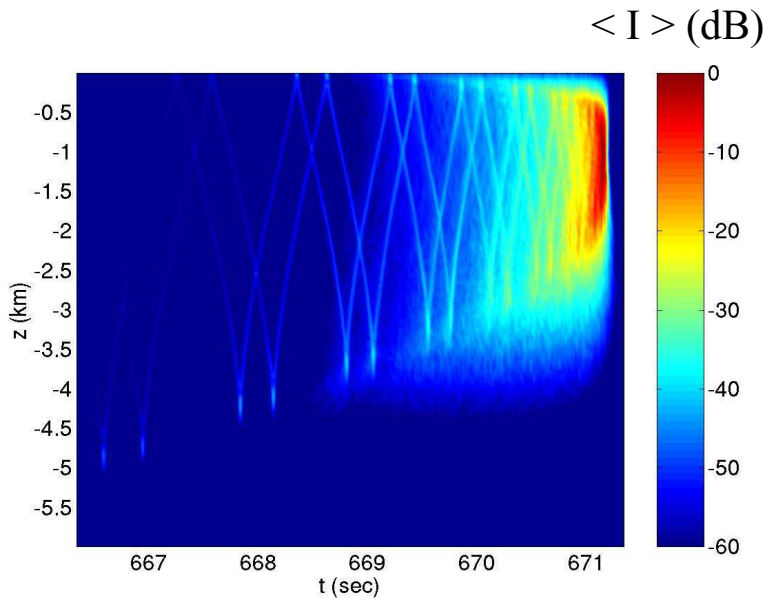

(a) Average Intensity of Timefronts from Propagation for 1000 km

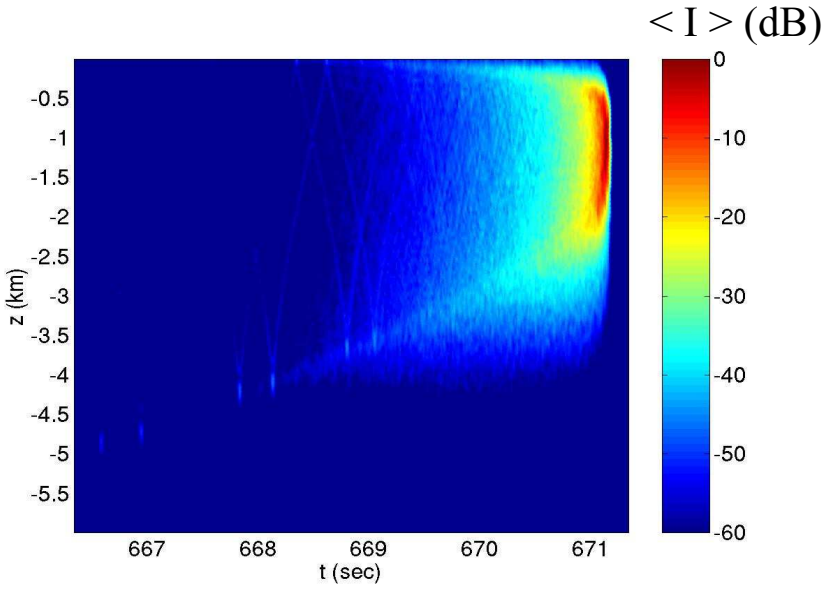

(b) Average Intensity of Timefronts from ensemble model for 1000 km

Figure 6.41: The average intensity $\langle I \rangle = \langle |\phi|^2 \rangle$ is shown as a contour plot with depth z and time t of the timefronts. (Upper) The average is taken over timefronts from the propagation through 28 independent sound speed models to 1000 km. (Lower) The average is taken over timefronts resulting from 25 independent random matrices for 1000 km. Note: the deep arrivals are a result of aliasing of the signal from earlier times.

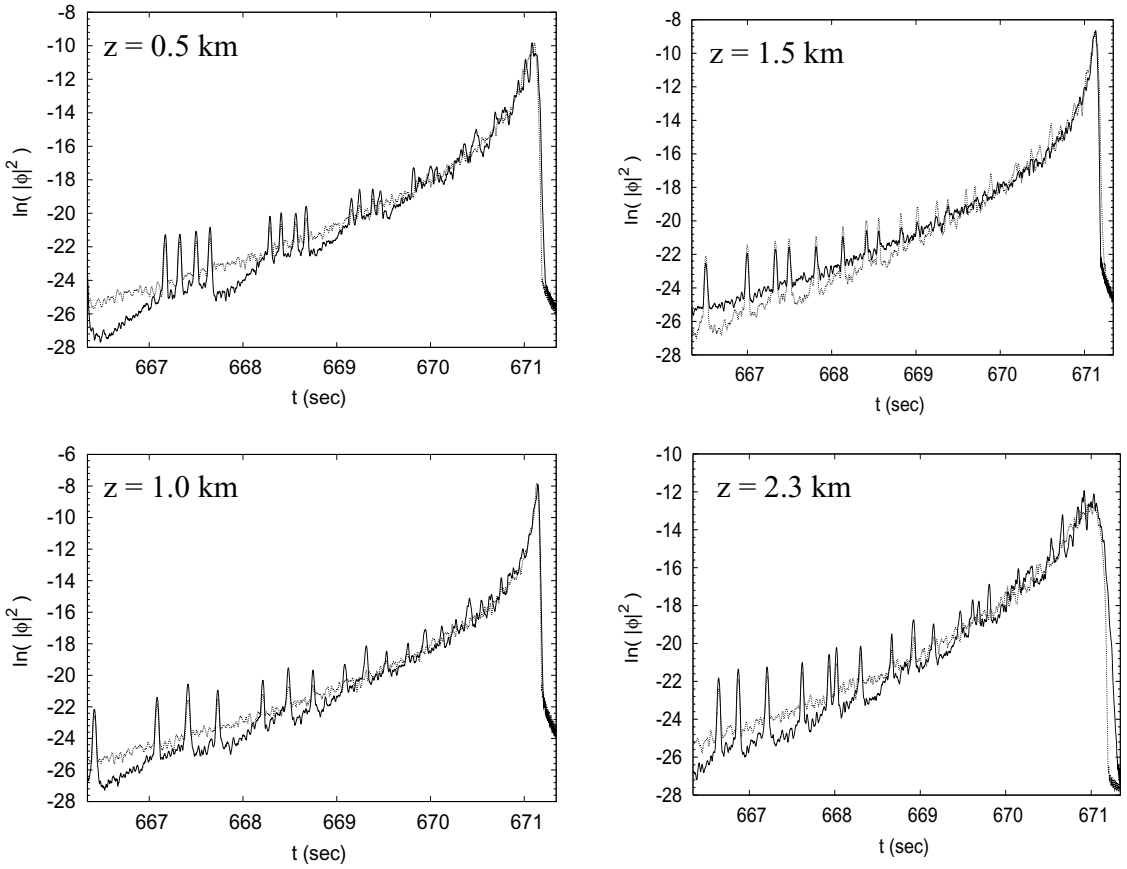

Figure 6.42: Traces of the average intensity $\langle I \rangle = \langle |\phi|^2 \rangle$ are shown for several final depths z as a function of time t. The average of the perturbed timefronts (solid line) is taken over timefronts from the propagation through 2500 independent sound speed models to 1000 km. The average of the ensemble model timefronts (dotted line) is taken over timefronts resulting from 1000 independent random matrices for 1000 km.

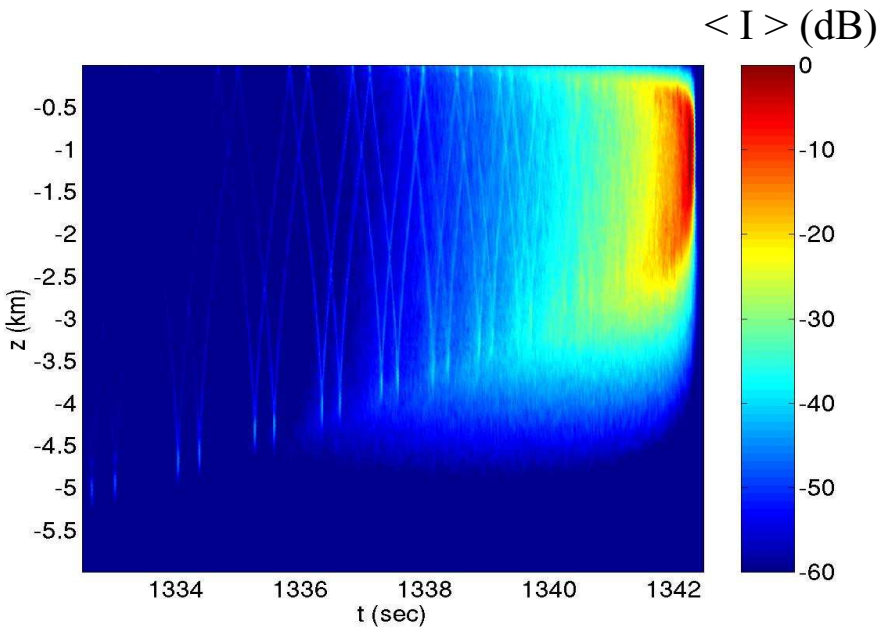

(a) Average Intensity of Timefronts from Propagation for 2000 km

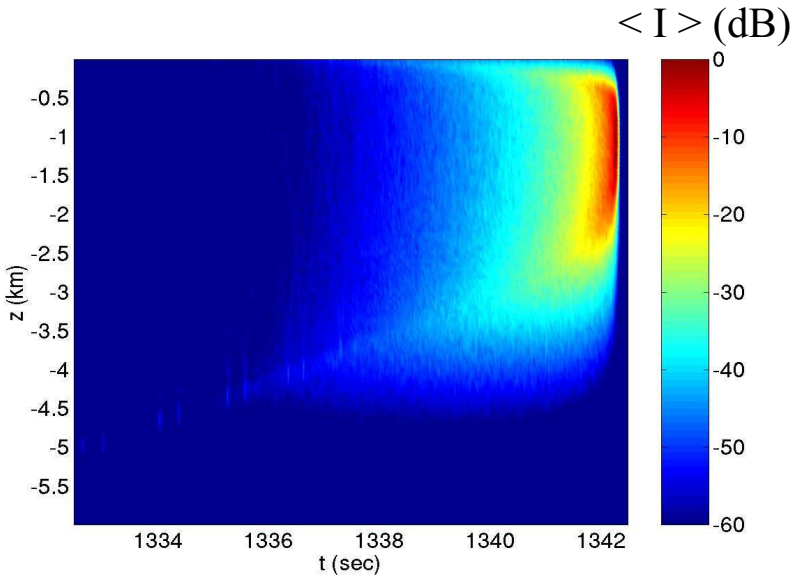

(b) Average Intensity of Timefronts from ensemble model for 2000 km

Figure 6.43: The average intensity $\langle I \rangle = \langle |\phi|^2 \rangle$ is shown as a contour plot with depth z and time t of the timefronts. (Upper) The average is taken over timefronts from the propagation through 28 independent sound speed models to 2000 km. (Lower) The average is taken over timefronts resulting from 25 independent random matrices for 2000 km. Note: the deep arrivals are a result of aliasing of the signal from earlier times.

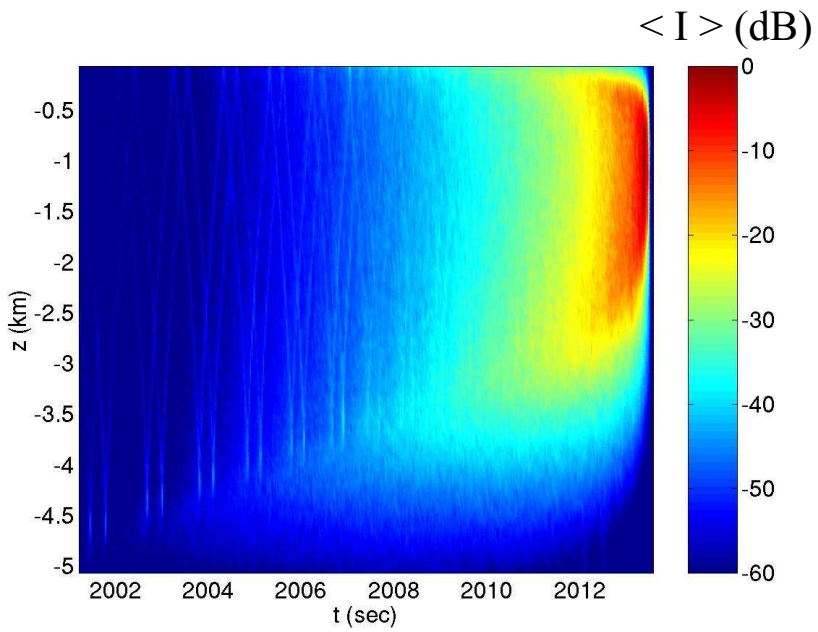

(a) Average Intensity of Timefronts from Propagation for 3000 km

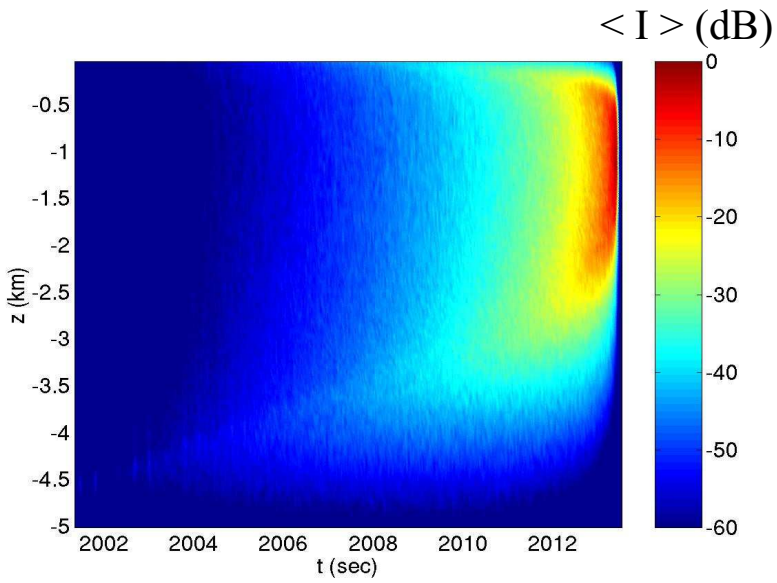

(b) Average Intensity of Timefronts from ensemble model for 3000 km

Figure 6.44: The average intensity $\langle I \rangle = \langle |\phi|^2 \rangle$ is shown as a contour plot with depth z and time t of the timefronts. (Upper) The average is taken over timefronts from the propagation through 28 independent sound speed models to 3000 km. (Lower) The average is taken over timefronts resulting from 25 independent random matrices for 3000 km.

6.3.3 Decay of Finale Region in Average Intensity Timefronts

The finale region of the average intensity timefronts for long ranges does not contain much structure beside the unperturbed arrivals and the fluctuation front. The fluctuation front can be described by the rate of decay from the finale in 1) depth and 2) time from the approximate location of the peak, $(z, t) = (1km, r/c_0)$. The decay of the average intensity timefronts for the perturbed timefronts and the ensemble model timefronts are compared in Figs. (6.45)-(6.47) in both the horizontal (time) and vertical (depth) directions for several ranges.

The rate of decay of the timefront with time between the ensemble model and perturbed propagation is very similar. For the building block range of 50 km, the decay of the fluctuation front in the ensemble model with time is very similar to the decay of the front from the propagation in Fig. (6.45), but is larger by a scale factor between the unperturbed arrivals. For the range of 250 km, the ensemble model decays with time again with a very similar decay scale in time as in Fig. (6.46), but again is larger by a scale factor between the unperturbed arrivals. This difference in scale is largest for the earliest arrivals for the range of 1000 km in Fig. (6.47).

The rate of decay of the timefront with depth between the ensemble model and perturbed propagation is very similar. The agreement is best near the sound channel $z = z_0$ in Figs. (6.46) -(6.47). The decay in depth of timefront of the ensemble model is slightly faster than the decay in depth of the timefront from the propagation both above and below the sound channel axis.

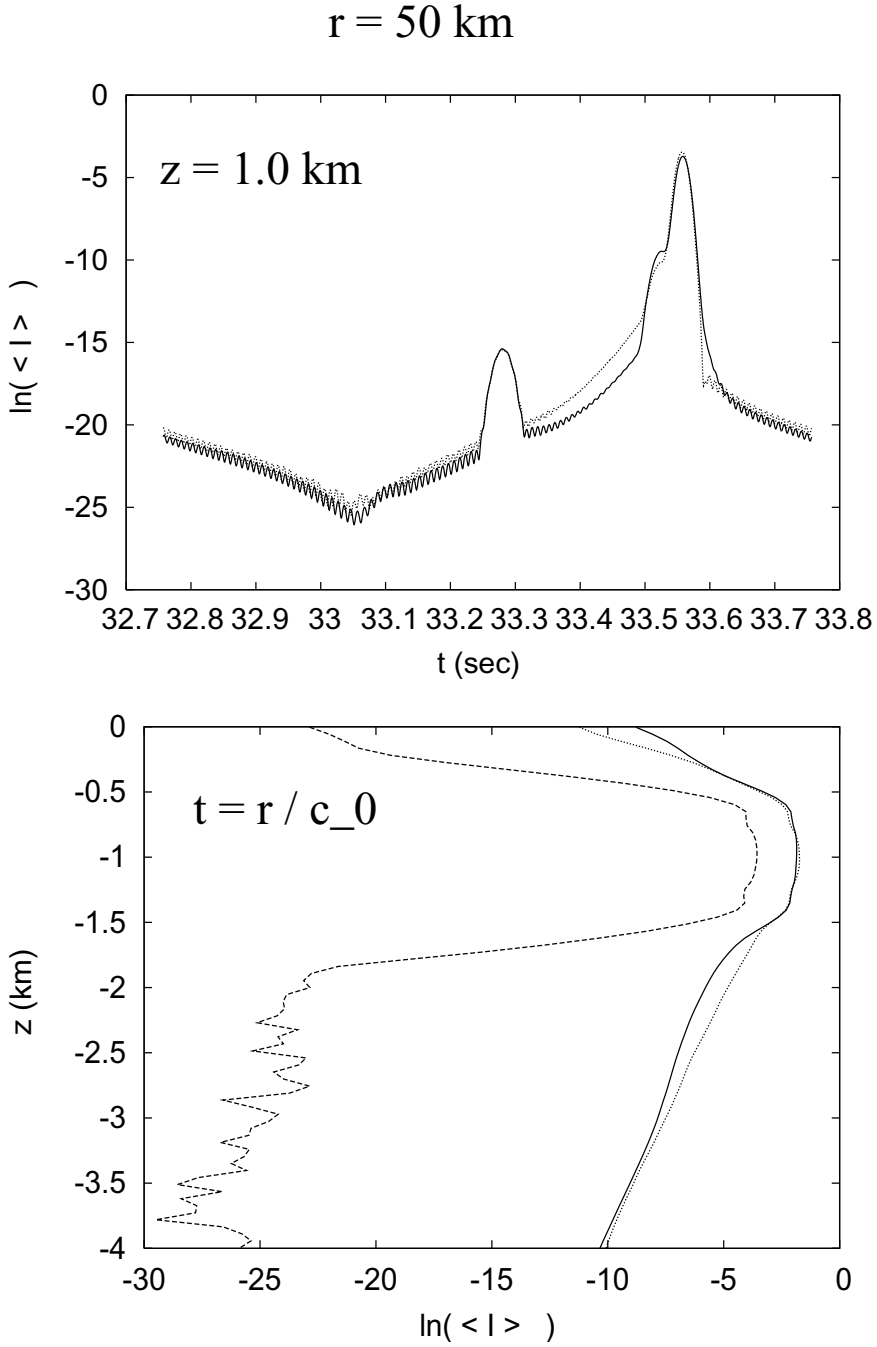

Figure 6.45: Vertical and Horizontal Decay of Finale Intensity from $(z, t) = (1.0, r/c_0)$ at 50 km. (Upper) The average intensity $\langle I \rangle = \langle |\phi|^2 \rangle$ is plotted as a trace along the sound channel axis $z = 1.0$ km as a function of time t. (Lower) The average intensity $\langle I \rangle = \langle |\phi|^2 \rangle$ is plotted for the time $t = r/c_0$ as a function of final depth z. The average of the perturbed timefronts (solid line) is taken over timefronts from the propagation through 2500 independent sound speed models to 50 km. The average of the ensemble model timefronts (dotted line) is taken over timefronts resulting from 1000 independent random matrices for 50 km. The decay of the unperturbed timefront (dashed line) is also plotted for 50 km.

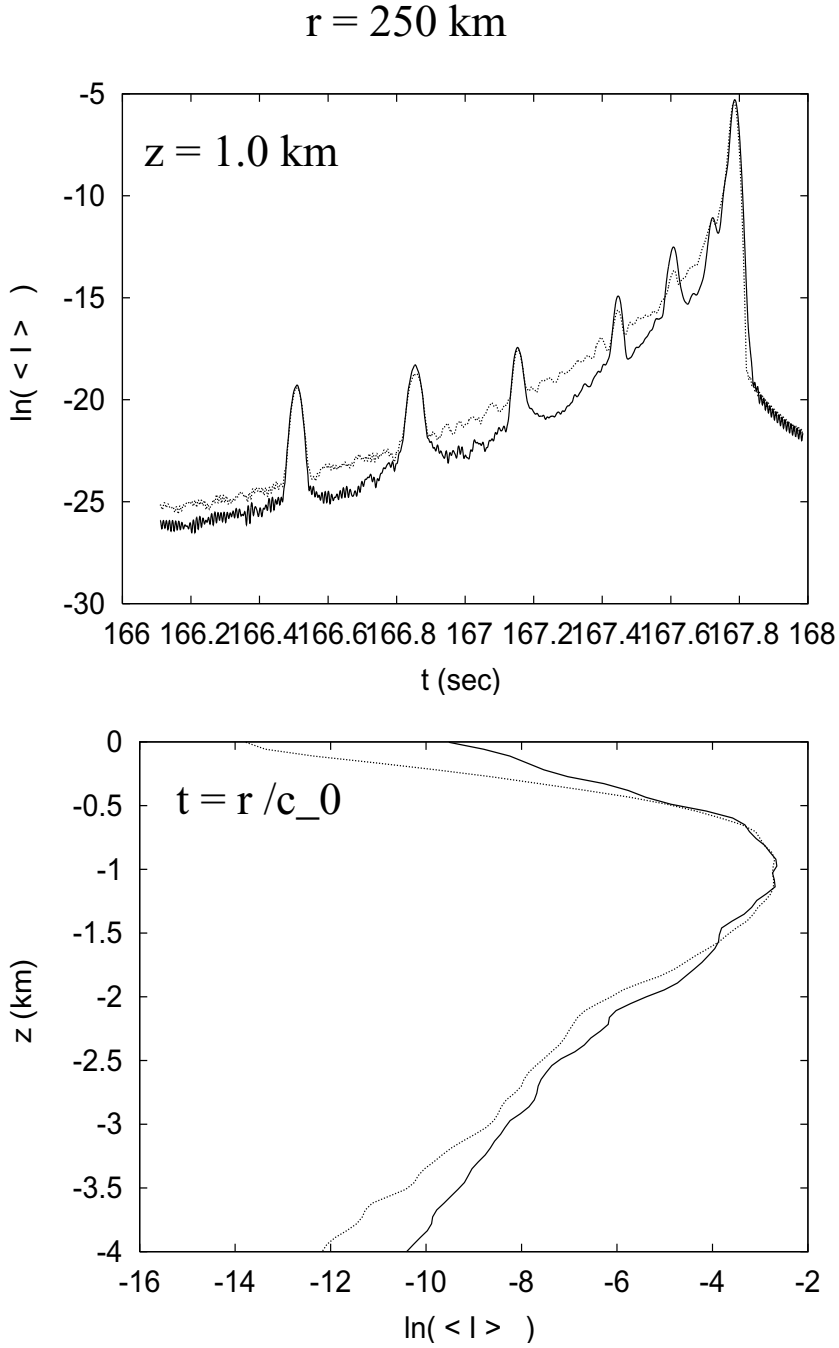

Figure 6.46: Vertical and Horizontal Decay of Finale Intensity from $(z, t) = (1.0, r/c_0)$ at 250 km. (Upper) The average intensity $\langle I \rangle = \langle |\phi|^2 \rangle$ is plotted as a trace along the sound channel axis $z = 1.0$ km as a function of time t. (Lower) The average intensity $\langle I \rangle = \langle |\phi|^2 \rangle$ is plotted for the time $t = r/c_0$ as a function of final depth z. The average of the perturbed timefronts (solid line) is taken over timefronts from the propagation through 2500 independent sound speed models to 250 km. The average of the ensemble model timefronts (dotted line) is taken over timefronts resulting from 1000 independent random matrices for 250 km.

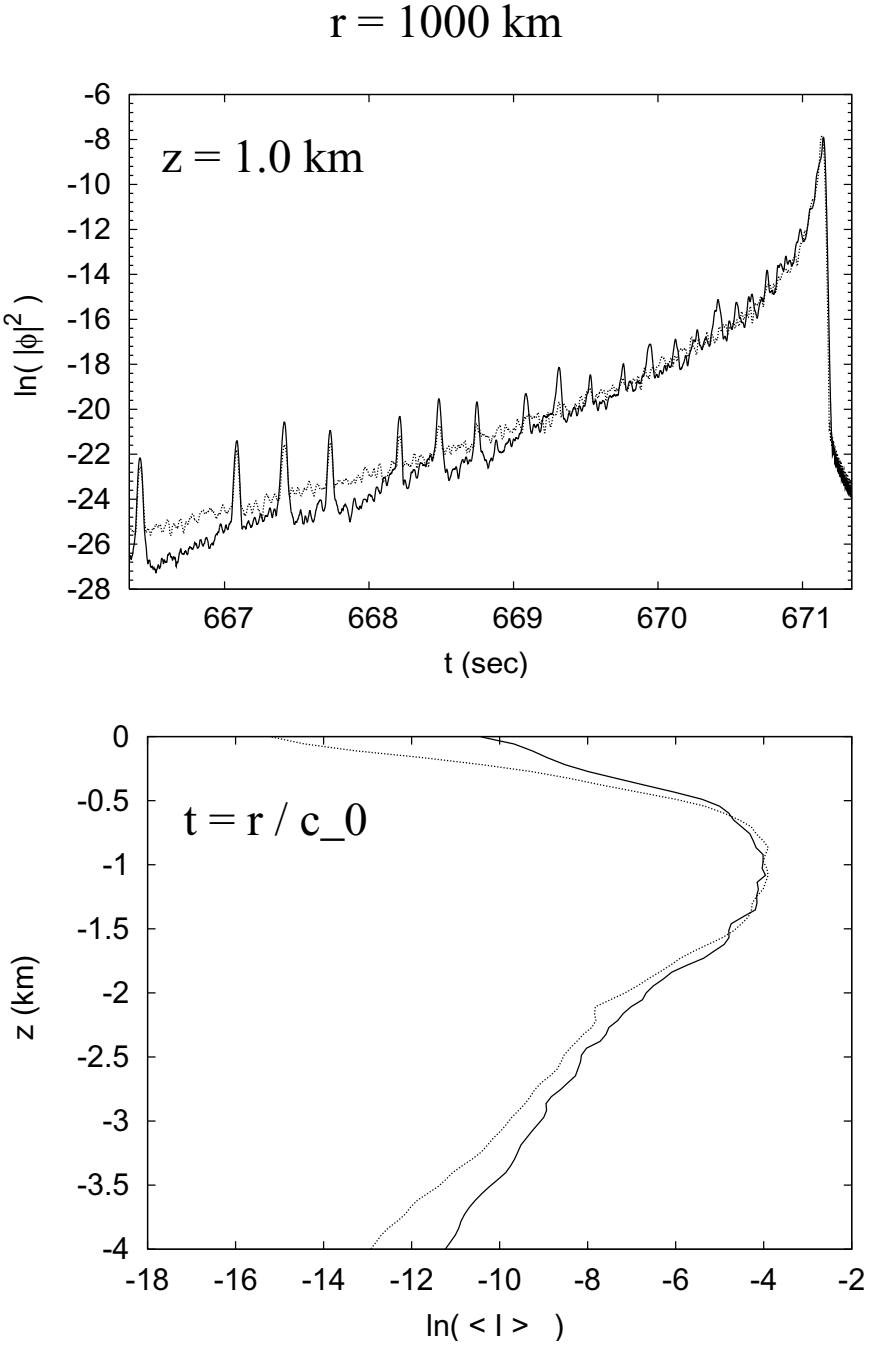

Figure 6.47: Vertical and Horizontal Decay of Finale Intensity from $(z, t) = (1.0, r/c_0)$ at 1000 km. (Upper) The average intensity $\langle I \rangle = \langle |\phi|^2 \rangle$ is plotted as a trace along the sound channel axis $z = 1.0$ km as a function of time t. (Lower) The average intensity $\langle I \rangle = \langle |\phi|^2 \rangle$ is plotted for the time $t = r/c_0$ as a function of final depth z. The average of the perturbed timefronts (solid line) is taken over timefronts from the propagation through 2500 independent sound speed models to 1000 km. The average of the ensemble model timefronts (dotted line) is taken over timefronts resulting from 1000 independent random matrices for 1000 km.

6.3.4 Pulse Width of Average Intensity Timefront

The uncertainty in the pulse width of the branches of individual timefronts makes it difficult to draw a conclusion as to if the ensemble model captures the information of spread and wander in the Perturbed Timefront. One way to get at the sum of the spread and wander is to consider the pulse width $\Delta\sigma_{\langle I\rangle}$ of branches of the average intensity timefront $\langle I\rangle$,

$$\Delta\sigma_{\langle I\rangle} \quad = \quad \sigma^{\epsilon}_{\langle I\rangle}(z,n) - \sigma^{\epsilon=0}_{t}(z,n)\rangle \ . \tag{6.22}$$

By performing the averaging over the timefront first, the timefronts are smoother and more easily processed by the methods to extract a pulse width. This quantity is more stable to calculate than either Eq. (6.11) or (6.12). Since the branches of the average timefront widen due to either a wander in the mean time of individual pulse arrivals or due to the width of individual pulse arrivals, the pulse width of the average intensity captures information about the sum of the spread and the wander.

Figures (6.48)-(6.50) illustrate the pulse width of the average timefront for the perturbed timefronts and the ensemble model timefront in comparison to the pulse width of the unperturbed timefronts for several ranges and compares the pulse width of the average intensity $\Delta\sigma_{\langle I\rangle}$ for the perturbed timefronts and ensemble model timefronts. The average pulse width shows the clearest trend for 50 km in Fig. (6.48), where the ensemble model does capture approximately the right scale for the pulse width of the average intensity and the linear decrease with travel time from $t = \frac{r}{c_0}$ for one branch of the timefront. However, the average pulse widths for larger ranges in Fig. (6.49)- (6.50) do not have such clear trends. There is a

broadening of the pulse width of the average intensity timefront from that of the unperturbed timefront. The ensemble model seems to capture some of this broadening, especially for the earlier arriving branches in the timefront.

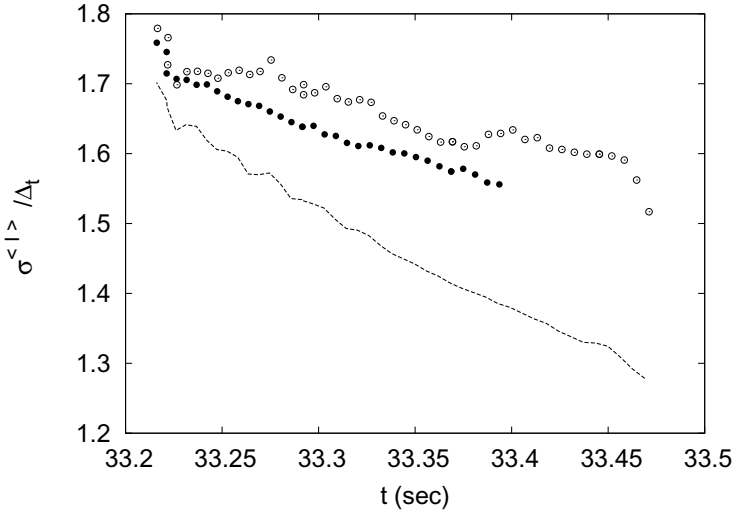

(a) Comparison of Pulse Widths of Average Intensity Timefronts for 50 km

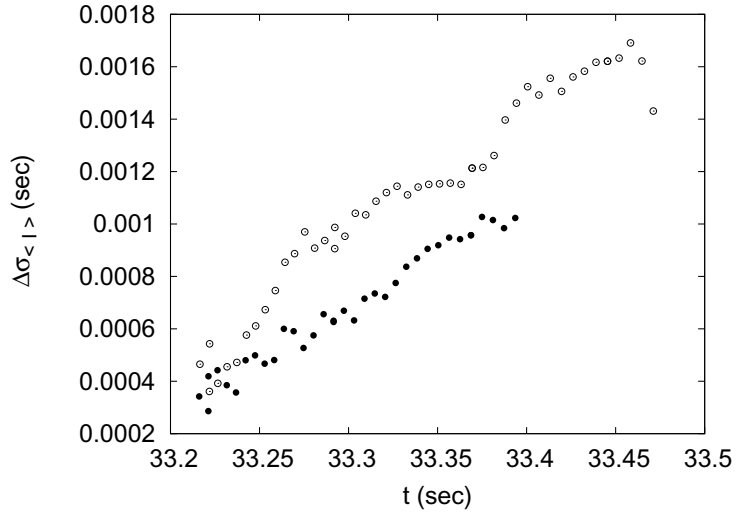

(b) Comparison of Pulse Width Deviations of Average Intensity Timefronts from the Unperturbed Timefronts for 50 km

Figure 6.48: (Upper) Pulse widths $\sigma_{\langle I \rangle}$ are scaled by the factor $\Delta_t = \frac{1}{\sqrt{2}c_0\sigma_k} \approx 6ms$ and plotted versus average pulse travel time t. (Lower) A quantity mimicking the sum of the spread and wander, $\Delta\sigma_{\langle I \rangle}$, is plotted versus average pulse travel time t. Quantities are shown for the unperturbed timefront (dashed line), perturbed timefronts (open circle) and the ensemble timefronts (filled circle). Quantities are shown only for the well-separated pulses on the branch with branch number $+2$. The calculation for the perturbed propagation uses 2500 timefront realizations, while the calculation for the ensemble model uses 1000 timefront realizations.

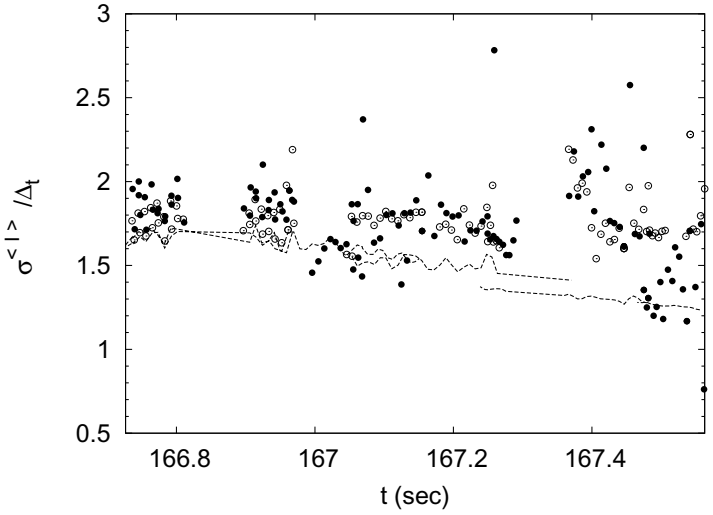

(a) Comparison of Pulse Widths of Average Intensity Timefronts for 250 km

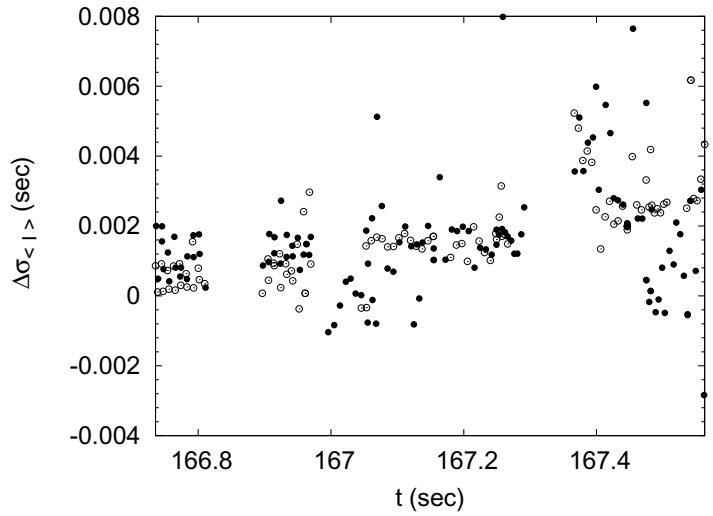

(b) Comparison of Pulse Width Deviations of Average Intensity Timefronts from the Unperturbed Timefronts for 250 km

Figure 6.49: Pulse widths $\sigma_{\langle I \rangle}$ of the average intensity timefront $\langle I \rangle$ are scaled by the factor $\Delta_t = \frac{1}{\sqrt{2}c_0\sigma_k} \approx 6ms$ and plotted versus average pulse travel time t. (Lower) A quantity mimicking the sum of the spread and wander, $\Delta\sigma_{\langle I \rangle}$, is plotted versus average pulse travel time t. Quantities are shown for the unperturbed timefront (dashed line), perturbed timefronts (open circle) and the ensemble timefronts (filled circle). Quantities are shown only for the well-separated pulses on the branch corresponding to the classical rays with initial angle $|\theta_0| \leq 15^\circ$. The calculation for the perturbed propagation uses 2500 timefront realizations, while the calculation for the ensemble model uses 1000 timefront realizations.

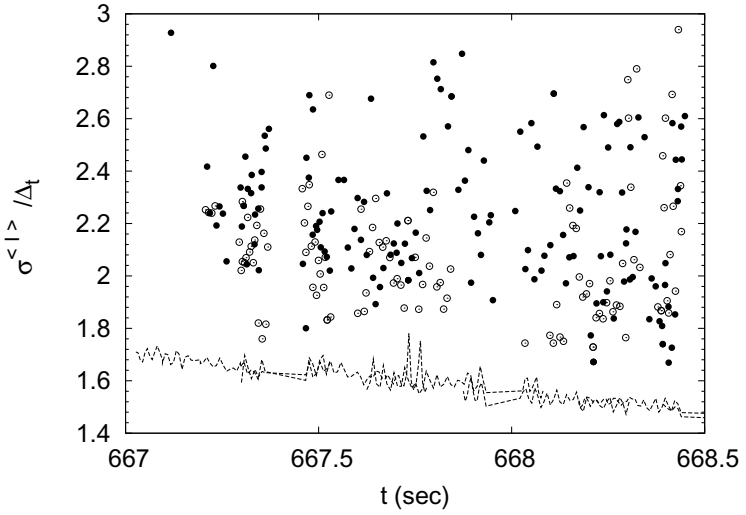

(a) Comparison of Pulse Widths of Average Intensity Timefronts for 1000 km

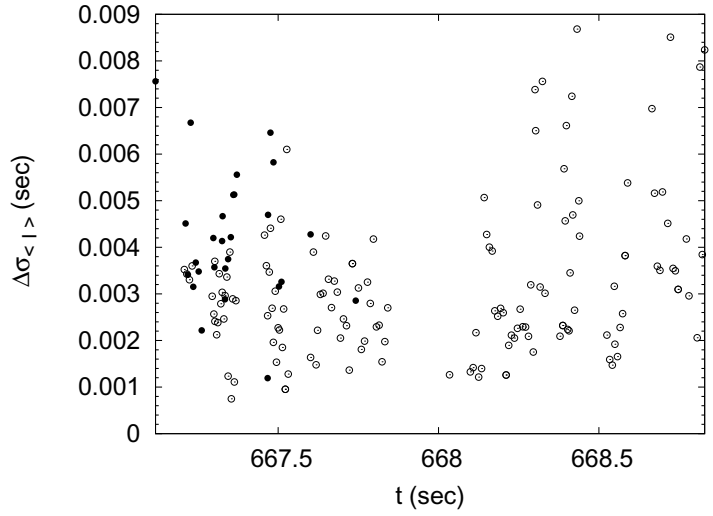

(b) Comparison of Pulse Width Deviations of Average Intensity Timefronts from the Unperturbed Timefronts for 1000 km

Figure 6.50: Pulse widths $\sigma_{\langle I \rangle}$ of the average intensity timefront $\langle I \rangle$ are scaled by the factor $\Delta_t = \frac{1}{\sqrt{2}c_0\sigma_k} \approx 6ms$ and plotted versus average pulse travel time t. (Lower) A quantity mimicking the sum of the spread and wander, $\Delta\sigma_{\langle I \rangle}$, is plotted versus average pulse travel time t. Quantities are shown for the unperturbed timefront (dashed line), perturbed timefronts (open circle) and the ensemble timefronts (filled circle). Quantities are shown only for the well-separated pulses on the branch corresponding to the classical rays with initial angle $|\theta_0| \leq 15\,^\circ$. The calculation for the perturbed propagation uses 2500 timefront realizations, while the calculation for the ensemble model uses 1000 timefront realizations.

6.3.5 Time Bias of Average Intensity Timefronts

The time bias is defined to be the average difference between the mean time of arrival of a pulse along a branch and the unperturbed time of arrival.

$$\mu_{\Delta t} \quad = \quad \langle t_t^{\epsilon} - t^{\epsilon=0} \rangle \ . \tag{6.23}$$

Since the mean phase $\mu_{n,n} = 0$ is taken for the ensemble model, it is not expected that there will be any time bias for the ensemble model.

Still, the time bias is calculated for the average intensity timefront of the perturbed timefronts and the ensemble model timefronts for several ranges in Figs. (6.51)-(6.53). These figures show two things. First, each branch has either a positive or negative bias for the entire length of the branch and the magnitude of the bias increases with depth along the branch. Second, surprisingly, the ensemble model is capturing some the time bias of the different branches of the perturbed timefronts to the right scale, despite $\mu_{n,n} = 0$ having been taken for the ensemble model.

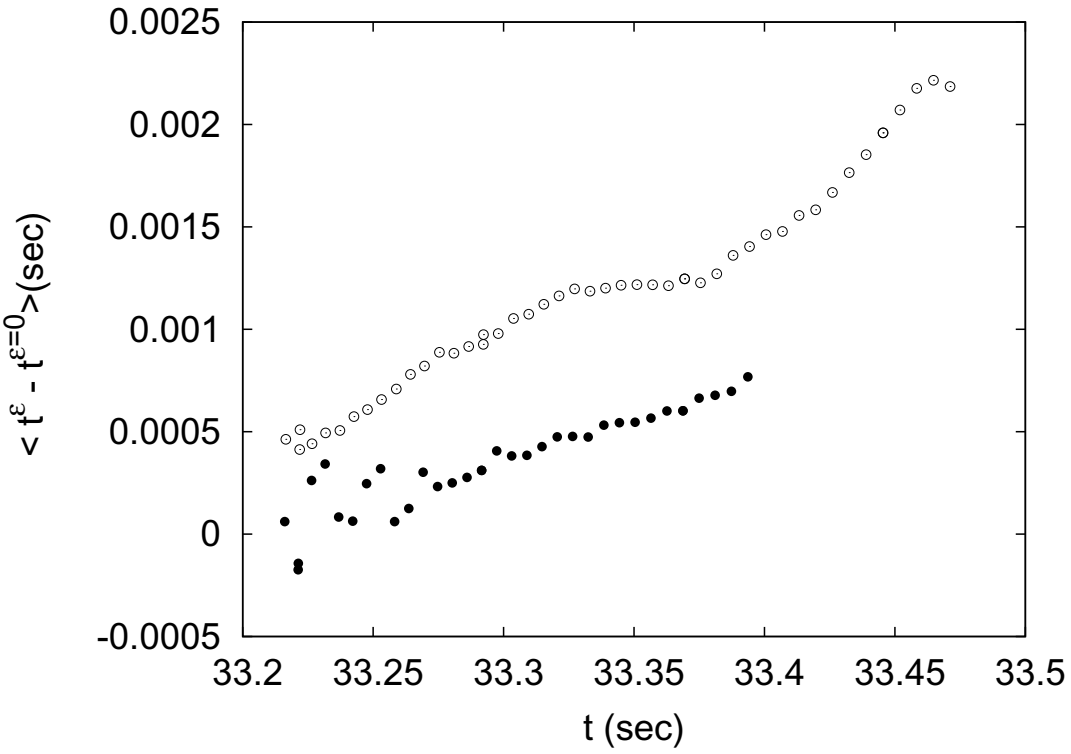

Figure 6.51: The time bias $\mu_{\Delta t} = \langle t^\epsilon - t^\epsilon \rangle$ of the well-separated pulses for the perturbed timefronts (open circles) and ensemble model timefronts (closed circles) is plotted with average travel time of the pulse arrival for 50 km. Time bias is shown only for the well-separated pulses on the branches corresponding to the classical rays with initial angle $|\theta_0| \leq 15\,^\circ$. The calculation of the time bias for the perturbed propagation uses 2500 timefront realizations, while the calculation of the pulse width for the ensemble model uses 1000 timefront realizations.

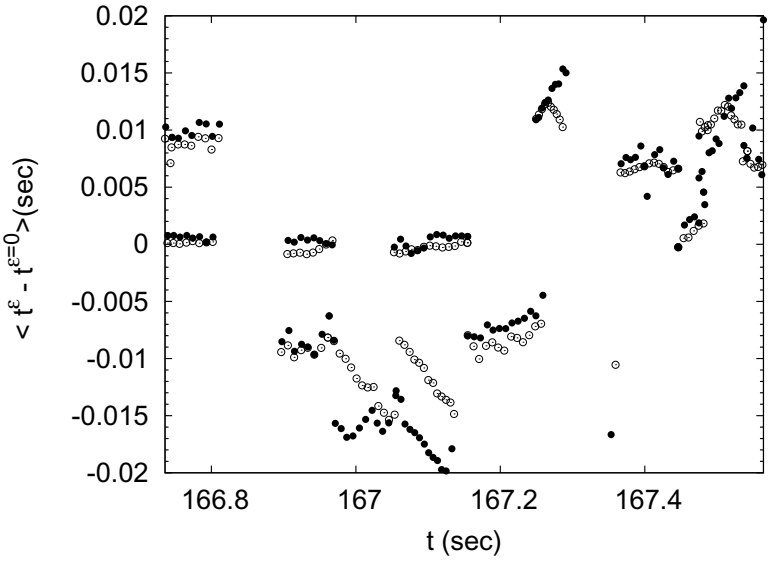

(a) Time Bias of Average Intensity Timefront at 250 km with time

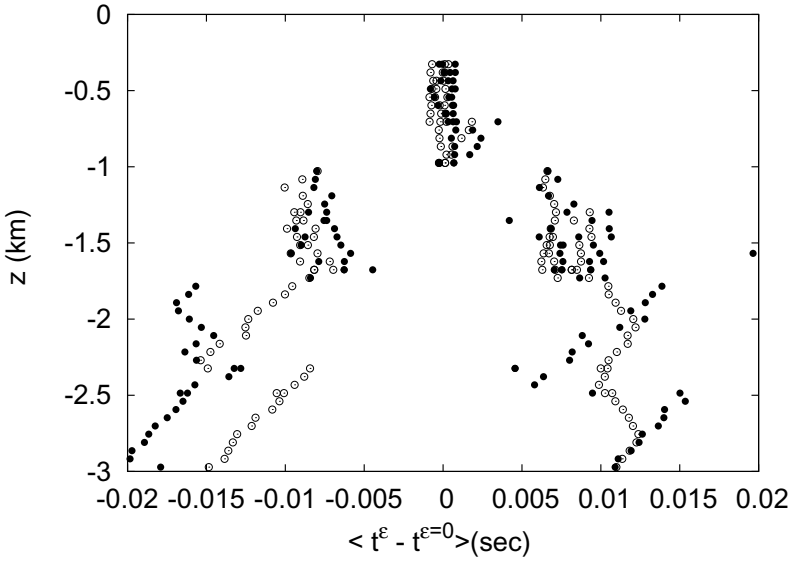

(b) Time Bias of Average Intensity Timefronts at 250 km with depth

Figure 6.52: The time bias $\mu_{\Delta t} = \langle t^\epsilon - t^\epsilon \rangle$ of the well-separated pulses for the perturbed timefronts (open circle) and ensemble model timefronts (filled circle) is plotted with (Upper) average travel time t of the pulse arrival and (Lower) final arrival depths z. Time bias is shown only for the well-separated pulses on the branches corresponding to the classical rays with initial angle $|\theta_0| \leq 15\,^\circ$. The calculation of the time bias for the perturbed propagation uses 28 timefront realizations, while the calculation of the pulse width for the ensemble model uses 25 timefront realizations.

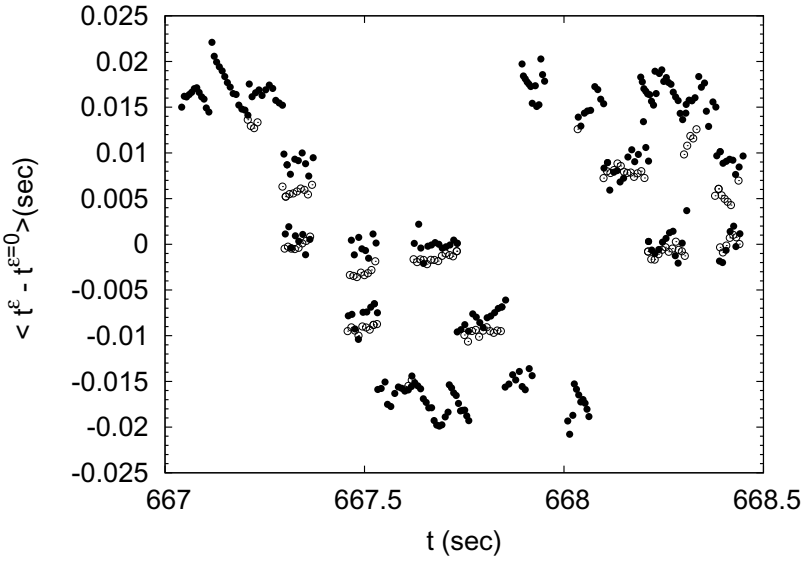

(a) Time Bias of Average Intensity Timefront at 1000 km with time

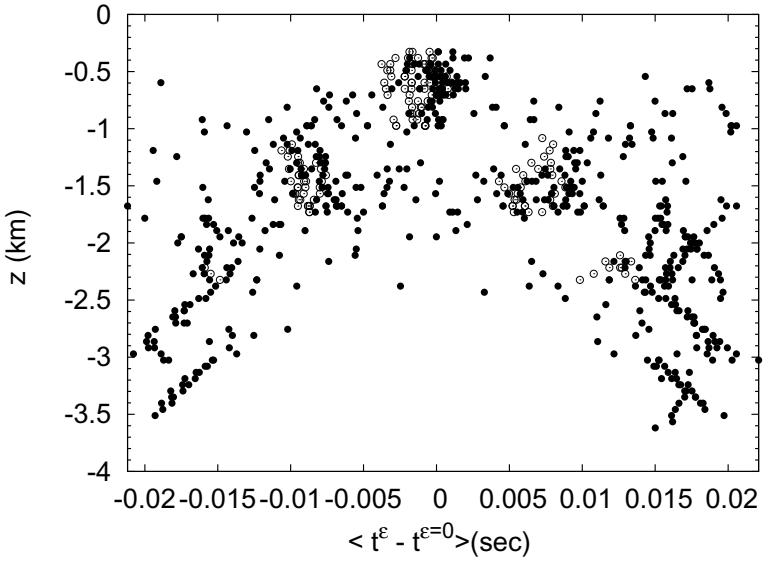

(b) Time Bias of Average Intensity Timefronts at 1000 km with depth

Figure 6.53: The time bias $\mu_{\Delta t} = \langle t^\epsilon - t^\epsilon \rangle$ of the well-separated pulses for the perturbed timefronts (open circle) and ensemble model timefronts (filled circle) is plotted with (Upper) average travel time t of the pulse arrival and (Lower) final arrival depths z. Time bias is shown only for the well-separated pulses on the branches corresponding to the classical rays with initial angle $|\theta_0| \leq 15\,^\circ$. The calculation of the time bias for the perturbed propagation uses 28 timefront realizations, while the calculation of the pulse width for the ensemble model uses 25 timefront realizations.

6.4 Chapter Summary

The goal of this chapter was to test the ensemble model described in Ch. (5) by comparing the timefronts generated by this model to the timefronts generated from the simulated acoustic propagation described in Ch. (3).

In determining which properties of the timefront should be compared, the structure of the acoustic timefronts first had to be studied. The properties of the acoustic timefront were explored using 1) the insight from several theoretical tools (i.e. perturbation theory, semi-classical theory and mode theory) and 2) the qualitative variations in the acoustic timefront simulated from the acoustic model. Through this exploration, it was discovered that very little information remains in the acoustic timefront for the perturbed propagation to long ranges. This information is qualitatively composed of two main properties: 1) the unperturbed timefront shifted in time by a time bias and 2) a fluctuation front which decays in both depth and time from a peak value located on the sound channel near the time of the direct arrival along the sound channel. This front has not been seen in previous work. Despite its presence in the timefronts in this thesis, there is no theory to explain its existence.

In comparing sample timefronts generated by the ensemble model with sample timefronts generated from the propagation, it was seen in Figs. (6.22)- (6.23) that there is good qualitative agreement of the basic structure of the timefronts. However, there are differences which cannot be expected to be captured by such a simple model. Recall that the ensemble model described in Ch. (5) contains only minimal information about the propagation to 50 km through the construction of the unitary propagation matrices as a product of Gaussian random matri-

ces. As derived in Sec. (6.3.1), the minimal information contained in the ensemble model is the information about the two main properties of the average intensities of the timefronts. Therefore, it is at least possible that the ensemble model could be capturing these two important properties properly.

However, the ensemble model used for the comparison in this chapter took $\mu_{n,n} = 0$ for the mean phase of the diagonal elements of the unitary propagation matrix in the construction of the random matrices. Though a best fit model for $\mu_{n,n}$ was obtained from the mode propagation data described in Ch. (4), the resulting timefronts utilizing the ensemble model and this model for $\mu_{n,n}$ resulted in timefronts which had curved branches which did not match the propagation to 50 km, as seen in Fig. (6.21). Therefore, $\mu_{n,n} = 0$ is taken in the ensemble model used in this chapter and it is expected that the model should only be able to capture the information about the unperturbed timefronts and the fluctuation field, but not the time bias of the unperturbed timefronts.

In comparing the average intensity timefronts generated from realizations of the ensemble model to that generated from the acoustic propagation, it was found that there is good qualitative agreement of the basic scattering and branch structure. However, the average intensity timefront from the ensemble model has more scattering to early times in the arrivals than does the propagation, as seen in Figs. (6.36)-(6.44). Upon closer view of the traces of the time series in Figs. (6.37), (6.39), and (6.42), though, it is revealed that the fluctuation structure of the ensemble model has the correct shape but just does not decay as fast as the acoustic propagation to early arrival times. This suggests that some adjustments of the scale of the variance matrix in the ensemble model may improve the comparison of the average

intensity traces.

Using the average intensity timefront, observables were found for both the late arriving finale region and the early arriving region of branches. Consistent with the qualitative agreement seen in the average intensity timefront contour plots, these observables also agreed very well.

An observable for the finale region of the average intensity timefront was taken as the rate of decay in depth and time from the location in the timefront at the sound channel depth and at the time of the direct arrival, $t = \frac{r}{c_0}$. The rate of decay in depth and in time are shown in Figs. (6.45)-(6.47). It was found that the decay scale for the ensemble model has approximately the same shape but is consistently larger than that of the acoustic propagation. The decay in depth for the ensemble model matched well with that of the acoustic propagation. Again, this suggests that some adjustments of the scale of the variance matrix in the ensemble model may improve the comparison of the decay scales.

Two observables for the early arrivals of the average intensity timefront were taken as the time bias and a pulse width representing the sum of the pulse spread and wander (discussed in Sec. (6.2.3) and (6.2.3)). These observables were calculated on the well-separated branches of the acoustic arrivals in the timefront and were compared for the average intensity timefront from the ensemble model and the acoustic propagation. Though there were large uncertainties in these calculations, it was still found in Sec. (6.3.5) that the average intensity timefront of the ensemble model captures correctly many aspects of the dependence of the time bias on the branch number and depth along the branch. Additionally, it was found in Sec. (6.3.4) that the ensemble model captures correctly some aspects of the pulse width, which is dominated

by the pulse wander.

The general conclusion of this chapter is that the ensemble model looks to contain the minimal information which survives the propagation to long ranges, but may need some adjustment of the scale of the variance matrix to improve the correspondence to the acoustic propagation. The conclusion of this chapter come at a surprise for several reasons.

First, it was seen in Ch. (4) that some of the matrix elements from the propagation have correlations with the matrix elements at the central wavenumber k_0 which decay rapidly from one. However, the ensemble model only approximates the wavenumber dependence of the variance of each matrix element. The model assumes perfect correlation with wavenumber, since the random matrix is chosen independent of wavenumber. Yet, the ensemble model is still able to generate good agreement with the timefronts and matrices from the propagation model. The agreement in the timefronts is surprising since the timefront is a superposition of different wavenumber contributions of the wavefield, where destructive and constructive interferences are critical to the appearance of the structure in the branches. If the proper wavenumber information is not captured by the model, one would think that the timefronts would not have the right structure or scattering. Yet, sample timefronts and matrices generated using the ensemble model are found to have many of the qualitative features of sample timefronts generated from the propagation, including both the branch structure in the earlier times and the scattering in the later times. The only resolution of this surprise is that capturing the wavenumber dependence of the variances of the random matrices is enough and the correlations with wavenumber are just not physically relevant.

Second, the variance matrix of the ensemble model was built from information about the

propagation to 50 km using the statistics of the first order perturbation theory prediction over the ensemble of internal wave sound speed models. Though perturbation theory is only valid to short ranges for this acoustic propagation, the success of this method suggests that the statistics of the first order perturbation theory result may be valid to much greater ranges. This comes as a surprise and may have use in applications of perturbation theory to other problems which are statistical in nature.

Third, though the ensemble model took $\mu_{n,n} = 0$ for the mean phases in the random matrix model for the unitary propagation matrixes, the resulting ensemble model for the average intensity timefront still gave time biases which agreed with the scale of the branch and depth dependence of the time biases from the acoustic propagation for several ranges. The conclusion that the wavenumber dependence of the mean phases were the cause of the time bias in the average intensity timefront was made in Sec. (6.3.1). This conclusion came from considering a first order approximation of the unitary construction in Sec. (5.1.1). It is possible that wavenumber dependence of the full unitary construction may have caused the time bias seen in the average intensity timefronts of the ensemble model.

Chapter 7

CONCLUSION

This chapter will serve to summarize the results of the work described in this thesis and the final conclusions about this work. Additionally, the outlook for the future will be described and suggestions for future work will be made.

7.1 Summary of Results

This section will be a recap of chapter summaries from Ch. (4)-Ch. (6). In Ch. (4), the focus was the unitary propagation matrix of complex probability amplitudes for transitions between acoustic modes during the propagation. In Ch. (5), the focus was the construction and validation of the statistical ensemble model for the unitary propagation matrix to 50 km (i.e. the building block matrix) and the construction of the ensemble model for longer ranges. In Ch. (6), the focus was the properties of the acoustic timefronts and the comparison of the timefronts from the ensemble model to those from the simulated propagation.

7.1.1 Summary of Important Properties For Propagation to 50 km

The important properties of the propagation to 50 km were investigated in Ch. (4).

An important property of the unitary propagation matrix was found to be the dynamic multiplication property shown in Eq. (4.9). This property allowed a unitary propagation matrix to be written as a product of unitary propagation matrices for previous range intervals. This served as the basis for multiplying independent building blocks to create the ensemble model for longer ranges.

First order quantum perturbation theory was used to obtain Eq. (4.10) and used to estimate the basic dependency of the unitary propagation matrices on other quantities relating to the experiments. A rough estimation of a good minimum range at which successive unitary propagation matrices decorrelate was found to be 50 km. This happened to be the average wavelength of one period of oscillation of a classical ray in the potential. This range served as the range for the building block matrix for modelling the properties of the unitary propagation matrix for 50 km.

The statistical properties of the unitary propagation matrix were explored by calculating the matrix elements $C_{m,n}$ from simulations of the mode propagation. It was found that the real and imaginary parts of the off-diagonal elements and the phase of the diagonal elements had distributions very similar to Gaussian random variables. Best fit functional forms for the means and variances of these quantities were found. The interdependence (correlations) between matrix elements was found to be most significant between matrix elements along the same band of the matrix. The dependence (correlations) of individual matrix elements on

wavenumber k was found to deviate from the value at the central wavenumber k_0 most for those elements furthest from the diagonal.

7.1.2 Summary of Building Block Ensemble Model

The building block model was constructed and verified in Ch. (5) and Ch. (6).

The building block ensemble was constructed to model the unitary propagation matrix to 50 km. A transformation involving a Hermitian matrix A and a diagonal matrix Λ was utilzed to guarantee the unitarity of the matrices. A model for matrix A was constructed using first order quantum perturbation theory - which resulted in a random phasor sum. Applying the theory of random phasor sums predicted that the elements of A are distributed approximately as complex Gaussian random matrices with zero mean and provided an analytic formula for the variance. Therefore, matrix A in the ensemble model was formed from a random matrix of independent Gaussian random variables of zero mean and with variances predicted by perturbation theory.

The statistics of matrices resulting from the ensemble model at the central wavenumber k_0 were verified to match those from the simulated propagation in the basic functional form, but with an error in a scale factor of close to 18%, as seen in Fig. (5.7). Modifications of the scale of the elements in A was attempted to improve the agreement, but were not successful. Therefore, the variances in the ensemble model will differ from the true propagation to 50 km by a scale factor and it is expected that this error will propagate with range.

Sample matrices at the central wavenumber k_0 from the ensemble model were verified to

agree with those from the simulated propagation in Ch. (5). Sample timefront realizations and sample average intensity timefronts were verified to agree with those from the simulated propagation in Ch. (6). Therefore, the building block model has been verified to be properly constructing matrices and timefronts for 50 km.

7.1.3 Summary of Long Range Ensemble Model

In Ch. (6), the properties of the timefronts were investigated.

Utilizing 1) the insight from several theoretical tools (i.e. perturbation theory, semiclassical theory and mode theory), 2) the qualitative variations in the acoustic timefront simulated from the acoustic model and 3) the qualitative properties of the average intensity timefront from the acoustic model, it was found that very little structure remains in the acoustic timefront to long ranges. This information is suspected to be composed of two main properties: 1) the unperturbed timefront shifted in time by a time bias and 2) an average noise level due to the internal waves (referred to as a fluctuation front), which decays in both depth and time from a peak value located on the sound channel near the time of the direct arrival along the sound channel.

Timefronts generated from the long range ensemble model were compared to those from the simulated propagation for several long ranges. It was seen in Figs. (6.22)- (6.23) that there was good qualitative agreement of the basic structure of the timefronts. However, there are differences which cannot be expected to be captured by such a simple model. Since there was only minimal information remaining in the propagation to long ranges, the average intensity

timefront was assumed to capture this average information. It was found in the derivation in Sec. (6.3.1) that the minimal information contained in the average intensity timefront from the ensemble model is exactly the information about the two main properties believed to survive to long range described above. The time shift in the unperturbed timefront is captured by the mean phases $\mu_{n,n} = 0$ and the properties of the fluctuation field are controlled by the variances $\sigma^2_{A_{m,n}}$ of the ensemble model.

Properties of the average intensity timefronts from the ensemble model were compared to those from the simulated propagation. In comparing the average intensity timefronts generated from realizations of the ensemble model to that generated from the simulated propagation, it was found that there was good qualitative agreement of the basic scattering and branch structure. However, the average intensity timefront from the ensemble model has more scattering to early times in the arrivals than does the propagation, as seen in Figs. (6.36)-(6.44). Upon closer view of the traces of the time series in Figs. (6.37), (6.39), and (6.42), though, it was revealed that the noise structure due to internal waves of the ensemble model has the correct shape but just does not decay as fast as the acoustic propagation to early arrival times. This suggests that some adjustments of the scale of the variance matrix in the ensemble model may improve the comparison of the average intensity traces.

An observable for the finale region of the average intensity timefront was taken as the rate of decay in depth and time from the location in the timefront at the sound channel depth and at the time of the direct arrival, $t = \frac{r}{c_0}$. The rate of decay in depth and in time are shown in Figs. (6.45)-(6.47). It was found that the decay scale for the ensemble model has approximately the same shape but was consistently larger than that of the acoustic propagation. The

decay in depth for the ensemble model matched well with that of the acoustic propagation. Again, this suggests that some adjustments of the scale of the variance matrix in the ensemble model may improve the comparison of the decay scales.

Two observables for the early arrivals of the average intensity timefront were taken as the time bias and a pulse width representing the sum of the pulse spread and wander (discussed in Sec. (6.2.3) and (6.2.3)). These observables were calculated on the well-separated branches of the acoustic arrivals in the timefront and were compared for the average intensity timefront from the ensemble model and the acoustic propagation. Though there were large uncertainties in these calculations, it was still found in Sec. (6.3.5) that the average intensity timefront of the ensemble model captured correctly many aspects of the dependence of the time bias on the branch number and depth along the branch. Additionally, it was found in Sec. (6.3.4) that the ensemble model captured correctly some aspects of the pulse width, which is dominated by the pulse wander.

7.2 Conclusions

The aim of the research described in this thesis has been to understand what information about the experiments are stored in the acoustic timefront data and to use this information in the construction of a statistical ensemble model for the propagation. To this effect, a building block model was constructed to model the propagation to 50 km and was found to agree (up to a scale factor) with the average properties of matrices and timefronts resulting from the simulated propagation. A long range ensemble model was constructed from a product of

building blocks to model the unitary propagation matrices to longer ranges and also found to agree (up to a scale factor) with the average properties of the matrices and timefronts resulting from the simulated propagation.

It was found that some of the matrix elements from the propagation have correlations with the matrix elements at the central wavenumber k_0 which decay rapidly from one. However, the ensemble model only approximates the wavenumber dependence of the variance of each matrix element. The model assumes perfect correlation with wavenumber, since the random matrix was chosen independent of wavenumber. Yet, the ensemble model was still able to generate good agreement with the timefronts, as seen in Fig. (6.23 and Figs. (6.38)-(6.44), and with the matrices from the propagation model, as seen in Fig. (5.16-5.17). The agreement in the timefronts is surprising since the timefront was a superposition of different wavenumber contributions of the wavefield, where destructive and constructive interferences are critical to the appearance of the structure in the branches. If the proper wavenumber information was not captured by the model, one would think that the timefronts would not have the right structure or scattering. Yet, sample timefronts and matrices generated using the ensemble model are found to have many of the qualitative features of sample timefronts generated from the propagation, including both the branch structure in the earlier times and the scattering in the later times. The only conclusion that can be drawn is that capturing the wavenumber dependence of the variances of the random matrices is enough and the correlations with wavenumber are just not physically relevant.

The general conclusion of this chapter is that the ensemble model looks to contain the minimal information which survives the propagation to long ranges, but may need some ad-

justment of the scale of the matrices to improve the correspondence to the acoustic propagation. Despite the scale factor, the results of this study suggest that a random matrix model is an appropriate model for characterizing the information contained in the acoustic timefronts at long ranges.

7.3 Outlook

The significance of the ensemble model in this chapter to researchers in the field could be great. The experiments are done in order to learn about the average properties of the ocean. Tomography is performed on the experimental timefronts in order to extract these mean properties. If the only information left in the propagation to long ranges is contained in a variance matrix and a phase matrix of the ensemble model, then it needs to be determined if the desired properties of the ocean are captured by this information. If the experiments cannot capture the desired properties, then they should be reevaluated. If the experiments can capture the desired properties, then the relationship between the parameters of the ensemble model and the desired ocean properties needs to be determined. It is likely that semiclassical theory [26] could be utilized in determining this relationship, since 50 km is a range where the classical rays are not fully chaotic yet. Once this relationship is identified, the ensemble model could be used to perform tomography more effectively to learn more about the ocean from the experiments.

The success of the statistics of first order quantum perturbation theory in predicting information about the propagation to 50 km through the varaince matrix of the ensemble model

suggests that the statistics of perturbation theory are much more robust than perturbation theory alone. Though perturbation theory is only valid to short ranges (i.e. $5 - 10$ km) for the acoustic propagation, the success of this method suggests that the statistics of the first order perturbation theory result may be valid to much greater ranges. This may have use in applications of perturbation theory to other problems in other fields which are statistical in nature.

7.4 Recommendations for Future Work

Though the work in this thesis is a only a start towards providing insight into the acoustic propagation to long ranges, there is still more work to be done.

First, the existence of the fluctuation front needs to be investigated. The fluctuation front discovered in the timefronts in Sec. (6.1.3) have not been seen before. Therefore, they are somewhat suspect. Previous work has suggested that the multiple scattering from internal waves works in tandem with the structure of the unperturbed timefront, with contributions smeared out in a neighborhood of the branches. The continuous nature of the fluctuation front is not consistent with previous work. Additionally, a physical picture has not been developed to support the existence of a fluctuation front, though this may be found in the use of tunneling or diffraction.

The ensemble model in this thesis could be improved. The scale discrepancy of the ensemble model at 50 km needs to be investigated. A correction to the model needs to be made so that the ensemble model for the building block more closely matches with the simulated

propagation to 50 km. If there is still a scale discrepancy in the long range ensemble model for the longer ranges, then the range of 50 km may need to be altered to optimize the performance of the ensemble model to longer ranges. Additionally, correlations with either wavenumber or other matrix elements may need to be built into the model if they are deemed an important reason why there is mismatch between the ensemble model and the propagation. However, the results seen already suggest that the addition of correlations to the ensemble model are not likely to be worth the additional complexity.

The computational efficiency of the ensemble model could be improved. While the analytic model for the variances from first order quantum perturbation theory seem to capture much of the important information about the propagation, this model is somewhat computational expensive. A simpler model could be constructed from best-fit functional forms on the results from the simulated mode propagation or from the perturbation theory result. This would considerably speed up the ensemble model construction, but may deteriorate the agreement.

More observable measurements need to be made on the timefronts and the range and frequency dependencies of the measurements needs to be calculated and checked. Since the goal of the research is to connect the properties of the timefronts to the properties of the experiment, it would be ideal to develop a set of observables on the timefronts which fully characterize the timefronts. By identifying the dependence of each observable on the parameters of the experiment, a complete set of observables could be found which contain all of the parameters of the experiment. Ideally, the set needs to be large enough such that each parameter can be extracted by measurements of the entire set of observables. This goal

would be the ultimate recommendation for future work, as this connection would improve the process of tomography the most.

Lastly, more theory needs to be done using true semiclassical theory and classical perturbation theory to connect analytically measurable properties with information about the ocean environment. A large amount of preliminary work has already been done towards this goal, but has not been included in this thesis.

Bibliography

[1] C. Catlett et al. *TeraGrid: Analysis of Organization, System Architecture, and Middleware Enabling New Types of Applications*. HPC and Grids in Action. IOS Press 'Advances in Parallel Computing' series, Amsterdam, 2007. edited by Lucio Grandinetti.

[2] W. M. Ewing and J. L. Worzel. Long range sound transmission. *Geol. Soc. Am. Mem.*, 27:part III, 1–35, 1949.

[3] S. M. Flatté, R. Dashen, W. H. Munk, K. M. Watson, and F. Zachariasen. *Sound Transmission through a Fluctuating Ocean*. Cambridge University Press, Cambridge, 1979.

[4] B. D. Dushaw, G. Bold, C. S. Chui, John. A. Colosi, B. D Cornuelle, Y. Desaubies, M. A. Dzieciuch, A. Forbes, F. Gaillard, P. Mikhaelvsky, W. H. Munk, I. Nakano, F. Schott, U. Send, R. Spindel, T. Terre, P.F. Worcester, and C. Wunsch. *Observing the ocean in the 2000's: A strategy for the role of acoustic tomography in ocean climate observation*, volume 1 of *Observing the Oceans in the 21st Century*, pages 391–418. GODAE Project Office and Bureau of Meteorology, Melbourne, 2001. edited by C. J. Koblinsky and N. R. Smith.

[5] Y. V. Lvov and E. G. Tabak. Hamiltonian formalism and the garrett-munk spectrum of internal waves in the ocean. *Phys. Rev. Lett.*, 87:168501, 2001.

[6] S. Flatte. Wave propagation through random media: Contributions from ocean acoustics. *Proc. of the IEEE*, 71:1267–1294, 1983.

[7] B. Helland-Hansen and F. Nansen. The norwegian sea. *Fiskeridirektoratets Skrifter Serie Havunderskelser*, 2:1–360, 1909.

[8] D.L. Rudnick and R. Ferrari. Compensation of horizontal temperature and salinity gradients in the ocean mixed layer. *Science*, 283:526–529, 1999.

[9] M. Fink. Time reversed acoustics. *Physics Today*, 50:34–40, 1992.

[10] K. G. Foote, R.T. Hanlon, P.J. Iampietro, and R.G. Kvitek. Acoustic detection and quantification of benthic egg beds of the squid loligo opalescens in monterey bay, california. *J. Acoust. Soc. Am*, 119:844–856, 2006.

[11] B.D. Dushaw, P. F. Worcester, W. H. Munk, R. C. Spindel, J. A. Mercer, B. M. Howe, K. Metzger Jr., T. G. Birdsall, R. K. Andrew, M. A. Dzieciuch, B. D. Cornuelle, and D. Menemenlis. A decade of acoustic thermometry in the north pacific ocean. *Journal of Geophysical Research*, 114:24 pp, 2009.

[12] M. G. Brown, J. A. Colosi, S. Tomsovic, A. L. Virovlyanksky, M. A. Wolfson, and G. M. Zaslavsky. Ray dynamics in long-range deep ocean sound propagation. *J. Acoust. Soc. Am*, 113:2533–2547, 2003.

[13] W. H. Munk, P. F. Worcester, and C. Wunsch. *Ocean Acoustic Tomography*. Cambridge University Press, Cambridge, 1995.

[14] S.M. Rytov, Yu.A. Kravtsov, and V.I. Tatarskii. *Wave Propagation Through Random Media*, volume 4 of *Principles of Statistical Radiophysics*. Springer-Verlag, Berlin, Germany / Heidelberg, 1978.

[15] B. J. Uscinski. *Wave Propagation and Scattering in Random Media*, volume Vol 2. Academic, 1978.

[16] D. Makarov, S. Prants, A. Virovlyansky, and G. Zaslavksy. *Ray and Wave Chaos in Ocean Acoustics: Chaos in Waveguides*, volume Vol 1 of *Complexity, Nonlinearity and Chaos*. World Scientific Publishing Company, 2009.

[17] G. Hasinger, R. Giacconi, J.E. Gunn, I. Legmann, M. Schmidt, D. P. Schneider, J. Trumper, J. Wambsganss, D. Woods, and G. Zamorani. The rosat deep survery iv. a distant lensing cluster of galaxies with a bright arc. *Astron. Astrophys.*, 340:L27 – L 30, 1998.

[18] P. W. Anderson. Absence of diffusion in certain random lattices. *Phys. Rev.*, 109:1492–1505, 1958.

[19] L. B. Schulman. *Techniques and Applications of Path Integration*. John Wiley and Sons,Inc, 1981.

[20] A. Crisanti, G. Paladin, and A. Vulpiani. *Products of Random Matrices in Statistical Physics*, volume 104 of *Solid-State Sciences*. Springer-Verlag, Berlin, Germany / Heidelberg, 1993.

[21] L. S. Froufe-Perez, M. Yepez, P. A. Mello, and J. J. Saenz. Statistical scattering of waves in disordered waveguides: From microscopic potentials to limiting macroscopic statistics. *Phys. Rev. E*, 75:03113, 2007.

[22] F.J.Beron-Vera, M. G. Brown, J. A. Colosi, S. Tomsovic, A. L. Virovlyanksky, M. A. Wolfson, and G. M. Zaslavsky. Ray dynamics in a long-range acoustic experiment. *J. Acoust. Soc. Am*, 114:1226–1242, 2003.

[23] D. R. Palmer, M. G. Brown, F. D. Tappert, and H. F. Bezdek. Classical chaos in nonseparable wave propagation problems. *Geophys. Res. Lett.*, 15:569–572, 1988.

[24] K. B. Smith, M. G. Brown, and F. D. Tappert. Ray chaos in underwater acoustics. *J. Acoust. Soc. Am*, 91:1939–1949, 1992.

[25] K. B. Smith, M. G. Brown, and F. D. Tappert. Acoustic ray chaos induced by mesoscale structure. *J. Acoust. Soc. Am*, 91:1950–1959, 1992.

[26] M.C. Gutzwiller. *Chaos in Classical and Quantum Mechanics*. Springer-Verlag, New York, 1990.

[27] C.W. J. Beenakker. Random-matrix theory of quantum transport. *Rev. Mod. Phys.*, 69:731–808, 1997.

[28] T. A. Brody, J. Flores, J. B. French, P. A. Mello, A. Pandey, and S. S. M. Wong. Random-matrix physics: spectrum and strength fluctuations. *Rev. Mod. Phys*, 53:385 –443, 1981.

[29] K. B. Efetov. *Supersymmetry in Disorder and Chaos*. Cambridge University Press, 1999.

[30] W. Kohler and G. C. Panpanicolaou. *Sound Propagation in a randomly inhomogeneous ocean*. Lecture Notes in Physics No. 70: Wave Propagation and Underwater Acoustics. Springer-Verlag, Berlin, 1977. edited by J.B. Keller and J. S. Papadakis.

[31] L.B. Dozier and F. D. Tappert. Statistics of normal mode amplitudes in a random ocean. i. theory. *J. Acoust. Soc. Am*, 63:353–365, 1978.

[32] L.B. Dozier and F. D. Tappert. Statistics of normal mode amplitudes in a random ocean. ii. computations. *J. Acoust. Soc. Am*, 64:533–547, 1978.

[33] V.I. Tatarskii. *The effects of the turbulent atmosphere on wave propagation*. Israel Program for Scientific Translation, Jerusalem. (Available from the National Technical Information Service, Springfield, Virginia), 1971.

[34] L. A. Chernov. *Wave Propagation in Random Media*. Nauka, Moscow, 1975.

[35] A. K. Morozov and J. A. Colosi. Stochastic differential equation analysis for sound scattering by random internal waves in the ocean. *Acoust. Physics*, 53:335–347, 2007.

[36] J. A. Colosi and A. K. Morozov. Statistics of normal mode amplitudes in an ocean with random sound-speed perturbations: Cross-mode coherence and mean intentisy. *J. Acoust. Soc. Am*, 126:1026–1035, 2009.

[37] A. L. Virovlyansky and G.M.Zaslavsky. Ray and wave chaos in problems of sound propagation in the ocean. *Acoustical Physics*, 53:329–345, 2007.

[38] A. L. Virovlyansky, A.Yu Kazarov, and L.Ya. Lyubavin. Ray-based description of normal mode amplitudes in a range-dependent waveguide. *Wave Motion*, 42:317–334, 2005.

[39] J. A. Colosi, E. K. Scheer, S. M. Flatté, B. D. Cornuelle, M. A. Dzieciuch, W. H. Munk, P. F. Worcester, B. M. Howe, J. A. Mercer, R. C. Spindel, K. Metzger, T. G. Birdsall, and A. B. Baggeroer. Comparisons of measured and predicted acoustic fluctuations for a 3250-km propagation experiment in the eastern north pacific ocean. *J. Acoust. Soc. Am*, 105:3202–3218, 1999.

[40] L. J. Van Uffelen, P. F. Worcester, M. A. Dzieciuch, and D. L. Rudnick. The vertical structure of shadow-zone arrivals at long range in the ocean. *J. Acoust. Soc. Am*, 125:3569–3588, 2009.

[41] L. J. Van Uffelen, P. F. Worcester, M. A. Dzieciuch, D. L. Rudnick, and J. A. Colosi. Effects of upper ocean sound-speed structure on deep acoustic shadow-zone arrivals at 500- and 1000-km range. *J. Acoust. Soc. Am*, 127:2169–2181, 2010.

[42] A.N.Zagrai, D.M. Donskoy, and A. Ekimov. Structural vibrations of buried land mines. *J. Acoust. Soc. Am*, 118:3619–3628, 2005.

[43] W. H. Munk, R.C. Spindel, A.B. Baggeroer, and T.G. Birdsall. Heard island feasibility test. *J. Acoust. Soc. Am*, 96:2330–2342, 1994.

[44] P. F. Worcester, B. D. Cornuelle, M. A. Dzieciuch, W. H. Munk, B. M. Howe, J. A. Mercer, J. A. Colosi R. C. Spindel, K. Metzger, T. G. Birdsall, and A. B. Baggeroer. A test of basic-scale acoustic thermometry using a large-aperture vertical array at 3250-km range in the eastern north pacific ocean. *J. Acoust. Soc. Am*, 105:3185–3201, 1999.

[45] B. M. Howe, J. A. Mercer, R. C. Spindel, P. F. Worcester, , J. A. Hildebrand, Jr. W. S. Hodgkiss, T. Duda, and S. M. Flatté. *Slice89: A single-slice tomography experiment*, pages 81–86. Ocean Variability and Acoustic Propagation. Kluwer Academic Publishers, 1991. edited by J. Potter and A. Warn-Varnas.

[46] T. F. Duda, S. M. Flatté, J. A. Colosi, B. D. Cornuelle, J. A. Hildebrand, W. S. Hodgkiss Jr., P. F. Worcester, B. M. Howe, J. A. Mercer, and R.C. Spindel. Measured wave-front fluctuations in 1000-km pulse propagation in the pacific ocean. *J. Acoust. Soc. Am*, 92:939–955, 1992.

[47] P. F. Worcester, B. M. Howe, J. A. Mercer, M. A. Dzieciuch, and Alternate Source Test (AST) Group. *A comparison of long-range acoustic propagation at ultra-low (28 Hz) and very-low (84 Hz) frequencies*, pages 93–104. Proc. of the US-Russia Work-

shop on Experimental Underwater Acoustics. Nizhny Novgorod: Institute of Applied Physics, Russian Academy of Sciences, 2000. edited by V.I. Talanov.

[48] P. F. Worcester and R. C. Spindel. North pacific acoustic laboratory. *J. Acoust. Soc. Am*, 117:1499–1510, 2005.

[49] J. Mercer, R. Andrew, B. Howe, and J. Colosi. Cruise report: Long range ocean acoustic experiment(loapex). *Technical Report: Applied Physics Laboratory, University of Washington*, pages 1–115, 2005.

[50] J. Mercer, J. A. Colosi, B. Howe, M. A. Dzieciuch, R. Stephen, and P.F. Worcester. Loapex: The long-range ocean acoustic propagation experiment. *IEEE J. Ocean. Eng.*, 34:1–11, 2009.

[51] A. Toshiaki, S. Takao, F. Hidetoshi, and N. Iwao. Measurement of characteristics for m-sequence signal of a 200hz source for ocean acoustic tomography. *Journal of the Marine Acoustics Society of Japan*, 31:241–250, 2004.

[52] J. A. Colosi and M. G. Brown. Efficient numerical simulation of stochastic internal-wave induced sound-speed perturbation fields. *J. Acoust. Soc. Am*, 103:2232–2235, 1998.

[53] J.J. Sakurai. *Modern Quantum Mechanics*. Addison-Wesley, 1994.

[54] N. S. Grigorieva, G. M. Fridman, J. Mercer, R. K. Andrew, M. A. Wolfson, B. M. Howe, and J. A. Colosi. Interference component of the acoustic field corresponding to

the long-range ocean acoustic propagation experiment. *J. Acoust. Soc. Am*, 125:1919–1929, 2009.

[55] A. L. Virovlyansky. Ray travel times at long ranges in acoustic waveguides. *J. Acoust. Soc. Am*, 113:2523–2532, 2003.

[56] F.B. Jensen, W. A. Kuperman, M.B. Porter, and H. Schmidt. *Computational Ocean Acoustics*. Springer-Verlag, New York, 2000.

[57] L. Brekhovskikh and Y. Lysanov. *Fundamentals of Ocean Acoustics*. Springer-Verlag, Berlin, Germany / Heidelberg, 2003.

[58] B. D. Dushaw, B. M. Howe, J.A. Mercer, R.C. Spindel, Fellow, IEEE, and the ATOC Group. Multimegameter-range acoustic data obtained by bottom-mounted hydrophone arrays for measurement of ocean temperature. *IEEE J. Ocean. Eng.*, 24:202–214, 1999.

[59] J. A. Colosi, F. Tappert, and M. Dzieciuch. Further analysis of intensity fluctuations from a 3252-km acoustic propagation experiments inthe eastern north pacific ocean. *J. Acoust. Soc. Am*, 110:163–169, 2001.

[60] R. H. Hardin and F. D. Tappert. Application of the split-step fourier method to the numerical solution of nonlinear and variable coefficient wave equations. *SIAM Rev.*, 15:423, 1973.

[61] K.C. Hegewisch, N.C. Cerruti, and Steven Tomsovic. Ocean acoustic wave propagation and ray method correspondence: Internal wave fine structure. *J. Acoust. Soc. Am*, 117(3):1–13, 2005.

[62] W. H. Munk. Sound channel in an exponentially stratified ocean with applications to sofar. *J. Acoust. Soc. Am*, 55:220–226, 1974.

[63] W. Munk. *Internal waves and small-scale processes*, pages 264–291. The Evolution of Physical Oceanography. MIT, Cambridge, 1981. edited by C. Wunsch and B. Warren.

[64] W. H. Munk and C. Garrett. Internal waves in the ocean. *Annu. Rev. Fluid Mech.*, 11:339–369, 1979.

[65] Fred D. Tappert. *The Parabolic Approximation Method*, volume 8 of *Topics in Current Physics: Wave Propagation and Underwater Acoustics*. Springer-Verlag, Berlin, 1977. edited by J.B. Keller and J. S. Papadakis.

[66] B.D. Dushaw, P. F. Worcester, B.D. Cornuelle, and B.M. Howe. On equations for the speed of sound in seawater. *J. Acoust. Soc. Am*, 93:255–275, 1993.

[67] J. Cairns and G. Williams. Internal wave measurements from a midwater float, ii. *J.Geophys.Res.*, 81:1943–1950, 1976.

[68] R.L. Liboff. *Introductory Quantum Mechanics*. Addison-Wesley, 1998.

[69] Y. Desaubies. A uniformly valid solution for acoustic normal mode propagation in a range varying ocean. *J. Acoust. Soc. Am*, 76:624–626, 1984.

[70] Y. Desaubies, C. S. Chiu, and J. H. Miller. Acoustic mode propagation in a range-dependent ocean. *J. Acoust. Soc. Am*, 80:1148–1160, 1986.

[71] W. H. Press, S. A. Teukolsky, W.T. Vettering, and B. P. Flannery. *Numerical Recipes in Fortran, The Art of Scientific Computing*. Cambridge University Press, 1992.

[72] H. B. Callen. *Thermodynamics and an Introduction to Thermostatistics*. Wiley, 1985.

[73] K. E. Wage, M. A. Dzieciuch, P. F. Worcester, B. M. Howe, and J. A. Mercer. Mode coherence at megameter ranges in the north pacific ocean. *J. Acoust. Soc. Am*, 117:1565–1581, 2005.

[74] K. E. Wage, A. B. Baggeroer, and J. C. Preisig. Modal analysis of broadband acoustic receptions at 3515 km range in the north pacific using short-time fourier techniques. *J. Acoust. Soc. Am*, 113(2):801–817, 2003.

[75] J. Rice. *Mathematical Statistics and Data Analysis*. Duxbury Press, 1995.

[76] R. Courant and D. Hilbert. *Methods of Mathematical Physics*. Wiley-Interscience, 1989.

[77] J.W. Goodman. *Statistical Optics*. John Wiley and Sons,Inc, 1985.

[78] P. Beckmann and A. Spizzichino. *The Scattering of Electromagnetic Waves from Rough Surfaces*. Pergamon Press, Oxford, 1963.

[79] A. L. Virovlyansky, A. Yu Kazarova, and L. Ya. Lyubavin. Reconstruction of the average ocean temperature from the measured travel times of sound pulses. *Acoustical Physics*, 53:216–225, 2007.

[80] A. L. Virovlyansky, A.Yu Kazarov, and L.Ya. Lyubavin. Statistical description of chaotic rays in a deep water acoustic waveguide. *J. Acoust. Soc. Am*, 121:2542–2552, 2007.

[81] Michael G. Brown, Francisco J. Beron-Vera, Irina Rypina, and Ilya Udovydchenkov. Rays, modes, wavefield structure and wavefield stability. *J. Acoust. Soc. Am*, 117(3):1607–1610, 2005.

[82] V. P. Maslov and M. V. Fedoriuk. *Semi-Classical Approximation in Quantum Mechanics*. Reidel Publishing Company, Dordrecht, 1981.

[83] I. Percival and D. Richards. *Introduction to Dynamics*. Cambridge University Press, Cambridge, 1982.

[84] A. L. Virovlyansky, A.Yu Kazarov, and L.Ya. Lyubavin. Ray-based description of normal modes in a deep ocean acoustic waveguide. *J. Acoust. Soc. Am*, 125:1362–1372, 2009.

[85] J. A. Fleck and M. D. Feit. Time-dependent propagation of high energy laser beams through the atmosphere. *Appl. Phys.*, 10:129–160, 1976.

[86] D.S. Watkins. *Fundamentals of Matrix Computations*. John Wiley and Sons,Inc, New York, 2002.

[87] E. Anderson, Z.Bai, C. Bischof, S. Blackford, J. Demmel, J.J. Dongarra, J.J. Du Croz, A. Greenbaum, S. Hammarling, A. McKenney, and D. Sorensen. *LAPACK Users' Guide (3rd Edition)*. SIAM, Philadelphia, 1999.

[88] M. Abromowitz and I. Stegun. *Handbook of Mathematical Functions*. Dover, New York, 1972.

[89] O. Bohigas, S. Tomsovic, and D. Ullmo. Manifestations of classical phase space structures in quantum mechanics. *Physics Reports*, 223:43–133, 1993.

[90] O.M. Phillips. *The Dynamics of the Upper Ocean*. Cambridge University Press, 1966.

[91] C. Eckart. *Hydrodynamics of the Oceans and Atmospheres*. Pergamon Press, New York, 1960.

[92] J. Simmen, S. M. Flatté, and G.-Yu Wang. Wavefront folding, chaos, and diffraction for sound propagation through ocean internal waves. *J. Acoust. Soc. Am*, 102:239–255, 1997.

[93] M. H. Brill and L.B. Dozier. Exact transition from two- to one- dimensional internal wave power spectra. *J. Acoust. Soc. Am*, 77:1248–1249, 1985.

[94] Eric J. Heller. *Wavepacket Dynamics and Quantum Chaology*, volume 1 of *Les Houches Session LII 1989: Chaos and Quantum Physics*. Elsevier, Amsterdam, 1991. edited by M.-J. Giannoni, A. Voros, and J. Zinn-Justin.

[95] S. Tomsovic and E. J. Heller. Long-time semiclassical dynamics of chaos: The stadium billiard. *Phys. Rev. E*, 47:282–299, 1993.

[96] D. Huber, E. J. Heller, and R. G. Littlejohn. Generalized gaussian wave packet dynamics, schrodinger equation, and stationary phase approximation. *J. Chem. Phys.*, 89:2003–2014, 1988.

Appendix A

APPENDIX-NUMERICAL METHODS

The work done in this dissertation requires three main numerical simulations. The first simulation is of the acoustic wave and timefront. The second simulation is of the classical rays (for the purpose of collecting classical information along the acoustic path). The third simulation is of the modal decomposition of the acoustic wave (for the purpose of calculating the matrix transition elements, C_{nm}). The former decomposition requires the calculation of the eigenmodes of the unperturbed Hamiltonian.

All simulations are done using fortran code developed by the author using double precision arithmetic. The Teragrid [1] is used for some larger, time intensive simulations.

This appendix describes the numerical methods programmed and the particular parameter choices made in carefully designing the simulations to ensure proper sampling and to minimize aliasing.

A.1 Sampling and Aliasing

When choosing a discrete representation for various continuous variables in the simulations, a grid size must be determined with careful attention to proper sampling. A general rule for adequate sampling requires a minimum of 10 points per wavelength.

Fourier and inverse fourier transforms are calculated numerically using a discrete fourier transform (DFT). If the input function for the DFT is represented on a grid with step size Δx, then only frequencies in the function with wavelengths larger than $2\Delta x$ can be detected. This corresponds to the Nyquist frequency [71], the minimum frequency detectable in the discrete sampling of a function. Frequencies present in the input function that are larger than k_{nyq} cannot be represented correctly and are 'aliased' back into the fourier transform domain, but at an incorrect frequency.

A.2 Numerical Acoustic Timefront

The acoustic timefronts corresponding to the propagation of an acoustic wave are calculated by discretizing the integration in Eq.(3.20) with the approximation $\int f(x)dx \approx \sum_i f(x_i)\Delta x$ so that

$$\Phi(z,r,t) \;=\; \frac{1}{\sqrt{2\pi\sigma_k^2}} \sum_{k=k_0-3\sigma_k}^{k_0+3\sigma_k} \Psi_k(z,r)\frac{e^{ik(r-c_0t)}}{\sqrt{r}} \exp\left[-\frac{(k-k_0)^2}{2\sigma_k^2}\right]\Delta k \;, \qquad \text{(A.1)}$$

where the standard deviation and center wavenumber are $\sigma_k = \frac{2\pi\sigma_f}{c_0}$ and $k_0 = \frac{2\pi f}{c_0}$. For $f = 75$ Hz, the standard deviation is chosen to be $\sigma_f = 18.75$ Hz to correspond to the 3-

dB bandwidth of 37.5 Hz from experiments. [12] The sum over wavenumbers k is done in increments of Δk over a range 3 standard deviations σ_k about the mean k_0 to prevent aliasing. The wavenumber stepsize Δk is chosen small enough to adequately sample the frequency spectrum of the source and to allow a large enough time window to adequately capture the spread in time of the timefront without aliasing.

A.2.1 Adequate Sampling

In the acoustic timefront, both the representation of the pulse in wavenumber k and in time t must be adequately sampled by the grid sizes Δk and Δt.

The wave number grid Δk for the source must be chosen to adequately sample the source. Requiring 10 points to sample 3 standard deviations of the Gaussian source in Eq. (3.16) gives $\Delta k \leq \frac{12\pi\sigma_f}{10c_0} = \frac{12\pi 37.5}{10c_0}$. For $f = 75$ Hz, $\Delta k \leq 47.5km^{-1}$. Yet, as seen in the next section, the limiting criteria for Δk is not the adequate sampling of the pules, but in reducing aliasing in the timefront window.

The time grid Δt for the acoustic arrivals must be chosen to adequately sample a single arrival. For the Gaussian source model described in Sec. (3.3), single pulse arrivals have a 4 standard deviation width of $4\sigma_t = \frac{4}{\sigma_k c_0} = \frac{2}{\pi\sigma_f}$, where $\sigma_f = \frac{f_0}{2}$. For $f = 75$ Hz, a single pulse width is approximately $4\sigma_t = \frac{2}{37.5\pi} \approx 0.0017$ sec. Requiring 10 points to sample the width of a single pulse gives $\Delta t < \frac{1}{5\pi\sigma_f}$. A proper sampling of a single pulse arrival implies by the Nyquist relation that the number of wave number points $N \geq \frac{2\pi}{c_0 \Delta t \Delta k}$. Since the frequency spectrum of the source dies off considerably after 3 standard deviations from the

Gaussian center of the spectrum, adding more wavenumber k points to the superposition with a weighting of zero (ie. zero padding) serves to increase the resolution Δt of the timefront with no computational propagation effort. The number of points to use in zero padding is chosen by the desired value of Δt.

A.2.2 Aliasing

Careful consideration of the Nyquist frequency and aliasing must be made in creating the acoustic timefronts since the timefront in Eq. 3.17 is calculated by performing a discretization of the Fourier transform integral. The discretization of the source wavenumber domain to N wavenumbers with stepsize Δk results in a restriction on the resolution of the timefronts to a stepsize of $\Delta t = \frac{2\pi}{c_0 \Delta k N}$ and a time window of $[-t_{nyq}, t_{nyq}]$, where $t_{nyq} = \frac{\pi}{c_0 \Delta k}$ is the Nyquist time. A shift of the time window to the proper domain enclosing the timefront for the acoustic arrivals can be made easily (ie. $[\frac{r}{c_0} - t_{nyq}, \frac{r}{c_0} + t_{nyq}]$) but the width of the window is solely determined by the discretization of the wavenumbers in Δk in determining t_{nyq}. Arrivals at a time t outside the time window $[\frac{r}{c_0} - t_{nyq}, \frac{r}{c_0} + t_{nyq}]$ are represented (aliased) in this time window at a time of $t + 2nt_{nyq}$, where n is the integer so that $t + 2nt_{nyq} \in [\frac{r}{c_0} - t_{nyq}, \frac{r}{c_0} + t_{nyq}]$. Thus, arrivals slightly earlier than the left boundary of the window will be aliased into the latest times in the window and arrivals slightly later than the right boundary of the window will be aliased into the early times in the window.

The spread of the timefront from early to late arrivals occurs over a window in time Δt_{window} and the Nyquist time t_{nyq} must be chosen $2t_{nyq} > \Delta t_{window}$ to properly contain this

timefront to prevent the aliasing of the significant parts of the timefront. Using the Nyquist relations, this requires $\Delta k \leq \frac{2\pi}{c_0 \Delta t_{window}}$ on the discretization of the wave numbers.

A.2.3 Desired Timefront Accuracy

Though the simulations in this thesis do not attempt to model the experimental simulations, the fact that the experiments can only measure pressure amplitudes to 2 significant figures (as discussed in Sec. (2.2)) means that a gross theory that gets the pressure amplitudes right to better than 1 percent will be very useful. Semiclassical theory is only good to around 1 percent. Thus, the numerical simulation for this work must be at least slightly more accurate than the semiclassical theory is expected to be. Thus, the simulations must guarantee that the amplitudes of the timefronts are measured accurately to at least 2 significant figures as well.

The accuracy of the timefront construction from Eq. (A.1) depends on the accuracy of the integration and the accuracy of the propagated wave field. Taking too few wavenumbers k in the integration results in a rippling effect on the arrival signals at each depth from poor sampling of the source. Taking Δk too large results in a Nyquist window in time that is too small to capture the signal, resulting in aliasing errors. Since the propagation is non-dispersive, the width of a single pulse is constant with propagation. The choice of (k_{min}, k_{max}) and Δk must only sample the pulse in k and the width of the timefront Δt_{window} properly. Choosing $(k_{min}, k_{max}) = (k_0 - 3\sigma_k, k_0 + 3\sigma_k)$ and $\Delta k \leq \frac{2\pi}{c_0 \Delta t_{window}}$ ensures this.

The dominant source of errors in the timefront comes from errors in the wave field from the propagation from the Split-Step method described in Sec. A.3.1. The wave field needs to

be a propagated so that it is accurate to within 2 significant figures.

A.3 Numerical Acoustic Wave

The wave field $\Psi_\omega(z,r)$ of the continuous wave with angular frequency ω, satisfies the parabolic equation in Eq. (3.8) with initial wave field in Eq. (3.18). The calculation of the wave field $\Psi_\omega(z,r)$ is an initial value problem in range that can be solved using a range marching technique. This type of problem has been widely solved in the underwater acoustics community by using either the split-step Fourier technique (aka Split Operator, Fast Fourier Transform method) [65] or various finite difference and finite element techniques. The split-step method is used in this work since it is more accurate for "narrow-angle problems with little or no bottom interaction". [56]

The potential V is calculated using Eq. (3.11) and Eq. (3.12). Using the split-step Fourier technique, the initial wave field in Eq.(3.18) is marched through the potential $V(z, r + \frac{\Delta r}{2}))$ (calculated at half range steps) on the spatial grid (z,r) with regular spacing $(\Delta z, \Delta r)$ to obtain the wave fields, $\Psi_\omega(z,r)$ at a range r. The spacing $(\Delta z, \Delta r)$ is chosen to adequately sample the fluctuations in the potential. The boundary conditions for this problem are not strictly enforced, but are implemented by restricting the initial source momenta to only those momenta that would avoid the ocean surface and floor (See Sec. (3.3.2 for a description on how the momenta is determined). Additionally, artificial regions are added to extend the vertical boundaries to allow the tails of the wave field to pass beyond the boundaries without being reflected. The timefront is constructed with careful attention to the proper sampling of

the source frequencies and consideration of aliasing.

A.3.1 The Split-Operator, Fast Fourier Transform Method

The split-operator Fourier transform method was invented by Feit and Fleck in 1976. [85] It was first used with the parabolic equation for underwater acoustics in 1977 by Hardin and Tappert [65]. This method is very efficient for long range propagation, narrow-angle propagation problems with negligible bottom interactions. Consider the parabolic equation in Eq. (3.8) with potential $V(z,r)$ which can be written in the form

$$\frac{\partial \Psi(z,r)}{\partial r} = \left(\frac{i}{2k} \frac{\partial^2}{\partial z^2} - ikV(z,r) \right) \Psi(z,r) = U(z,r)\Psi(z,r) \; .$$

Given the solution $\Psi(z,r_0)$ at the range $r = r_0$, the solution $\Psi(z,r_0+\Delta r)$ at the next range step $r = r_0 + \Delta r$ is

$$\Psi(z,r_0+\Delta r) = e^{\int_{r_0}^{r_0+\Delta r} U(z,r)dr} \Psi(z,r_0) \approx e^{\tilde{U}\Delta r} \Psi(z,r_0) \; ,$$

where $\tilde{U}\Delta r$ is the average operator of the integral operator $\int_{r_0}^{r_0+\Delta r} U(z,r)dr$. Here, it is assumed that U is constant over the interval Δr, which gives an error for the approximation of $(\Delta r)^2$. This error could have been reduced to $(\Delta r)^3$ had U been assumed to be linear over the range Δr.

The split operator method gets its name from the splitting of the operators in the following

approximation

$$e^{\tilde{U}\Delta r} = e^{(A+B)\Delta r} \quad = \quad e^{\frac{A}{2}\Delta r} e^{B\Delta r} e^{\frac{A}{2}\Delta r} + O\left((\Delta r)^3 f(A,B)\right) \ ,$$

where $A = \frac{i}{2k}\frac{\partial^2}{\partial z^2}$ and $B = -ikV(z, r + \frac{\delta r}{2})$. The error is a function of

$$f(A,B) = \frac{1}{24}\left(2B[A,B] - [A,B]2B + A[A,B] - [A,B]A\right)$$

where the commutator of operators A and B is $[A,B] = AB - BA$. Note that this approximation is exact if $[A,B] = 0$ and is of the order of $(k\Delta r)^3$ otherwise. The split operator method approximates the propagation by the dynamics of a propagation in three stages. The first stage propagates a plane wave with the current momentum for a range step $\frac{\Delta r}{2}$. The second stage treats the effects of a delta function potential of $V(z, \Delta r/2)$ at $r = \frac{\Delta r}{2}$. The final stage propagates a plane wave with the new momentum for another range step of $r = \frac{\Delta r}{2}$.
The Fourier transform relations for $\Psi(\cdot, r_0)$ are

$$\begin{aligned} \mathcal{F}\left[\Psi(z, r_0)\right] &= \Psi(k_z, r_0) = \int dz' e^{-ik_z z'} \Psi(z', r_0) \\ \mathcal{F}^{-1}\left[\Psi(k_z, r_0)\right] &= \Psi(z, r_0) = \int dk_z' e^{ik_z' z} \Psi(k_z', r_0) \ , \end{aligned}$$

where $\mathcal{F}[\cdot]$ and $\mathcal{F}^{-1}[\cdot]$ denote the Fourier and inverse Fourier transform respectively of a function and k_z is the wavenumber conjugate to the position variables z.

Then a function can be written in terms of it's own fourier transform as

$$\Psi(z, r_0) \;=\; \int dk e^{ik_z z} \int dz' e^{-ik_z z'} \Psi(z', r_0) \; .$$

The solution $\Psi(z, r_0 + \Delta r)$ at the first range step $r = r_0 + \Delta r$ is found by using the fourier transform relations and performing the operators A and B to give

$$\begin{aligned}
\Psi(z, r_0 + \Delta r) &= e^{\frac{A}{2}\Delta r} e^{B\Delta r} e^{\frac{A}{2}\Delta r} \Psi(z, r_0) \\
&= e^{\frac{A}{2}\Delta r} e^{B\Delta r} e^{\frac{A}{2}\Delta r} \int dk_z e^{ik_z z} \int dz' e^{-ik_z z'} \Psi(z', r_0) \\
&= e^{\frac{A}{2}\Delta r} e^{B\Delta r} \int dk_z e^{\frac{a}{2}\Delta r} e^{ik_z z} \mathcal{F}\left[\Psi(z, r_0)\right] \\
&= e^{\frac{A}{2}\Delta r} e^{B\Delta r} \mathcal{F}^{-1}\left[e^{\frac{a}{2}\Delta r} \mathcal{F}\left[\Psi(z, r_0)\right]\right] \\
&= e^{\frac{A}{2}\Delta r} \int dk e^{ik_z z} \int dz' e^{-ik_z z'} e^{b\Delta r} \mathcal{F}^{-1}\left[e^{\frac{a}{2}\Delta r} \mathcal{F}\left[\Psi(z', r_0)\right]\right] \\
&= \int dk e^{\frac{a}{2}\Delta r} e^{ik_z z} \int dz' e^{-ik_z z'} e^{b\Delta r} \mathcal{F}^{-1}\left[e^{-\frac{a}{2}\Delta r} \mathcal{F}\left[\Psi(z', r_0)\right]\right] \\
&= \mathcal{F}^{-1}\left[e^{\frac{a}{2}\Delta r} \mathcal{F}\left[e^{b\Delta r} \mathcal{F}^{-1}\left[e^{\frac{a}{2}\Delta r} \mathcal{F}\left[\Psi(z, r_0)\right]\right]\right]\right] \; ,
\end{aligned}$$

where the following identifications are made for the integral approximations

$$\begin{aligned}
\frac{a}{2}\Delta r &\approx -\frac{i}{k}\,\frac{k_z^2}{4}\,\Delta r \\
b\Delta r &= -ik\Delta r\; V(z, r_0 + \frac{\Delta r}{2}) \; .
\end{aligned}$$

The solution $\Psi(z, r_0 + 2\Delta r)$ at the next range step $r = r_0 + 2\Delta r$ combines the two inner

operators $e^{\frac{A}{2}}e^{\frac{A}{2}} = e^{A}$ for efficiency and gives

$$\Psi(z, r_0 + 2\Delta r) \;=\; \mathcal{F}^{-1}\left[e^{\frac{a}{2}\Delta r}\mathcal{F}\left[e^{b\Delta r}\mathcal{F}^{-1}\left[e^{a\Delta r}\mathcal{F}\left[e^{b\Delta r}\mathcal{F}^{-1}\left[e^{\frac{a}{2}\Delta r}\mathcal{F}\left[\Psi(z, r_0)\right]\right]\right]\right]\right] \; .$$

Extending all of the iterations in this manner, the wave field $\Psi(z, r_0 + n\Delta r)$ at n range steps $r = r_0 + \Delta r$ can be calculated with the following pseudo code

$$\begin{aligned}
FFT(1) &\approx \mathcal{F}\left[e^{-ik\left(V(z,r_0+\frac{\Delta r}{2})\right)\Delta r}\mathcal{F}^{-1}\left[e^{-\frac{i}{k}\frac{k_z^2}{4}\Delta r}\mathcal{F}\left(\Psi(z, r_0)\right)\right]\right] \\
\Psi(z, r_0 + \Delta r) &= \mathcal{F}^{-1}\left[e^{-\frac{i}{k}\frac{k_z^2}{4}\Delta r}FFT(1)\right] \\
IFFT(1) &\approx \mathcal{F}^{-1}\left[e^{-\frac{i}{k}\frac{k_z^2}{2}\Delta r}FFT(1)\right] \\
FFT(2) &\approx \mathcal{F}\left[e^{-ik\left(V(z,r_0+\Delta r+\frac{\Delta r}{2})\right)\Delta r}IFFT(1)\right] \\
\Psi(z, r_0 + 2\Delta r) &= \mathcal{F}^{-1}\left[e^{-\frac{i}{k}\frac{k_z^2}{4}\Delta r}FFT(2)\right] \\
IFFT(2) &\approx \mathcal{F}^{-1}\left[e^{-\frac{i}{k}\frac{k_z^2}{2}\Delta r}FFT(2)\right] \\
&\vdots \\
FFT(n-1) &\approx \mathcal{F}\left[e^{-ik\left(V(z,r_0+(n-2)\Delta r+\frac{\Delta r}{2})\right)\Delta r}IFFT(n-2)\right] \\
\Psi(z, r_0 + (n-1)\Delta r) &= \mathcal{F}^{-1}\left[e^{-\frac{i}{k}\frac{k_z^2}{4}\Delta r}FFT(n-1)\right] \\
IFFT(n-1) &\approx \mathcal{F}^{-1}\left[e^{-\frac{i}{k}\frac{k_z^2}{2}\Delta r}FFT(n-1)\right] \\
FFT(n) &\approx \mathcal{F}\left[e^{-ik\left(V(z,r_0+(n-1)\Delta r_+\frac{\Delta r}{2})\right)\Delta r}IFFT(n-1)\right] \\
\Psi(z, r_0 + n\Delta r) &= \mathcal{F}^{-1}\left[e^{-\frac{i}{k}\frac{k_z^2}{4}\Delta r}FFT(n)\right] \; .
\end{aligned}$$

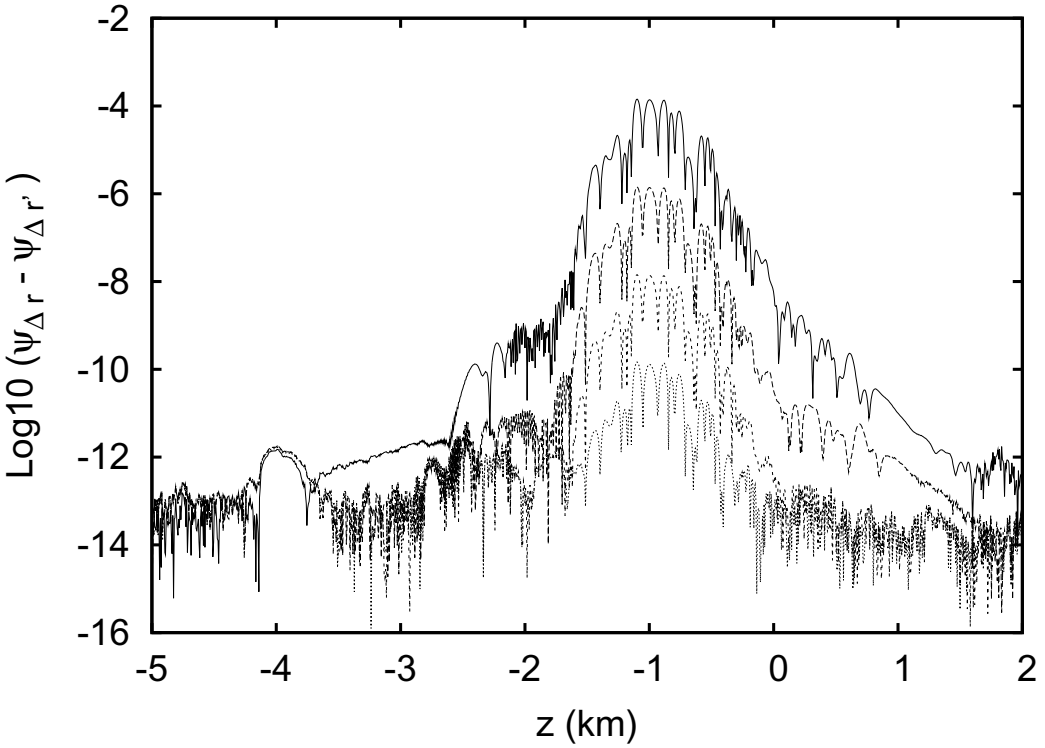

Figure A.1: Convergence of the split-step fourier method with decreasing range step size Δr. The wave function $\Psi_{\Delta r}$ after propagation to a range of 1 km for $\Delta r = 0.1, 0.01, 0.001, 0.0001$ km is compared to the wave function $\Psi_{\Delta r'}$ for $\Delta r' = 0.00001$ km by taking the log base 10 of the difference as a function of the depth z. The source frequency is 75 Hz and propagation is in the Munk potential. The errors in the convergence all peak at $z = -1$ km since this is where the bulk of the wave function lies. The peak errors of order $10^{-4}, 10^{-6}, 10^{-8}, 10^{-10}$ are for $\Delta r = 0.1, 0.01, 0.001, 0.0001$ km, respectively. This shows that for a factor of 10 reduction in Δr, there is a factor of 100 improvement in the accuracy of Ψ.

This method can be significantly sped up by using fast fourier transforms(FFT) to calculate the fourier and inverse fourier transforms. Numerically, the transforms are calculated using a discrete fast fourier transform where the vertical grid is chosen to have N points in the vertical extent $[z_{min}, z_{max}]$, where N is a power of 2.

The split-step fourier method should be accurate to order $(k\Delta r)^2$ indicating that a factor of 10 reduction in the range step size Δr would lead to a factor of 100 improvement in the accuracy of the wave field Ψ. Figure (A.1) indicates this improvement in the wave field.

A.3.2 Boundary Conditions

The ocean surface and floor reflect and absorb acoustic waves, respectively. The free surface is usually treated as a pressure-release boundary condition requiring $\Psi(r, 0) = 0$, which can be achieved by using a fourier sine transform instead of the fourier transform in the Split Step Operator Method. The absorbing seafloor boundary condition is usually modelled with an artificial absorption layer having a complex index of refraction, resulting in exponential attenuation of the wave in this artificial region so that wave energy entering this artificial region does not reenter the propagation.

Due to the extra complexity in implementing and analyzing the exact boundary conditions, the effect of the boundary conditions is modelled only by removing high angled wave energy from the propagation. The surviving arrivals in long range propagation correspond to only those classical rays within a range of initial momentum (ie. $p \in [-\tan 10^o, \tan 10^o]$). The initial momenta given to an initial wave packet can be controlled by the choice of its vertical extent (σ_z in Eq.(3.19)). Restricting the momentum in the initial wave packet then restricts the initial energies present in the wave to those that survive to long range propagation without encountering either the surface or ocean floor. Within this extended ocean, waves experience a soft reflection mainly from the background sound speed potential (ie. Munk's canonical model, Eq. (3.11)) instead of a hard reflection from the surface at $z = 0$.

Since the wave fronts corresponding to rays with classical turning points at the surface or ocean floor have significant energy in the tails, the vertical grid is extended to $[z_{min}, z_{max}]$ (km), where $z = 0$ is the ocean surface and $z = 5$ km is the ocean floor and $z_{min} < 0$ and

$z_{max} > 5$. Thus, wave energy is allowed to pass into the artificial region above and below the ocean boundaries at $z = 0$ and $z = 5$, so that minimal wave energy actually reflects from the boundary conditions at $z = z_{min}$ and $z = z_{max}$.

One consequence of extending the 'ocean' above the surface is that waves experience the potential above the surface. The background part of the potential serves to reflect the wave, but the fluctuations serve to scatter the wave. Since the internal wave sound speed fluctuations increase exponentially above the surface, wave energy passing above the surface is substantially scattered. In order to minimize this consequence, the surface filter is applied as described in Sec. (3.2.4). This choice should not severely impact the essential physics of the wave propagation.

Another consequence of this choice for dealing with the boundary conditions is that the tails of the wave are not reflected and absorbed by the boundaries as they would be in the real ocean. This absorption of the tails serves to strip acoustic energy from the wave, which diminishes the intensity of the wave.

A.3.3 Vertical Extent

The vertical extent (z_{min}, z_{max}) of the propagation region in depth is chosen to be large enough so that the wave field only experiences soft reflections from the Munk potential rather than hard reflections from the boundary. Unfortunately the tails of the wave will still experience hard reflections from the boundaries, but as long as the wave field at the boundaries stays zero to within 4 decimal places, this will be within the desired accuracy for the propagations.

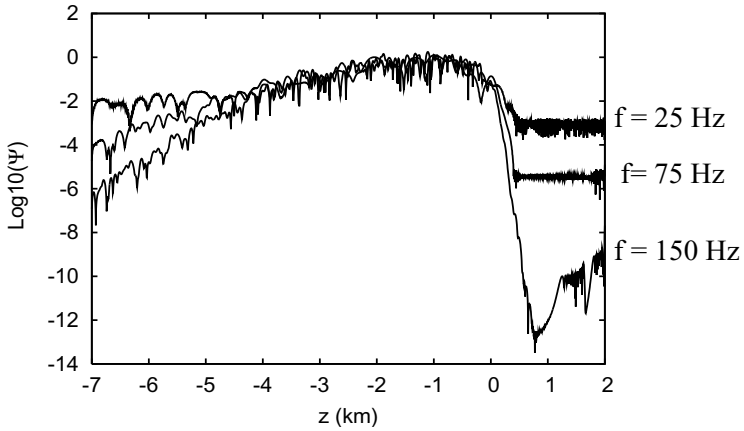

Figure A.2: Logarithm of wave field Ψ versus depth z for propagation to a range of 3000 km for source frequencies of $f = 25, 75, 150$ Hz. The longer tails of the lower frequency wave fields is reflected more from the lower boundary in the ocean leading to a wave field of 10^{-2} at the lower boundary for $f = 25$ Hz. This error is aliased to the upper ocean from the fourier transforms in the split-operator method.

Hard reflections from the boundaries for propagation to 3000 km with internal wave effects lead to nonzero boundary values for the wave field. Lower source frequencies have larger wave tails and hit the boundaries with a larger amplitutde. As shown in Fig. (A.2), a vertical extent of $[z_{min}, z_{max}] = [-2, 7]$ is large enough for the boundaries to stay below 10^{-2} for 25 Hz propagations and 10^{-4} for 75 Hz propagations.

A.3.4 Adequate Sampling

The spatial grid $(\Delta z, \Delta r)$ must be chosen small enough that the variations in the wave field at all propagation ranges can be properly sampled by the grid. This statement is equivalent to having all frequencies in the fourier transform of the wave field properly represented. Additionally, the extent of the vertical grid (z_{min}, z_{max}) must be large enough that the wave field at all propagation ranges is zero to within the accuracy desired.

An adequate sampling of the potential in both depth and range is necessary for convergence of the wave field. The horizontal fluctuations in the potential have largest wavenumber $k_r = \frac{2\pi}{1\ km}$ corresponding to a smallest wavelength of 1 km. Adequate sampling with 10 points per wavelength requires $\Delta r < 0.1$. Since errors in the split-step method go like $k_0(\Delta r)^3$, smaller values of Δr must be chosen to ensure the same accuracy in the wave field for longer propagations and larger source frequencies. For the source frequencies $25, 75, 150, 250$ Hz, the range stepsize chosen is $\Delta r = 0.01, 0.01, 0.005, 0.0025$ km to ensure accuracy in the wave fields. Note that this is much less than the required $\Delta r < 0.1$ to sample the potential adequately.

The vertical fluctuations in the potential have been smoothed with the smoothing filter as in Ref. [61] to produce only vertical fluctuations larger than the maximum vertical wavelength of the source, $\frac{c_0}{f \tan \theta_{max}}$, where f is the source frequency and $\theta_{max} = 10^0$, corresponding to the maximum initial angle a ray can have and avoid the surface. For a source frequency of 75 Hz, the vertical fluctuations have a wavelength greater than 20 m. Adequate sampling with 10 points per wavelength requires $\Delta z < 0.02$ m. For source frequencies $25, 75, 150, 250$ Hz, $N = 1024, 2048, 2048, 2048$ points are chosen for the vertical extent $[-2, 7]$. This gives $\Delta z \approx 0.009, 0.0045, 0.0045, 0.0045$ m for the source frequencies $25, 75, 150, 250$ Hz, respectively, These values satisfy $\Delta z < \frac{c_0}{10 f \tan 10^0}$.

f (Hz)	n_{max}	J_{max}	$(\Delta z)^n_{min}$ km	$(\Delta z)^V_{min}$ km
25	20	20	0.012	0.0028
75	61	50	0.009	0.0093
150	123	90	0.007	0.0047
250	205	145	0.0035	0.0031

Table A.1: Frequency f, maximum number of wave modes, n_{max}, maximum number of internal wave modes, J_{max}, resolution needed to sample modes at 10 points per wavelength, $(\Delta z)^n_{min}$ and resolution needed to sample potential at 10 points per wavelength, $(\Delta z)^V_{min} = \frac{c_0}{10f \tan 12^0}$.

A.3.5 Aliasing

Fourier and inverse Fourier transforms are performed using the split-operator Fourier method. The initial wave function is represented with a stepsize in depth, Δz. Therefore, only wavenumbers k_z within the range $[-k_{nyq}, k_{nyq}]$, where $k_{nyq} = \frac{\pi}{\Delta z}$ is the Nyquist wavenumber and the step size is $\Delta k_z = \frac{2\pi}{z_{num}\Delta z}$, can be resolved during the propagation. Frequencies in the propagated wave field that are not sampled properly by the grid in depth will result in aliasing in the wave function.

Additionally, due to the shallow slope of the Munk potential in Eq. (3.11), tails of the wave energy are longer near the ocean floor than near the surface. Wave energy that reaches the vertical boundaries in depth will be aliased near the surface. Thus, it is very important that the vertical extent be chosen large enough and the boundaries checked for aliasing to ensure accuracy in the method.

A.3.6 Desired Wave Field Accuracy

The wave field is calculated using the split-operator method described in Appendix A.3.1. This method has range steps that are accurate to order $k\,(\Delta r)^3$. In order to understand the accumulation of errors in the wave field with propagation range, an experiment is done to test the accuracy of the split-step method with varying range step sizes Δr, frequencies and propagation ranges. The results of this experiment for 75 Hz are shown in Fig. (A.1).

The vertical extent of the grid (z_{min}, z_{max}) is chosen so that the wave field remains essential zero to within 4 significant figures at the boundaries z_{min} and z_{max} throughout the propagation range. The vertical grid $[-2, 7]$ satisfies this requirement.

A.4 Numerical Eigenmodes of Munk Potential

The parabolic equation in Eq. (3.8) with the Munk potential V in Eq. (3.11) has separable solutions

$$\Psi_\omega(z, r) = \sum_m e^{ikrE_m}\psi_m(z)$$

where $\Psi_m(z)$ are the eigenmodes and E_M are the eigenenergies satisfying the Sturm-Liouville eigenvalue problem in Eq. (4.3),

$$-\frac{1}{2}\frac{d^2\psi_m}{dz^2} + k_0^2 V(z)\psi_m = k_0^2 E_m \psi_m \ .$$

The eigenmodes are orthogonal, so they serve as a basis set of functions for writing the

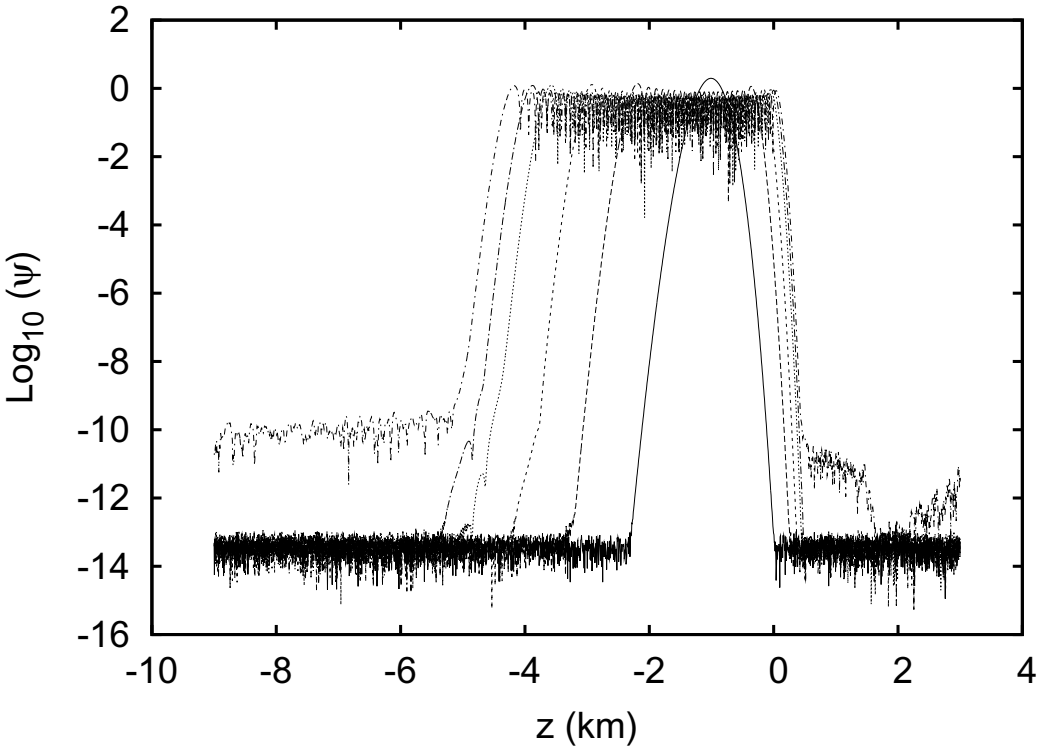

Figure A.3: Accuracy of the wavefield at boundaries as a function of initial acoustic mode taken for the propagation. Log base 10 of the wave field Ψ is plotted versus final depth z for the propagation of mode $n = 0, 20, 40, 60, 70, 80$ in only the Munk potential for 3000 km. The source frequency is 75 Hz and the range step size is $\Delta r = 0.01$ km. Propagation of modes $n = 0, 20, 40, 60, 70$ are all reflected by the potential with little or no effect of the boundary on the tails of these propagated modes.

solutions $\psi(z, r)$ of the parabolic equation with the full range dependent potential as

$$\Psi_\omega(z, r) = \sum_m \alpha_m(r)\psi_m(z)$$

where $\alpha_m(r)$ are the weightings of each mode in the wave field solution which evolve with range due to the mixing of modes caused by the scattering from the range dependent potential. This mixing of modes is explored through calculation of the transition matrix elements C_{nm} in Sec. (4.5).

In the underwater acoustics community, the eigenvalue problem in Eq. (4.3) with the Munk potential V is usually solved by using either an implicit finite difference method or recasting the problem as an initial value problem and using a shooting technique. Some numerical instability occurs with the shooting technique [56]. In this work, however, the eigenvalue problem is solved numerically in a very different way by diagonalizing a matrix representation of the Hamiltonian.

The method used here is motivated by the fact that at small energies, a harmonic potential is a good approximation to the Munk Potential so the modes and energies for the harmonic potential approximate the modes and energies for the Munk potential. Since the Hamiltonian corresponding to the Munk potential can be analytically constructed in the representation of the modes of the harmonic potential, numerically diagonalizing the resulting analytic matrix gives the energies and the weightings for forming the Munk modes as a superposition of the harmonic modes. Several computational tricks are necessary to ensure convergence of this method for the higher modes. The form of the harmonic potential is optimally chosen so that

the fewest harmonic modes are needed to represent the Munk modes.

A.4.1 Analytic Hamiltonian Matrix

The Hamiltonian $H = p^2 + V(z)$ corresponds to the parabolic equation with V the Munk potential in Eq. (3.11) and p the momentum. The Hamiltonian $H_0 = p^2/2 + V_{HO}$ corresponds to the parabolic equation with the harmonic potential $V_{HO} = 1/2\omega^2(z - z_{HO})^2$ with free parameters ω_{HO} and z_{HO}. The eigenenergies for H_0 are $E_n^{HO} = (n + 1/2)\omega/k$ and the corresponding eigenmodes,ψ_n^{HO}, are

$$\psi_n^{HO}(z) = \frac{1}{\sqrt{2^n n!}} \left(\frac{\omega k}{\pi}\right)^{1/4} \exp\left[-\frac{\omega k}{2}(z - z_{HO})^2\right] H_n\left(\sqrt{\omega k}(z - z_{HO})\right) ,$$

where $H_n(z)$ are the Hermite polynomials such that $H_n(z) = (-1)^n e^{x^2} \frac{d}{dx^n} e^{-x^2}$ with orthogonal condition $\int e^{-x^2} H_n(x) H_m(x) dx = \sqrt{\pi} 2^n n! \delta_{m,n}$.

The matrix elements of H can be written in the basis of harmonic modes $|\psi_n^{HO}>$ as

$$\begin{aligned} H_{n,m} &= <\psi_n^{HO}|H|\psi_m^{HO}> \\ &= <\psi_n^{HO}|H_0|\psi_m^{HO}> + <\psi_n^{HO}|V - V_{HO}|\psi_m^{HO}> \\ &= E_n^{HO}\delta_{n,m} + <\psi_n^{HO}|V|\psi_m^{HO}> - <\psi_n^{HO}|V_{HO}|\psi_m^{HO}> . \end{aligned} \tag{A.2}$$

The matrix elements for V are

$$
\begin{aligned}
& < \psi_n^{HO}|V|\psi_m^{HO} > \\
= & \int dz \left(\psi_n^{HO}(z)\right)^* V(z)\psi_m^{HO}(z) \\
= & \frac{B\gamma}{2}\sqrt{\frac{\omega k}{\pi 2^{(n+m)}n!m!}}\int dz \left[e^{-2/B(z-z_A)} - 1 + \frac{2}{B}(z-z_A)\right] \\
& e^{-\omega k(z-z_{HO})^2} H_n\left(\sqrt{\omega k}(z-z_{HO})\right) H_m\left(\sqrt{\omega k}(z-z_{HO})\right) \\
= & \frac{B\gamma}{2}\left[\left(-1+\frac{2}{B}\left(z_{HO}-z_A\right)\right)\delta_{m,n} + \frac{1}{B\sqrt{2\omega k}}\left(\sqrt{(n+1)}\delta_{m,n+1} + \sqrt{n}\delta_{m,n-1}\right)\right] \\
& + \frac{B\gamma}{2}\sqrt{\frac{1}{n!m!}} e^{-\frac{2}{B}(z_{HO}-z_A)+\frac{1}{B^2\omega k}} \sum_{k=0}^{\min m,n} \binom{n}{k}\binom{m}{k}\left(-\frac{1}{B\sqrt{\omega k}}\right)^{n+m-2k} 2^{-k}k!\sqrt{2^{n+m}}\,,
\end{aligned}
\tag{A.3}
$$

where the substitution $x = \sqrt{\omega k}(z - z_{HO})$, $dx = \sqrt{\omega k}dz$ is made and $\int e^{-x^2} H_n(x)H_m(x)dx = \sqrt{\pi}2^n n!\delta_{m,n}$, $xH_n(x) = \frac{1}{2}(H_{n+1}(x) + 2nH_{n-1}(x))$ and $H_n(x+y) = \sum_{k=0}^{n}\binom{n}{k}H_k(x)(2y)^{n-k}$ are used. The matrix elements for V_{HO} are

$$
\begin{aligned}
< \psi_n^{HO}|V_{HO}|\psi_m^{HO} > &= \int dz \left(\psi_n^{HO}(z)\right)^* V(z)\psi_m^{HO}(z) \\
&= \frac{\omega^2}{2}\sqrt{\frac{\omega k}{\pi 2^{(n+m)}n!m!}}\int dz(z-z_{HO})^2 e^{-\omega k(z-z_{HO})^2} \\
&\quad H_n\left(\sqrt{\omega k}(z-z_{HO})\right) H_m\left(\sqrt{\omega k}(z-z_{HO})\right) \\
&= \frac{\omega}{4k}\left(\sqrt{(n+2)(n+1)}\delta_{m,n+2} + (2n+1)\delta_{m,n} + \sqrt{n(n-1)}\delta_{m,n-2}\right)\,,
\end{aligned}
\tag{A.4}
$$

where the previous substitution is used and $xH_n(x) = \frac{1}{2}(H_{n+1}(x) + 2nH_{n-1}(x))$ is used

twice to get $x^2 H_n(x)$.

Using Eq. (A.2), Eq. (A.3) and Eq. (A.4) gives the matrix elements of H

$$
\begin{aligned}
< \psi_n^{HO}| \quad H \quad |\psi_m^{HO} > & \\
&= \delta_{m,n}\left[\frac{B\gamma}{2}\left(-1+\frac{2}{B}\left(z_{HO}-z_A\right)\right)+\frac{\omega}{4k}(2n+1)\right] \\
&\quad -\frac{\omega}{4k}\left(\sqrt{(n+2)(n+1)}\delta_{m,n+2}+\sqrt{n(n-1)}\delta_{m,n-2}\right) \\
&\quad +\frac{\gamma}{\sqrt{2\omega k}}\left(\sqrt{(n+1)}\delta_{m,n+1}+\sqrt{n}\delta_{m,n-1}\right) \\
&\quad +\frac{B\gamma}{2}e^{-\frac{2}{B}(z_{HO}-z_A)+\frac{1}{B^2\omega k}}\sum_{k=0}^{\min m,n}(-1)^{n+m-2k}\sqrt{\binom{n}{k}\frac{(2x^2)^{n-k}}{(n-k)!}}\sqrt{\binom{m}{k}\frac{(2x^2)^{m-k}}{(m-k)!}},
\end{aligned}
$$

where $x = \frac{1}{B\sqrt{\omega k}}$.

For the numerical stability of this calculation for the larger values of n, the following is used

$$
\begin{aligned}
\sqrt{\binom{n}{k}\frac{(2x^2)^{n-k}}{(n-k)!}} &= \sqrt{\frac{n(n-1)\ldots(k+1)}{(n-k)!^2}(2x^2)^{n-k}} \\
&= \prod_{j=1}^{n-k}\frac{x\sqrt{2(k+j)}}{j}.
\end{aligned}
$$

A.4.2 Numerical Matrix Diagonalization

The LAPACK routine, dsyev, is used to diagonalize the matrix reprentation of H. This routine computes all eigenvalues and eigenvectors of a real symmetric matrix A using a QR algorithm[86]. This algorithm proceeds by orthogonal similarity transforms and thus is numerically stable. For example, it takes $A_0 = A$ as the first step and at the kth step, it takes

A_k as the product of an orthogonal matrix Q_k and an upper triangular matrix, R_k. Then $A_{k+1} = R_k Q_k = Q_k^T Q_k R_k Q_k = Q_k^T A_k Q_k$, so all the A_k are similar and have the same eigenvalues. The columns of Q_k converge to the eigenfunctions of A. Under certain conditions, the A_k converge to a triangular matrix and the eigenvalues of A are listed on the diagonal of this triangular matrix.

The computed eigenvalues and eigenfunctions are exact for a nearby matrix $A+E$, where E is the error matrix from A. Convergence is determined when the the Euclidean norm of the error matrix is the Euclidean norm of the matrix A to a factor within machine precision. [87]

A.4.3 Numerical Eigenmodes

The result of the matrix diagonalization is an ordered list of eigenvalues, E_n, and an orthogonal matrix Q, whose columns, Q_n, are the eigenvectors of the matrix. The eigenvalues and eigenmodes for the Munk potential are then E_n and Q_n, but Q_n is in still in the harmonic mode basis. For $Q(n,i)$ the ith row and nth column of Q, the eigenvectors of H for the Munk potential are

$$\psi_n(z) \quad = \quad \sum_{i=1}^{n} Q(i,n)\psi_n^{HO}(z) \; .$$

In superposing harmonic modes to obtain the Munk modes, high accuracy is needed in the Hermite Polynomials even for large n. The harmonic modes $\psi_n^{HO}(z)$ in Eq. (A.2) are of the form $A_n(x)H_n(x)$, where $A_n(x) = \frac{e^{-x^2/2}}{\sqrt{n!2^n}}$ and $x = \sqrt{\omega k}(z - z_{HO})$. The Hermite Polynomials

can be calculated using the nested form

$$\begin{aligned} H_0(x) &= 1 \\ H_1(x) &= 2x \\ H_{n+2}(x) &= 2xH_{n+1}(x) - 2(n-1)H_n(x) \ . \end{aligned}$$

But for large n (ie. $n > 60$), this form is numerically unstable and diverges. Since the harmonic modes are of the form $A_n(x)H_n(x)$, where $A_n(x) = \frac{e^{-x^2/2}}{\sqrt{n!2^n}}$ and $x = \sqrt{\omega k}(z - z_{HO})$, the instability in the Hermite polynomials can be delayed past $n = 60$ by incorporating the $\frac{e^{-x^2/2}}{\sqrt{n!2^n}}$ into the nested calculation of the Hermite polynomials. Since $A_{n+1} = \frac{A_n}{\sqrt{2(n+1)}}$,

$$\begin{aligned} A_0(x)H_0(x) &= e^{-x^2/2} \\ A_1(x)H_1(x) &= \frac{2x}{\sqrt{2}}e^{-x^2/2} = \sqrt{2}xe^{-x^2/2} \\ A_{n+2}(x)H_{n+2}(x) &= 2xH_{n+1}(x)\frac{A_{n+1}(x)}{\sqrt{2(n+2)}} - 2(n+1)H_n(x)\frac{A_n}{2\sqrt{(n+2)(n+1)}} \\ &= \sqrt{\frac{2}{n+2}}xA_{n+1}(x)H_{n+1}(x) - \sqrt{\frac{n+1}{n+2}}e^{-x^2/2}A_n(x)H_n(x) \ . \end{aligned}$$

Due to finite precision arithmetic, high accuracy in the Hermite Polynomials for large values of N require the use of the asymptotic forms. [88] For even/odd Hermite Polynomials, H_n, the following asymptotic forms approximate the oscillatory nature of the Hermite Polynomi-

als (interior to the classical turning points),

$$\begin{aligned}\lim_{n\to\infty}\left[\frac{(-1)^n\sqrt{n}}{4^n n!}H_{2n}\left(\frac{x}{2\sqrt{n}}\right)\right] &= \frac{1}{\sqrt{\pi}}\cos x \\ \lim_{n\to\infty}\left[\frac{(-1)^n}{4^n n!}H_{2n+1}\left(\frac{x}{2\sqrt{n}}\right)\right] &= \frac{2}{\sqrt{\pi}}\sin x\ .\end{aligned}$$

In order to obtain stable computations, these even/odd Hermite polynomials can be rewritten as a product of bounded numbers,

$$\begin{aligned}A_{2n+1}H_{2n+1} &= \frac{1}{\sqrt{\pi}}(-1)^n\sin(2\sqrt{n}x)\sqrt{\frac{2}{2n+1}}\prod_{k=1}^{n}\frac{\sqrt{2ke^{-\frac{x^2}{n}}}}{\sqrt{2k-1}} \\ A_{2n}H_{2n} &= \frac{1}{\sqrt{\pi}}(-1)^n\cos(2\sqrt{n}x)\sqrt{\frac{2}{2n}}\prod_{k=1}^{n}\frac{\sqrt{2ke^{-\frac{x^2}{n}}}}{\sqrt{2k-1}}\ .\end{aligned}$$

Using this method, the modes are calculated accurately beyond $n = 60$.

The convergence of the eigenvalues and the eigenfunctions is tested by comparing the results for the diagonalization with a matrix of size N with that of a larger matrix of size N'. Figures (A.6- A.5) illustrate the convergence of the eigenvalues with mode number as a function of the matrix size N.

The accuracy of the eigenvalues and the eigenfunctions of the Munk potential is tested by propagating each eigenfunction in the Munk potential for a large distance r. The propagated wave field should only differ from the initial eigenfunction by a phase $e^{ik_0E_nr}$. The theoretical phase of k_0E_nr can be compared to the numerical phase of the propagated eigenfunctions. By comparing the eigenenergies from the numerical phases to the eigenenergies from the di-

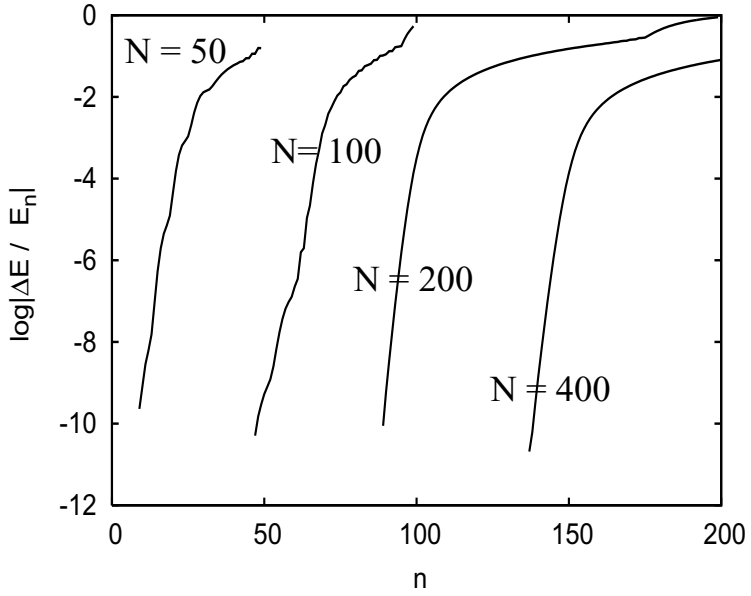

Figure A.4: Comparison of the convergence of the diagonalization method with mode number n as a function of the size of the matrix N. The relative difference in energy ΔE between the eigenenergies E_n of the Munk potential from the matrix diagonalization for a matrix size $N = 50, 100, 200, 400$ and that for a matrix of size $N' = 800$ is plotted versus mode number n. The source frequency is 75 Hz. Therefore to guarantee that the eigenenergies are accurate to 8 significant figures for modes up to $n = 50$, the matrix size would need to be taken at least $N = 100$.

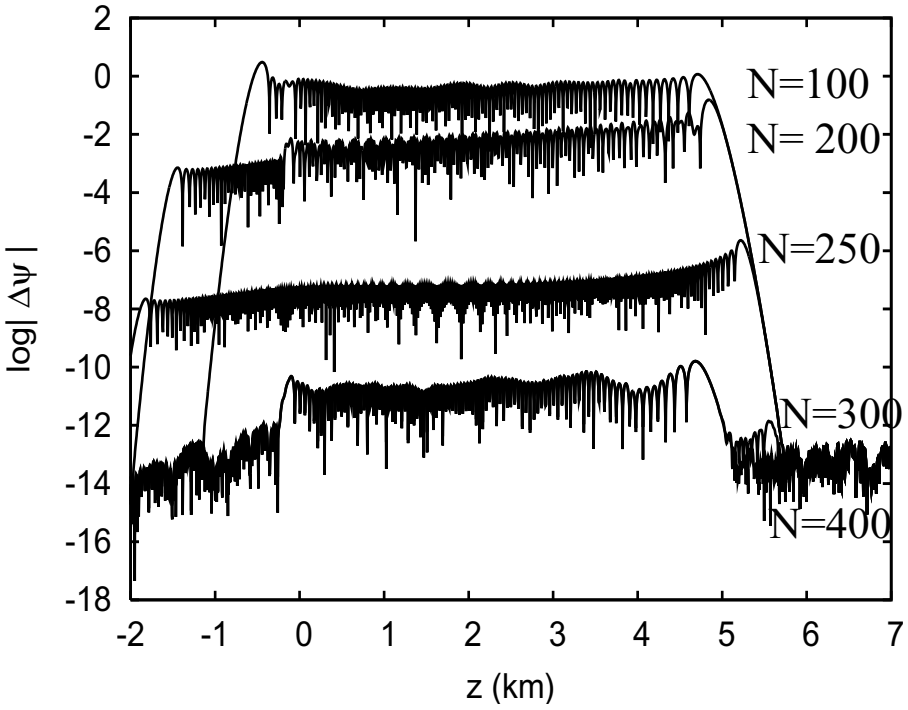

Figure A.5: The logarithm of the difference $\Delta\psi$ of the eigenfunction ψ_{100} when taking a matrix of size N and when taking a matrix of size $N' = 800$ is plotted as a function of depth z for different matrix sizes N in the diagonalization method. The source frequency is 75 Hz. Since ψ_{100} is of order 1 in the region about $z = 1$ km, the number of significant figures in the eigenfunction near $z = 1$ km is about $1, 3, 7, 100$ for $N = 100, 200, 250, 300$ respectively. The result for $N = 300$ and $N = 400$ was approximately the same to machine precision.

agonalization routine, the convergence and accuracy of the eigenenergies with mode number n is illustrated in Fig. A.6 for two different source frequencies.

A.4.4 Modes Present in Initial Wavefield

The initial Gaussian wavefunction $\Psi(z,0)$ in Eq. (3.18) can be written as a superposition over the Munk modes $\psi_n(z)$ from Eq. (4.3) as $\Psi(z,0) = \sum_0^N a_n \psi_n(z)$. The coefficients a_n oscillate in sign. Figures (A.7) and (A.8) illustrates the manner in which the probabilities $|a_n|^2$ exponentially decay to zero with increasing mode number n for a source frequency of 75 Hz.

In order to adequately represent the initial wave field by the superposition $\sum_0^N a_n \psi_n(z)$, N must be chosen large enough. If it is the general agreement of the wave field and the superposition that is desired, then the overlap measure O_N (similar to that used in Ref. ([61])) can be used to determine N. The overlap measure O_N is

$$O_N = \int dz \Psi(z,0) \sum_{n=0}^{N} a_n \psi_n(z) = \sum_{0}^{N} |a_n|^2 , \tag{A.5}$$

where the simplification uses the orthonormalization of the modes. Note that as the higher modes become more negligible, the overlap approaches one. As the higher modes become less neligible, the overlap deviates from one. Figure. (A.10) illustrates how the difference in the overlap from one increases with maximum mode number N in the superposition. This is also the loss in the conservation of the probability by neglecting the higher modes. Modes up to $n = 20$ are necessary to capture the initial wave field to 99.9% in Figure. (A.10).

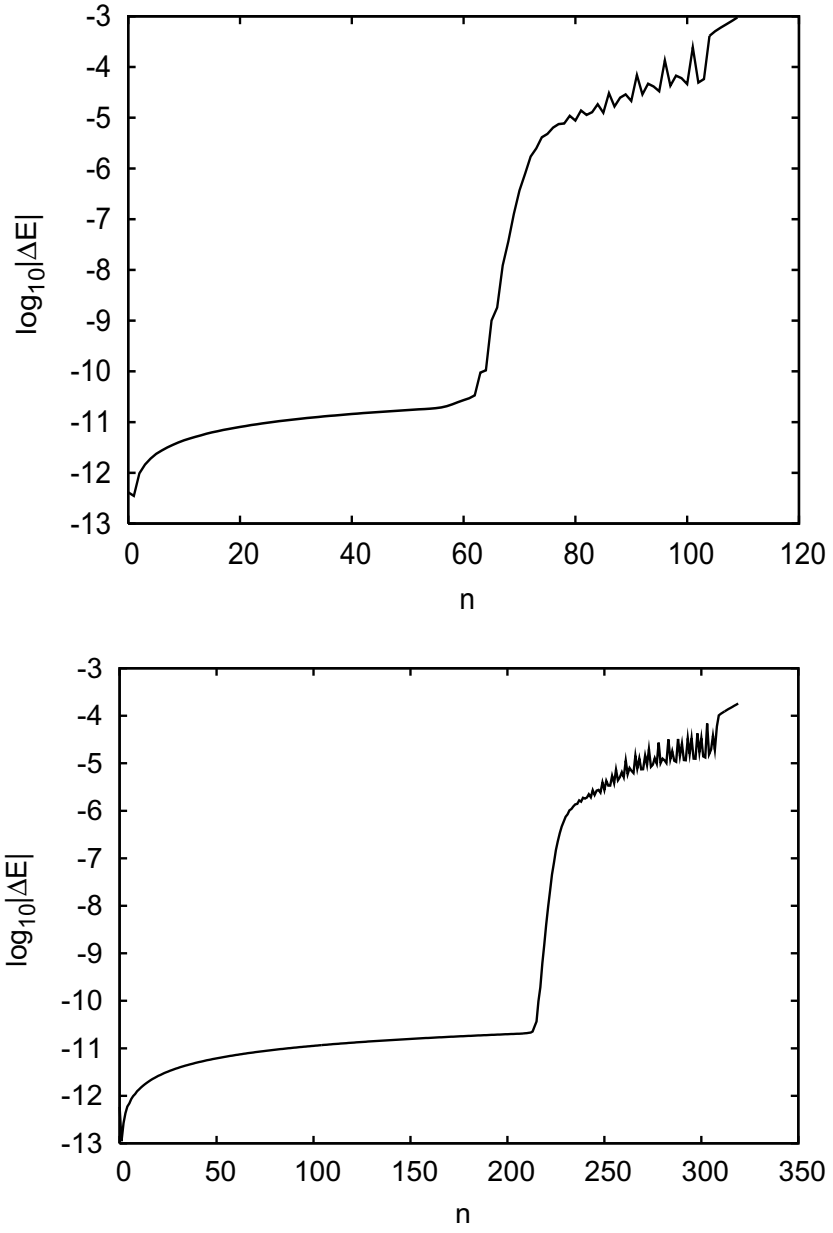

Figure A.6: Comparison of the accuracy and convergence of the diagonalization method for 75 Hz (upper plot) and 250 Hz (lower plot). The difference in energy ΔE between the eigenenergies E_n of the Munk potential from the matrix diagonalization and that calculated from the phase accumulation for a propagated eigenmode in the Munk potential is plotted with mode number n. The propagation is done for a 75 Hz and 250 Hz source frequency for a short range (ie. 0.1 km) The diagonalization has converged with stable small errors in the 11th decimal places for modes up to 60 and 210, for 75 Hz and 250 Hz, respectively. Beyond these modes, the exponentially fast failure to converge is illustrated. Note that the ratio of the converged states is $60/110 = 0.5454$ and $210/320 = 0.65625$, for 75 Hz and 250 Hz, respectively, so that 250 Hz is an improvement over the 75 Hz case.

If it is the accuracy of the superposition as a function of depth that is desired, then plots of the error of the superposition $\sum_0^N a_n \psi_n(z)$ as a function of depth, as shown in Fig. (A.9), are needed. As shown in Fig. (A.9), modes up to $N = 60$ would need to be considered for errors less than 10^{-3} between the wave field and superposition.

A.4.5 Modes Present in Ocean Waveguide

Since acoustic propagation serves to remove acoustic energy that encounters the surface and ocean floor, only certain modes can be present in the propagation to long range. It is then of interest to know how many modes are present in the vertical region between $z = 0$ and $z = H]$ so that the maximum number of modes needed to represent the wave field is known as a function of frequency.

To determine these maximum number of modes, consider a semiclassical approximation to the acoustic wave. The classical ray that just intersects the surface has energy $E = V_0(z = 0)$. In the Munk potential, this ray has action, $I \approx 0.196$. The quantized modes have classical action $I = \frac{1}{k}\left(n + \frac{1}{2}\right)$. Therefore, the maximum mode that remains in the propagation is

$$n_{max} = Ik - 0.5 = 0.196k - 0.5 = \frac{2\pi f(0.196)}{c_0} - 0.5$$

A classical approximation for the maximum mode number, n_{max}, that can occur in the wave propagation in the Munk potential versus the source frequency, f, is given in Table A.4.5 using this formula.

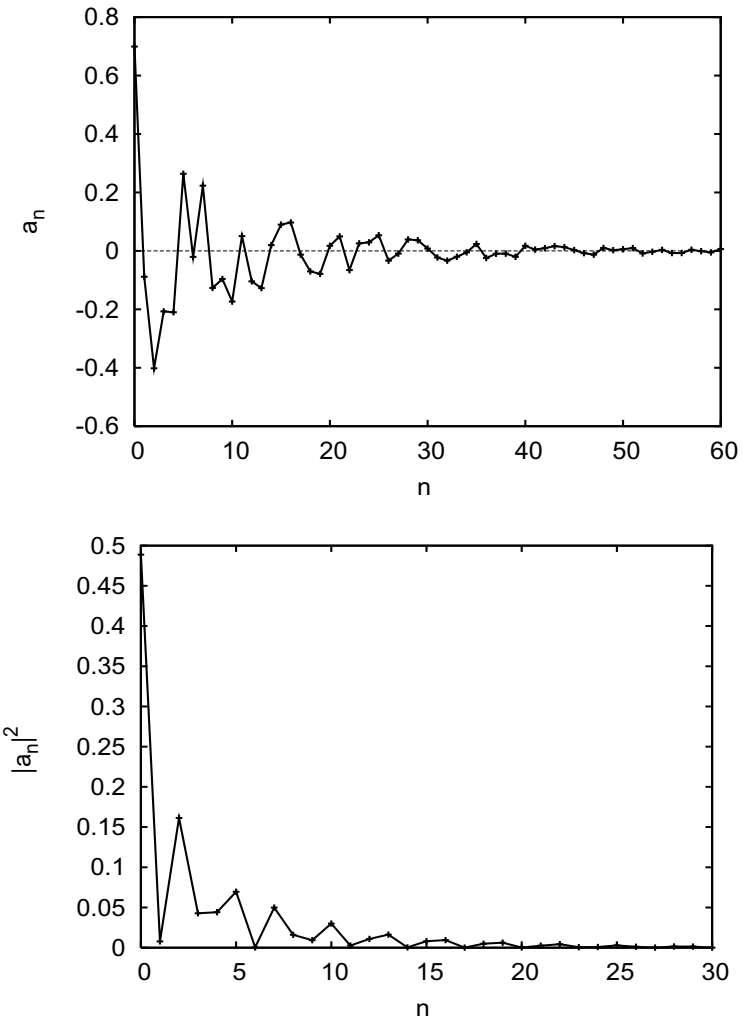

Figure A.7: Values of a_n(upper plot) and $|a_n|^2$(lower plot) are plotted versus mode number n, where the coefficients a_n are such that $\Psi(z,0) = \sum_n a_n \psi_m(z)$, for the initial wave field $\Psi(z,0)$ for a frequency of 75 Hz. The even symmetry of the lower modes due to the local harmonic shape of the potential near the minimum causes the odd modes $n = 1, 3, 5$ to be reduced from the even mode contributions. But there is a lack of symmetry for higher modes due to the shape of the Munk potential so that the odd modes contribute more with larger n. Though the dominant amplitudes from the plots are $0 < n < 30$, there are still obvious oscillations in the tails in the construction of ψ using the first 70 modes. The first 100 modes are needed to visibly remove the oscillations to adequately represent the initial wave field in terms of modes.

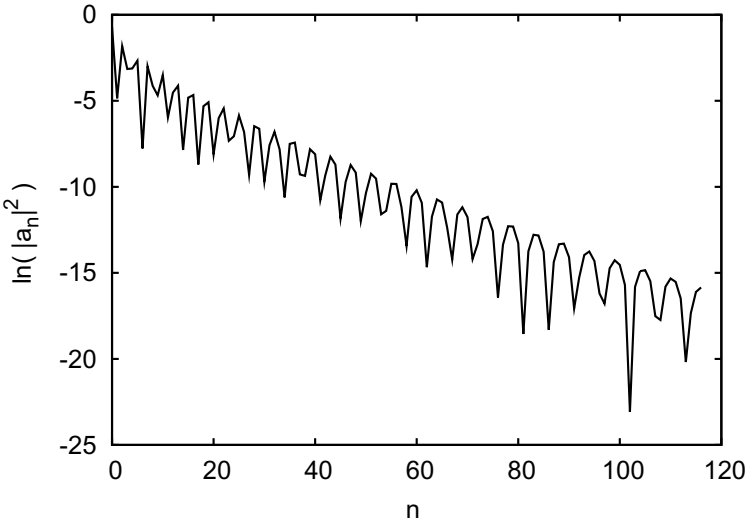

Figure A.8: Values of $ln(|a_n|^2)$ are plotted versus mode number n, where the coefficients a_n are such that $\Psi(z,0) = \sum_n a_n \psi_m(z)$, for the initial wave field $\Psi(z,0)$ for a frequency of 75 Hz. Based upon this graph, an approximate model for the probabilities is exponential $|a_n|^2 = e^{-4-0.1n}$

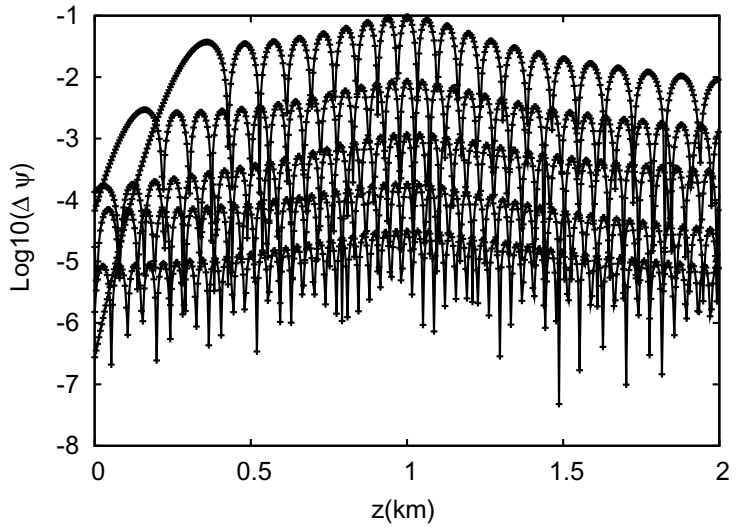

Figure A.9: Logarithm base 10 of the difference in the wave fields $\Delta\Psi = |\Psi_0 - \sum_{n=0}^{N} a_n \psi_n(z)|$ for each N is plotted with depth z, where the initial wave field $\Psi_0(z)$ is for a source frequency of 75 Hz. The log plot shows the magnitude of the error of the superposition for $N = 20, 40, 60, 80, 100$ (largest oscillations down to smallest oscillations). For example, the superposition of up to $N = 20$ modes gives the initial wave field to a maximum accuracy of 10^{-1}, while for the superposition up to $N = 100$ modes gives the initial wave field to an accuracy of roughly 10^{-5}. For errors less than 10^{-3}, modes up to $N = 60$ would need to be considered.

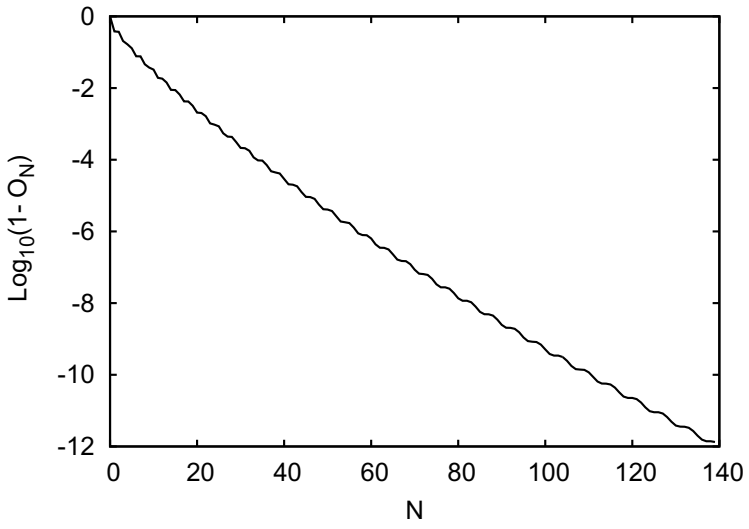

Figure A.10: Logarithm of the difference in the overlap from one,$1 - O_N$, is plotted with maximum mode number N from the superposition $\Psi(z, 0) \approx \sum_{n=0}^{N} a_n \psi_n(z)$. The overlap O_N in Eq. (A.5) is a measure of how well the superposition approximates the initial wavefield for 75 Hz. At $N = 20$, one minus the overlap is 10^{-3}, so the overlap is 0.999. This indicates that modes up to $n = 20$ are necessary in representing the initial wave field to 99.9%.

Frequency (Hz)	n_{max}
25	20
75	61
150	123
250	205

Table A.2: A classical approximation to the maximum number n_{max} of acoustic modes that can travel in the waveguide from the Munk potential is estimated by the formula $n_{max} = \frac{2\pi f(0.196)}{c_0} - 0.5$, where f is the source frequency.

A.4.6 Optimal Harmonic Potential Basis Functions

Using the matrix diagonalization method to find the eigenmodes of the Munk potential can result in more harmonic modes than are absolutely necessary if the optimal harmonic potential is not used. Figure. A.11 illustrates the fundamental problem for two different choices of the harmonic potential by showing how well the highest harmonic mode circumscribes the largest Munk mode that it fully encloses. [89] This fit is much better for the optimal harmonic potential choice of the lower plot in Fig. (A.11). The optimal choice results in less harmonic modes needed in representing the modes of the ocean waveguide. For example, 170 harmonic modes centered at $z = 1$ and with $\omega = \sqrt{\frac{2\gamma}{B}}$ are needed in order to resolve the 61 Munk modes needed for a source frequency of 75 Hz. The upper plot in Fig. (A.11) shows the nonoptimal fit of the maximum mode circumscribing the largest Munk mode that it fully encloses. Thus, many more harmonic modes are necessary to represent all of the Munk modes than are needed.

Using the minimum number of harmonic modes minimizes the matrix to diagonalize. An optimal harmonic potential can be found using the methods in Ref. [89], but a near optimal harmonic potential can be found by adjusting the free parameters until the largest harmonic mode visually circumscribes with the minimum area of overlap. The near optimal harmonic potential for resolution of 61 Munk states for 75 Hz requires 80 harmonic modes and has parameters $\omega = \frac{1}{1.2}\sqrt{\frac{2\gamma}{B}}$ and $z_a = 1.7$. The near optimal harmonic potential for resolution of 200 Munk states for 75 Hz requires 300 harmonic modes and has parameters $\omega = \frac{1}{1.3}\sqrt{\frac{2\gamma}{B}}$ and $z_a = 3.4$.

As evidence of the improvement provided, consider how in semiclassical quantization, a state occupies an area $\hbar$ for this 1 dimensional potential. In accordance with this, the ratio of the two areas in the upper plot of Fig. (A.11) is $1.22857/3.40713 = 0.360587$ and the ratio of the converged states is $61/171 = 0.356725$. The ratio of the two areas in the lower plot in Fig. (A.11) is $1.22857/1.59927 = 0.7682$, and the ratio of the converged states is $61/80 = 0.7625$.

A.4.7 Mode Sampling

In order for the vertical modes to be sampled properly by the vertical grid Δz, the modes must be contained within the vertical extent $[z_{min}, z_{max}]$ and their smallest wave length must be sampled at least 10 points per wave length.

Each mode is most oscillatory near the minimum of the Munk potential (ie at $z = z_a = 1$). As seen in the classical phasespace contours, (ie see Fig. 4.8), the largest classical momentum in each mode n is $p = \sqrt{2E_n}$. Then the largest classical wavenumber in each mode is $k = k_0 p = k_0\sqrt{2E_n}$. Since, it is necessary to sample the local wavelength of each mode near $z = z_a = 1$ at 10 points per wavelength in order to get good resolution of the modes, $\Delta z \leq \frac{2\pi}{10k_0\sqrt{2E_n}}$. In order to guarantee that modes greater than $n = 200$ are well represented on the vertical grid, $N = 4096$ points are taken with the vertical extent $[-3, 10]$.

The chosen vertical extent must be large enough to contain each mode within in it. Each mode has Airy tails that extend from the classical turning points. These Airy tails must be adquately represented in order for the mode to be contained within the vertical extent. A

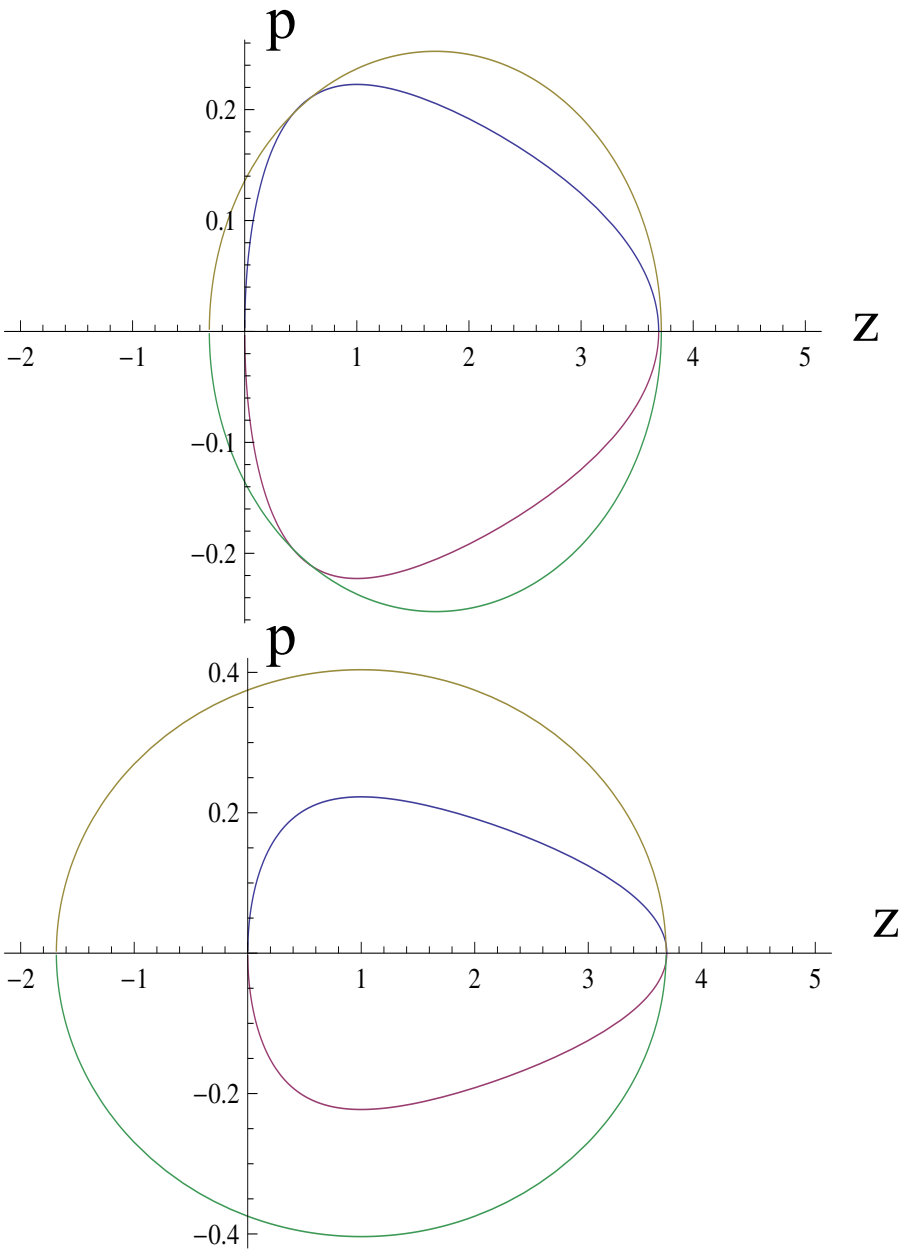

Figure A.11: Comparison of the efficiency of two Harmonic potentials as a basis for the matrix diagonalization. The energy contours for the largest necessary Harmonic mode is circumscribed on the largest Munk mode that is fully enclosed by it is plotted in phase space, where $p = \pm\sqrt{2(E - V(z))}$ is classical momentum and z is depth in the ocean. The upper plot has harmonic potential with free parameters $z_{HO} = 1.0$ and $\omega_{HO} = \sqrt{\frac{2\gamma}{B}}$, while the lower plot has $z_{HO} = 1.7$ and $\omega_{HO} = \frac{1}{1.2}\sqrt{\frac{2\gamma}{B}}$. The energy contour of the 171st Harmonic mode just circumscribes the energy contour of the 61 Munk mode in the upper plot. The energy contour of this 80th harmonic mode just circumscribes the energy contour of the 61 Munk mode and minimizes the area of overlap.

failure to do this would result in aliasing with the FFTs. Using the vertical extent $[-3, 10]$, the tails of each mode are on the order of 10^{-100} at the boundaries of the vertical grid.

A.5 Numerical Ray Propagation

A.5.1 Classical Trajectories

The classical ray propagation in space (z, r) is performed by numerically solving the system of differential equations consisting of Hamilton's equations in Eq. (C.4) with the initial condition of (z_0, p_0), where $z_0 = z_a$ (the sound channel axis) and $p_0 = \tan\theta_0$, with θ_0 the initial ray angle from the horizontal. The ray paths $(z(r), p(r))$ are found by solving a the system of differential equations with a 4th order Runga Kutta method. An adaptive stepsize is used for the range stepping to guarantee the accuracy of the values of (z, p) to a desired precision (ie. 10^{-8} to 10^{-4}). Exact derivatives are used with this method since analytic forms for the potential from Eq. (3.11) and Eq. (3.12) are known.

A.5.2 Classical Timefront

The classical timefront is generated by numerically propagating a discrete set of rays with initial angles $\theta_0 \in [\theta_0^{min}, \theta_0^{max}]$ to a fixed range R. The final depth of a ray in this set is the location of the receiver in the timefront. The arrival time of the ray is calculated by using Eq. C.6 with Hamilton's Principle function S calculated for the ray by adding Eq. (C.5) to the system of differential equations to be solved by the Runge Kutta method for each ray.

The amplitude of the ray arrival is calculated by using Eq. (C.7), where the stability matrix elements m_{ij} are calculated by adding the differential equations in Eq. (C.10) to the system of differential equations to be solved. This results in the following system of equations.

$$\begin{aligned}
\frac{\partial m_{11}}{\partial r} &= -V''(z)m_{21} \\
\frac{\partial m_{12}}{\partial r} &= -V''(z)m_{22} \\
\frac{\partial m_{21}}{\partial r} &= m_{11} \\
\frac{\partial m_{22}}{\partial r} &= m_{12} \ ,
\end{aligned}$$

with initial condition $m_{11} = m_{22} = 1$ and $m_{12} = m_{21} = 0$, the identity matrix.

Appendix B

APPENDIX-INTERNAL WAVE SOUND SPEED

In this appendix, the details of the construction of the internal wave model by Brown and Colosi [52] is presented. The details are based on Brown and Colosi's construction [52], the details from many older sources[3, 63, 64] and the basic ideas of semiclassical Wentzel-Kramers-Brillouin (WKB) theory [68, 19].

B.1 Sound Speed Fluctuations Induced by Vertical Displacements

A simple model for the internal wave sound speed fluctuations induced by vertical displacements considers the dominant effect from the buoyancy force in restoring a fluid parcel to its

equilibrium location in the fluid.

A fluid parcel at a depth z is displaced from it's equilibrium position by a small vertical distance, $\zeta(z) = \Delta z$. Let $\rho_0(z)$ be the density of a fluid parcel, which is a small perturbation from it's surrounding density so that the oscillations are small. From Newton's 2nd law, the vertical displacements, $\zeta(z)$ from equilibrium satisfy [63]

$$\rho_0(z)\frac{\partial^2\zeta}{\partial t^2} \quad = \quad g\frac{\partial\rho_0}{\partial z}\zeta\,, \tag{B.1}$$

where $\frac{\partial^2\zeta}{\partial t^2}$ is the acceleration of the displaced fluid parcel and $g\frac{\partial\rho_0}{\partial z}\zeta$ is the restoring force per volume necessary to bring the fluid parcel to equilibrium, with g the gravitational acceleration. These vertical displacements are sinusoidal harmonic oscillations with the Brunt-Vaisala buoyancy frequency [63], $N(z) = \sqrt{-\frac{g}{\rho_0}\frac{\partial\rho_0}{\partial z}}$. For small displacements, $\zeta(z)$, the relative changes in the sound speed compared to the surrounding water can be approximated by [52]

$$\frac{\delta c}{c} \quad = \quad = \frac{1}{c}\frac{\partial c}{\partial z}\zeta = \frac{1}{c}\frac{\partial c}{\partial\rho_0}\frac{\partial\rho_0}{\partial z}\zeta = \frac{1}{c}\frac{\partial c}{\partial\rho_0}\left(\frac{\rho_0}{g}N^2\right)\zeta = \frac{\mu}{g}N^2(z)\zeta\,, \tag{B.2}$$

where $g = 9.81\times10^{-3}$ km/s and $\mu = \frac{\rho_0}{c}\frac{\partial c}{\partial\rho_0} \approx 24.5$ is a dimensionless constant typical of depths near 1 km (but which varies with temperature and pressure). The buoyancy frequency, N, varies from $3cph$ (cycles per hour) near the surface to $0.2cph$ near the bottom of the ocean. The buoyancy frequency can be modeled well by the exponential, $N(z) = N_0e^{-z/B}$, where $B \approx 1$ km and $N_0 = 1$ cycle per 10 min is the buoyancy frequency at the surface[3].

B.2 Vertical Internal Wave Displacement Modes

An adequate model for the vertical internal wave displacements considers only those displacements arising from linear internal waves traveling along the source-receiver (horizontal) direction at a snapshot in time [63]. The range dependent displacement due to such an internal wave with a horizontal wavenumber k_r oscillating with an angular frequency ω_f is

$$\zeta(r, z, t) = Re\left[\zeta(z) \exp i(k_r r - \omega_f t)\right]$$

where $\zeta(z)$ contains the depth dependence. Due to the rotation of the earth, the frequencies, ω_f, of oscillation are restricted to $\omega_i < \omega_f < N(z)$, where ω_i and N are the inertial and buoyancy frequencies, respectively.

The basic physical equations for the movement of a parcel of water are the Euler equation (Newton's 2nd Law), the continuity equation and the incompressibility restriction. Linearizing these equations for infinitesimal motions and collecting only first order terms as in Ref. [3], gives plane wave solutions for the vertical velocities w of parcels of water, $w = W(z)e^{i(kr-\omega_f t)}$, where k is the wavenumber, ω_f is the angular frequency of the plane wave and $W(z)$ is an envelope function containing the depth dependence of the velocity [3]. The amplitudes W satisfy [3]

$$\frac{n^2(z)}{g} W'(z) = W''(z) + \left(\frac{N^2(z)}{\omega_f^2} - 1\right) k^2 W(z)\,. \tag{B.3}$$

In the ocean, a Boussinesq approximation[90] can be made by neglecting the term on the left

hand side, since it is 1000 times smaller than the second order depth derivative of W,

$$0 = W''(z) + \left(\frac{N^2(z) - \omega_f^2}{\omega_f^2} \right) k^2 W(z) \, .$$

The equation above can be modified to account for the fact that the frequencies of oscillation must be greater than the internal frequency, ω_i, [91]

$$0 \;\; = \;\; W''(z) + \left(\frac{N^2(z) - \omega_f^2}{\omega_f^2 - \omega_i^2} \right) k^2 W(z) \, . \tag{B.4}$$

Since velocity is the derivative of position, $w(r,z,t) = \frac{d}{dt}\zeta(r,z,t) = -i\omega_f \zeta(r,z,t)$, so that cancelling the phases yields $W(z) = -i\omega_f \zeta(z)$. Then Eq. (B.3) in the vertical velocity amplitudes, $W(z)$, can be integrated to give the equation in the vertical displacements, $\zeta(z)$, of water parcels from their equilibrium positions.

$$0 \;\; = \;\; \zeta''(z) + \left(\frac{N^2(z) - \omega_f^2}{\omega_f^2 - \omega_i^2} \right) k^2 \zeta(z) \, . \tag{B.5}$$

The boundary conditions for Eq. (B.5) come from the ocean surface and bottom. At the surface, any surface wave driven by an internal wave will have small amplitude so that $\zeta(0) \approx 0$. The bottom of the ocean is a horizontal impermeable bed, so that $\zeta(H) \approx 0$ [90], where H is the approximate depth of the ocean. This creates an eigenvalue problem where only discrete frequencies $\omega_f(k)$ can lead to a solution. This differential equation can be solved numerically or analytically to determine the modes of the vertical displacements, ζ.

An analytic solution to Eq. (B.5) exists for the exponential buoyancy model, $N = N_0 e^{-z/B}$.

In this case, the substitutions

$$\beta(z) = \frac{aN(z)}{\omega_f} \tag{B.6}$$

$$a = \frac{Bk}{\sqrt{1-\left(\frac{\omega_i}{\omega_f}\right)^2}} \tag{B.7}$$

transform Eq. (B.5) to Bessel's Equation of order a

$$0 = \beta^2\zeta''(\beta) + \beta\zeta'(\beta) + \left[\beta^2 - a^2\right]\zeta(\beta)\,, \tag{B.8}$$

which has general solutions

$$\zeta(z) = c_1 J_a(\beta(z)) + c_2 Y_a(\beta(z)) \tag{B.9}$$

$$= c_1\left[J_a(\beta(z)) - Y_a(\beta(z))\frac{J_a(\beta(H))}{Y_a(\beta(H)}\right]\,, \tag{B.10}$$

where J_a, Y_a are Bessels solutions of the first and second kind, respectively [64]. The boundary condition $\zeta(H) = 0$ gives $c_2 = -J_a(\beta(H)/Y_a(\beta(H))c_1$ using the form in Eq. (B.10). The boundary condition $\zeta(0) = 0$ gives discretized modes $\zeta_j(z)$ subject to the condition [64]

$$0 = J_a(\beta(0))Y_a(\beta(H)) - Y_a(\beta(0))J_a(\beta(H))\,, \tag{B.11}$$

where the modes are orthogonal and are subject to the orthogonality condition [64] (derived

from the differential equation in Eq. (B.5))

$$\int_H^0 \zeta_j(z)\zeta_{j'}(z)\left(N^2-\omega_i^2\right)dz = \delta_{j,j'}\int_H^0 \left(\zeta_j(z)\right)^2\left(N^2-\omega_i^2\right)dz\,. \tag{B.12}$$

B.3 WKB Approximation for Vertical Internal Wave Displacement Modes

It is often useful when analyzing an ordinary differential equation such as that in Eq. (B.8) to consider stationary plane wave solutions [64]. This limit occurs as the order, a, of the Bessel solutions increases. Thus, the limit $a \to \infty$ gives the Wentzel-Kramers-Brillouin (WKB) [68] approximation to the solutions which is achieved as $\omega_f \to \omega_i$.

In this asymptotic limit, both the argument and the order of the Bessel function solution in Eq. (B.10) diverge. The argument diverges by a factor $N(z)/\omega_f > 1$ faster than the order, so the large argument asymptotic approximations to the Bessel function, $J_a(x) \approx \sqrt{\frac{2}{\pi x}}\cos(x-\frac{a\pi}{2}-\frac{\pi}{4})$ and $Y_a(x) \approx \sqrt{\frac{2}{\pi x}}\sin(x-\frac{a\pi}{2}-\frac{\pi}{4})$ are used [64]. This simplifies Eq. (B.11) to $0 = \sin\left(\beta(0)-\beta(H)\right)$ or $\beta(0)-\beta(H) = j\pi$ for integer j. Writing this as $\frac{aN_0}{\omega_f} = \frac{j\pi}{(1-e^{-H/B})}$ and then in terms of ω_f and k gives the dispersion relation for $\omega(k)$ [64],

$$\omega_f^2 = \omega_i^2 + k^2\left(\frac{N_0 B\left(1-e^{-H/B}\right)}{j\pi}\right)^2 = \omega_i^2\left(1+\frac{k^2}{k_j^2}\right) \tag{B.13}$$

$$k_j = \omega_i\frac{\pi j}{N_0 B}\,. \tag{B.14}$$

Substituting $\frac{aN_0}{\omega_f} = \frac{j\pi}{(1-e^{-H/B})}$ into Eq. (B.11) and simplifying gives solutions to Eq. (B.5) which satisfy both boundary conditions. These solutions are the modes

$$\zeta_j(z) = c_1 \left[J_a(\beta(z)) - Y_a(\beta(z)) \frac{J_a(\beta(H))}{Y_a(\beta(H)} \right] , \tag{B.15}$$

where $\beta(z) = j\pi \frac{N(z)}{N_0(1-e^{-H/B})} = j\pi \frac{e^{-z/B}}{(1-e^{-H/B})}$ and $a = \frac{\omega_f \pi}{N_0(1-e^{-H/B})} j$.

The simplified asymptotic form for large arguments is

$$\zeta_j(z) = c_1 \sqrt{\frac{N_0}{N(z)}} \sin\left(j\pi\xi(z)\right) \tag{B.16}$$

$$\xi(z) = \frac{e^{-z/B} - e^{-H/B}}{1 - e^{-H/B}} \approx e^{-z/B} - e^{-H/B} , \tag{B.17}$$

where several constants have been lumped in with c_1. This WKB approximation was derived by the author. Note that Colosi and Brown[52] derived these modes in a different way with more approximations.

The orthogonality relation in Eq. (B.12) for the solutions to the Bessel Equation is not the orthogonality relation for the asymptotic solution in Eq. (B.16), so the modes need to be normalized a different way. Brown and Colosi [52] normalize their modes with

$$\int_H^0 \zeta_j^2(z) N^2(z) dz = 1 . \tag{B.18}$$

However, this equation is dimensionally inconsistent.

Taking $\zeta_j(z)$ from Eq. (B.16), one obtains the exact result $\int_H^0 \zeta_j(z)\zeta_{j'}(z)N^2(z)dz = c_1^2 \frac{BN_0^2}{2}$

so that the normalization condition used by Brown and Colosi gives $c_1 = \sqrt{\frac{2}{N_0^2 B}}$. Then the normalized modes are

$$\zeta_j(z) \;=\; \sqrt{\frac{2}{N_0 B N(z)}} \sin\left(j\pi\xi(z)\right) \;. \tag{B.19}$$

B.4 Statistical Ensemble

The set of all possible internal wave field displacements that can occur in the ocean is a statistical ensemble. The statistical properties of the possible displacements come from observations, ie the Garrett-Munk sprectrum [64]. The physics of the internal wave displacements comes from the vertical modes in Eq. (B.16).

A statistical model for the ensemble of field displacements is taken to be a mixture of linear internal wave displacements with horizontal wavenumbers, k_r [92]. The general displacement amplitudes $\zeta(z)$ from each internal wave can be written as a random superposition of the displacement modes, $\zeta_j(z)$, weighted by a complex Gaussian random variable, $g(k_r, j)$.

$$\zeta(z,r) \;=\; Real\left[\int dk_r \zeta(z) e^{ik_r r}\right] = Real\left[\int dk_r \sum_j g(k_r,j)\zeta_j(z) e^{ik_r r}\right] \;.$$

The weightings satisfy observed statistics for the displacements. They are centered about a mean $< g(k_r, j) >= 0$ with a variance $\sigma_g^2(k_r, j) =< g(j, k_r) g^*(j', k_r' >= \delta_{j,j'}\delta_{k_r,k_r'} G(k_r, j)$, where $< \cdot >$ denotes the average of the quantity over the entire ensemble of possible internal wave fields.

A random model for $g(k_r, j)$ has an amplitude $\sigma_g(k_r, j) = \sqrt{G(k_r, j)}$ and a random phase ϕ_{j,k_r} chosen to be a delta correlated random variable uniformly distributed in $[0, 2\pi)$ [52],

$$\zeta(z, r) \approx Real\left[\int dk_r \sum_j \sqrt{G(k_r, j)} e^{i\phi_{j,k_r}} \zeta_j(z) e^{ik_r r}\right] . \tag{B.20}$$

A statistical realization of the internal wave field of displacements, $\zeta(z, r)$ is calculated by choosing a random seed and then using a random number generator to generate a sequence of random numbers $\phi_{j,k_r} \in [0, 2\pi)$ for the phases of the internal wave with vertical mode, j, and horizontal wavenumber, k_r.

by choosing independent random seeds to generate a sequence of random phases, $\phi_{j,k_r} \in [0, 2\pi)$, for each internal wave with vertical mode, j, and horizontal wavenumber, k_r.

Calculating the ensemble average $< \zeta^2 >$ by using Eq. (B.20) and the property of the delta correlated random variables, ϕ_{j,k_r} gives

$$< \zeta^2 > = \frac{1}{2} \int dk_r \sum_j G_\zeta(j, k_r) \zeta_j^2(z) . \tag{B.21}$$

The observed statistics of the displacements $\zeta(z, r, t)$ come from the empirical 1979 Garrett-Munk [63, 64] internal wave spectrum. This model gives an expression for the power spectrum $F(j, \omega)$ of the displacements $\zeta(z, r, t)$ as

$$F_\zeta(j, \omega) = E_0 H(j) B(\omega) , \tag{B.22}$$

where $< \zeta^2 >= \int_{\omega_i}^{N(z)} d\omega \sum_{j=1}^{\infty} F_\zeta(j,\omega)$ and the functional forms are

$$E_0 = \frac{B^2 E N_0}{2N} \tag{B.23}$$

$$H(j) = \frac{1/M}{j^2 + j*^2} \tag{B.24}$$

$$B(\omega) = \frac{4}{\pi} \frac{\omega_i \sqrt{\omega^2 - \omega_i^2}}{\omega^3} , \tag{B.25}$$

with the normalization $\sum_{j=1}^{\infty} H(j) = 1$ (where j_* is a "mode scale number") and the approximate normalization $\int_{\omega_i}^{N} B(\omega) d\omega = 1 + O\left(\frac{\omega_i}{N}\right)$. The overall "energy parameter", E, is a dimensionless quantity and the Garret-Munk energy parameter is $E_{GM} = 6.3 \text{ x } 10^{-5}$. Therefore, $< \zeta^2 > \approx E_0$.

An important quantity that can be derived from the Garrett-Munk spectrum in Eq. (B.22) is that of the energy stored in the internal wave displacements [3]. Consider a differential mass at a depth z displaced $\zeta(z)$ from it's equilbrium location. The potential energy density due to the buoyant force and the coriolis force from the earth's rotation are $\frac{\rho}{2} N^2(z) |\zeta|^2$ and $-\frac{\rho}{2} \omega_i^2(z) |\zeta|^2$, respectively. (Note that the gravitational potential energy and radius of the earth are used to define the equilibrium location and that zero of the potential energy). Adding up the energy contributions from all displacements gives the total vertically integrated potential energy density [3] ,

$$< U > = \frac{\rho}{2} \int_H^0 (N^2(z) - \omega_i^2) < \zeta^2 > dz . \tag{B.26}$$

Using $< \zeta^2 >= E_0 = \frac{B^2 E N_0}{2} \frac{1}{N(z)}$ and integrating gives

$$< U >= -\frac{\rho}{4} B^3 N_0^2 E \left(1 - e^{-H/B} + \left(\frac{\omega_i^2}{N^2} e^{H/B}\right)\right) \approx -\frac{\rho}{4} B^3 N_0^2 E \left(1 - e^{-H/B}\right) \ . \quad \text{(B.27)}$$

Using Eq. (B.21) and the orthonormality relation in Eq. (B.12) gives

$$\begin{aligned} < U > &= \frac{\rho}{2} \int_H^0 (N^2(z) - \omega_i^2) < \zeta^2 > dz \\ &= \frac{\rho}{4} \int dk_r \sum_j G_\zeta(j, k_r) \int_H^0 (N^2(z) - \omega_i^2) \zeta_j^2(z) dz \\ &= \frac{\rho}{4} \int dk_r \sum_j G_\zeta(j, k_r) \ . \end{aligned} \quad \text{(B.28)}$$

Note that F_ζ in Eq. (B.22) has the same depth dependence in $N(z)$ as do the vertical modes $\zeta_j(z)$ in Eq. (B.19), while G_ζ should not have any depth dependence. Assuming that G_ζ can be written $G_\zeta(j, k_r) = c F_\zeta(j, k_r)$ gives

$$< U > \ = \ \frac{\rho}{4} c \int dk_r \sum_j F_\zeta(j, k_r) = \frac{\rho}{4} c E_0 \ , \quad \text{(B.29)}$$

where the the integration over the arguments of $F_\zeta(j, k_r)$ is the same as that of integrating over the arguments of $F_\zeta(j, \omega)$ [52].

Then in order for $< U >$ to be constant, Eq. (B.27) must equal Eq. (B.29) so that $c = 2BN_0N\left(1 - e^{-H/B}\right)$ and

$$G_\zeta(j, k_r) \ = \ 2BN_0N\left(1 - e^{-H/B}\right) F_\zeta(j, k_r) \ , \quad \text{(B.30)}$$

where it is then necessary to find $F_\zeta(j, k_r)$ [52].

For $< U >$ to be constant when transforming the coordinates of $F(j, \omega)$ to $F(j, k_r)$, $< \zeta^2 >$ is constant as well. Thus the integration over the variables of F_ζ must be preserved under each coordinate transformation [52].

Through the dispersion relation in Eq.(B.13), ω is related to the wavenumber, k with $\frac{\partial \omega}{\partial k} = \frac{k}{\omega}\left(\frac{\omega_j^2}{k_j^2}\right)$ where k_j is defined in Eq. (B.14). The wavenumber is $k = \sqrt{k_r^2 + k_y^2}$, where k_r is the horizontal wavenumber. The preservation of $< |\zeta|^2 >$ demands that $F_\zeta(j, \omega)d\omega = F_\zeta(j, k)dk\frac{\partial \omega}{\partial k}$ and $F_\zeta(j, k)2\pi k dk = F_\zeta(j, k_r, k_y)dk_r dk_y$ so that

$$F_\zeta(j, k) = E_0 H(j)\frac{4}{\pi}\frac{k_j k^2}{(k^2 + k_j^2)^2} \tag{B.31}$$

$$F_\zeta(j, k_r, k_y) = E_0 H(j)\frac{2}{\pi^2}\frac{k_j\sqrt{k_r^2 + k_y^2}}{(k_r^2 + k_y^2 + k_j^2)^2}\,. \tag{B.32}$$

To obtain $F_\zeta(j, k_r)$, the integration of $F_\zeta(j, k_r, k_y)$ over k_y can be done analytically. [93]

$$\begin{aligned} F_\zeta(j, k_r) &= \int_{-\infty}^{\infty} F_\zeta(j, k_r, k_y)dk_y = E_0 H(j)\frac{2}{\pi^2} I_{j,k_r} \\ k_j I_{j,k_r} &= \frac{1}{\beta^2 + 1} + \frac{1}{2}\frac{\beta^2}{(\beta^2 + 1)^{\frac{3}{2}}}\ln\left(\frac{\sqrt{\beta^2 + 1} + 1}{\sqrt{\beta^2 + 1} - 1}\,,\right) \end{aligned} \tag{B.33}$$

where $\beta = k_r/k_j$.

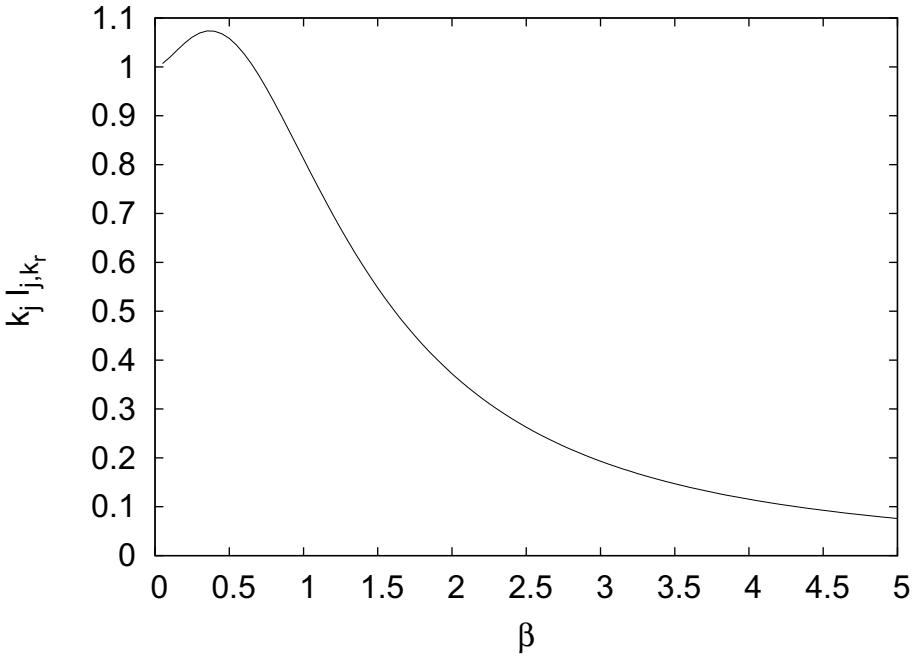

Figure B.1: The function $k_j I_{jk}$ in Eq. B.33 is plotted versus parameter $\beta = \frac{k_r}{k_j}$ and the peak occurs at approximately $\beta \approx 0.38$. Note that $k_j \approx 0.0218j$ and $k_r = 2\pi/\lambda_r$, where $\lambda_r \in [1, 100]$ km is the horizontal wavelength of the internal wave, so $\beta \approx \frac{288}{j\lambda_r}$. Then β decreases for larger mode numbers j and for longer wavelengths λ_r. For a fixed j, this range is $\beta \in [\frac{2.88}{j}, \frac{288}{j}]$. Since most of the wavelengths are nearer to $\lambda_r = 1$, most of the internal wave contributions have $\beta \approx \frac{2.88}{j}$.

Then Eq. (B.30) becomes

$$\begin{aligned} G_\zeta(j,k_r) &= 2BN_0N\left(1-e^{-H/B}\right)E_0H(j)\frac{2}{\pi^2}I_{j,k_r} \\ &= B^3N_0^2E\left(1-e^{-H/B}\right)H(j)\frac{2}{\pi^2}I_{j,k_r} \\ &\approx B^3N_0^2EH(j)\frac{2}{\pi^2}I_{j,k_r}\ , \end{aligned} \tag{B.34}$$

where the author is unsure if the approximation $\left(1-e^{-H/B}\right)\approx 1$ should be made. This approximation is necessary for agreement with Eq. (3.12).

Substituting Eq. (B.34) into Eq. (B.20) gives

$$\begin{aligned} \zeta(z) &\approx Real\left[\int dk_r \sum_j \sqrt{G(k_r,j)}e^{i\phi_{j,k_r}}\zeta_{j,k}(z)e^{ik_rr}\right] \\ &= \int dk_r \sum_j \sqrt{B^3N_0^2E\ H(j)\ \frac{2}{\pi^2}\ I_{j,k_r}}\sqrt{\frac{2}{N_0BN(z)}}\sin(j\pi\xi(z))Re\left[e^{i(\phi_{j,k}+k_rr)}\right] \\ &= \frac{2B}{\pi}\left(\frac{E\ N_0}{M\ N(z)}\right)^{1/2}\sum_j \frac{\sin\left(j\pi\xi(z)\right)}{(j^2+j_*^2)^{1/2}}\int dk_r I_{j,k_r}^{1/2}\cos\left(\phi(j,k_r)+k_rr\right)\ . \end{aligned} \tag{B.35}$$

This last expression is that of Colosi and Brown [52]. In preparing for numerical integration, Colosi and Brown approximate the integral over k_r as a discrete sum, i.e. $\int dk_r \approx \frac{1}{(\delta k_r)^{1/2}}\sum_{k_r^{min}}^{k_r^{max}}\delta k_r = \sum_{k_r^{min}}^{k_r^{max}}(\delta k_r)^{1/2}$.

$$\begin{aligned} \zeta(r,z) &= \frac{2B}{\pi}\left(\frac{E}{M}\right)^{1/2}\left(\frac{N_0}{N(z)}\right)^{1/2}(\delta k_r)^{1/2} \\ &\quad \sum_j \frac{\sin\left(j\pi\xi(z)\right)}{(j^2+j_*^2)^{1/2}}\sum_{k_r} I_{j,k_r}^{1/2}\cos\left[\phi(j,k_r)+k_rr\right]\ . \end{aligned} \tag{B.36}$$

The full model for sound speed fluctuations δc, induced by internal waves comes from Eq. (B.2) and Eq. (B.36).

Appendix C

APPENDIX-MATH TOOLS

C.1 Classicals Rays and Ocean Acoustics

Using the analogy between the parabolic equation in Eq. (3.8) and the Schrödinger equation[53], semiclassical theory [19, 82] can be used to approximate the propagation of a continuous acoustic wave with a superposition of plane waves following the wave front. Each plane wave follows the classical path connecting the initial position to the final position of the wavefront and each path contributes an amplitude $A_j(z,t)$ and a phase $k_0 S_j(z,t)$ to the wave function approximation

$$\Psi_{sc}(z,r) = \sum_j A_j(z,r) e^{ik_0 S_j(z,r)} \ , \tag{C.1}$$

where S_j is Hamilton's principle action function [83]. Since this approximation improves as the source wavenumber $k_0 \to \infty$, it is only valid when the acoustic wavelength, $\lambda_0 = \frac{2\pi}{k_0}$,

of the source is much smaller than all lengths that characterize variations in the potential, $V(z,r)$. Note that though the ansatz in Eq. (C.1) is a guess for the form that the solutions will take, this does not guarantee that A_j is not a function of wavenumber k_0. It turns out that for the ocean acoustic propagation, A_j is a function of wavenumber if this ansatz is taken.

Further, the semiclassical solution can be viewed as the exact solution expanded in the small parameter, $\hbar = 1/k_0$, i.e. the WKB solution [68]. The equations for the amplitudes, A_j, and phases, S_j can be found by substituting the ansatz in Eq. (C.1) into the parabolic equation in Eq. (3.8) and gathering powers of $1/k_0$. Equating the zeroth order terms in $(1/k_0)^0$ gives the Eikonal equation [56] in Hamilton's Principle Function, S_j,

$$-\frac{\partial S_j}{\partial r} = \frac{1}{2}\left(\frac{\partial S_j}{\partial z}\right)^2 + V(z,r)\,. \tag{C.2}$$

Equating the first order terms in $1/k_0$ gives the Transport equation [56] in the 'intensities', A_j^2,

$$-\frac{\partial A_j^2}{\partial r} = \frac{\partial}{\partial z}\left(A_j^2\frac{\partial S}{\partial z}\right)\,. \tag{C.3}$$

In the transport equation in Eq. (C.3), there is only a transient term, $-\frac{\partial A_j^2}{\partial r}$ and a convection term, $\frac{\partial}{\partial z}\left(A_j^2\frac{\partial S}{\partial z}\right)$. From the convection term, the intensity, A_j^2, is transported due to the velocity field, $\frac{\partial S}{\partial z}$. Due to the lack of either a source or diffusion term, there are no sources of intensity along the propagation (except at the initial condition at $r = 0$) and there is no diffusion of the intensity in this model.

C.1.1 Equations for Classical Propagation

The dynamics of classical ray propagation in canonical coordinates is subject to Hamilton's equations of motion [83],

$$\begin{aligned} \frac{dz}{dr} &= \frac{\partial H}{\partial p} = p \\ \frac{dp}{dr} &= -\frac{\partial H}{\partial z} = -\frac{\partial V(z,r)}{\partial z} \,, \end{aligned} \tag{C.4}$$

where the classical ray has a canonical depth z, and a canonical 'momentum', p. Since $dz/dr \approx \Delta z/\Delta r = \tan\theta$, and $p = dz/dr$ from Hamilton's equations, the generalized momentum is defined to be $p = \tan\theta$, where θ is the angle that a classical ray makes with the horizontal as it propagates. The Hamiltonian, H, gives the energy of a classical ray as it propagates and is defined so that $H(z,p;r) = -\frac{\partial S}{\partial r}$, where S is Hamilton's principle function which also satisfies $p = \frac{\partial S}{\partial z}$. Each classical ray accumulates action, S, as it propagates in range according to

$$\frac{dS}{dr} = p\frac{dz}{dr} - H \,. \tag{C.5}$$

Using Eq. (C.5) and $p = \frac{\partial S}{\partial z}$, the Eikonal equation in Eq. (C.2) becomes the Hamiltonian

$$H(z,p;r) = \frac{p^2}{2} + V(z,r)$$

where $V(z,r)$ is given in Eq. (3.9). Figure (C.1) illustrates numerical ray paths through

the full ocean potential given by Eq. (3.10), while Fig. (C.2) illustrates the timefront of ray arrivals propagated through the potential given by Eq. (3.11). These are calculated using the numerical methods described in Appendex A.5.

Within the level of accuracy of the other approximations made to arrive at the parabolic equation, the travel time t for a trajectory propagating to a range R is related to Hamilton's principle function, S,

$$t \;=\; \frac{1}{c_0}\,(R+S)\;. \tag{C.6}$$

The point source solution to the Transport equation in Eq. (C.3) is

$$A_j(z,r) = A_j(z_0,0)|M_{21}|^{-1/2}e^{-i\nu_j\pi/2}\;, \tag{C.7}$$

where $A_j(z_0,0)$ is the initial amplitude of the point source, ν_j is the Maslov index [82] (the number of caustics the ray passes through) and M_{21} is a matrix element of the stability matrix M describing the spreading of an infinitesimal ray.

The stability matrix [94] of a ray is such that

$$\begin{pmatrix} \delta p \\ \\ \delta z \end{pmatrix} = M_r \begin{pmatrix} \delta p_0 \\ \\ \delta z_0 \end{pmatrix}\;, \tag{C.8}$$

where another ray separated from this ray by $(\delta z_0, \delta p_0)$ has final separation from the ray of

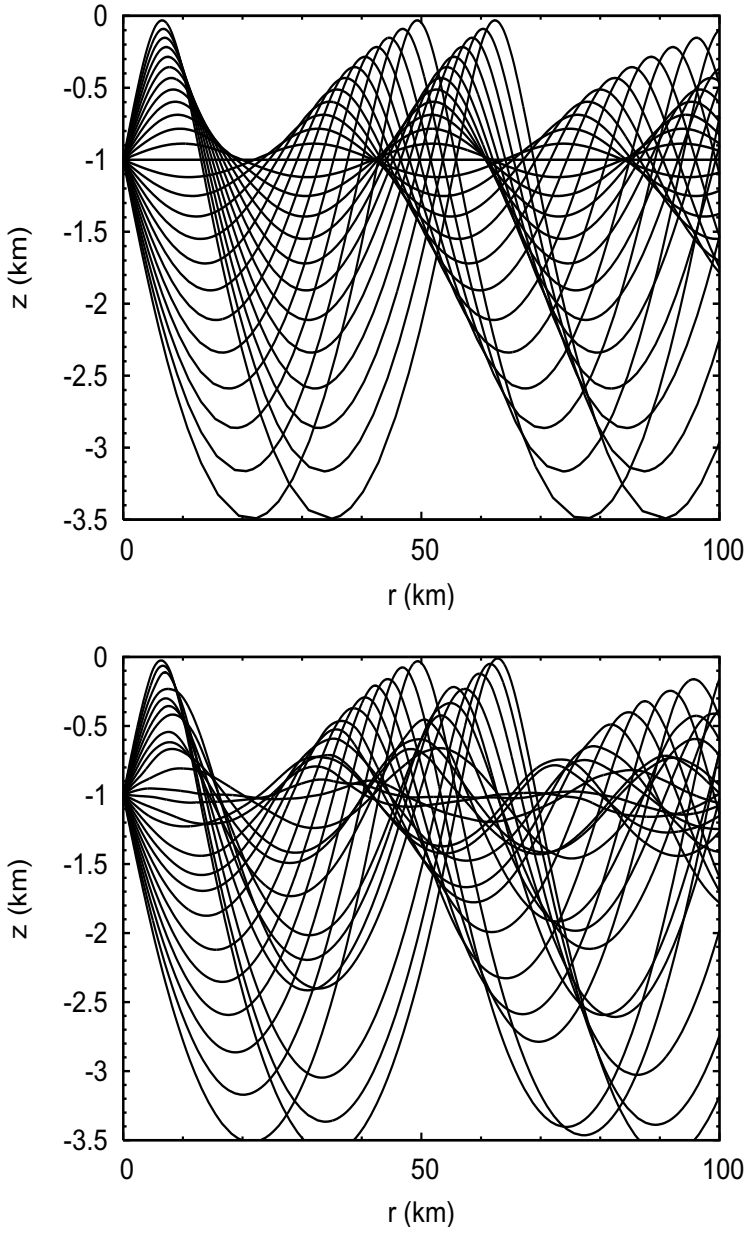

Figure C.1: The propagation of the classical rays with initial ray angle of $-12^o < \theta_0 < 12^o$ in increments of 1^o is shown here as a function of depth, z, and range, r through the potential V. The upper plot is for a potential V consisting of just the Munk potential from Eq. (3.11). The lower plot is for a potential V consisting of the Munk potential and a realization of the internal wave fluctuations from Eq. (3.12).

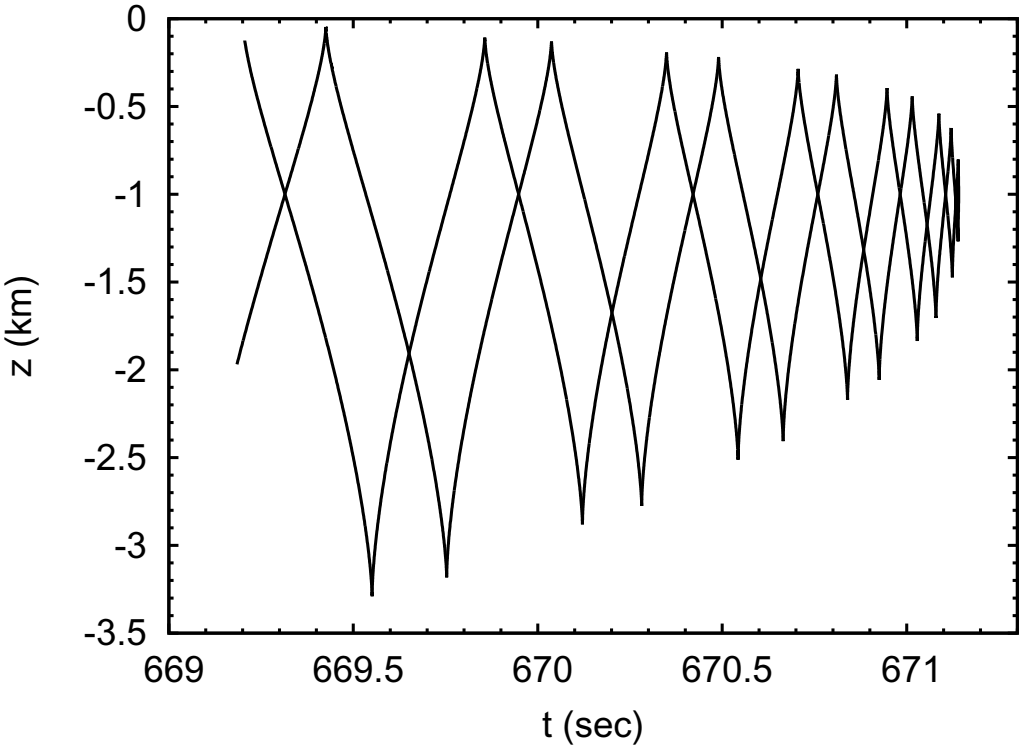

Figure C.2: The classical timefront is the structure of the arrival times t with depth z of the classical rays propagated through the Munk potential from Eq. (3.11) to a fixed range of $r = 1000$ km. The classical rays plotted have an initial ray angle of between $-12^o < \theta_0 < 12^o$.

$(\delta z, \delta p)$ after an infinitesimal range step.

$$M_r = \begin{pmatrix} m_{11} & m_{12} \\ m_{21} & m_{22} \end{pmatrix} = \begin{pmatrix} \left.\frac{\partial p}{\partial p_0}\right|_{z_0} & \left.\frac{\partial p}{\partial z_0}\right|_{p_0} \\ \left.\frac{\partial z}{\partial p_0}\right|_{z_0} & \left.\frac{\partial z}{\partial z_0}\right|_{p_0} \end{pmatrix} , \tag{C.9}$$

which at $r = 0$ is the identity matrix. The stability matrix evolves according to

$$\frac{d}{dr} M_r = K_r M_r , \tag{C.10}$$

where

$$K_r = \begin{pmatrix} -\frac{\partial^2 H}{\partial z_r \partial p_r} & -\frac{\partial^2 H}{\partial z_r^2} \\ \frac{\partial^2 H}{\partial p_r^2} & \frac{\partial^2 H}{\partial z_r \partial p_r} \end{pmatrix} = \begin{pmatrix} 0 & -\frac{\partial^2 V}{\partial^2 z} \\ 1 & 0 \end{pmatrix} . \tag{C.11}$$

Note that in general, the sum in Eq. (C.1) is over general complex rays (rays with complex coordinates for (z, p)). Complex rays are needed for a Gaussian wave packet [95, 96], but intuition implies that initial conditions in the neighborhood of the center of the wave packet should work well. Considering only real rays is yet another approximation made in this thesis.

C.2 Semiclassical Wavefunction For Acoustic Propagation

Classical ray methods can be used to reconstruct propagating wave fields in detail through the use of semiclassical Green functions [26]. The wavefield at a range r can be calculated by propagating the initial wavefield using a Green's function [26]. All depths z' in the initial Gaussian wavepacket which eventually pass through the point (z, r) contribute to the wavefield at (z, r)

$$\Psi_{sc}(z; r) = \int_{-\infty}^{\infty} G_{sc}(z, z'; r)\, \Psi(z'; r = 0)\, dz' \; . \tag{C.12}$$

Using the linearized semi-classical green's function gives

$$G_{sc}(z, z'; r) \;\; = \;\; \left(\frac{1}{2\pi i\hbar}\right)^{1/2} \sum_j \left|\frac{\partial^2 S_j(z, z'; r)}{\partial z\, \partial z'}\right|^{1/2} \exp\left(iS_j(z, z'; r)/\hbar - i\pi\nu_j/2\right) \tag{C.13}$$

where $\hbar = 1/k$ for the CW parabolic equation propagation, ν_j is the Maslov index representing the number of turning points the jth ray incurs with S_j the classical action of $j$the ray.

The classical action S of the rays emanating from the Gaussian wavepacket can be approximated [94] by considering a Taylor expansion of these rays about the center of the Gaussian wave packet, z_0,

$$\begin{aligned} S_j(z, z'; r) \;\; = \;\; & S_j(z_r, z_0) + \frac{\partial S}{\partial z_r}|_{z_0}(z - z_r) + \frac{\partial S}{\partial z_0}|_{z_r}(z' - z_0) + \\ & \frac{1}{2!}\frac{\partial^2 S}{\partial z_r^2}|_{z_0}(z - z_r)^2 + \frac{1}{2!}\frac{\partial^2 S}{\partial z_0^2}|_{z_r}(z' - z_0)^2 + \frac{\partial^2 S}{\partial z_0 \partial z_r}|_{z_0, z_r}(z' - z_0)(z - z_r) \; . \end{aligned}$$

The derivatives of the action can be simplified by writing them in terms of the elements of the stability matrix, M_r in Eq. (C.9). Since $p = \frac{\partial S}{\partial z}$ then $\delta p = m_{11}\delta p_0 + m_{12}\delta z_0$ and $\delta z = m_{21}\delta p_0 + m_{22}\delta z_0$ can be used to obtain

$$\left(\frac{\partial p_0}{\partial z_0}\right)\Big|_{z_0} = -\frac{m_{22}}{m_{21}} \, .$$

Similar other relationships can be derived and used to obtain

$$\begin{aligned}\left(\frac{\partial^2 S}{\partial z \partial z_0}\right) &= \left(\frac{\partial p}{\partial z_0}\right)\Big|_z = \left(\frac{\partial p}{\partial p'}\right)\Big|_z \left(\frac{\partial p'}{\partial z'}\right)\Big|_z + \left(\frac{\partial p}{\partial z'}\right)\Big|_z \left(\frac{\partial z'}{\partial z'}\right)\Big|_z \\ &= -m_{11}\frac{m_{22}}{m_{21}} + m_{12} = \frac{m_{21}m_{12} - m_{11}m_{22}}{m_{21}} = -\frac{1}{m_{21}} \, ,\end{aligned}$$

where $det(M) = m_{11}m_{22} - m_{12}m_{m21} = 1$. Similarly,

$$\begin{aligned}\frac{\partial^2 S}{\partial z^2}\Big|_{z_0} &= \frac{m_{11}}{m_{21}} \\ \frac{\partial^2 S}{\partial z_0^2}\Big|_z &= \frac{m_{22}}{m_{21}} \, .\end{aligned}$$

Then,

$$G_{sc}(z, z'; r) = \left(\frac{1}{2\pi i\hbar}\right)^{1/2} \sum_j \left|\frac{1}{m_{21}}\right|^{1/2} \exp\left(iS_j(z, z'; r)/\hbar - i\pi\nu_j/2\right)$$

and the approximate action for the jth ray is

$$S_j(z, z'; r) = S_j(z, z_0; r) - p_0(z' - z_0) + \frac{m_{22}}{2m_{21}}(z' - z_0)^2 \, . \tag{C.14}$$

This simplification works very well and allows the analytic computation of the Gaussian integral for $\Psi_{sc}(z;r)$,

$$\begin{aligned}
\Psi_{sc}(z;r) &= \int_{-\infty}^{\infty} G_{sc}(z,z';r)\,\Psi(z';r=0)\,dz' \\
&= \sum_j \frac{1}{(2\pi i\hbar)^{1/2}\,|m_{21}|^{1/2}\,(2\pi\sigma_z^2)^{1/4}} \int_{-\infty}^{\infty} \exp\left(iS_j(z,z';r)/\hbar - i\pi\nu_j/2 - \frac{(z'-z_0)^2}{4\sigma_z^2}\right) dz' \\
&= \sum_j A_j(z,r)\exp[ikS_j(z,z'=z_0;r)]\ ,
\end{aligned}$$

where the amplitudes, A_j satisfy

$$\begin{aligned}
A_j &= \frac{1}{(2\pi i\hbar)^{1/2}\,|m_{21}|^{1/2}\,(2\pi\sigma_z^2)^{1/4}} \\
&\quad \times \int_{-\infty}^{\infty} \exp\left(-(z-z_0)^2\left(\frac{1}{4\sigma_z^2} - \frac{im_{22}}{2m_{21}\hbar}\right) - \frac{ip_0}{\hbar}(z-z_0) - i\pi\nu_j/2\right) \\
&= \frac{1}{(2\pi i\hbar)^{1/2}\,|m_{21}|^{1/2}\,(2\pi\sigma_z^2)^{1/4}} \int_{-\infty}^{\infty} \\
&\quad \times \exp\left(-(z-z_0)^2\left(\frac{\xi}{4\sigma_z^2 m_{21}\hbar}\right) - \frac{ip_0}{\hbar}(z-z_0) - i\pi\nu_j/2\right) \\
&= \frac{1}{(2\pi i\hbar)^{1/2}\,|m_{21}|^{1/2}\,(2\pi\sigma_z^2)^{1/4}} \sqrt{\frac{\pi 4\sigma_z^2 m_{21}\hbar}{\xi}}\exp\left(-\frac{p_0^2\sigma_z^2 m_{21}}{\hbar\xi} - i\pi\nu_j/2\right) \\
&= \left(\frac{2\sigma_z^2}{\pi\xi^2}\right)^{1/4} \sqrt{\frac{sign(m_{21})}{i}}\exp\left(\frac{-kp_0^2\sigma_z^2 m_{21}}{\xi} - i\frac{\pi\nu_j}{2}\right)\ ,
\end{aligned}$$

where $\xi = m_{21}\hbar - 2i\sigma_z^2 m_{22} \neq 0$ and the Gaussian integral has been simplified for $a \neq 0$,

$$\int_{-\infty}^{\infty} \exp\left(-az^2 + bz\right) dz = \sqrt{\frac{\pi}{a}}\exp\left(\frac{b^2}{4a}\right)\ .$$

Note: $Re(a) = Re\left(\frac{\pi 4\sigma_z^2 m_{21}\hbar}{\xi}\right) > 0$ if $m_{21} > Re(\xi) = \frac{m_{21}}{k_0}$. Note that $\xi = m_{21}\hbar - 2i\sigma_z^2 m_{22} \neq$

0 since m_{11} and m_{22} cannot be zero at the same time (else $det(M) = 0$ but $det(M) = 1$).

Simplifying $1/\sqrt{i} = \exp(-i\pi/4)$,

$$A_j = \left(\frac{2\sigma_z^2}{\pi}\right)^{1/4} \sqrt{\frac{sign(m_{21})}{\xi}} \exp\left(\frac{-kp_0^2\sigma_z^2 m_{21}}{\xi} - i\frac{\pi(\nu_j + 0.5)}{2}\right) . \quad \text{(C.15)}$$

C.3 Semiclassical Approximation to the Acoustic Timefront

The semiclassical timefront is constructed using Eq. (3.17), where the semiclassical wavefield construction led to $\psi(z,r;k) = \sum_j A_j(k)\exp(iS_jk)$ described in the previous section. Because of the ocean acoustic identification $\hbar = \frac{1}{k}$ for use with semiclassical theory, the semiclassical amplitudes A_j are a function of source wavenumber, $A_j = A_j(z,z_0;r,k)$, in addition to being a function of initial and final depths, z_0 and z and range, r. Inserting the semiclassical approximation for the wavefield $\psi(z,r;k) = \sum_j A_j(k)\exp(iS_jk)$ in Eq. (3.17 gives

$$\begin{aligned}
\phi(z,r;t) &= \frac{1}{\sqrt{2\pi\sigma_k^2}\sqrt{r}}\sum_j \int_{-\infty}^{\infty} dk A_j(z,z_0;r,k)\exp\left(-\frac{(k-k_0)^2}{2\sigma_k^2} + ik(r - c_0t + S_j)\right) \\
&= \frac{1}{\sqrt{2\pi\sigma_k^2}\sqrt{r}}\sum_j \int_{-\infty}^{\infty} dk A_j(z,z_0;r,k)\exp\left(-\frac{(k-k_0)^2}{2\sigma_k^2} - ikc_0(t - T_j)\right)
\end{aligned}$$

where $S_j = S_j(z,z_0;r)$ is the classical action and $T_j = (r + S_j(z,z_0;r))/c_0$ is the travel time of the jth ray traveling from $z = z_0$ to a final depth of z.

Inserting the expression for the semiclassical amplitudes in Eq. (C.15), gives

$$\begin{aligned}
\phi(z,r;t) &= \left(\frac{2\sigma_z^2}{\pi}\right)^{1/4}\frac{sign(m_{21})}{\sqrt{2\pi\sigma_k^2}\sqrt{r}}\sum_j \exp\left(-i\frac{\pi(\nu_j + 0.5)}{2}\right) \\
&\quad \times \int_{-\infty}^{\infty} dk \sqrt{\left(\frac{k}{m_{21} - 2ik\sigma_z^2 m_{22}}\right)} \\
&\quad \times \exp\left(-\frac{(k-k_0)^2}{2\sigma_k^2} - k^2\frac{p_0^2\sigma_z^2 m_{21}}{m_{21} - 2ik\sigma_z^2 m_{22}} - ikc_0(t - T_j)\right) .
\end{aligned}$$

Note that the wavenumber dependence of the integrand is very complicated. However, if

the semiclassical amplitude is approximated $A_j(z, z_0; r, k) \approx A_j(z, z_0; r, k_0)$ with the central wavenumber k_0 dependence, then the integral in Eq. (C.16) can also be performed analytically giving

$$\phi(z = z_0, r; t) \;=\; \frac{1}{\sqrt{r}} \sum_j A_j(z_0, z_0; r, k_0) \exp\left(-\frac{\sigma_k^2 c_0^2}{2}(T_j - t)^2 + ikc_0(T_j - t) \right) ,$$

where the A_j is given by Eq. (C.15). This approximation suggests that the timefront is a superposition of ray arrivals, where each ray arrival is a Gaussian pulse centered on the ray arrival time T_j and with a constant variance $\sigma_t^2 = \frac{1}{\sigma_k c_0}$. It turns out that the true timefronts have pulse arrivals that look very close to Gaussian and are centered close to the ray arrival time T_j, but their variance varies with depth z as seen in Sec. (6.1.6) and (6.2.3). The amplitudes also vary a lot from that predicted by this formula. Therefore the wavenumber dependence of $A_j(z, z_0; r, k)$ is an important effect in the construction of the timefront.

Additionally, for the classical ray with $p_0 = 0$, the path is $z = z_0$ for the unperturbed case and $m_{21} = 0$ and $m_{22} = 1$. In this case, the integral in Eq. (C.16) can also be done analytically giving

$$\begin{aligned} \phi(z = z_0, r; t) \;&\approx\; \left(\frac{2\sigma_z^2}{\pi}\right)^{1/4} \frac{sign(m_{21})}{\sqrt{2\pi\sigma_k^2}\sqrt{r}} \sum_j \exp\left(-i\frac{\pi(\nu_j + 0.5)}{2} \right) \sqrt{\left(\frac{1}{-2i\sigma_z^2 m_{22}} \right)} \\ &\quad \exp\left(-\frac{\sigma_k^2 c_0^2}{2}(T_j - t)^2 + ikc_0(T_j - t) \right) \\ &= \frac{1}{\sqrt{r}} \sum_j A_j(z_0, z_0; r, k_0) \exp\left(-\frac{\sigma_k^2 c_0^2}{2}(T_j - t)^2 + ikc_0(T_j - t) \right) \end{aligned}$$

Therefore the latest arrival in the unperturbed timefront at $z = z_0$ arriving at $t = \frac{r}{c_0}$ is

approximately a Gaussian pulse with variance $\sigma_t^2 = \frac{1}{\sigma_k c_0}$. This is in agreement with the results seen for the variance in Sec. (6.1.6) and (6.2.3).

C.4 Statistical Averaging of the Internal Wave Model

The following are some statistical averages that are used in the theoretical portion in Ch. (5) of this thesis.

If a random variable Φ is Gaussian distributed, then $< e^{i\Phi} >= e^{i<\Phi>}e^{-\sigma_\Phi^2/2}$, where $<\Phi>$ and σ_Φ^2 are the mean and variance of the variable Φ.

In performing the ensemble averages over the different internal wave seeds, recall that ϕ_{j,k_r} is uniformly distributed on $[0, 2\pi]$ and delta-correlated. Then

$$\begin{aligned} < \cos(\phi_{j,k} + kr) > &= \int_0^{2\pi} \dots \int_0^{2\pi} \frac{d\phi_{j,k}^{N_k N_j}}{(2\pi)^{N_k N_j}} \cos(\phi_{j,k} + kr') \\ &= \int_0^{2\pi} \dots \int_0^{2\pi} \frac{d\phi_{j,k}^{N_k N_j}}{(2\pi)^{N_k N_j}} (\cos\phi_{j,k} \cos kr - \sin\phi_{j,k} \sin kr) \\ &= 0 \end{aligned}$$

and similiarly $< \sin(\phi_{j,k} + kr) >= 0$.

Then the ensemble average for a fixed R is

$$
\begin{aligned}
< \cos(\phi_{j,k_r} + k_r r') \quad & \cos(\phi_{j',k'_r} + k'_r(r' + R)) >= \\
&= \int_0^{2\pi} \dots \int_0^{2\pi} \frac{d\phi_{j,k_r}^{N_k N_j}}{(2\pi)^{N_k N_j}} \cos(\phi_{j,k_r} + k_r r') \cos(\phi_{j',k'_r} + k'_r(r' + R)) \\
&= \int_0^{2\pi} \dots \int_0^{2\pi} \frac{d\phi_{j,k_r}^{N_k N_j}}{(2\pi)^{N_k N_j}} \cos\phi_{j,k_r} \cos\phi_{j',k'_r} \cos(kr) \cos(k'_r(r' + R)) \\
&+ \sin\phi_{j,k_r} \sin\phi_{j',k'_r} \sin(kr) \sin(k'_r(r' + R)) \\
&- \sin\phi_{j,k_r} \cos\phi_{j',k'_r} \sin(kr) \cos(k'_r(r' + R)) \\
&- \cos\phi_{j,k_r} \sin\phi_{j',k'_r} \cos(kr) \sin(k'_r(r' + R)) \\
&= \frac{\delta_{j,j'}\delta_{k_r k'_r}}{2} (\cos(k_r r) \cos(k'_r(r' + R)) + \sin(kr) \sin(k'_r(r' + R))) \\
&= \frac{\delta_{j,j'}\delta_{k_r k'_r}}{2} \cos(k_r R)
\end{aligned}
$$

Similarly, $< \sin(\phi_{j,k_r} + k_r r') \sin(\phi_{j',k'_r} + k'_r(r' + R)) >= \frac{\delta_{j,j'}\delta_{k_r k'_r}}{2} \cos(k_r R)$.